Università dell'Insubria
Dipartimento di Matematica e Fisica
and
Istituto Nazionale di AstroFisica
Osservatorio Astronomico di Brera

Doctor of Philosophy Dissertation

Thin glass sheets for innovative mirrors in astronomical applications

by

Rodolfo Canestrari

Supervisors: dott. Mauro Ghigo
dott. Giovanni Pareschi

XXII ciclo di Dottorato di Ricerca - Astronomia ed Astrofisica
Como, 2009

Contents

Preface

This dissertation describes the work done by the author during his PhD program, the main topic is on optical manufacturing technologies for Astrophysical applications. These activities were carried out at the INAF-Astronomical Observatory of Brera and cover about four years.
The work is focused on the development of innovative techniques for the manufacturing of segmented optics for the next generation of ground based telescopes, with particular respect to the European-Extremely Large Telescope and the Cherenkov Telescope Array. Indeed, the Thesis is divided in two Parts each one devoted to a project.

Part I describes the upcoming E-ELT presenting a technical description of the telescope with its main science cases. The following chapters have a detailed description of the work and results obtained by the author and collaborators. The activities concern the investigation of a glass slumping technique for the production of thin and lightweight mirror shells for adaptive optics applications, with particular attention to the secondary mirror of E-ELT. This study is part of a larger effort dedicated to the Design Study of E-ELT and financed in the framework of OPTICON FP6.
It is presented a research and trade-off between different materials, also we have studied and developed a proprietary technology for the slumping of high precision optics made of borosilicate glass. At this regard, we have analyzed various aspects of the technology such as the thermal behavior, the sticking attitude of the materials at high temperature, the influence of the dust, the limitations (on the replication) induced by the gravity. Moreover, we have performed surface and optical characterization of the mirror shells covering a wide spatial wavelength range.

Part II is centered on the new field of ground-based Very High Energy Gamma-ray Astrophysics, whose birth dates to only twenty years ago. Imaging Atmospheric Cherenkov Telescopes have opened a new intriguing observational window, initi-

ating de facto to new research opportunities.
It is reported a brief history of the Cherenkov astronomy, describing the imaging technique adopted by these telescopes and the present day experiments. In the following chapters are presented the CTA project and its main scientific topics. Then, the author presents a new technology specifically ideated, developed and industrialized for the mass production of mirror panels for Cherenkov telescopes. These mirrors implement a sandwich-like mechanical structure made of two borosilicate thin glass sheets and a reinforcing core. Through a proprietary procedure, the glass sheets are bended at room temperature on a precise master up to copy its shape. With this technology have been produced stiff, lightweight, cheap and robust mirrors for the MAGIC II Cherenkov telescope. Furthermore, it is presented an ongoing study aimed to refine the technology for the future CTA. In particular, the author describes the activities and the related results of the investigation for using innovative materials such as foam of glass and glues. It is presented a preliminary mechanical design of a mirror panel made with the new materials proposed, and optical characterizations performed on mirror prototypes.

Furthermore, the author worked (although not reported in this dissertation) on the Ion Beam Figuring technique: a non-contact figuring technique capable to correct surface shape's errors on the low spatial frequencies domain for optical elements of very high accuracy.
The Ion Beam Figuring uses a beam of accelerated Argon ions (at about 1 keV) impacting against the surface under test, this action removes material. The removal power of the beam can be mapped, and since it is very stable in time the overall process can be considered (with good approximation) deterministic. This technique permits to obtain optical surfaces of very high quality in terms of shape's accuracy, and it is probably one of the best corrective process for optics among those available nowadays.
In this context, it has been developed and tested (patent pending) a system capable to concentrate the ion beam emitted from the source on a smaller beam with typical FWHM of about $7 - 5$ mm or less. This permits the correction of small optical surfaces and/or the correction of errors with content of higher spatial frequencies, not otherwise machinable with standard ion source equipments, maintaining a high removal power.
Using this concentrator the author has corrected three small (50×46 mm^2) elliptical mirrors made of ZERODUR®; these mirrors are now installed within the optical elements train of the Laser Launching Telescope (LLT). LLT is used to generate the virtual reference star for the adaptive optics system of the Subaru Telescope. Moreover, LLT mounts also a corrective entrance window (40 mm in diameter) used to compensate some errors arising from stresses of its mechanical

support structure. The author also provided the optical figuring of the entrance window.
Another application is the surface correction of a demonstrative mirror for the Refocusing Mechanism Assembly of the NirSpec instrument that will be on board the James Webb Space Telescope. This mirror is a lightweighted ZERODUR® substrate of about 150×150 mm^2, with a strict requirement on the surface planarity below 5 nm rms.

Part I

Thin glass mirror shells for adaptive optics

Chapter 1

The ESO E-ELT project

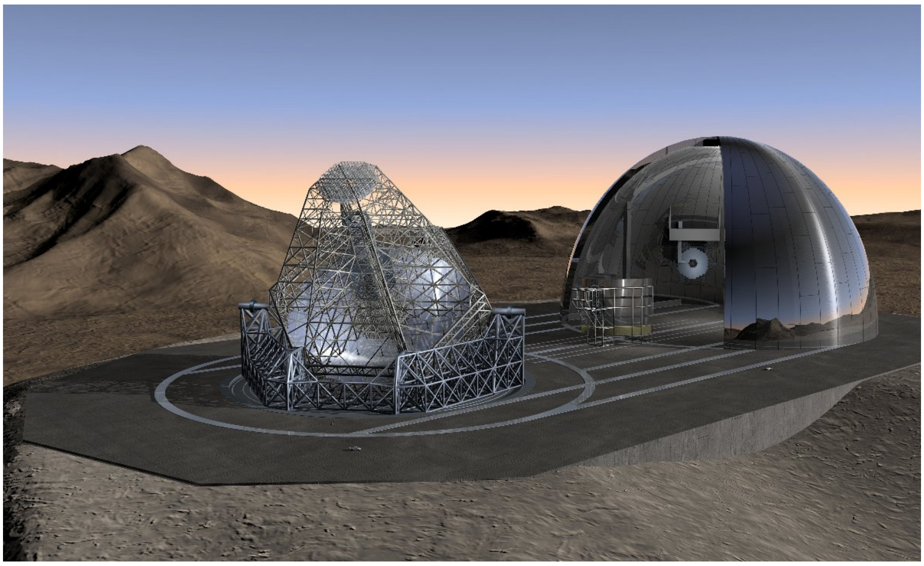

Figure 1.1: An artistic view of the OWL telescope and its enclosure.

Since 1998 ESO has been pursuing a conceptual study for an extremely large optical-infrared telescope with a primary mirror diameter up to 100 meter [1]. It was called OWL for the eponymous bird keen night vision and for being Over-Whelmingly Large (see Figure 1.1).
The first step was the building of a thorough science case for a $50 - 100$ meter ELT by a large segment of the community, the second was the preliminary definition and analysis of an instrument that could cover its science case.
The OWL was based on a spherical primary that allowed the advantages of mass production to contain costs, but at the expense of a complex optical design to

correct for the enormous spherical aberration introduced by the primary (see Figure 1.2).
The OWL had a Phase A review by an ESO international panel in November 2005 and its results collected in the "Blue Book" report (http://www.eso.org/projects/owl/Phase_A_Review.html). The review panel judged the project feasible, but identified some technical risks that might affect the schedule and the budget. Although, early collaboration with industry has led to much progress in a number of crucial telescope design areas such as serial production of (spherical) mirror segments, cheap yet high performance position actuators, large deformable mirrors, etc. These developments give a strong basis to break the classical (and potentially lethal) $D^{2.6}$ cost law. A much more shallow law ($\sim D^{1.4}$) has been established instead, owing in particular to serial production of identical mirror segments, standardized mechanical parts and actuators. And, a strong positive technical point stressed by the panel was the integrated approach chosen for the OWL active/adaptive optics system, in particular with at least one large adaptive mirror as an integral part of the telescope. The panel concluded recommending to consider a smaller diameter, less complex and less risky ELT.

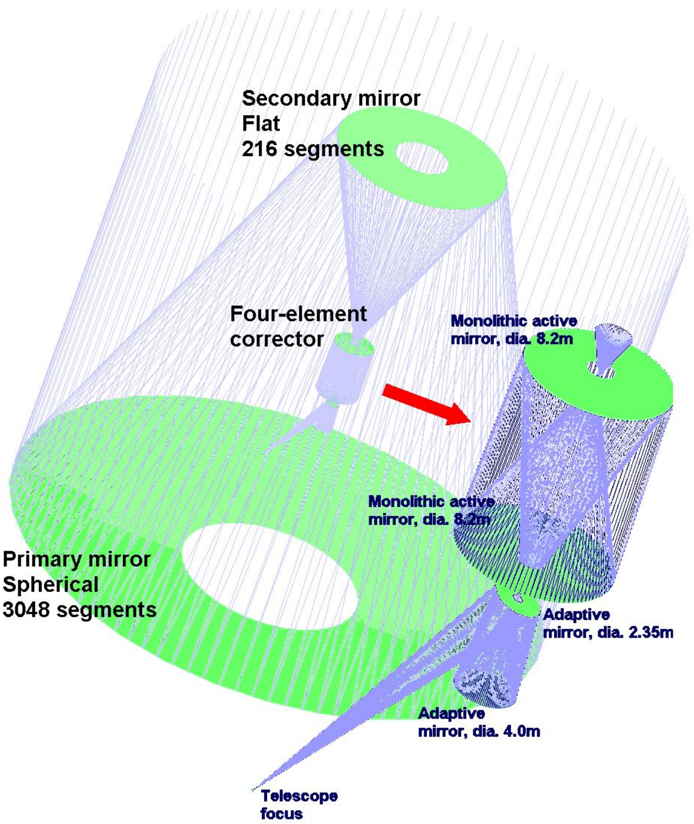

Figure 1.2: The optical design proposed for OWL.

What followed was the definition of a European Extremely Large Telescope [2] that involved extensive community consultation through five Working Groups namely (a) its Science case, (b) an Instrument suite, (c) the associated Adaptive Optics systems, (d) the Telescope and Observatory Design and (e) potential Sites evaluation.
The specific goals to be addressed in the basic reference design were that the E-ELT *should have*:

- a primary mirror of 42 m in diameter (considered a good compromise between ambition and timeliness),
- the primary should not be preferably spherical,
- the telescope should have adaptive optics built into it,
- and should deliver a science field of view of at least five arcminutes in diameter with a strong preference for larger fields.

Additional inputs to the design of the telescope came from the conclusions of the OWL review. In the new telescope design *should be avoided*:

- the double segmentation (M1 and M2),
- the highly asphericity of mirrors unit (M4),
- the high complexity of the adaptive mirror (M6 combined field stabilization and adaptive corrections in a single unit),
- the fast focal ratio of the telescope (not favorable to instrumentation),
- the absence of gravity invariant focal stations,
- and the concept of open-air operation.

All the above points were considered risks that would delay or jeopardize the project and hence things to be avoided in the redesign.

1.1 The optical designs

In the process of evaluating the options for the European ELT, many designs of a fully adaptive telescope were considered [3], but two of these in more detail: a classical Gregorian design and a novel five-mirror design proposed by Bernard Delabre [4] (see Figure 1.3). Both telescopes are based on 42-m diameter aspheric primary mirror, on the elliptical side of the parabola, and to be assembled using more than 900 hexagonal segments (petals are also an option but not in the current baseline), each approximately 1.45 m peak-to-peak in size. However, the latter being an on-axis three mirror anastigmatic with two additional flat mirrors conveniently located to serve as adaptive optics and field stabilization mirrors. Both optical designs deliver a 10 arcminutes diameter, f/15 beam at the Nasmyth focus.

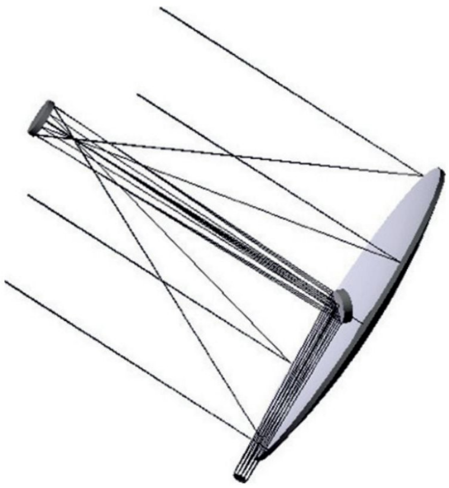

(a) The Gregorian design.

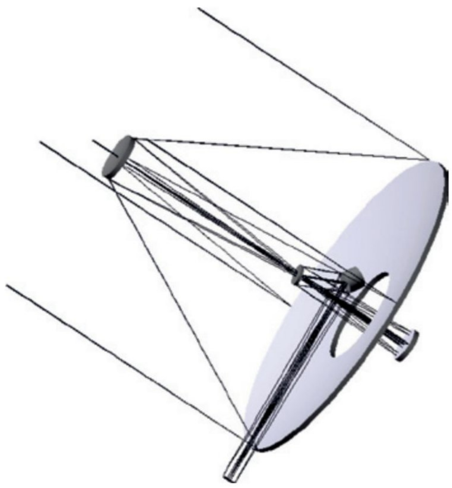

(b) The five-mirror design.

Figure 1.3: The two optical designs considered for the E-ELT project, see [5].

1.1.1 The Gregorian design

This design belongs to the family of Gregorian designs to which the GMT belongs too. The main difference is that in this particular design, there is the possibility to have a Cassegrain focus and one or two Nasmyth foci using a two-mirror relay system. The basic feature of Gregorian designs is the concave secondary mirror which makes its manufacturing considerably easier at the expense of a longer tube length.

An optical layout is shown in Figure 1.4. The configuration combines Gregorian foci under the primary mirror with gravity stable foci on the Nasmyth platforms. The design is here shown with a 4.8 m concave Gregorian secondary, but may also be used with a convex Ritchey-Chrètien secondary.

A Gregorian focus with SCAO may be established with only two reflections and will therefore provide a high throughput, a large field, good IR performance, alignment on one single element, and low polarization. If a folding flat is added, more Gregorian observing stations can be obtained.

With a deformable secondary, it is possible to establish a Nasmyth observing station on the other platform without a powered relay system, simply by using one or two folding flats, re-focusing the secondary, and adjusting the aspherical form of the primary and the secondary. Adjustment of the primary mirror shape

can be done using the segment alignment system and low-order active control systems for each of the segments. The shape of the secondary must also be adjusted, either using active optics or a deformable mirror. With that approach, an additional Nasmyth station with only three reflective mirrors can be obtained. For a rigid secondary, a relay system must be used also for the second Nasmyth platform, requiring totally 5 or 6 reflections in total.
The simplicity and elegance of the Gregorian design would make it a front-runner. The minimum number of mirrors is necessary to relay the beam and it provides a prime focus, particularly useful when wishing to calibrate the adaptive mirror. Furthermore concave mirrors that are easier to polish.

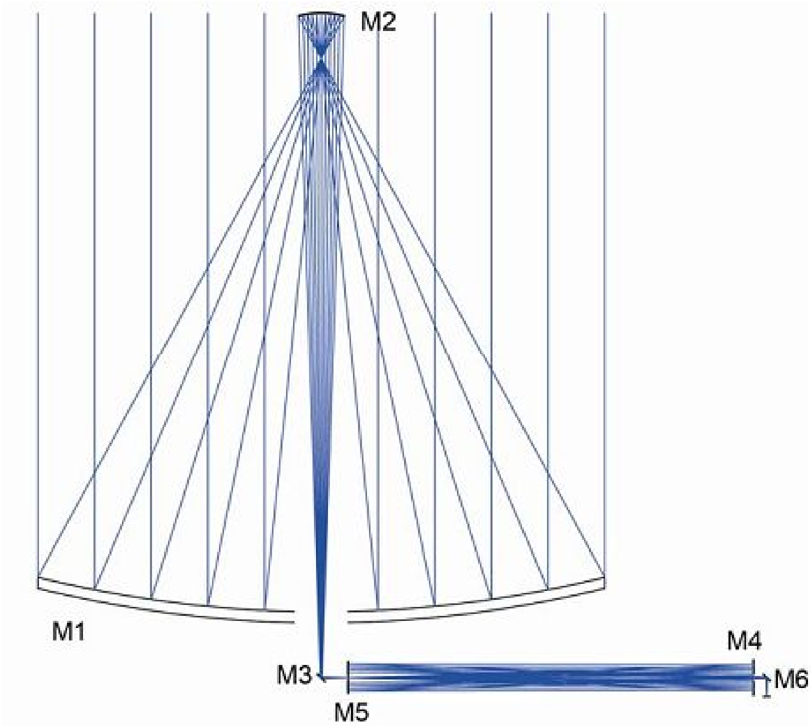

Figure 1.4: Optical layout of the Gregorian/Nasmyth 1 design, see [3].

Advantages:

- small obscuration (1% area). Low emissivity and high throughput;
- provides a Cassegrain/Gregorian focus with only two-mirror reflections;
- equally usable with a deformable or an active, stiff secondary;
- can be implemented with a concave or convex secondary (RC or Gregorian);
- several observing stations can in principle be implemented;

- infrared and polarization friendly at Cassegrain/Gregorian focus;
- the conjugation height of the secondary (a few hundred meters above ground) and the possibility to calibrate a deformable secondary in-situ. A shorter telescope tube can be obtained with a convex Cassegrain mirror but there is risk involved in polishing and testing of a large convex mirror.

Disadvantages:

- aspherical primary mirror;
- a field of maximally 2.4 arcminutes at Nasmyth focus;
- the Nasmyth field is in most cases too small for laser guide stars. Wavefront sensing at the intermediate Cassegrain/Gregorian focus overcomes the problem;
- a Gregorian has a longer tube than a Cassegrain, so the enclosure for a Gregorian is larger than for a Cassegrain. The present optical concept can be adapted for both configurations.

1.1.2 The five-mirror design

The optical design is a five-mirror combination consisting of the two main mirrors of a conventional telescope and of a relay system made of 3 mirrors which accommodate a flat deformable mirror and a flat tip-tilt mirror for field stabilization. A sixth mirror can possibly be added to send the beam downward for a gravity stable instrument.

The “fast” primary mirror (f/1) is aspheric (mildly elliptical), segmented and has a 42 m clear aperture diameter. The secondary mirror is convex and hyperboloid. The image given by these two mirrors is relayed by a third concave near spherical mirror located to the same level of the central obstruction of the primary to improve its ventilation. Two additional flat mirrors, M4 and M5, relay the beam to the Nasmyth foci of the telescope (see Figure 1.5). The size of the hole in the quaternary mirror defines the field and the central obstruction. The deformable mirror is the quaternary while the fifth mirror in the optical train provides for tip-tilt compensation. This optical system was optimised for 10 arcmin field of view and has a flat focal surface.

With three powered mirrors, this design delivers a focal plane that is largely unaberrated at all field locations, the chief ray and the axis of the very limited field curvature (radius of 36 m and convex as seen from the instrument) are parallel. To all intents and purposes it does not matter where in the focal plane you mount your instrument. The focal plane properties are uniformly excellent in the five-mirror design.

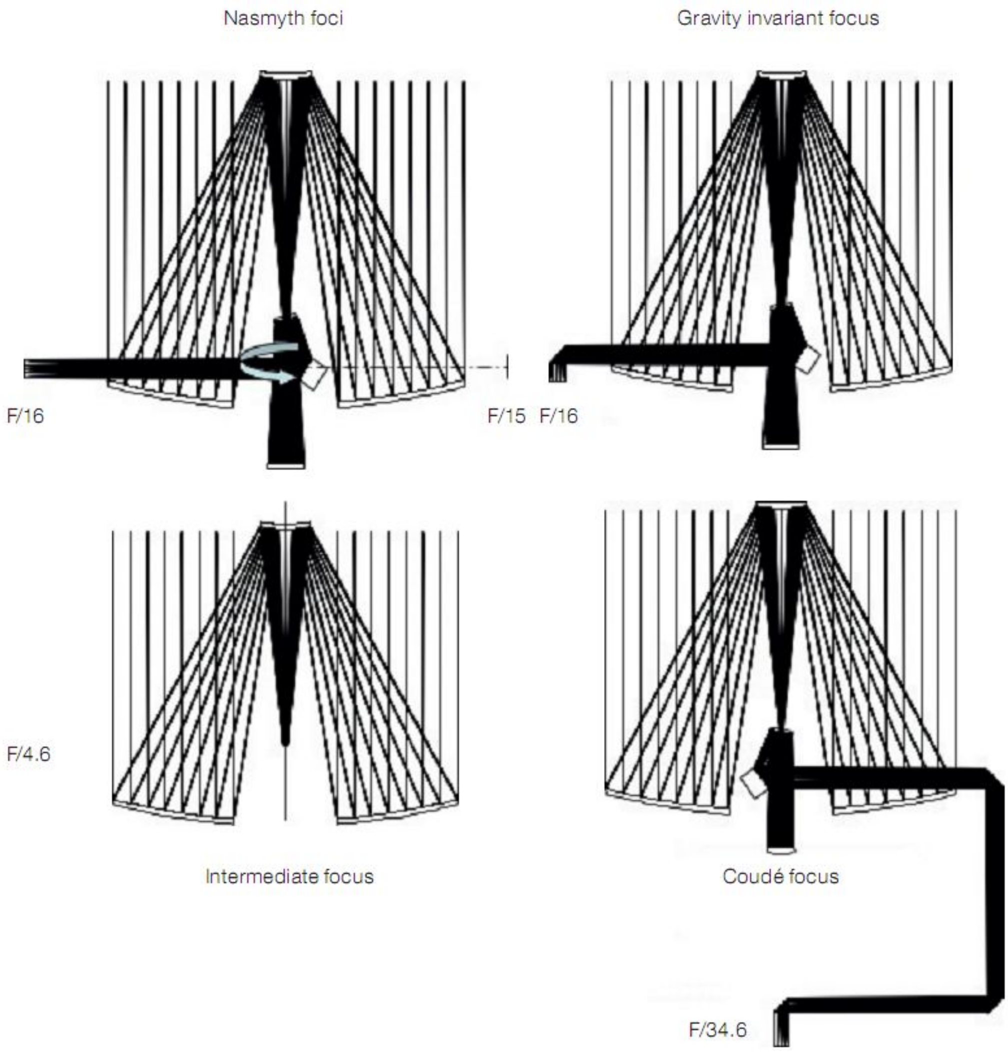

Figure 1.5: Four possible configurations for the foci of the E-ELT. Clockwise from top-left: Nasmyth, gravity invariant, Coudé and intermediate 2-reflection, see [5].

Advantages:

- diffraction limited all over the field at all wavelengths. No field curvature;
- excellent baffling possibility due to intermediate focus and pupil;
- separation of adaptive and field stabilization functions. The fast tip/tilt is done with a dedicated 2.5 m lightweight mirror located at the center of gravity of the telescope;
- relaxed alignment tolerances on M2. Corrections can be shifted to mirrors further down in the optical train at more stable locations and with a lower

accuracy;

- the AO mirror is flat and has a convenient size for foreseeable technology;
- good image quality for LGS;
- possible use of intermediate focus;
- possibility to refocus LGS at intermediate focus (shorter course due to longitudinal magnification);
- short tube, would decrease the size of enclosure
- the M3/M4/M5 makes a separate unit that can be tested independently in a laboratory and relatively protected from the environment.

Disadvantages:

- aspherical primary mirror;
- large convex secondary mirror with delicate manufacturing and testing;
- two additional mirrors with respect to a conventional Nasmyth solution;
- Adaptive Optics mirror tilted by 11.5°;
- Relatively large central obscuration (10% area);
- Delicate access to M3-M4 if elevation axis is above the primary mirror.

1.1.3 Trade-off between optical designs

A detailed trade-off between the Gregorian and the five-mirror design has been performed by ESO [5].
Both the Gregorian and the five-mirror designs provide excellent image quality across the field of view. The Gregorian has field aberrations increasing with distance from the center of the field of view, but their contribution to the image quality is limited to well below any reasonable expectation for the natural seeing. Also, on the basis of the industrial studies it appeared that for a 42 m telescope the complexity, cost and schedule risk of a Gregorian deformable secondary mirror would seriously endanger the project.
The advantages of the five-mirror design, in separating the field stabilization function from the adaptive mirror, make it a very attractive design, because this provides an instrument friendly focal plane. Moreover, with three powered mirrors, the five-mirror design delivers nearly perfect image quality across the entire field of view. However, the manufacturing of the flat thin deformable M4 is anything but easier. With its 2.5 m of diameter, it is more than twice the linear

size of the VLT deformable secondary mirror currently under manufacture. It will have $5 - 10$ times the number of actuators. Also the 2.7 m field stabilization mirror (M5) is far from simple. Significant attention shall be focused on the development of both of the "adaptive" mirrors. Another major challenge for the five-mirror design is the meniscus secondary mirror. Polishing and testing such a mirror requires some innovative approaches. The complexity of this mirror is comparable to that of the very large flat tertiary mirror of a classical design.
The two additional reflections contribute to the total photons count that arrive at the instrumentation detectors. The use of novel coatings, currently under development, can mitigate the effect of more reflections.
Nevertheless, the selection of the five-mirror design as the baseline does not exclude the evolution of many of the design choices.

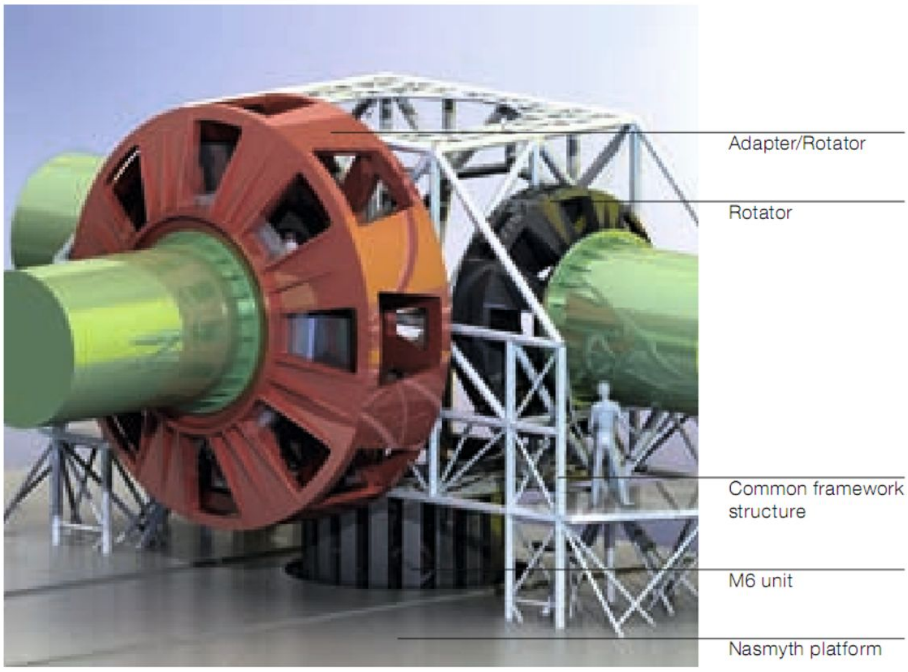

Figure 1.6: CAD rendering of the Nasmyth platform of the E-ELT. The green cylinders represent the volumes of the instruments, see [6].

Furthermore, big telescopes have awkward focal planes. The linear dimensions of the ten-arcminute field of view (see an example in Figure 1.6) of the E-ELT are similar to those of the VLT at Nasmyth, but only one ninth of the area of the sky is imaged. The plate scale and its matching to any detector system or slit are serious challenges for instrumentation, while at the same time a faster focal ratio would severely limit the working volume for the construction of instruments.

Another problem is how to provide for a relatively flat focal plane for the instruments. Classical designs of telescopes, such as the Ritchey-Chrétien or the Gregorian, have significant field curvature (for an E-ELT with the Gregorian solution, the radius of curvature at the focal plane is of the order of 4 m) and rely upon field flattening lenses or mirrors in the instruments to generate the field flatness. This solution is economical in optical surfaces, as often some optics would be required in any case and does not overcomplicate the instrument. This, however, places very strict alignment requirements on the instrument relative to the telescope.

1.2 The mirror units

In order to deliver good images, a telescope not only has to be at a good site, but also has to be a good telescope. More than just having the right optics, the optics has to be properly aligned and kept that way.
In the past century, colossal advances were made in optical materials that allowed the mirrors to maintain their polished surfaces to the correct prescription. With the use of the Serrurier truss, classical telescopes maintained their collimation to the accuracy needed for arcsecond and even sub-arcsecond images. Nowadays, adaptive telescope is the natural evolution of the active ones.
With exacting requirements on image quality, an E-ELT will need to keep objects with good PSFs in very precise positions on the focal plane. In addition to the instruments requiring excellent images, the wavefront sensors also benefit from this good image quality. The distortions of the wavefront, whether from the telescope or the atmosphere, need to be taken into account. Active optics can handle slow variations. For an E-ELT still remain some residual errors (tip-tilt) and therefore other low-order aberrations will need to be corrected.

1.2.1 The primary mirror

The primary mirror of the telescope is composed by 1148 (984 plus spares) segments. Each segment has an hexagonal tile's shape with a diagonal of about 1.45 m. Two large industrial contracts were placed, they entail the production of seven prototype segments. While seven segments out of 1148 may not sound very much, it is required to demonstrate the industrialization of the production process and test the mass production techniques on a variety of mirror substrates. A new big polishing machine is under manufacture for the 1.45 m segments and the design of the test set-up used to determine the performance of the polishing is well advanced.

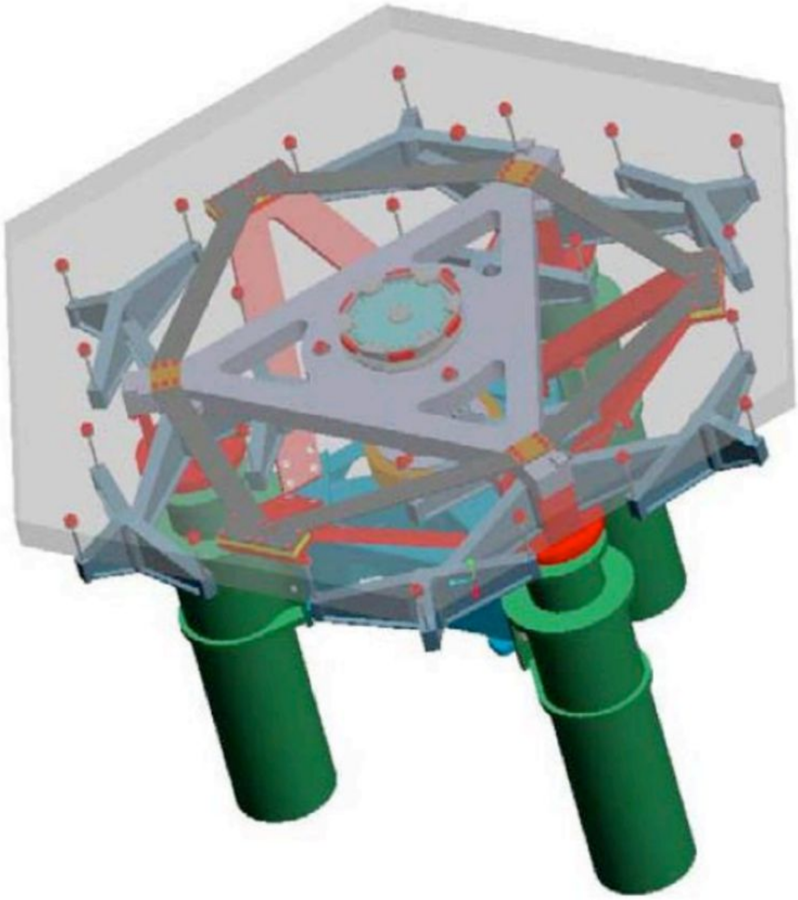

Figure 1.7: The innovative 27-point design with the whiffle tree structure, see [7].

Simultaneously, a study for the design of the primary mirror cell and the supporting elements has been started. Two types of support have been analyzed, one with 27 points and one with 18. A thickness of about 50 mm for the mirror segments is foreseen to reduce the weight of the mirror. However, the thin segments are susceptible to deformation due to imperfections in their supports and the print-through of these supports onto the reflecting surface, which could limit the performance of the telescope. The selection was for the 27-point one. The supporting principle is that the axial loads (i.e. in the direction through the segment) are taken with a whiffle tree structure, while the lateral loads are taken by a membrane implanted in the center of the segment. A moving frame carries the whiffle tree and the central membrane. The moving frame is moved in piston and tip-tilt by three actuators (the green cylinders in Figure 1.7). Additionally six motorized warping harnesses are foreseen to allow for the necessary corrections to the segment shape. A further restraint is designed to limit the clocking (i.e. rotation in the plane of the segment). The side of the segment not facing the sky

is likely to be very complex as Figure 1.7 implies.
In addition to the design of the segment support, a significant amount of work has been undertaken to understand the wavefront sensing needs of the telescope and to develop strategies for phasing the primary mirror, distributing the aberrations among the various mirrors. The prototype edge sensors, as well as the actuators, were also been tested in a climatic chamber.

1.2.2 The secondary mirror

The 6 m diameter and 100 mm thin secondary mirror (Figure 1.8) is significantly smaller than the 8 m blanks made for the VLT and Gemini telescopes so there is confidence in the industrial partners in the production of the blank. The polishing of the mirror that is convex is more challenging but sub-aperture stitching techniques have already been used for the VLT secondary mirrors. Industrial contracts are being prepared for the preliminary design of the secondary mirror unit [7].

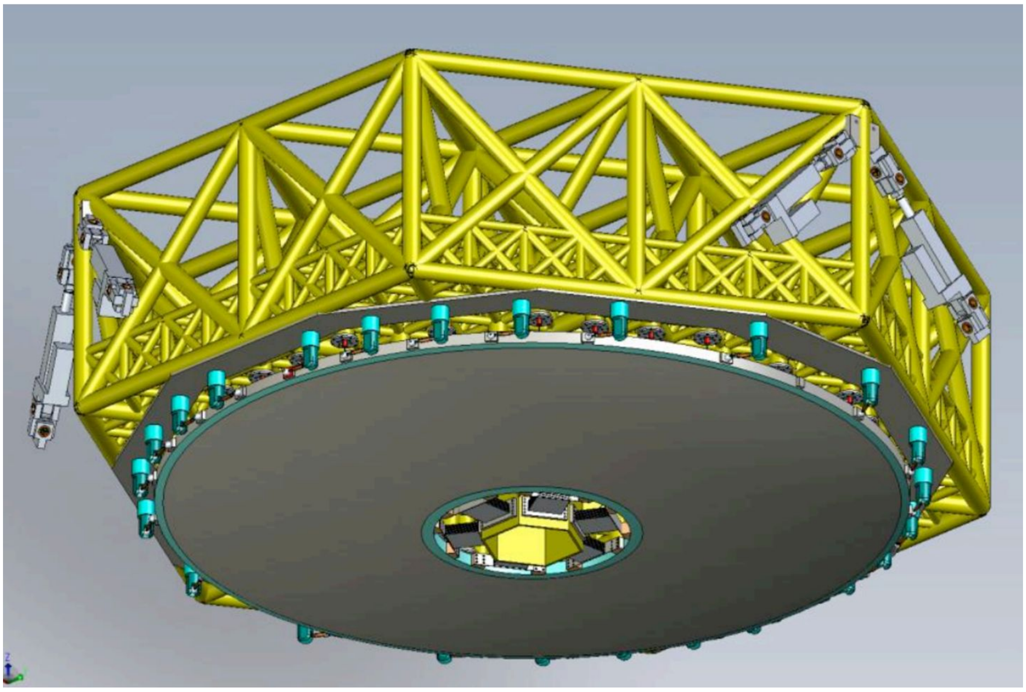

Figure 1.8: The conceptual design of M2 and its supporting structure, see [7].

1.2.3 The Adaptive Relay Unit: M3, M4 and M5

A source of error, actually the major one, is the turbulence of the atmosphere. Of course the adaptive mirror will correct this kind of wavefront errors. This challenge can be translated into a requirement of spatial and temporal flexibility of

the glass. The spatial requirement is typically expressed with two numbers: the pitch of the actuators (or inter-actuator spacing) and their stroke. The temporal requirement is: how fast an actuator can get to the required position and with what accuracy.
When the actuator spacing, as projected on the primary of the telescope, is small, then the actuators map better on to the atmospheric turbulence scale-length and the resulting correction is better. The stroke has to be sufficient to correct the low-order aberrations; the temporal issue is relatively simple: faster is better. Stroke, pitch and actuator rise times are all technological issues.

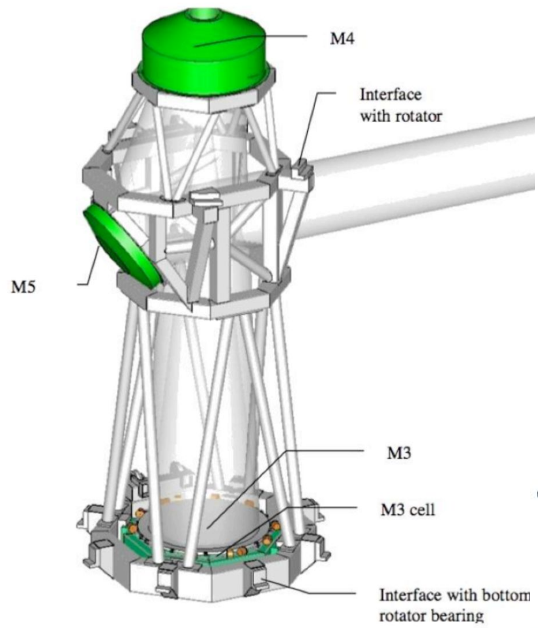

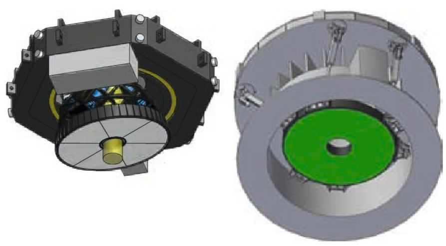

(b) Two possible designs for M4, see [6].

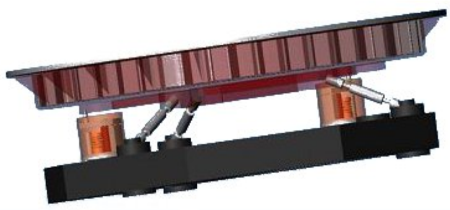

(a) The Adaptive Relay Unit with visible the three mirrors M3, M4 and M5, see [7].

(c) The supporting structure of M5, see [8].

Figure 1.9: The whole active/adaptive system under study for the E-ELT.

The Adaptive Relay Unit is shown in Figure 1.9(a). Three large contracts for the adaptive optics subsystems of the telescope were placed to industries. Two of them were for a preliminary design and prototyping of the adaptive quaternary mirror (M4; see Figure 1.9(b)). The mirror will have over 5000 actuators and will provide ground layer correction for all instruments. The third contract was for the design and 1:1 scale prototype of the electro-mechanical unit to support the fifth tip-tilt mirror in the telescope optical train (M5; see Figure 1.9(c)). This mirror is a tip-tilt mirror and needs to be light-weighted.
The tertiary mirror is mildly aspheric and with a diameter of just over 4 m, neither it nor its cell pose a particular challenge.

1.3 Other aspects

1.3.1 The mount

The telescope mount is of the altitude azimuth type. This structure is a critical component of the telescope design because it should support the multiple segments of the primary mirror with relative displacements of fractions of millimetres as the telescope inclines from zenith to horizon. Meanwhile, it should be accessible for the maintenance of the mirror's segments (Figure 1.10) [7]. The range of the actuators for the primary mirror is directly related to the extent to which the cell will deform as the telescope is inclined from the zenith towards the horizon. Two industrial contractors have provided ESO with designs that meet the requirements for supporting the primary. A rocking chair mount with two cradles, instead of four, is sufficient to provide the required stiffness (Figure 1.11). The first eigen frequency of the structure is around 2.6 Hz. The reduction in moving mass is also an overall cost saver, both in quantity of steel and in all the associated hardware. The design for the telescope mount has been extensively analyzed using FEA models and fairly sophisticated control simulations (see Figure 1.11). In the current baseline both the azimuth and altitude bearings are of hydrostatic type although boogies may be used instead.

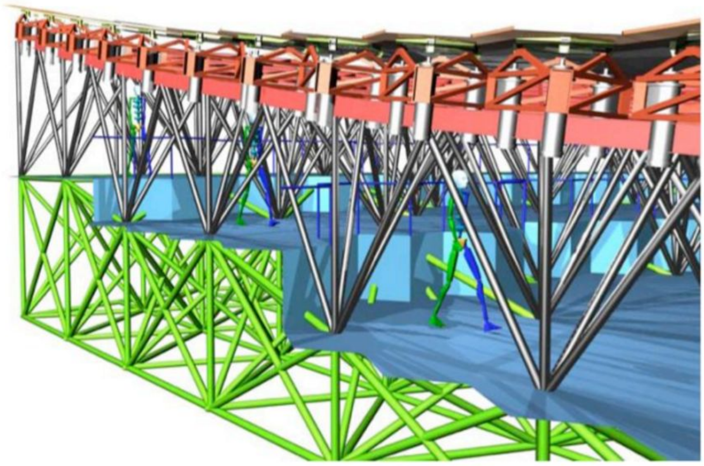

Figure 1.10: The framework structure that supports the primary mirror, see [7].

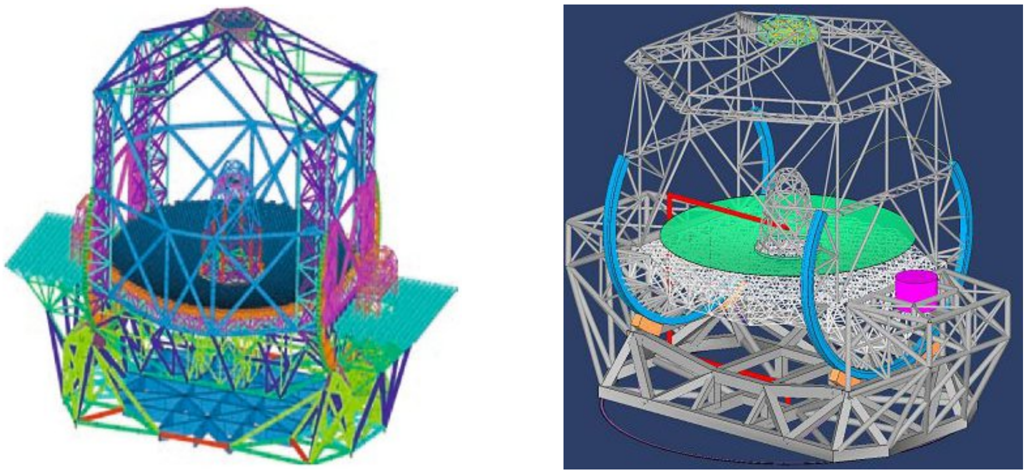

Figure 1.11: Two possible telescope alt-azimuthal mounts have been studied with complex FEA models, see [6] and [8].

1.3.2 The building and the dome

The E-ELT dome will be of similar size to that of a football stadium, with a diameter at its base of order 100 m and a height of order 80 m.
Many challenges have been faced during the design of the dome, such as the wind screen that shields the telescope from the effects of the wind; and the twenty-tonne crane that can access the entire volume of the dome. Two designs have been proposed having elegant solutions for these two aspects. Both designs are similar to the extent that both assume a hemispherical dome but quite different in how the dome is supported and in the nature of the observing doors. One design proposes a single pair of large doors, while the other proposes two sets of nested doors [7].

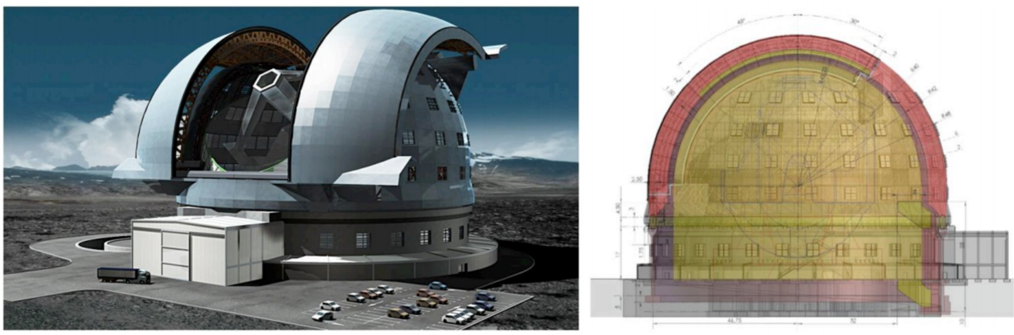

Figure 1.12: The building of the E-ELT and a cross section of the dome, see [7].

1.3.3 The site evaluation

A tool dedicated to tracking climatic trends, FRIOWL has been developed by the Department of Geography of the University of Fribourg (http://archive.eso.org/friowl). This tool has also a first function of helping to locate the most promising areas worldwide on the basis of the longterm average value of preselected parameters. FRIOWL is a geographical information system with a spatial resolution of 2.5° (about 300 km), composed of several layers containing a minimum of 15 years of data stored as monthly averages. The study of the temporal variability of the layers gives later access to the seasonal and longterm climatology of the areas containing selected sites. It is possible to combine the layers with different weights such as to compose dedicated maps of suitability. An example is given in Figure 1.13(c) where topography, precipitable water vapor and cloudiness have been used as reference parameters for IR astronomy. It is easy to see that only a few regions on Earth are suitable, which are however wide enough to provide many candidates which then are compared using the full parameter space [9].

A number of potential sites have been investigated for the E-ELT [7], including (alphabetically) locations in Argentina, Canaries, Chile, Morocco and Mexico. The site characterization process, extensively supported by the community through the FP6 activities, lasted until late 2009. In the mean time the project is making assumptions for the infrastructure needed on the basis of the ESO experience opening the Paranal observatory in Chile. Site selection will take place in Spring of 2010, through the advice of a Site Selection Advisory Committee that has recently been formed. The technical report from the committee concludes that Cerro Armazones, near Paranal, stands out as the clearly preferred site, because it has the best balance of sky quality across all aspects and it can be operated in an integrated fashion with the existing ESO Paranal Observatory. The ESO Council will take the final decision.

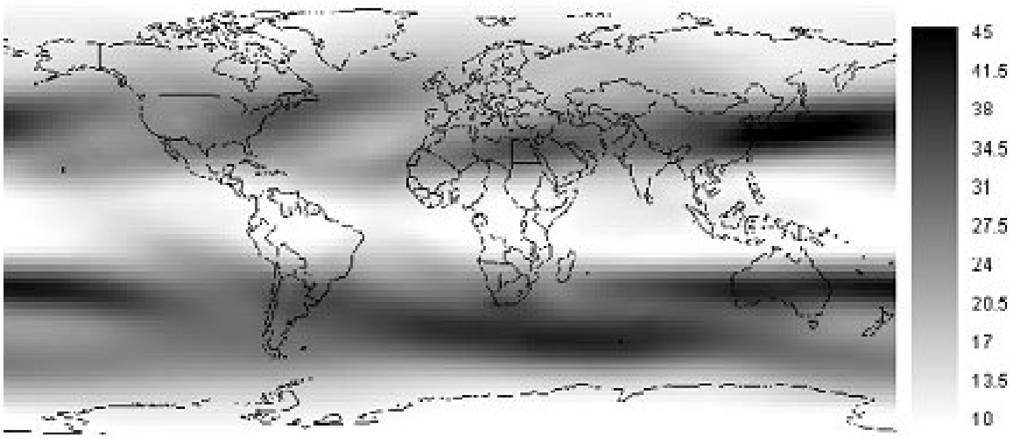

(a) Mean wind speed from 1979-1993 (expressed in m/s).

(b) Mean aerosol index from 1980-2002.

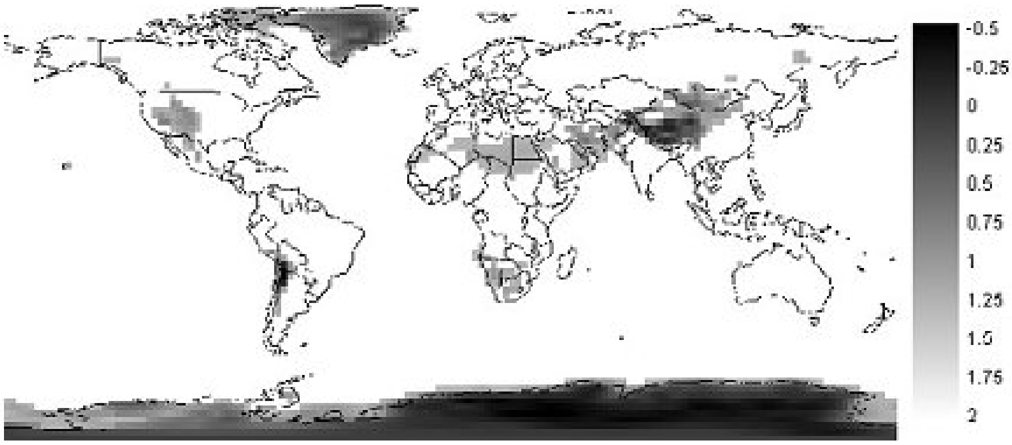

(c) Overlay distinguishing areas providing both high summits, low cloudiness and low precipitable water vapor.

Figure 1.13: Examples of analysis done with FRIOWL, see [9].

Chapter 2

The E-ELT's science case

The ELT will enable fantastic science, from planets to cosmology, and it will enable a very large step forward in all aspects of astronomy. However, careful trade-offs will need to be made to find an optimal design, location and instrumentation. This should be done in order to accomplish the science cases of the project that are based on expected performance at the start of the project, and these will be quite different from the performance at the end.
A second important consideration concerns the synergy with other facilities, the synergy with JWST is a very important driver for the ELT in many of the science cases. JWST and ELT will be very complementary in their capabilities. Above 2 micron, JWST will be the prime instrument for deep imaging with medium spatial resolution. ELT will provide very high spectral resolution spectroscopy, and diffraction limited imaging with a very high spatial resolution. Between 1 and 2 micron, ELT will be most effective for spectroscopy, but JWST will be very suitable for very deep imaging of extended sources. Overall, the complementarity between the capabilities of JWST and ELT is a strong motivation to try to build ELT on a fast timescale. The nominal mission lifetime of JWST of 5 years with a goal of 10 years would only allow substantial overlap if ELT is build in less than 10 years from now.
The examples of HST and the Keck and the VLT are showing that the most interesting science is often the unexpected one. The opening-up of the high redshift universe by 8 m class telescopes was largely unexpected when the 8 m telescopes had been developed. Similarly, the most interesting science that will be done by the 30-40 m telescopes may be very different from the cases here below. Hence, it is important to construct a facility which is efficient and effective in a general sense, and not just optimized to do one or two science cases well.
The scientific use of modern facilities is strongly shaped by the operational models with which they are run. The optimal use of atmospheric and other conditions

requires that the telescope is equipped with a set of instruments to make best use of the prevailing conditions. At the same time sufficient observational programs for the given conditions are necessary for an optimal scheduling of the resources. It is assumed that there will be instruments to cover bright time as well as dark time periods. The success of queue scheduling appears to make the use of service mandatory for the future telescopes as well. Another advantage of this mode is the improved performance for target of opportunity observations.

Since the parameter space has been expanded considerably to shorter and more sudden events, a rapid response mode should be considered. Even though time dilation will slow down the most distant GRBs they still have durations of only a few hours. Other astrophysical processes have very short duration or rapid changes (e.g. flashes from the galactic center, outbursts on stellar surfaces, neutron stars and black holes, shock emission from the shock outburst in core-collapse supernovae, etc.). Opening up this time domain will happen with smaller telescopes, but the rapid spectroscopic follow-up is needed with the largest facilities available. Hence, the telescope should be able to point within minutes at any accessible part of the sky. The acquisition process should be trimmed accordingly.

Operational models should explore the entire chain from proposal submission to data delivery and analysis. The optimal use of the telescope implies that the extraction of the information from the data will need to be facilitated as much as possible.

Issues are the time scale for proposal submission, quality control, data distribution, data reduction and analysis support, archiving and combination with data from other telescopes. Some of these issues depend on the site selection (e.g. data rates from remote sites).

Another item is the coordination of proposals among different facilities. There have been attempts to do this with the existing telescopes (space- and ground-based) and it is quite possible that there will be further scientific integration among different facilities. After all it is one of the stated goals to have synergies between JWST and the ELTs.

For all the considerations mentioned above, the list of science cases here presented is not complete anyway, but it should be useful as a guideline on what science is expected. The science cases are extracted from [10].

2.1 Extrasolar planets

The ELT will be a uniquely powerful facility for the study of exoplanets, from direct or indirect detection through characterization by spectroscopy, to elucidating their evolution.

The recent discovery that at least 7% of solar-type stars host giant planets at separations of less than 5 AU has opened a new domain for research. Through indirect detection techniques, high precision radial velocity measurements of stars and microlensing techniques provide increasing evidence that planets with terrestrial mass and radius may also be abundant. The diversity of the properties (orbital distances, eccentricities and projected mass distributions) of known giant exoplanets has already challenged traditional theories of planet formation: do these planets form via gravitational instabilities in protoplanetary disks or via accretion of planetesimals? what are the planetary environments around other stars? how typical is our Solar System? are there other Earths? how important is evolution for habitability? Characterization via direct imaging and low-resolution spectroscopy of exoplanets in various evolutionary stages will be key to answer these questions. Direct detection will make feasible the determination of masses, radii, composition, atmospheres and temperatures both for giant and terrestrial planets at different times of evolution. This will offer unique information to understand how planets form and evolve. Extremely large telescopes will enable the direct study of planetary systems during their formation from proto-planetary discs for many nearby very young stars. Observations of giant planets in young stellar clusters and star forming regions will trace their evolution as a function of age. An ELT will also be capable of detecting reflected light from mature giant planets (Jupiter to Neptune-like) orbiting at separations smaller than 1 AU around thousands of stars up to distances of 50 pc. It will explore and characterize other solar systems including possible terrestrial planets around nearby stars ($d < 25$ pc). Direct detection of earth-like planets in extra-solar systems may also lead to the search for bio-markers (e.g. water in the near infrared and oxygen bands in the optical far red) via low resolution spectroscopy with a sufficiently large diameter telescope.

2.2 Circumstellar disks

Circumstellar disks appear to be an inevitable consequence of the birth of low-mass stars and brown dwarfs, a repository for excess angular momentum as a molecular cloud core collapses to form one or more protostars. These disks are also thought to be launching pads of the highly-collimated jets and outflows seen to arise during the first few million years in the life of a young star, as twisting magnetic fields lift material off the disk along the polar axes of the star. Most importantly, however, they are believed to be the progenitors of planets, born out of dust and gas in the disks.

While this basic paradigm is well established, there are many key details which remain poorly understood, including the mechanism by which gas giant planets are formed, the time scales over which dust particles agglomerate into planetesimals

and over which the gas is removed from a disk, the chemical processing in a disk and how it is affected by the central protostar and its surrounding environment, and how young planetary systems evolve dynamically into the broad and largely unanticipated array of architectures observed in the solar neighborhood today. Finally, even though almost all young low-mass stars are known to have disks, it is still not yet clear what fraction actually form long-lived planetary systems.
Thus, the formation and evolution of circumstellar disks is an important area of study in astrophysics, from the optically-thick, gas-rich disks seen at 1 Myr to the debris disks of reprocessed dust surrounding stars of 100 Myr and beyond. The European ELT will make crucial contributions to this field, alongside complementary observations to be made with infrared long-baseline interferometers such as the VLTI, millimeter imaging arrays such as ALMA, and highly-sensitive thermal infrared observatories such as the JWST.
The first core capability of an ELT in this context will be high spatial resolution and high contrast imaging to investigate the spatial structure of disks in the putative habitable terrestrial planet-forming zone of young disks in nearby star-forming regions. High spatial resolution is the key requirement and where an ELT will win over the JWST.
The second capability is spectroscopy in the near- and mid-infrared (3-20 microns), in order to study the dynamics of the disks and the chemical processing of dust, gas, and ices. Disk spectra will include features from a wide variety of gas-phase molecules, amorphous and crystalline silicates, PAHs, ices, and organic materials. It is important to trace the processing of these materials by UV radiation, X-rays, and thermal radiation from the central protostar and other, more massive stars in the local environment. These materials cycle back and forth between gas a solid phases as a disk evolves and by studying the astrochemical evolution in detail, it will be possible to trace the formation history of planetesimals and other solid bodies, their composition, their processing, and search for signs of complex organic molecules, the precursors of life.
Finally, it will be important to study the evolution of warm molecular gas is disks as the building material for giant planets. Spatially resolved, simultaneous spectroscopy in a number of rotational lines of H_2 will make it possible to determine the radial distribution of mass and temperature and, in tandem with ALMA studies in the dust continuum, the gas-to-dust ratio.

2.3 Young stellar clusters

The entire mass function of embedded clusters down to a few Jupiter masses (depending on age) will be available to observations for clusters across the Galaxy. A detailed spectral characterization of members over the full mass range will become

possible for the nearest aggregates, including spectroscopy down to ~0.7 microns for the least obscured brown dwarfs. High spatial resolution imaging will make it possible to probe the full range of stellar and brown dwarf companion masses in nearby regions such as ρOph, Lupus, R CrA, or Chamaeleon down to separations of ~2 AU, well within the brown dwarf desert. Direct imaging with high contrast will enable the detection of brown dwarfs and giant planets orbiting within several AU of the central star.
With an ELT, studies of embedded clusters in the Magellanic Clouds and other Local Group dwarf irregular galaxies will be possible to a level of detail comparable to that available only a little more than one decade years ago for the nearest embedded clusters. ELT goals: i) complete census of the stellar content of embedded clusters up to distances of several kpc; ii) spectroscopic characterization of brown dwarf members from the red to the near-IR; iii) spectroscopic characterization of planetary-mass members in the IR; iv) direct detection of planetary-mass companions; v) photometric studies of embedded clusters in the Magellanic Clouds; vi) orbital determination of all stars in the proximity of SgrA*.

2.4 Imaging and spectroscopy of resolved stellar population

With a 42 m diameter telescope it is possible to make photometry and spectroscopy of Red-Giant Branch stars at various distances aiming for: imaging of individual stars; intermediate resolution spectroscopy to determine abundances and velocities at distances of up to 5-10 Mpc and high resolution spectroscopy in M31 and NGC5128.
To understand the formation and evolution of any galaxy we investigate the different stellar components, which together carry a memory of the entire star forming history. We know that galaxies fall more or less into a Hubble sequence, but we do not understand the details of why and how massive galaxies find themselves separated into these different classes. Ellipticals are perhaps the biggest mystery because we do not have an example that is easy in detail nearby.
Low mass stars have extremely long life times, comparable to the age of the Universe, and can retain in their atmospheres the gas, with the elemental abundances intact, from the time of their birth. Thus, if the stars of different ages are picked out of a stellar population, and this is most accurately done if the population is resolved into individual stars, then the star formation rate and metallicity at different times is measured directly. This requires accurate photometry: the measurement of luminosity and color for each star. By counting stars of different ages in a color-magnitude diagram at the main sequence turnoffs the rate at which stars are formed throughout time is directly obtained. This information becomes less direct if brighter evolved stellar evolutionary phases are used. Abundances

and kinematics can be measured from spectra of individual stars of known ages and thus the varying abundance of different elements and their kinematic history can be directly measured with time. It is also interesting to study (young) massive stars in a range of environments to try and understand the reasons for star formation to occur at different rates at different times in a variety of environments. The separation of a galaxy into its individual stars for the detailed reconstruction of the history of its formation and evolution requires high spatial resolution and sensitivity (see Figure 2.1). The exact requirements depend upon the stellar density at a given magnitude in the region being probed.

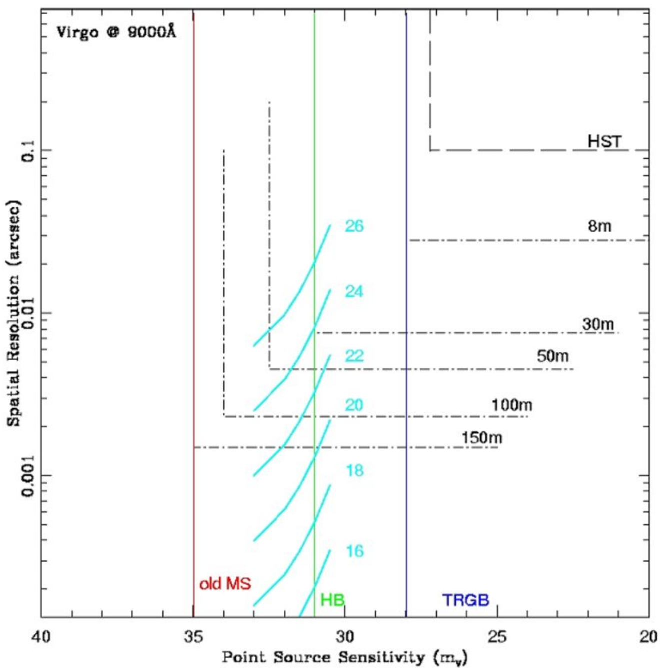

Figure 2.1: The results of ELT sensitivity and spatial resolution calculations. The dashed half-box lines show the parameter space accessible to different aperture telescopes at an observing wavelength of 900 nm.

It is difficult to reach definitive conclusions on the general formation path of massive galaxies with a sample of just two (the Milky Way and Andromeda). However, to enlarge our sample we need to move considerably further away in distance, the Sculptor Group and the M81 group (both at about 2-3 Mpc distance) contain several more large spiral galaxies, but still no elliptical galaxy. For the nearest large elliptical galaxy we have to go to NGC5128 (Centaurus A, which is a very peculiar galaxy, S0+Spec) at 3.5 Mpc distance, but unfortunately as this system is so complex it is unlikely to be representative. The Leo Group at ∼10 Mpc distance contains the nearest nearly normal elliptical galaxy, NGC3379 (E1 or S0). But of course the Virgo cluster is the real prize for studying elliptical galaxies. Virgo at an average distance of 17 Mpc, with over 2000 member galaxies of all morphological types, is the nearest large cluster of galaxies, and the nearest "dense" environment which may be better representative of the surroundings in which most galaxies live and hence most star formation occurs in the Universe. It has a sequence of bright elliptical galaxies and a luminosity sequence reaching down the smallest dwarf elliptical. The Virgo Cluster also contains spiral and irregular galaxies of all luminosities with a variety of globular cluster populations as well as dwarf galaxies, and intracluster stellar populations. These galaxies have never been studied in such detail in a galaxy cluster. This would also have implications for understanding high redshift observations.

2.5 Black holes and AGN

The relationship between host galaxy bulge mass and Black Hole mass (m_{BH}) is well established for both active and currently inactive galaxies [11]. Except for the very nearest galaxies, including the Milky Way, m_{BH} is determined rather indirectly using methods that rely on various geometric assumptions. To confidently detect and measure m_{BH}, we need to probe the volume within which the black hole dominates the galactic dynamics. Called the "sphere of influence", this region has a radius defined as:

$$r_i = \frac{GM_{BH}}{\sigma^2} = 4.3pc \left[\frac{B_{BH}}{10^7 M\odot}\right] \left[\frac{\sigma}{100km/s}\right]^{-2}$$

where σ is the stellar velocity dispersion. A typical scale is around 7 pc.
There are currently only two cases where this region has been probed directly to show that a massive black hole is the only physical possibility: our Galaxy and NGC4258. However, using AO instruments on the VLT, other nearby galaxies are being examined.
The high angular resolution and sensitivity of an ELT will allow:

- to resolve nuclear sub-structures down to a few pc at distances of tens of Mpc. This will allow mass determination of black holes with masses similar to the one in the center of the Milky Way out to the distance of Virgo;

- to resolve bright stars in the circumnuclear region and so the measurement of age, metallicity and velocities of the nuclear stellar populations in the host galaxy, an extension of the work in our Galaxy to other hosts;

- to carry out R$\sim$1000 resolution spectroscopy of indicative lines in bright QSOs out to very high redshifts and thereby obtain estimates of m_{BH} throughout the universe. Such measurements are fundamental to the understanding of the relationship between the evolution of the black hole and the host galaxy, including the possible connection between AGN and starburst activity.

2.6 The highest redshift galaxies (z > 10)

One of the important challenges in astronomy is to find the earliest galaxies. Obviously, we currently know very little about $z > 10$ galaxies. Bremer and Lehnert (2005) estimated the surface density of UV bright galaxies at $z = 9 - 10$ at $m_{AB} = 27$ to be as high as 0.2 per arcmin^2. Given that multiple studies indicate that the space density of these galaxies is likely to be significantly lower than that of similar star forming galaxies at $z = 3 - 4$, the very high redshift population is both faint and rare.

The faintness of the galaxies will make continuum spectroscopy with JWST hard, and only achievable to about $m_{AB} = 29$ in very long exposures at low resolution. Hence ELT will play a very important role in this field, by doing high resolution spectroscopy. Ultra deep imaging by JWST or ELT should identify $z > 10$ candidates over large areas and to very faint magnitudes (to $m_{AB} \sim 29.8$ with JWST in one band in 10 hours).

In typical integration times of 100 hours one can expect to achieve a depth of about $28 - 28.5$ depending on the source sizes with a 30 m telescope. Given these long integration times and the rather low surface density, it is clear that the ELT must have a relatively wide-area spectroscopic capability. The desired area is 10×10 arcmin^2 to allow studies of large scale structure at these redshifts, providing 10 or more such fields are studied to overcome cosmic variance.

Although various studies have shown that galaxies become smaller with increasing redshift, the high redshift galaxies observed to date are resolved with typical half-light radii of $0.1 - 0.2$ arcsec. Consequently, diffraction-limited performance is not necessary, it is more important to have sufficient image quality to concentrate the light from galaxies on the $0.1 - 0.2$ arcsec scale.

These observations will give us redshifts, but also spectral characteristics like emission lines, etc, leading to significant insight into the nature of these sources. It might be expected that the earliest galaxies have dramatically different spectral properties from $z = 3 - 5$ galaxies. At extremely low metallicities, the emission lines of NIV, CIV, HeII, etc. are expected to become very strong. These unique diagnostic lines can be used to determine the ionization state of the gas and thereby constrain its metallicity.

The same spectral information will allow determination of the spectral properties of the earliest stars, possibly allowing identification of galaxies with a substantial population III component.

The next step in this research is to determine the clustering, giving crucial insight into the properties of the dark matter halos in which they reside. Quantifying this in a statistically useful manner at the highest redshifts requires large samples with spectroscopic redshifts (at least 1000 redshifts). This again requires a large multiplex and field-of-view.

2.7 Dynamical measurement of the expansion history of the universe

Measuring the time derivative of the redshift z of objects at fixed coordinate distance offers the unique possibility to measure the expansion history of the Universe directly. Recent observations of the luminosity distance of moderate and high redshift supernovae of type Ia in tandem with other observations have established the presence of a form of dark energy which appears to have a very similar effect to that of Einstein's cosmological constant within the framework of a Friedman-Robertson-Walker universe as described by 4D general relativity. The introduction of the concept of dark energy is somewhat reminiscent of the "Ether" in 19th century physics and is arguably the biggest conundrum of present-day physics. It is thus important to measure the dynamical effects of "dark energy" directly.
The time derivative of the redshift of light emitted by a source at fixed coordinate distance is related in a simple manner to the evolution of the Hubble parameter between the epoch of emission and receiving,

$$\dot{z} = \frac{dz}{dt} = (1+z)H_0 - H(t_e)$$

The wavelength shift corresponds to a Doppler shift of about $2 - 20\ cm/s$ over a period of 10 years. It has a very characteristic redshift dependence and increases linearly with time. Measuring such a small wavelength shift requires a substantial improvement in the accuracy of the wavelength calibration compared to existing spectrographs and a sufficient numbers of photons to measure the shift statistically from a large number of spectral features observed with very high signal-to-noise ratio.
The CODEX concept study [12] identified the numerous absorption lines in the spectra of high-redshift QSOs in the redshift range from $1.5 < z < 4$ as the most promising targets for a measurement of $\dot{z}$. A detection of the dynamical effect of dark energy should be feasible with a 30 m telescope over a period of 20 years. A quantitative characterization of the dark energy and its evolution would require either a larger collecting area or a longer time baseline or both. Note that the total collection area not the aperture is relevant and that results obtained at different telescopes can be combined provided a suitable wavelength standard is available. Note further that the spectra obtained for measuring $\dot{z}$ will

also be tremendously useful to study the variation of fundamental constants and the metal enrichment of the IGM.

2.8 Physics of high redshift galaxies

About ten years ago, the advent of the 10 m class optical/near-IR telescopes opened the possibility to identify spectroscopically normal galaxies out to $z \sim 7$ and to perform the first studies on galaxy formation and evolution in the framework of the successful scenario of ΛCDM cosmology. However, these observations have rapidly reached their limits both in the spectroscopic identifications and in obtaining the moderate- to high-resolution (R∼1000+) spectra of high-z galaxies required to derive their physical and evolutionary properties (with the exception of the brightest galaxies at each redshift). Future ELTs will allow to overcome the above limitations and to identify and to perform detailed spectroscopic studies of high-z galaxies that now are simply impossible. The availability of high-performance AO and Integral Field Unit systems will also allow obtaining spatially resolved spectral information. This will provide crucial information on baryon physics in galaxy evolution models and to drive the transition from current phenomenological models to a physical understanding of galaxy formation and evolution. The information that can be derived with future ELT observations in the optical and/or near-IR is extended to several cases that can be divided into three main groups and summarized as follows.

2.8.1 Physical parameters from integrated spectroscopy at moderate- to high-resolution

Dust extinction is currently very difficult to estimate because the Balmer lines are redshifted in the near-IR, where the current sensitivity is often not enough to detect lines such as H_β. With ELT spectroscopy it will be possible to easily derive E(B-V) from Balmer line ratios. The knowledge of E(B-V) is essential to derive physical parameters reliably and to break the complex degeneracies due to dust extinction.

The Star Formation Rate will be derived from the extinction-corrected emission line luminosity, and compared with other indicators coming from multi-wavelength observations (e.g. ALMA, Herschel, JWST). The knowledge of the dynamical masses will constrain the specific star formation rates and the mass growth history in galaxies.

The ratios of rest-frame optical emission lines redshifted in the near-IR will allow to constrain the ionization processes (e.g. stellar vs AGN photo-ionization, shock-ionization) and the metallicity of the ionized gas. Additional constraints on metallicity will come from UV absorption lines redshifted in the optical.

The detailed properties of the stellar continuum, absorption and emission lines

will be used to derive the age, metallicity and star formation history of the stellar population and to break the degeneracies between these quantities that affect the interpretation of the current results.
The relative velocity of emission and absorption lines of different species will place important constraints of the ISM physical state and dynamics. This will also allow to identify the sources of feedback processes (energy injection into ISM, superwinds, outflows, AGN) and the origin of the Star Formation quenching in massive halos and its possible link with the onset of the massive black hole - bulge relation and galaxy/AGN co-evolution.
It will be possible to quantify the role, physics and rate of merging in modulating star formation, mass assembly and morphology evolution by studies of galaxy pairs and groups as a function of redshift.
By measuring masses, ages, and metallicities of galaxies along the red sequence, it will be possible to understand the physical origin and evolution of the old early-type galaxy population and the onset and evolution of their scaling relations (e.g. Fundamental Plane, Mass-Size, ...).
It will be possible to study in details the dependence of several physical and evolutionary properties as a function of the environment.

2.8.2 Detailed Physics of individual galaxies

The large diameter of the ELT will enable very high spatial resolution imaging and spectroscopy, and thereby unique insight into the physical processes occurring in the high redshift galaxies. The resolution will be of order 0.01 arcsec in the H band, equivalent to 80 pc at $z = 3$. Imaging at this resolution will give immediate insight into the dynamical state of the galaxy, and will address questions like: is the galaxy merging; is there a rain of small galaxies/units falling in; does the galaxy have a wind; does it have a cold disc, etc. We will be able to analyze these galaxies with the same physical resolution as we can observe galaxies in Virgo with 1 arcsec resolution imaging.
High spatial resolution spectroscopy will be able to provide direct kinematics of stars and gas. To allow reasonable integration times, the spectroscopy will be performed at lower resolution (0.05 arcsec) over the full galaxy (typical sizes of $0.5 - 1$ arcsec). The central parts can be observed at the highest resolution (0.01 arcsec). The spatially resolved spectroscopy will provide unique insight into the interaction between stars and gas, flows, and possibly, ordered motion in either the stars or the gas, enabling much more accurate mass estimates. The high spatial resolution spectroscopy will not be achievable by any other means (ALMA, JWST, etc), and therefore completely unique.

2.8.3 Spectroscopic identification of high-z galaxies and surveys

ELTs will be essential to derive the spectroscopic redshifts and the main physical properties of the high-z galaxies that are too faint for the current optical and near-IR spectroscopy. Examples are represented by old/passive systems at $z > 1.5 - 2$, dust-obscured systems, very faint Lyman-break galaxies, galaxies belonging to protocluster structures, high-z clusters found with S-Z surveys. Future imaging surveys in the near-IR to millimeter (e.g. HAWK-I, VISTA, Herschel, ALMA, JWST) will provide large samples of distant galaxy targets that will be beyond the spectroscopic capabilities of the 10 m class telescopes.

Chapter 3

The Hot Pressed Direct Slumping technique

In this chapter is described the glass slumping technique applied to manufacture thin glass mirror shells for AO. This work has followed a roadmap within a time-frame of 2.5 years. The study is part of the OPTICON activities financed by the FP6 of the European Community. The investigation is also part of a larger effort dedicated to the the E-ELT Design Study.
In particular, for this investigation has been produced a demonstrative scaled size slumped shell having a diameter of 0.5 m. The purpose is to demonstrate its feasibility within the requested tolerances and investigate its optical performances, but keeping inside a reasonable limit the cost of the equipment and materials. Nevertheless, all choices done and the equipments used during the activity have been taken without foreclose the capability of manufacture a demonstrator with larger dimensions.
Further purposes are: (a) to demonstrate the manufacturing of either concave or convex thin glass shells; (b) to investigate the application of this technique to glass sheets with thicknesses in the range of 1-10 mm; (c) to provide underlying cost estimates.

3.1 The description of the process

Slumping is a word used to describe an area of techniques for the forming of glass by applying heat to the point where the glass becomes plastic. The increasing fluidity of the glass with temperature causes the glass to "slump" onto a mould under the force of gravity.

The process here discussed uses commercially available borosilicate glass sheets, not specifically addressed to optical applications, to manufacture thin substrates for deformable mirrors. Through this process the glass sheet will copy with a very high degree of fidelity the shape of a mould. The mould can be reused to produce many substrates, one identical to each other, exploiting the concept of "replication process". This is a very attractive possibility to reduce strongly the costs, production time and possible damages arising during the standard figuring and polishing steps. Indeed, the aim of this study is to develop a process able to deliver replication of a master shape within optical requirements.

In more details, this slumping process uses a mould made in a suitable material, heat resistant. Its upper surface has a shape complementary to that required for the glass shell because the surface of the latter in *direct* contact with the mould will be the optical one. For this application the surface of the mould has a convex spherical profile with 5 m of radius of curvature, it is optically figured and polished. The latter requirement is necessary because the process gave proofs to be able to copy not only the geometry of the mould, but also part of its microroughness. The glass sheet that will transform into a mirror substrate is a disk of 0.5 m in diameter and 1.6 mm of thickness. Its resulting profile will be a concave sphere f/5*.

In a oven the glass sheet is heated following a predetermined thermal cycle, usually composed by a number of phases. The heating rises up the temperature till the glass is soft enough to copy the shape of the mould; this occurs in a range varying typically from 550 ℃ to 700 ℃ depending on the type of glass.

The overall process happens inside an hermetical stainless steel box called muffle. The muffle ensures a uniform temperature distribution during the entire slumping because it spreads the heat around the mould and it permits to remove a large fraction of the air (by a mechanical vacuum pump), reducing the convection in advantage of the irradiation. Furthermore, it prevents dust particles to be trapped between the surface of the mould and that of the glass sheet. In fact, the dust, even small grains, can be detrimental for the process because it prevents a correct copy of the mould's shape.

In a cleanroom environment both the mould and the glass sheet are accurately cleaned from any residual grease by inaccurate handling and from dust particles. Then, they are placed into the muffle, the glass above the mould, and it is sealed. A thermal cycle is executed rising the temperature up to about 650 ℃. To ensure a full and homogeneous slumping of the glass onto the mould, the process does not occur merely with the gravity force, but it is assisted by an additional force that pushes or *presses* the glass. This force is applied on the top side of the glass sheet when the oven approaches the slumping temperature. Also, it speeds up

*The choice of these values (radius of curvature, thickness of the glass sheet and concave/convex shape) is explained in later sections.

the procedure. At the end, the glass sheet will be adapted to the shape of the mould and it can be released.
In Figure 3.1 is shown a summary of the process so far described.

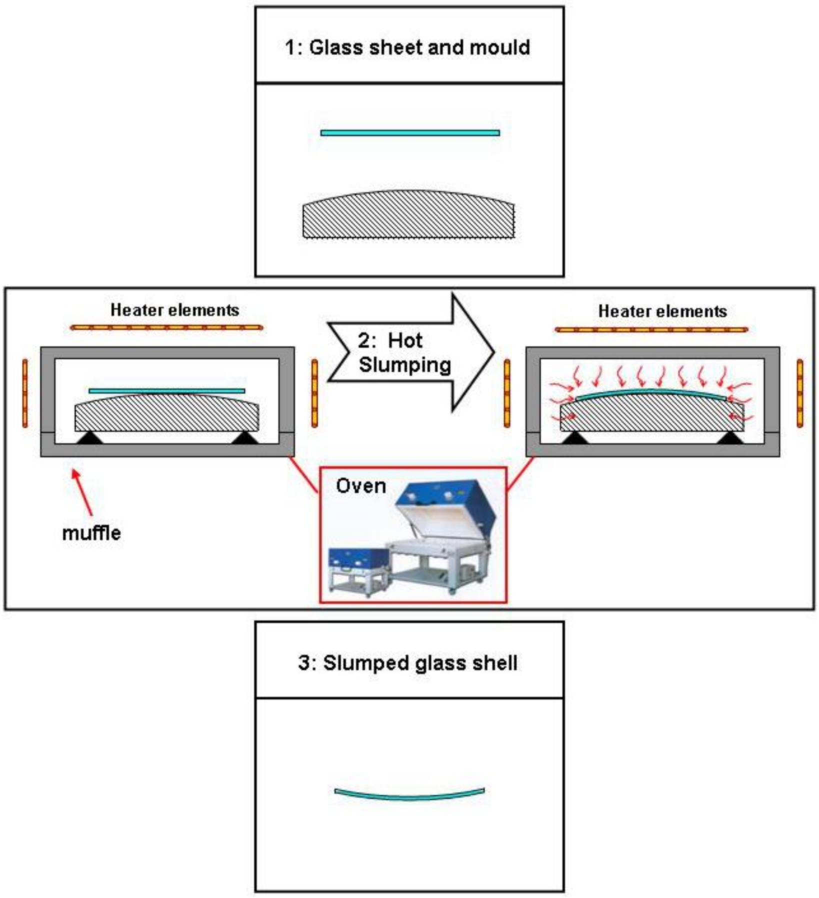

Figure 3.1: The glass slumping process.

Four major phases have been conducted for this study and prototype realization. The following sections recall these phases:

§ 3.2 Determination of the optimal oven's configuration and of the thermal cycle necessary to obtain a uniform temperature distribution on the mould and of the glass during the process.

§ 3.3 Definition of the material and surface quality, procurement of the mould, definition of the type of glass for the thin shell demonstrator.

§ 3.4 Development and manufacture of the support to sustain the thin shell during its characterization.

§ 3.5 and § 5.5 Manufacture and characterization of one thin shell demonstrator.

3.2 The oven, the thermal cycle and the muffle

At the beginning of the activities a study has been conducted to determine the thermal characteristics of the oven and the configuration needed to obtain the most uniform temperature distribution on the mould during a thermal cycle.
To this purpose, a FEA software program has been used and a modeling of the oven has been performed. The model takes as input parameters both constants (i.e. the thermal characteristic of the materials used: mould, muffle, oven ect) and variables:

- the dimensions (x,y,z) of the oven's cavity;
- the number, length, location and emitted power of the heater elements;
- the dimensions, shape and location of the mould;
- the dimensions, shape and location of a stainless steel muffle (if any).

To validate the FEA model a real thermal cycle has been performed using an oven available in a glassblowing firm. The experiment consisted in running a thermal cycle and recording the temperatures read in different points of the oven. We have used 6 thermocouple probes with a multi channel data recorder. In addition we placed a stainless steel box inside the oven to simulate a muffle.
The comparison between the experimental data and the simulated thermal behavior of the oven has been used to refine the FEA model. In Figure 3.2 are plotted the two sets of data (real and simulated), they show the good agreement achieved. In particular, at the plateau and the cooling phase, that are the most critical and important steps of the process.

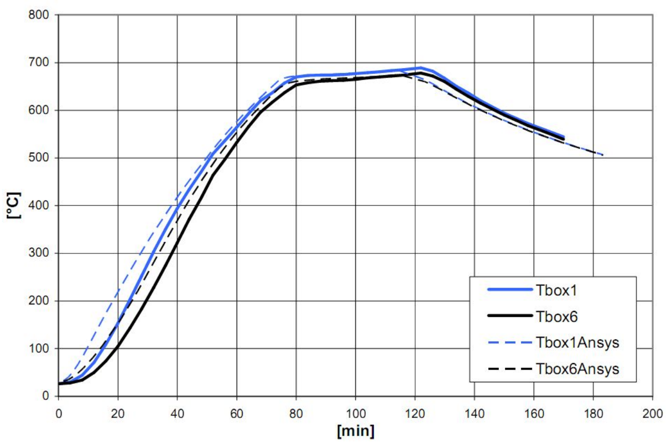

Figure 3.2: Comparison between measurements and the thermal model of the oven.

Using this model, we derived the specification for the oven to be used for these activities. In addition to the thermal characteristics discussed above, some more general features are required. The oven should:

- permit an easy access to its internal cavity, i.e. employing a system with a sliding carriage;
- have a programmable electronic control device allowing a direct control of the temperature cycle and a feedback from the temperature sensors;
- have the lower main plane able to support a maximum load up to about 900 kg (to take into account a possible follow-up study with mould up to 1 meter);
- reach a maximum temperature of 900 ℃ (the typical temperatures for glass slumping are in the range of 550 – 700 ℃)

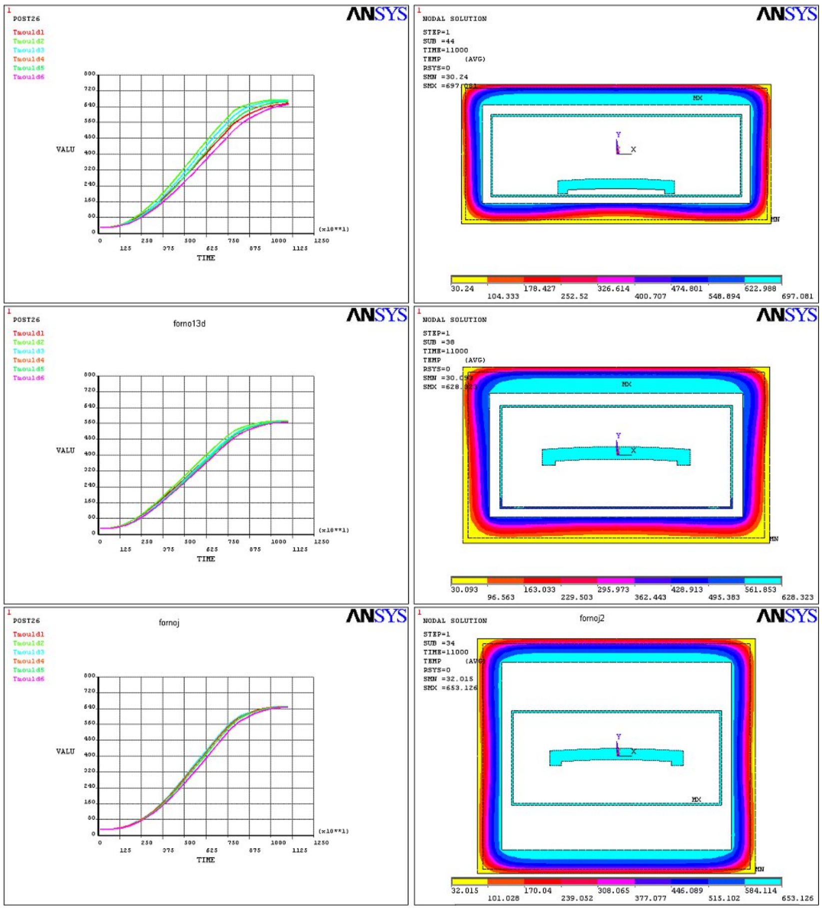

Figure 3.3: Some of the 37 configurations explored to determine the oven/muffle/mould configuration.

In total, a set of 37 different configurations were investigated changing the parameters listed above, some of these are visible in Figure 3.3. The configuration selected is in Figure 3.4 [13], the maximum difference in temperature between six representative points monitored in the simulation is less than 4 ℃ after the heating of the oven. The oven should have a rectangular cross section, with the base larger than height. It is useful the use of a muffle for having a better temperature distribution. The muffle should be located at the center of the oven's cavity, with its height that fills the oven. The mould should be located inside the muffle, in its center.

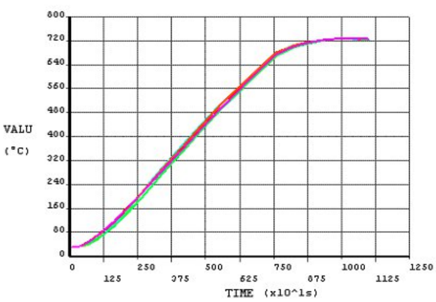

Parameters used:

internal oven lenght	1.4
internal oven high	0.6
box thickness	0.005
box lenght	0.8
box high	0.5
mould thickness	0.1
mould distance from box	0.18
mould material	Alumina
position of the heaters:	center up&down
presence of an insulating material	no

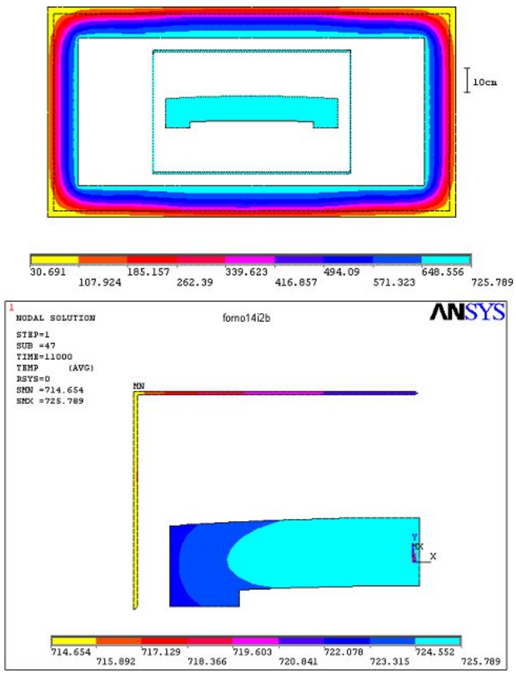

Figure 3.4: The configuration chooses for the oven.

3.2.1 The oven

Internal size Since, in general, segmented optics are composed by segments with a symmetric tile's shape, we have chosen to have an oven with squared cavity. Its internal dimensions are $1.4 \times 1.4 \times 0.6$ m^3, this permits to host moulds having a diameter up to about one meter, which is an interesting size in case of a follow-up demonstrator to be developed with a 1:1 scale (or near). In Figure 3.5 it is shown a picture and the technical drawing.

The value for the internal height has been chosen to permit to position the muffle/mould at different levels inside the oven. This is an important parameter to facilitate a uniform heating, as the thermal analyses have shown. In fact, a large height produces a better distribution of temperatures, however, an upper limit is imposed by outer conditions like the accessibility or the handling of the muffle and mould (a higher oven implies a higher hence heavier muffle).

(a) The oven installed in the lab.

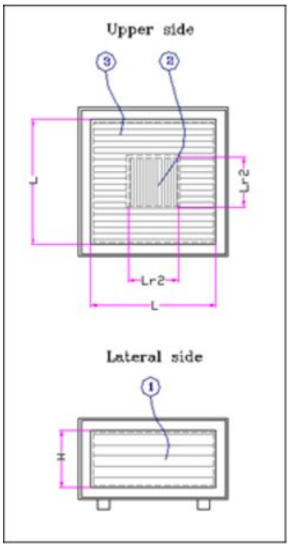

(b) The technical drawing.

Figure 3.5: The large oven used to slump the glass sheets, it can host moulds up to 1.2 m width.

Power supply and heaters The oven is an electrical industrial oven for glass and ceramic applications equipped with electrical resistances as heater elements, the internal cavity is covered by isolating bricks. The maximum electrical power the oven should have, is limited from the availability of the electric grid line. In our case it is set to 50 kW, an oven that needs a power supply exceeding this value will be oversized and will not perform properly.

The thermal analyses performed to simulate the heat distribution onto the mould show that the best results occur if the heater elements have about the same length of the diameter of the mould. They should be positioned onto the upper and the lower surfaces of the oven's cavity. Moreover, it is preferable that these two elements are able to supply different thermal fluxes to compensate eventual gradients as those due to the convection present outside the muffle. From these considerations follow that the major part of the heating power could be concentrated on these sectors.

To correct the expected radial temperature gradients between the center and the edges of the mould, it has been chosen to divide further each one of the upper and lower elements in two independent segments, as seen in Figure 3.5(b).

Summarizing, the oven is divided into 2 major sectors (upper and lower) plus one covering the four sides of the cavity. Both the upper and the lower sectors are formed by two separate heating elements, one internal and one external. The Table 3.1 lists the specifications of the five heater elements forming the oven.

Sector	**Heater length** $[mm]$	**Power** $[kW]$
Central upper side	Lr2 = 700	15.5
External upper side	L = 1300	16.5
Central lower side	Lr2 = 700	15.5
External lower side	L = 1300	16.5
Lateral side	L = 1300	19

Table 3.1: Specification of the five heater elements forming the oven.

The controller The oven has an internal PLC controller that manages the hardware such as the thermocouples, the heaters, the security switches and so on. The PLC is a very flexible system and can be programmed by the user to its needs. Moreover, the PLC has memorized the thermal model that describes the oven, on the basis of the temperature ramps requested by the user and the reading from the thermocouples the PLC triggers the switch on/off of each heater.
The oven can be remotely controlled through a RS485 serial communication interface. A dedicated software has been written with the Microsoft Visual Basic 6.0 language. It is possible to execute some common operations using dedicated buttons or even to have a complete access to the PLC through a command line terminal. The GUI (see Figure 3.6) permits an easy and quick access to operations like check the oven status (on/off, thermal cycle running, ecc), monitor the temperatures inside the cavity, program a thermal cycle and start/stop it.
The software is installed on a dedicated computer connected to the net so that the oven can be checked/controlled 24 hours a day. Moreover, the computer is powered through an UPS system to access it in case of power breakdown. This feature is very useful because permits to know the elapsed time since the failure and hence, at the power on, takes the decision if going on or not with the experiment[†].
Finally, the software has a routine that checks the status of the oven once a second and reports an alert in case of error. The alert can be sent via e-mail message, using the chat protocol of the Skype™ software or even though SMS to mobile phones.

[†] The oven's PLC has been programed to continue the thermal cycle after a power breakdown.

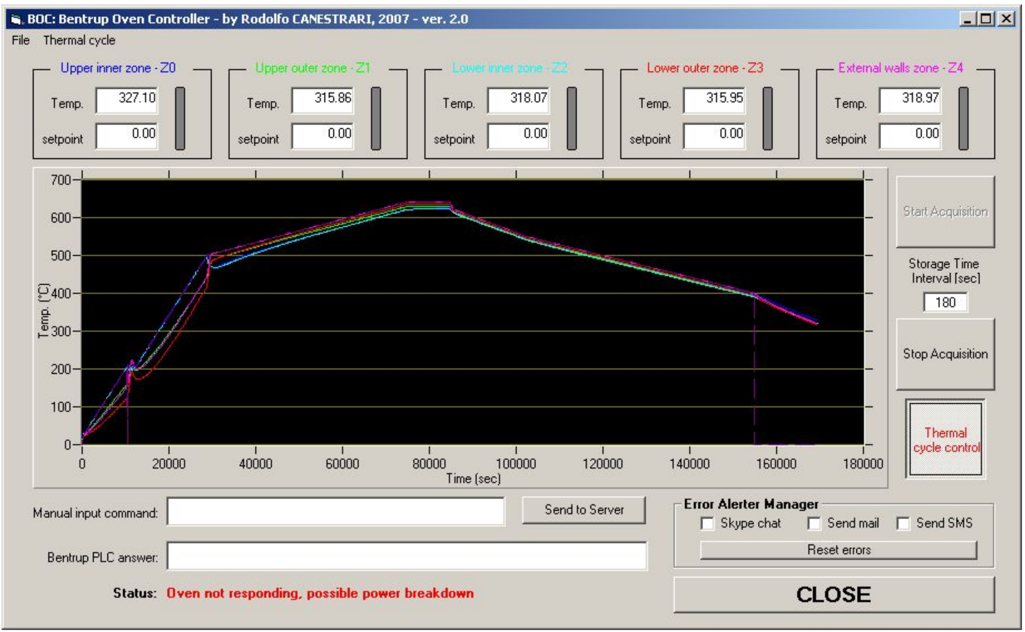

Figure 3.6: The GUI of the software for the remote control of the oven.

3.2.2 The thermal cycle

The FEA model that describes the oven permits also to address the thermal cycle heating and cooling rates. In addition to this, a number of experimental tests have been performed to optimize the timing, in particular using a scaled-down setup of the entire process. The thermal cycle that has been found reporting the best results in term of shape's accuracy of the glass shells is composed by 6 phases, as shown in the graph of Figure 3.7.

An initial heating of the oven up to the *slumping temperature* that occurs in a range varying typically from 550 ℃ to 700 ℃ depends on the type of glass. For the BOROFLOAT® 33 we adopted a temperature near 630 ℃. At this stage the glass starts to soften and to copy the shape of the mould. However, to access the sticking behavior of mould and glass, and hence the maximum slumping temperature, some dedicated tests have been done as described in § 3.3.4.

Afterward, there is a period of wait, called *soaking time*, to allow the temperature to uniform and the glass to sag onto the mould.

A slow drop of the temperature down to the *annealing point* of the glass and a second waiting period. This is a critical step of the process and should be done very slowly to give time to the glass to anneal and, hence, relieve the stress that has built up in it.

After the annealing, a second slow cooling until the *safety temperature*. The safety temperature has been found experimentally being at about 400 ℃, below which the glass can be considered again a "solid", this means that the temperature does

not induce any other permanent changes on the shape of the shell (apart from the expansion due to the not null CTE).
The final step is the cooling down to room temperature that can be done turning off the oven and allowing it to natural cool.
The glass shells obtained have been then characterized in terms of shape accuracy, the results are reported in Chapter 5. An heating ramp of 2.5 °C/min and a slow cooling at 0.5 °C/min return radial thermal gradients limited to less the 5 ℃, but for the slumping of the glass shell demonstrator the thermal cycle follows more mild heating and cooling phases due to the considerable mass (and hence thermal inertia) of the mould.

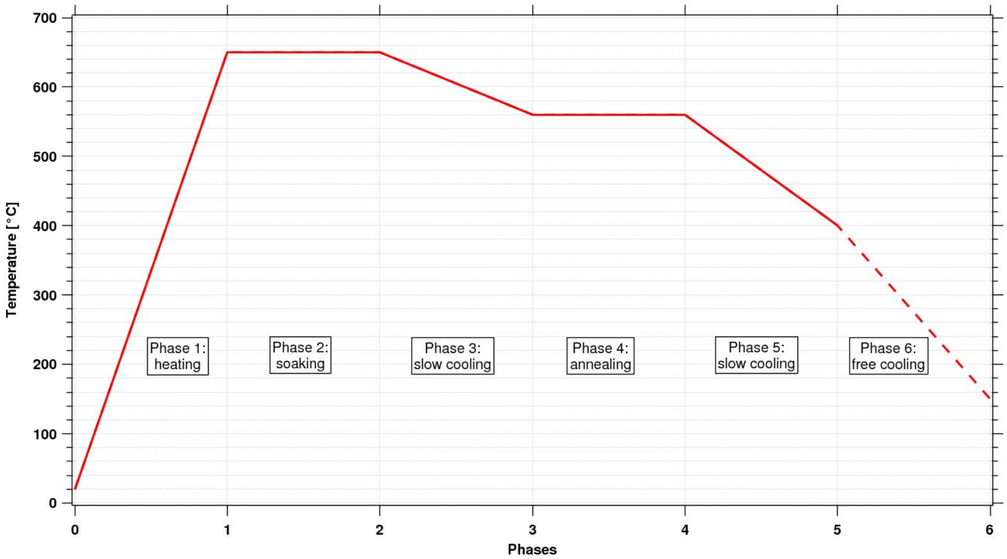

Figure 3.7: The thermal cycle used to slump the glass sheets.

3.2.3 The muffle

The muffle is a box, usually made in metal, able to withstand repeated thermal cycles. It is placed inside the oven and generally used as a protective container for the things that go into the oven.
From the thermal analyses performed it is found out that the use of a muffle gives a number of appreciable advantages to the overall process. Its walls act as a shield from the direct heating generated by the resistances preventing a localized overheating. Even better, it permits to obtain a more uniform temperature distribution on the mould because the metal spreads evenly the heat generated by the heating elements of the oven.
As second advantage, it physically separates the mould (and the glass sheet) from the environment of the oven's cavity. This permits a drastic reduction of

the dust contamination, a critical parameter to be kept under control when very high precision replications are required.
Finally, it is possible to conduct the experiments in an inert atmosphere (and hence to limit possible chemical contaminations) or even into vacuum, at least partial, removing the air from the muffle‡. The latter strongly reduces, if not eliminates, the convection generated by heating the air, allowing heating only through thermal irradiation. This permits to further increase the uniformity in the temperature distribution on the mould and on the glass.
The muffle used during the activities performed is made of a special type of stainless steel namely AISI 310, poor of Carbon and specific for repeated temperature cycling. In Figure 3.8 is shown a picture of the muffle, while in Figure 3.9 is reported its technical drawing.

Figure 3.8: The muffle in the INAF-OAB's lab.

‡A graphite rope has been used as "O-ring" sealant.

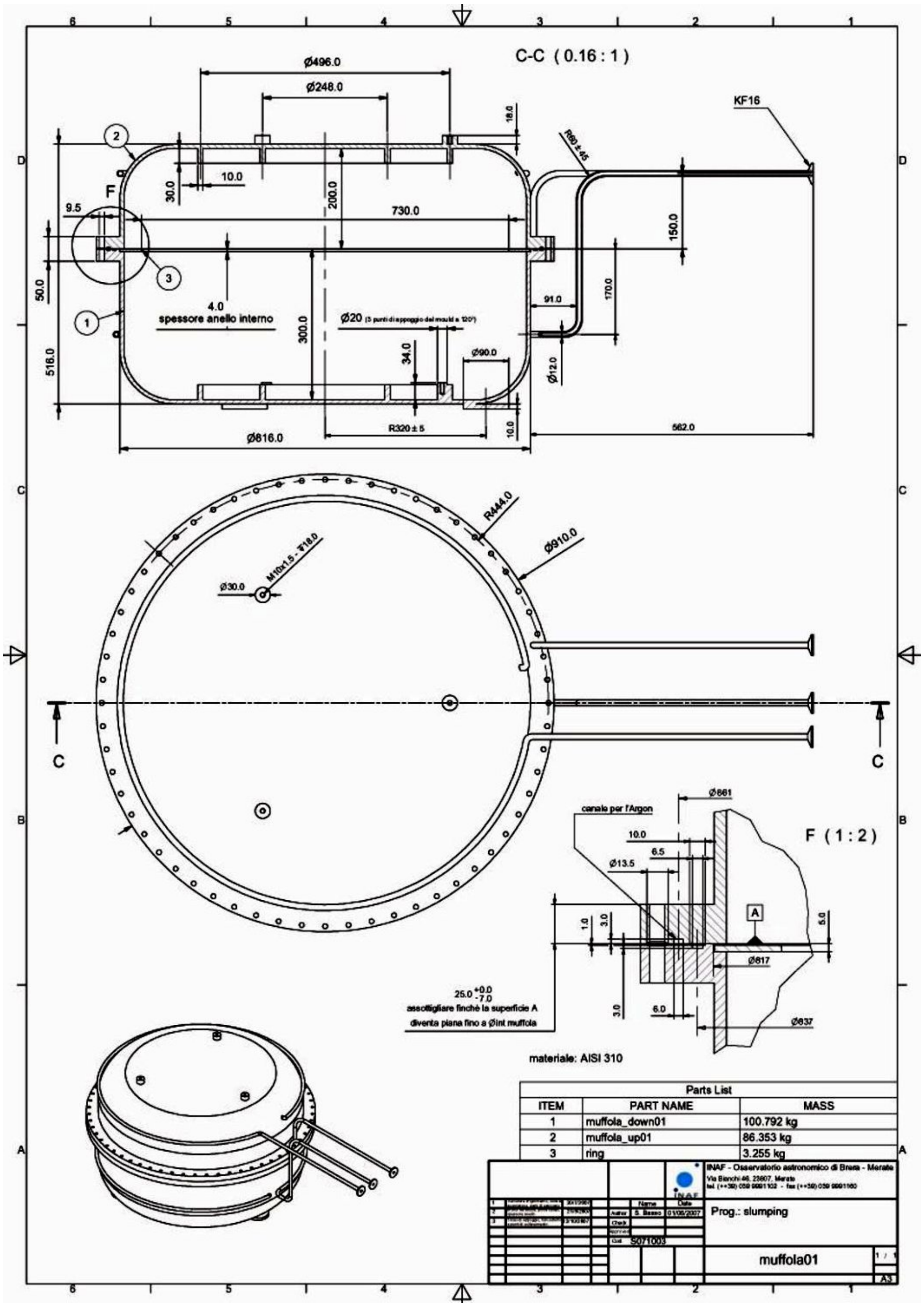

Figure 3.9: The technical drawing of the stainless steel muffle.

3.3 The mould and the thin glass sheets

The purpose of this part of the activity was the definition of the material and the surface quality (in terms of shape's accuracy and microroughness) of the mould, and the definition of the type of glass sheets to be used for the demonstrator. This was achieved through a number of steps:

§ **3.3.1** the identification of a list of parameters of interest for this specific application;

§ **3.3.2** the individuation of a set of suitable materials either for the mould and for the glass sheets;

§ **3.3.3** a critical comparison between the materials;

§ **3.3.4** some experimental tests using the materials selected.

The following subsections go through these points, while in 3.3.5 are given the final choices.

3.3.1 The space of parameters

For the specific application of the manufacturing of a mould for glass slumping, the parameters we highlight being of interest are listed in the Table 3.2. It should be noted that some of the properties listed are temperature-dependent.

Mechanical	Physical	Structural	Fabrication	General
Young's modulus	CTE	Voids and inclusions	Machinability	Availability
Hardness	Homogeneity of the CTE	High temp stability	Polishability	Scalability
	Thermal conductivity		Microroughness	Costs
	Density		Shape's metrology	
	Adhesion to glass			
	Transparency			

Table 3.2: Investigated properties for the materials

A consideration that must be kept in mind is that the choice of the mould material cannot be driven only in terms of thermo-mechanical properties of the material itself. Both the process under development and the final application for which the technology is addressed, could in principle affect or be affected by the characteristics of the mould (and/or of the glass type). Indeed, they have to be considered part of the selection. For example, if the deliverable of the study

is a mirror segment of $x \times y$ in sizes with a requirement on the scalability up to 10 times, the choice of the mould has to take into account the possibility for larger dimensions. Our demonstrator is planned to have a diameter of 0.5 m, but in realistic future applications the mirrors will have size of $1 - 1.5$ m or more.
The selection of the type of glass is close to some of the characteristics of the mould itself. For example, finding a good match in the CTEs between the glass and the mould helps to manufacture the glass shell with the desired shape; the temperature necessary to slump the glass has to be in the service range of the mould; the chemical composition of the glass can result in different behaviors in the sticking between the glass and the mould.
The thermo-mechanical properties of the glass itself are important, too. They are related to the final application which the glass shell will be used. For example, during their operation the adaptive support's actuators heat the mirror, hence the glass shell should be able to dissipate the heat with adequate efficiency; different glass types are produced/sold in different sizes ranges (depending on the technology used and the market they are addressed to), so the linear dimensions and the thickness of the glass sheets have to be compliant with this application and its possible scale-up.
All these considerations shall be properly weighted in a merit function to reach an acceptable trade-off between the many input parameters in the effort to choose the best couple of materials for the mould and the glass shell.

3.3.2 The materials investigated

Concerning the mould, it has been individuated a list of four candidate materials on which focus the investigation: Alumina (Al_2O_3), Silicon Carbide (SiC), Technical Quartz[§] (SiO_2) and Keatite (ZERODUR® K20). These materials are well known both in the field of optics's manufacturing and of the slumping of glass: Quartz has been used by the MSFC for manufacturing the mandrels used for the development of a slumping process for the X-ray optics of the Constellation-X mission [14]; the German firm Zeiss was using Alumina during an internal development of a procedure of glass slumping, while the ZERODUR® K20 was used by the MPE for the development of glass segments for the XEUS X-ray mission [15].
The behavior of all these materials has been investigated, also with respect at different types of sheets of glass. In particular, the attention has been focused on the glass types BOROFLOAT® 33 and D263T.

[§]Technical Quartz, in the following named Quartz, is a particular grade of synthetic fused silica recommended only for technical applications, where the optical transmission characteristics of the material are not required, as it is in this application.

	Materials			
Properties	Alumina	SiC	Quartz	ZERODUR® K20
Young's modulus [GPa]	90	476	72	83
Density [g/cm^3]	2.85	3.21	2.21	2.53
Knoop's hardness [HK 0.1/20]	1900	3000	580	620
CTE @ 25℃ [$\mu m/(m \cdot K)$]	8.2	4.0	0.5	2.0
CTE homogen. [$\mu m/(m \cdot K)$]	n.d. but good	0.01 good	n.d. but not very good	0.004 very good
Thermal conduct. [$W/(m \cdot K)$]	24	102	1.31	1.60
Glass adhesion (see § 3.3.4)	yes	yes	yes	no
Transparency (color)	no (white)	no (black)	yes	no (white)
Voids, inclusions	no	no	possible	no
High temp. stability	very good	very good	very good	very good
Max temp. [℃]	1900	1450	1200	850
Machinability	green body	green body	very good	good
Polishing, figuring	slow	very slow	fast	quite fast
Microroughness [Å]	10-20	< 5	< 5	< 10
Shape characterization	CMM and patch map	CMM and patch map	interferometric	CMM and patch map
Material's sellers	many	many	many	SCHOTT
Scalability to ø = 1.5 m	Sectors brazing	Sectors brazing	Difficult	Several meters
Finished mould's cost estimate (ø = 0.7 m)	60 k€	100 k€	60 k€	70 k€

Table 3.3: Properties of the four materials investigated for the mould's manufacturing.

The characteristics that a good couple of materials mould/glass-sheet should satisfy are:

- the CTEs of the two materials should be as similar as possible to each other;
- thermal conductivity as high as possible;
- possibility to easily scale-up the pieces, both for the mould and for the glass sheets;
- for the mould, to be easy workable with machining tools and to be easy polishable with standard techniques;
- low surface porosity;
- heat resistance and mechanical stability up to 650-700 ℃;

- good Young's module;
- no sticking of the two materials at the process's temperature.

Following this approach, it has been done a comparison of the thermo-mechanical characteristics of the candidate materials. All the characteristics that we have evaluated come from an extensive literature search, some experimental tests and contacts with international specialized firms. In Table 3.3 are collected all these informations for the four candidates for the mould. Instead, Table 3.4 is the corresponding one for the different types of glass sheets.

	Glass types and sellers				
	SCHOTT			**Corning**	**Pilkington**
Properties	Borofloat® 33	AF32	D263T	Eagle 2000	Microfloat™
Young's modulus [GPa]	64	74.8	72.9	70.1	73
Density [g/cm^3]	2.2	2.43	2.51	2.37	2.49
CTE @ 20-300 ℃ [$\mu m/(m \cdot K)$]	3.25	3.2	7.2	3.61	9
Thermal conduct. @ 90 ℃ [$W/(m \cdot K)$]	1.2	1.16	n.a.	1.02	< 0.9
Transformation temperature [℃]	525	715	557	670	567
Strain point [℃]	518	686	529	666	530
Annealing point point [℃]	560	728	557	722	557
Available thickness [mm]	0.7 - 25.40	0.1 - 1.1	0.03 - 1.1	0.5 - 0.7	0.95 - 1.7
Thickness constancy [μm]	±70 better upon selection	n.a.	±30	±20	n.a.
Scalability to ø = 1.5 m	yes	no	difficult	yes	yes

Table 3.4: Properties of the different types of glass sheets for slumping.

3.3.3 Comments on the materials

In the following a critical analysis is proposed of the many parameters listed above. While some of them are distinctly related to the mould or to the glass sheets, someone refers to both.

Young's modulus and density The Young's modulus has been used to define the deformation that the mould will experience, under the gravity load, when it is supported (on 3 points at 120°) inside the oven. The best performances are with the Silicon Carbide that is very stiff. The comparison of the other three materials shows that they are not far from each other. Concerning the densities of the four materials, they are not so different from each other. However, a more interesting parameter to check is the flexural rigidity. It is defined as the ratio between the Young's modulus and the density of the material. Using this parameter it is immediate to know the relative deflections between the materials. In particular, for a mould of 700 mm in diameter, 110 mm of thickness and supported on 3 points at 120° the deflections are:

Material	**Deflection** $[\mu m]$
Alumina	-0.41
Silicon Carbide	-0.09
Quartz	-0.40
ZERODUR® K20	-0.39

Knoop's hardness The hardness of the material is relevant for two conflicting reasons. First, the grinding, polishing and figuring of the surface is very time consuming for hard materials like Silicon carbide and Alumina. In fact, this is one of the reason why the costs of SiC optics is generally very high. Second, the advantage in having an hard surface makes very unlike that scratches will be generated on it during the handling and the cleaning of the mould and, eventually, during the slumping process itself.

CTE If the CTEs of a couple of materials (i.e. the mould and the glass sheet) are matched, this will result in a common expansion and contraction at all the temperatures occurring during the whole process. At the end of the slumping cycle, the glass shell will not suffer any change in the radius of curvature and will maintain the same one of the mould. On the contrary, if there is a mismatch between the CTEs, the glass shell will change the radius of curvature following the 3.1:

$$R(\Delta T) = R_0 \cdot (1 + \Delta\alpha \cdot \Delta T) \tag{3.1}$$

where R_0 and R are the radii of curvature of the mould and that of the glass shell, ΔT is the variation of temperature that the mould and the glass undergo during the process and $\Delta\alpha$ in the difference between the two CTEs.
The Silicon Carbide (CTE = 4 $\mu m/(m \cdot K)$) and the ZERODUR® K20 (CTE = 2 $\mu m/(m \cdot K)$) are the best choices when is used the BOROFLOAT® 33 glass type (CTE = 3.3 $\mu m/(m \cdot K)$). This is because the difference of the CTEs is very limited.
As example, considering a mould made in ZERODUR® K20 with a radius of curvature of 5000 mm and a glass shell of BOROFLOAT® 33, the 3.1 gives a variation of radius of curvature of the shell of only -3.25 mm, the 0.065% of the nominal value. If instead it is used the D263T glass type (CTE = 8 $\mu m/(m \cdot K)$), the best choice for the mould becomes the Alumina.

This effect is anyway a problem that can be strongly minimized or solved manufacturing the mould with the appropriated radius of curvature, tailored to compensate the deviation introduced by the CTEs mismatch.

CTE homogeneity The inhomogeneity of the CTE of a material results in local changes of the thickness of the material itself. In the case of the mould it is crucial because this implies the variation of the shape of its surface (optically polished). In our specific application, where the temperature rises up to 650 ℃, it is easy to find that for a mould with a thickness of 110 mm, an inhomogeneity of the CTE of only 0.1 $\mu m/(m \cdot K)$ introduces surface's errors up to 7 μm P-V. This clearly destroys (optically speaking) the shape of the surface of the mould, the material of the mould should have a CTE homogeneity much more stringent to avoid unpredictable deformations of its surface.
In literature, numerical data have been found only for Silicon Carbide and ZERODUR®. The information about the Quartz specify that the material is not certified for what concern the material homogeneity of the blank, striae and striations. It is possible to use a Quartz with higher grade that has higher three-dimensional homogeneity, but the drawbacks are the costs and the scalability. The best material, among the four, is surely the ZERODUR® K20 since it is produced by thermal transformation of the standard ZERODUR®. The ZERODUR® shows a CTE homogeneity within 0.004 $\mu m/(m \cdot K)$ for pieces up to 1.3 m in diameter. The ZERODUR® K20 retains the same kind of performances in CTE homogeneity. With this value for the homogeneity parameter the maximum local deviation that can be expected on a mould with thickness of 110 mm is of 286 nm P-V, about $\lambda/2$ in the visible light range, still acceptable for applications on deformable optics.

Thermal conductivity It describes how fast the heat is spread in a material. A high value is preferred since it means that the material reaches quickly a uniform distribution of the temperature. This is an important requirement, necessary to avoid the stresses in the glass shell, particularly during the cooling down phase of the thermal cycle. The glass shell should have the most homogeneous temperature's distribution when passing through the critical temperatures.
All the glass types evaluated show poor thermal conductivity, the BOROFLOAT® has the higher value.
Concerning the mould, the best material is the Silicon Carbide that has a thermal conductivity comparable to that of the metals. On the contrary, all the ceramic materials, and hence also Alumina, ZERODUR® K20 and Quartz, generally show poor performances. Anyway, it is still possible their use simply increasing the heating and cooling rates of the thermal cycle at the expenses of the production time.

Adhesion of the glass This information has been obtained through the experimental tests. It has been found that the Silicon Carbide, the Alumina and the Quartz stuck to the glass and hence, during the cooling phase, the mould or the glass will break. Meanwhile, the ZERODUR® K20 has never presented problems of sticking up to 660 ℃.
The sticking problem can be solved applying a coating of some kind of anti-sticking material. The known ones are Boron Nitride or Platinum. However, it is better to avoid this further step that will add complexity to the process. A more detailed discussion about the mould-glass sticking tests is presented in the section 3.3.4.

Transparency The transparency of the material is important in particular during the manufacturing of the convex mould and its characterization and certification. The Quartz is the only transparent material. For further comments refer to the paragraph “Shape characterization”.

Voids and inclusions The mould should not have bubbles or inclusions because these could indicate a non homogeneous material. Alumina, Silicon Carbide and ZERODUR® K20 are materials free from these imperfections, while the Quartz is not certified for striae and striations.

High temperature stability over repeated cycles It is important that the mould's material shows high temperature stability and that it does not change shape after repeated temperature cycles. All the materials here considered appear to be very stable under this condition.

Maximum service temperature Within this activity, it is foreseen a service temperature around 650 ℃. Three materials have no problem on plenty overcome this temperature, while the ZERODUR® K20 can reach, for long periods of time, a maximum temperature of 850 ℃. This value anyway suits comfortably the maximum temperature foreseen for the process.

Machinability This parameter refers to the easiness of manufacturing of the piece (i.e. the mould) from the mechanical point of view, it depends from the hardness of the material. This step brings the blank to have the final shape of the mould. For Alumina and Silicon Carbide this step is generally done when the raw material is in the green body phase[¶]. In this state the material can be easily machined

[¶] The *green body* is an intermediate phase of the sintering process of ceramics. The dried powder mixture is put into a mold and pressed, the result is an unsintered ceramic item called green body.

and shaped near to the final dimensions. Afterward, the piece is sintered‖ and it becomes very hard and difficult to work. During this phase there is also an isotropic dimensional shrinkage of the material up to 20%.
The Quartz is a very well known material that poses no difficulties during the manufacturing.
The ZERODUR® K20 is obtained from the standard ZERODUR®. The mould can be manufactured completely in ZERODUR® (that is softer than the K20) and then the piece is converted in ZERODUR® K20. This phase essentially does not change the dimensions of the blank.

Polishability and figuring As mentioned above, Alumina and Silicon Carbide become very hard materials after the sintering. Their polishing and figuring phases make use of specific grinding materials and are time consuming. The Quartz is quite easily figured compared to the previous two. The ZERODUR® K20 is harder than the Quartz, but it fits well the conventional polishing and figuring techniques used in optics.

Microroughness This parameter fixes the limit at which it is possible to polish the surface of a material, hence the lower the better. Both the Silicon Carbide and the Quartz can be super-polished to a level of microroughness of less than 5 Å rms, while for the Alumina this value is slightly higher. The ZERODUR® K20 can be polished down to 10 Å. Since the slumping process is done in the "direct mode" the microroughness of the surface of the mould becomes potentially important. In fact, it is possible to copy, at least partially, the microroughness of the mould into the surface of the glass shell. It is important to polish adequately the surface of the mould if a very high copy capability is requested.

Shape characterization For convex surfaces, the most suitable metrology depends strongly on the transparency (or not) of the mould. It is possible to recognize two characterization methods:

- if the material is transparent to the visible light, like the Quartz, it is possible to capitalize this feature. Since concave surfaces are quite easy to measure, at least with interferometric setups, it is sufficient to look through the material from its back and the upper surface will appear concave. In this way it will be possible, assuming a constant index of refraction (into the entire volume of the mould), the measure of the shape and the determination of the errors occurred during the figuring;

‖Sintering is a method for making objects from powder, by heating the material in a sintering furnace below its melting point (solid state sintering) until its particles adhere to each other. Sintering is traditionally used for manufacturing ceramic objects.

- if the material is opaque, as for the other three, an alternative approach could be the use of a high precision CMM device. This can be used to asses the overall geometry of the mould, meanwhile the higher spatial frequencies will be locally checked using a transparent reference optic. This lens should have on one surface exactly the opposite concavity of the mould, its surface will be assumed to be perfect and will be used as reference. When it is placed in contact with the mould some interference fringes will appear, their number and path are related to the errors on the mould's surface.

Material availability Alumina, Silicon Carbide and Quartz are materials available from a number of suppliers worldwide. In the case of the ZERODUR® K20 the only supplier in the world is the SCHOTT firm, from Germany.

Scalability For Alumina and Silicon Carbide the maximum blank size available at the starting time of this activity was near to the requirement of this study (mould's diameter of 0.7 m). The manufacturing of blanks with diameter up to 1.5 m it is feasible only brazing a number of smaller petals. This process has been used to manufacture large mirrors in Silicon Carbide for space missions (e.g. the 3.5 m primary mirror for the IR telescope on board Herschel). The use of this technique for the manufacturing of a mould, that must withstand high temperature and repeated thermal cycles, should be carefully studied. Moreover, problems could arise if the material used for the brazing has a different hardness respect to the main one: the grinding and the figuring steps could remove material with different abrasion rates with obvious problems in terms of shape accuracy. Or, the brazing material could have different thermal conductivity and introduce artifacts or stresses in the glass shell.
The Quartz and the ZERODUR® K20 can be easily produced with the actual size. In particular, the ZERODUR® K20 can be produced with dimensions of several meters.
Concerning the glass sheets, three over five of the selected types can be easily scaled up.

Mould's cost The most expensive mould would be the one in Silicon Carbide and requires almost 100 k€. For the other three materials the costs are similar to each other, the value is about 60-70 k€.

Transformation temperature The glass transformation (or transition) temperature, T_g, is for glasses what the melting point is for crystalline solids. At higher temperatures, and hence lower viscosities, the structural units are able to reorganize themselves quickly as a quasi-equilibrium liquid. At temperatures below T_g reorganization among the structural units virtually ceases and the resulting rigid material is referred to as a glass. The transformation temperature of a given "glass composition" depends on its constituents and upon the rate of cooling.

Strain point It is defined as the temperature at which the viscosity η reaches the value of $10^{14.5}\ Pa \cdot s$. When cooling down, the strain point is the temperature at which internal stresses in a piece of glass are substantially relieved. This process is called annealing, it occurs between an upper and a lower point: the strain point is the lowest annealing temperature. Below the strain point molecules are trapped where they are, if there is any stress in the glass at this point, it is permanent. At the strain point, stress relaxes within several hours.

Annealing point It is defined as the temperature at which the viscosity η reaches the value of $10^{13}\ Pa \cdot s$. It is the highest annealing temperature, also known as the stress-relief point, where the annealing process starts. The glass should be allowed to cool-and-soak until its temperature is even throughout. This process proceed down to the strain point with a timing that varies depending on the type of glass and its maximum thickness. At the annealing point, stress relaxes within several minutes.

Available thickness The best suitable glass thickness for substrate in adaptive optics application is in the 1.6 to 3 mm range. Following this consideration, the focus of this investigation will be put in this thickness range and hence the only glass type available is the BOROFLOAT® 33.

Thickness constancy Thickness variations on the glass sheet do not affect it from the mechanical point of view, but from the optical one. If there were no thickness variations both surfaces of the glass (the one in contact with the mould and the opposite one) could be, in principle, usable as optical surfaces after the slumping. Since this is not the case, these variations translate in a worsening of the optical shape, but only if the slumping process is done with an "indirect" approach. The process dealt in this development is the "direct" approach, but also in this case the thickness variations could be still a problem. The thickness variations of the glass sheet should not exceed about 10 μm on about 100 mm length to avoid to erode too much the available stroke of the actuators. Moreover, since this length scale is close to the inter-actuator distance there is the risk to create non-correctable artifacts on the glass front face. Finally, if this parameter will reveal to be critical for the performances of the curved glass shell, a solution can be envisaged like a pre-polishing of both sides of the glass sheets before their slumping.
None of the glass types are certified to have thickness constancy within the requirement given above. In particular the BOROFLOAT® 33 type has quite large thickness variations, but sheets with better behavior can be selected.

3.3.4 Mould-glass sticking tests

The sticking of the glass on the mould is an event that creates an heavy damage to the mould, requiring a re-figuring of the surface. To address this issue a series of tests on dummy moulds were performed. Pieces of glass sheet were slumped on small flat moulds and the adhesion, or not, was checked. In addition, experience regarding the problems related to the slumping of glass was gained.
The moulds were made with the four candidate materials and BOROFLOAT® 33 type of glass was used. Square samples with dimensions of 50×50 mm^2 were made in Alumina and Silicon Carbide and polished to a microroughness level of about 0.5 μm rms. Other larger moulds (about 150 mm in diameter) were made in Quartz and ZERODUR® K20 and polished down to $1-2$ nm rms. The moulds's surfaces were cleaned from dust particles before the test. The glass sheets were cut in smaller pieces and cleaned. The test was repeated increasing each time the temperature of the oven up to 660 ℃.
In Figure 3.10 are shown the Alumina moulds after the thermal cycles. Small chips of glass are barely visible still glued on their surfaces. When inside the oven some temperature was reached, the glass pieces were stuck on the Alumina and during the cooling down were subject to compression forces due to the difference in CTEs (8.2 $\mu m/(m \cdot K)$ vs 3.3 $\mu m/(m \cdot K)$). The glass was compressed till it was ejected in pieces, away from the Alumina samples.

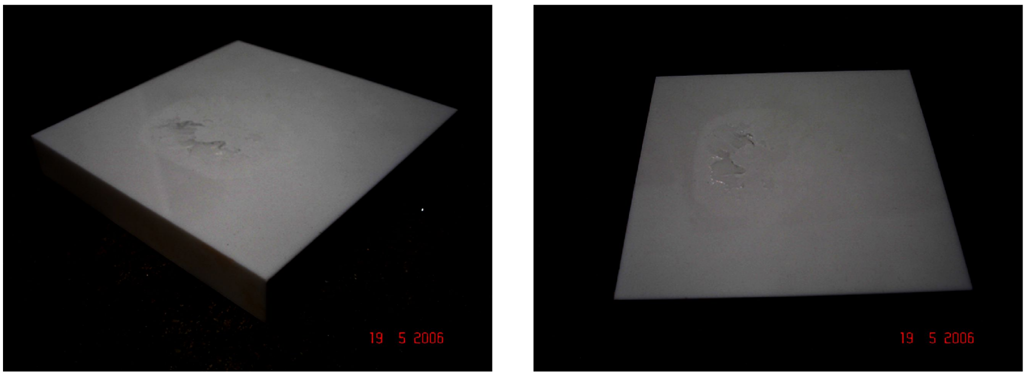

Figure 3.10: Glass chips stuck on the surfaces of the two dummies of Alumina.

The glass pieces onto the Silicon Carbide stuck also to the material, but since the two CTEs are very similar (4 $\mu m/(m \cdot K)$ vs 3.3 $\mu m/(m \cdot K)$) the glass pieces did not broke. A possible explanation of the sticking could be the following. The surface of the Silicon Carbide is populated also with free Si atoms. At high temperature and in an atmosphere rich of O_2, as it is the air, a chemical reaction is triggered and SiO_2, i.e. glass is formed. In the Figure 3.11(a) are visible respectively, an air bubble trapped inside the sticking area and a piece of glass completely stuck.

The same behavior is observed for the couple Quartz and BOROFLOAT® 33, the glass pieces stick to the surface of the mould. Since the CTEs are 0.5 $\mu m/(m \cdot K)$ vs 3.3 $\mu m/(m \cdot K)$, the glass was subjected to traction forces (the opposite case of the Alumina). In Figure 3.11(b) is possible to recognize on the glass pieces the area of sticking along the perimeter of the pieces themselves, while the inner circular area is separated from this corona.

(a) Pieces of glass stuck on the Silicon Carbide after the test.

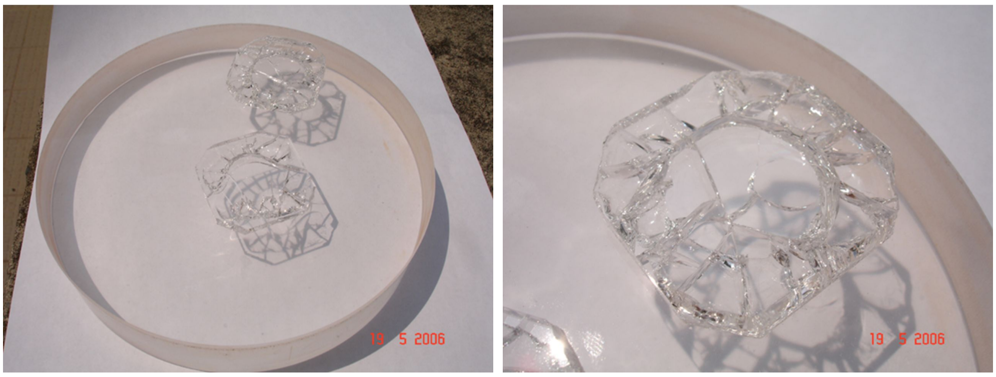

(b) Pieces of glass stuck on Quartz.

Figure 3.11: Mould-glass sticking tests with Silicon Carbide and Quartz

On the contrary, the BOROFLOAT® 33 glass was never found stuck on the ZERODUR® K20, only overcoming 660 ℃ the glass shows attitude to sticking. Concerning the D263T type of glass, it has been found that it stuck also to the ZERODUR® K20.
It is clear from these tests that the use of Alumina, Silicon Carbide and Quartz requires an anti sticking coating, while *the ZERODUR® K20 can be used as it is* at least *with the BOROFLOAT® 33*.

3.3.5 Definition of the mould and of glass shells

The choice of the more performing couple of materials, the mould and the glass sheet, undergoes a trade-off between the many and conflicting parameters just described.
On the basis of what is reported and discussed in § 3.3.3 it has been decided that *a good trade-off for the material of the mould is the ZERODUR® K20 coupled with glass sheets of BOROFLOAT® 33 type.* The main considerations that support this decision are:

- the ZERODUR® K20 and the BOROFLOAT® 33 show a difference between the two CTEs acceptably small;
- the CTE homogeneity of the ZERODUR® K20 is the highest of all the other materials;
- the BOROFLOAT® 33 has never shown permanent sticking to the ZERODUR® K20 after the slumping process and hence there is no needs of any anti-sticking coating;
- the dimensions of both the ZERODUR® K20 blank and the BOROFLOAT® 33 glass sheets can be easily scaled-up to 1.5 m in diameter;
- the cost of the finished mould in ZERODUR® K20 is within the others;
- the characterization of a not-transparent mould is more demanding, but still doable using standard equipments (as discussed in the paragraph "Shape characterization");
- the BOROFLOAT® 33 shows the best viscosity dependency from the temperature (i.e. lowest temperature);
- the only glass type available on the desired thickness range is the BOROFLOAT® 33.

The mould's design To avoid temperature's gradients due to edge effects, as thermal FEAs show, the diameter of the mould should be larger respect the diameter of the glass shell demonstrator. Still from thermal analyses, the thickness should be constant to permit a more uniform temperature distribution. From mechanical considerations, to minimize the bending due to the gravity, the thickness of the mould should be not less than 90 mm.
The design chosen is a meniscus of circular shape with a diameter of 0.7 m and thickness of 110 mm, on the back side there is a flat annular area where the mould will be supported (see Figure 3.13). Concerning the upper surface of the mould, it has a spherical convex profile with a radius of curvature of about 5 m.

The choice to use a convex mould is driven by the thickness variations on the glass sheets: a glass substrate with a concave surface is desired, hence a convex mandrel is chosen (because of the "direct" approach) and the glass thickness variations do not affect the resulting concave surface of the shell. Moreover, the characterization of a concave surface is much easier than a convex one, specially if interferometric techniques are used. The choice of the value for the curvature is driven mainly by technical considerations on the equipments already available for the metrology (i.e. the optical bench for the interferometric measurements). In Figure 3.12 is shown a picture of the mould.

Later on, it has been decided to change the profile of the mould convex surface. The radius of curvature has been brought to about 10 m and the optical bench used for the metrology has been redesigned to accomplish the new measurements.

Figure 3.12: The white ZERODUR® K20 mould in the INAF-OAB's glass slumping lab.

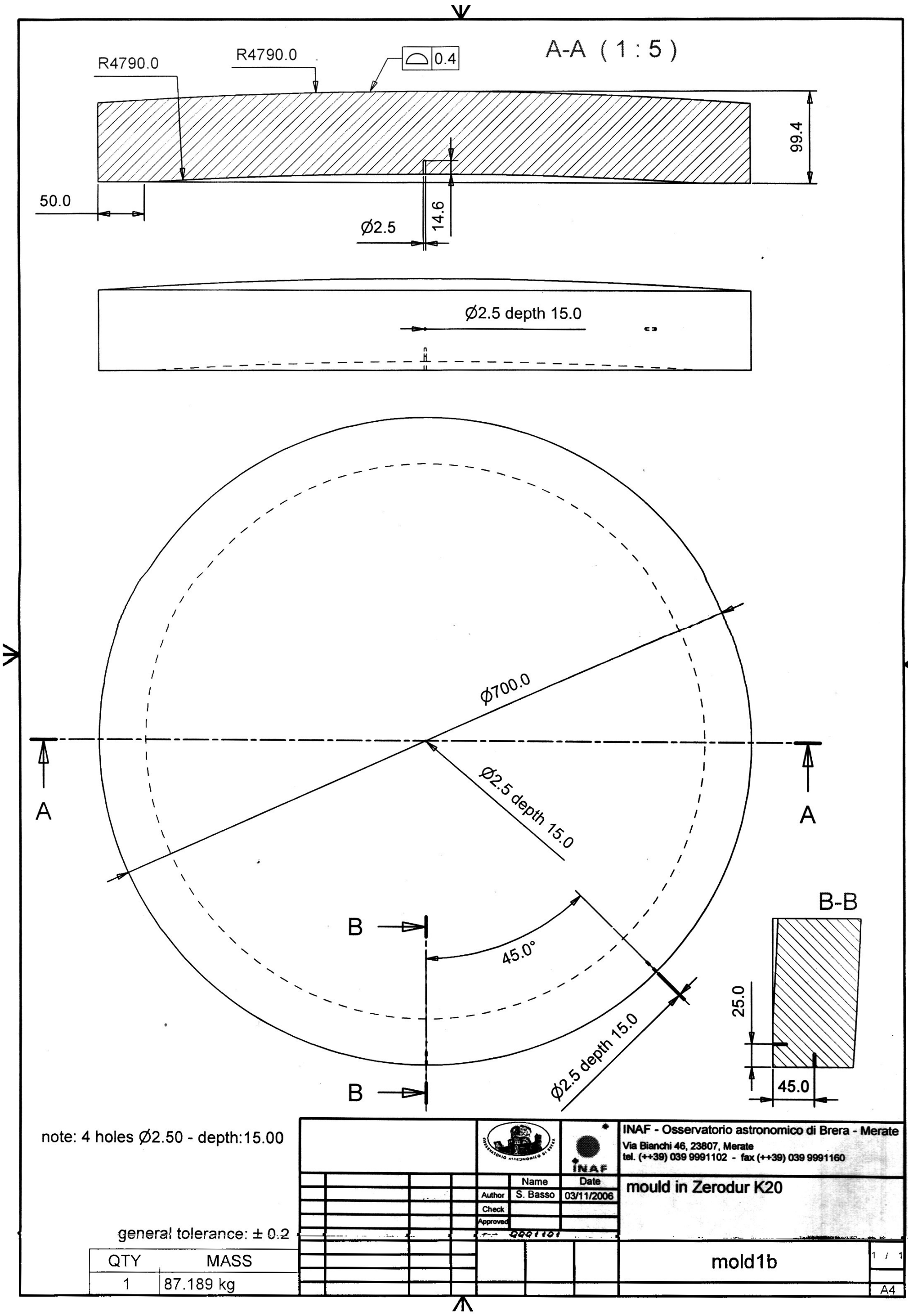

Figure 3.13: The technical drawing of the first version (5 m) of the ZERODUR® K20 mould.

The mould's surface quality requirements The surface quality requirements given in the Table 3.5 shall be considered valid only for the upper surface of the mould. For their computation were assumed that [16]:

- the slumped shell will copy exactly the figuring errors of the mould;
- residual of figuring error compensation (using actuators) equal to or less than 40 nm rms. This corresponds to expected AO fitting error in case of "serendipity" seeing condition (0.2 arcsec at 500 nm);
- the actuator separation is 30 mm;
- the maximum force per actuator for figuring error flattening is 0.1 N.

The surface finishing level of the mould shall be within optical requirements. This is derived from experimental tests, since the mould's microroughness can be, at least partially, transferred into the surface of the glass shell. Hence, the mould's surface has to be polished down to a microroughness of 5 nm rms, or better.

Spatial wavelength range d $[mm]$	**Max allowed surface rms** $\sigma(d)$ $[nm]$
0-20	7.71
0-40	13.7
0-60	19.2
0-80	20.3
0-100	24.5
0-120	34.8
0-140	53.5
0-160	82
0-180	122
0-200	175
0-240	330
0-280	566
0-320	903
0-360	1360
0-400	1970
0-450	2980
0-500	4310

Table 3.5: The maximum errors acceptable for the mould's surface expressed on different scale ranges.

The mould's procurement The ZERODUR® K20 is a white glass ceramic material with high temperature stability and low thermal expansion. It contains a crystal phase of over 90% Keatite, produced by thermal transformation from the semi transparent ZERODUR® material. The material has high temperature stability and does not change during multiple temperature cycles.
The blank in ZERODUR® K20 has been purchased from the German firm SCHOTT, that is the unique producer and seller worldwide.
The machining and the optical figuring and polishing of the first version of the mould were done by a leading firm, the French SESO. This firm provides also the characterization of the shape and surface of the mould, giving a certification for the product. The total time for the procurement (i.e. blank, optical work and certification) was about 1 year. In Figure 3.14 is visible the mould, still at the SESO laboratory, while it is checked the surface microroughness level before the final polishing.

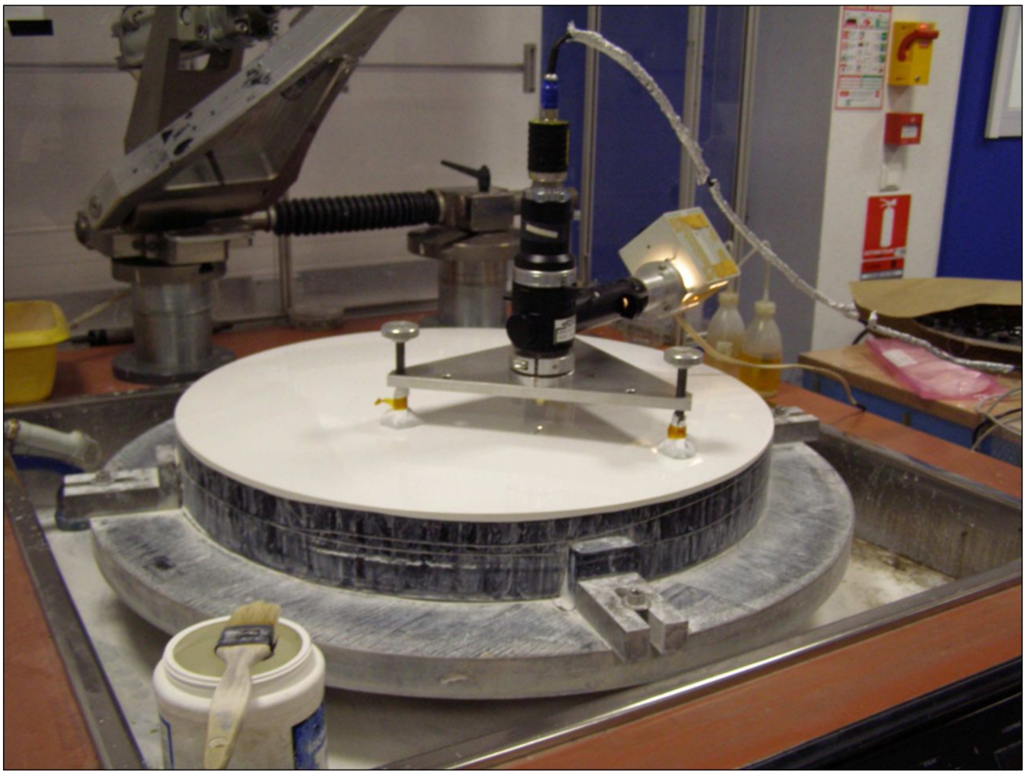

Figure 3.14: The ZERODUR® K20 mould at SESO during the surface's microroughness characterization.

In Table 3.6 are compared the requirements with the actual values. In Figure 3.15(a) is visible the surface map of the mould described with the first 8 orders of the Zernike polynomials, in Fig 3.15(b) the residuals after their subtraction. The measure and the surface analysis were provided from SESO.

The machining and the optical figuring and polishing of the second version of the mould were done by the Italian firm SILO. SILO was not able to provides accurate characterization of the shape and surface of the mould, hence the product is not certified to be within the above mentioned specifications. The radius of curvature is 9850 ± 50 mm.

	Requirement	**Measured**
Mould's thickness $[mm]$	100 ± 1	99.6 ± 0.5
Radius of curvature $[mm]$	4790 ± 20	4808 ± 16
Surface's shape error	P-V < 16	~ 8
(expressed as $\lambda @ 633nm$)	rms < 3	~ 1
Surface's microroughness $[nm]$	rms < 5	$2.68 < rms < 4.75$
Scratch and dig (on 0.5 m)	60 / 40	ok / ok

Table 3.6: Comparison between requirements and actual value for the mould, as provided by SESO.

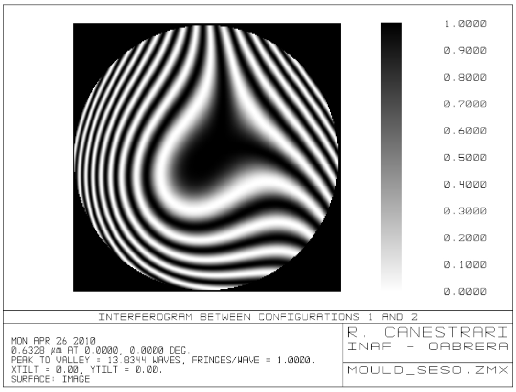

(a) Synthetic fringes generated by the mould (as described by Zernike polynomials) and a reference sphere.

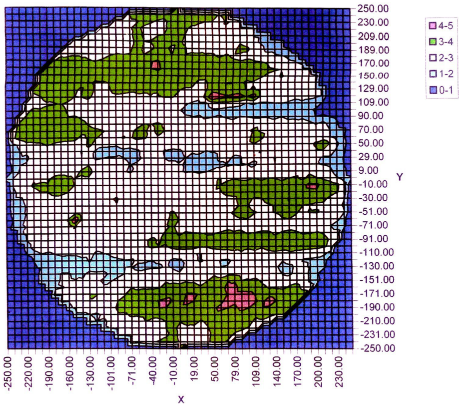

(b) The residuals after the subtraction

Figure 3.15: The surface of the ZERODUR® K20 mould on 500 mm inner diameter. The measures were taken with a CMM at SESO.

The glass sheets procurement The BOROFLOAT® 33 is a high quality borosilicate glass with outstanding properties. This glass type is a homogeneous material that has an excellent mirror-like surface, a high degree of flatness and an outstanding optical quality. BOROFLOAT® 33 is a clear and transparent colorless glass. It shows very weak fluorescence intensities over the entire light spectrum. The BOROFLOAT® 33 has been purchased from the German firm SCHOTT, that is the unique producer and seller worldwide, in the form of disks 1.7 mm thick and 500 mm in diameter. Despite the quite high thickness variations of the BOROFLOAT® 33 glass type, these thin sheets were used "as manufactured" without any post-process (i.e. figuring or polishing). But, the specific requirement to have a selection of sheets with the lowest thickness variations was made to the seller.

The thickness constancy has been verified by measuring the glass thickness, using two incremental length gauges from Heidenhain having accuracy of $\pm 0.2\mu m$, over a length of approximately 1 m. It has been found that each sheet has two preferential directions, due to the production process: along the melted tin flow and orthogonal to it. Measured thickness variations are of about $\pm 2\mu m$ along the flow and about $\pm 10\mu m$ on the other one [17].

3.4 The astatic support

The way in which it is supported a thin, lightweight and very flexible "thing" becomes a fundamental question especially if the purpose of the support is to allow accurate measures of the "thing's" shape, and where "accurate" means "optical" or anyway with (sub-)micron precision. In addition to the support itself, a second important source of distortion of the "thing's" shape is the force of gravity. Hence, a good support should not introduce deformations and should counteract the force of gravity. A support that has these characteristics is usually named "astatic support".

The most common astatic support is obtained by a grid of point-like contact points where the optic is placed. All the contact points can slide up and down around a central position, except for three of these that have a fixed height. These latter providing the reference plane in 3-D space, where the optic is located. Meanwhile, the movable points sustain the local weight of the optic, pushing with a calibrated force. Their number, relative position and pushing force are determined by FEA from a theoretical configuration in which the density of the material is perfectly uniform and the shape of the optic is the ideal one. The configuration resulting from the FEA should minimize the deformations induced by the gravity force. This kind of support becomes quite complicate as soon as the linear dimensions of optics increase and its thickness decreases, because the number of contact points grows up and this reflects also on the cost issue.

Since these glass shells are quite floppy, it is necessary to use an astatic support to measure their real shape. And since these glass shells are quite large and thin the classic concept of astatic support is not easy to implement. During this study has been developed an astatic support that uses an innovative design: some fixed points for the reference position of the shell and an airbag to support the weight of the glass. In this way there is no need to use the large number of contact points that over-complicate the classical approach.

The support has been designed and realized and it is visible in Figure 3.16. Its description is in the next lines. The main body of the support is a short cylinder with one end closed, the internal diameter is slightly larger that the glass shell. Along the circumference (of the astatic support) is placed a strip with a magnetic line (few mm wide) running for all its length. On the base of the cylinder are located four contact points, each point on the corner of a square. These points are the fixed points by whom the glass gets the reference position. This position is such that the edges of the glass shell are at the same height as the magnetic line is. The resulting gap between the shell edges and the strip is of the order of some tenth of millimeter. This is filled by a ferrofluid, a liquid with ferrous particles. In this way it has been created a sort of hermetic container formed by the cylinder sealed on its top by the glass shell and the ferrofluid. Blowing air inside this cavity it is generated an over-pressure that sustains the glass weight. The over-pressure is calibrated with FEA calculations and measured through load cells placed on the contact points, the air is injected till it is read the desired value. In Figure 3.17 is shown the mechanical drawing of the support.

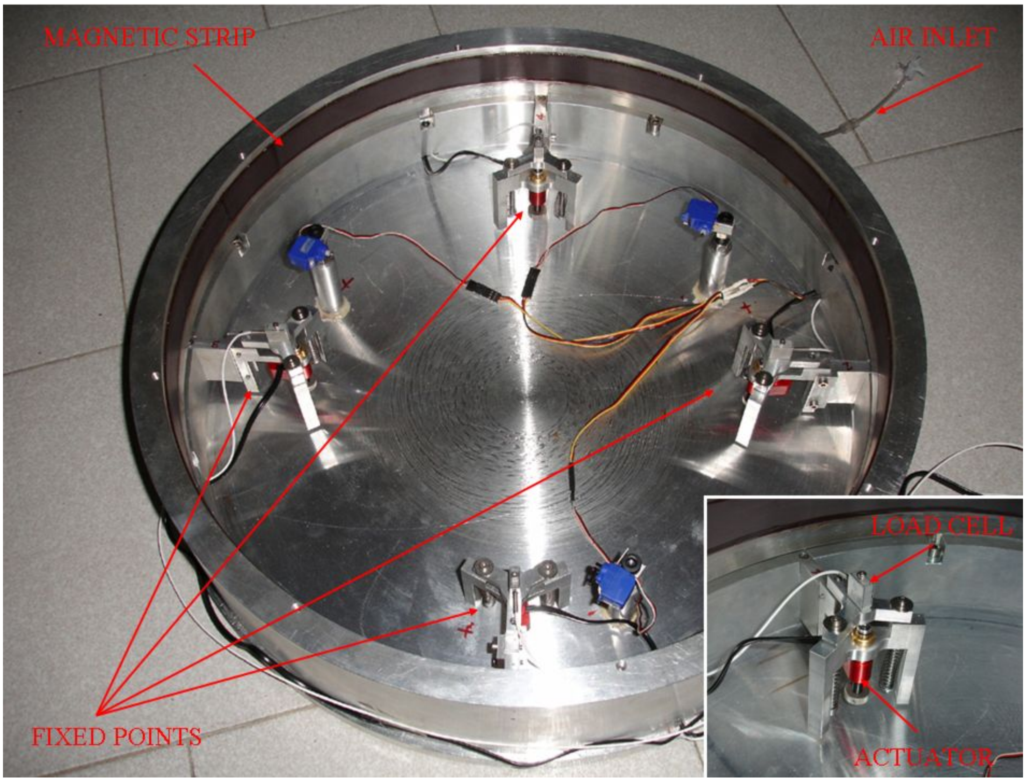

Figure 3.16: A picture of the astatic support.

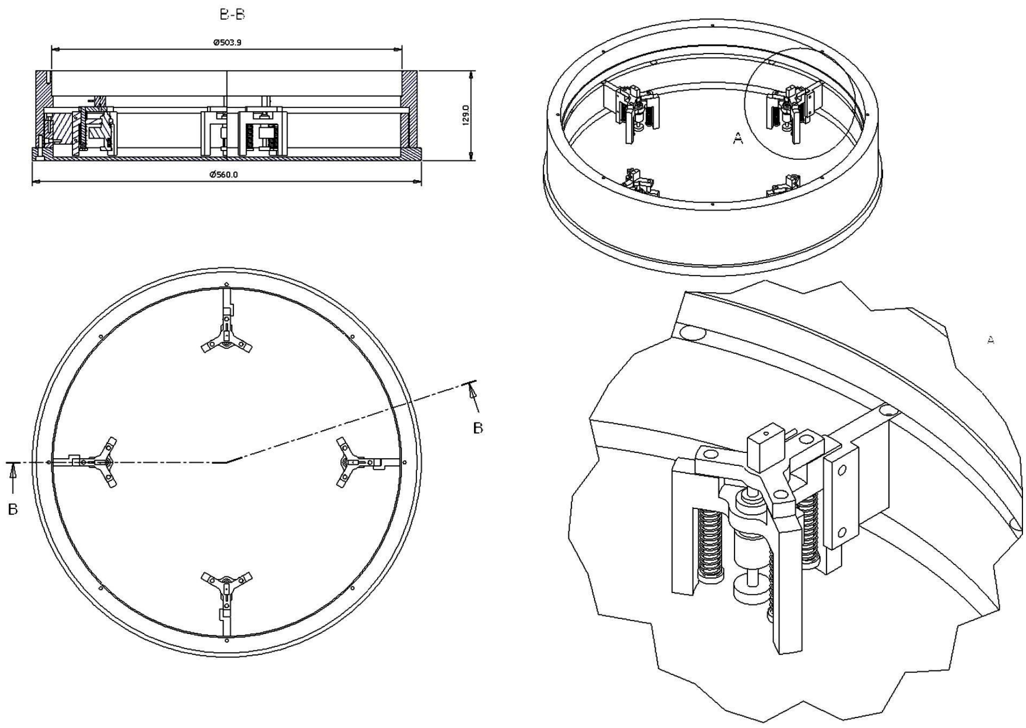

Figure 3.17: Technical drawing of the astatic support.

3.5 The manufacturing of thin glass shells

Transforming a standard float glass into a highly precise shaped glass shell involves a number of phases: from the cleaning of the tools used, to the stacking of the glass; from the carrying out of the thermal cycle, to the metrological characterization of the final product.
In the following pages are reported some photos taken during the crucial phases of the experiment. The captions describe the pictures and highlight some interesting points.

Figure 3.18: Before each experiment both the mould and the glass disk are washed with soap and bi-distilled water. This first step ensures an initial cleaning from possible residuals of grease due to inaccurate handling of the materials. They are dried quickly with filtered compressed air.

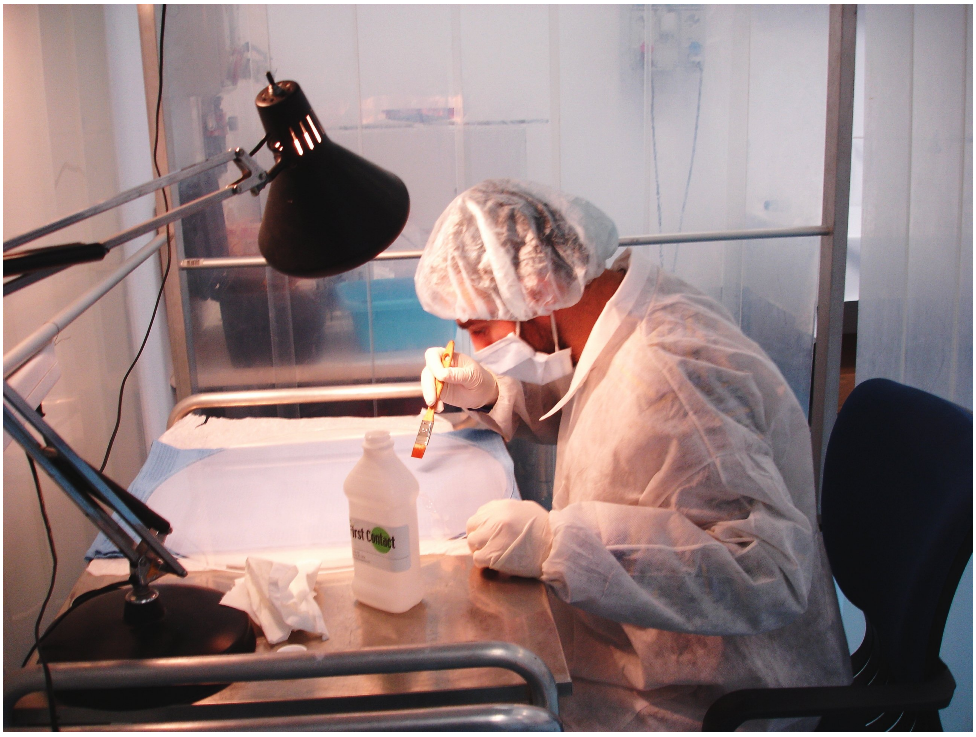

(a) Application of the First Contact optical paint on the glass.

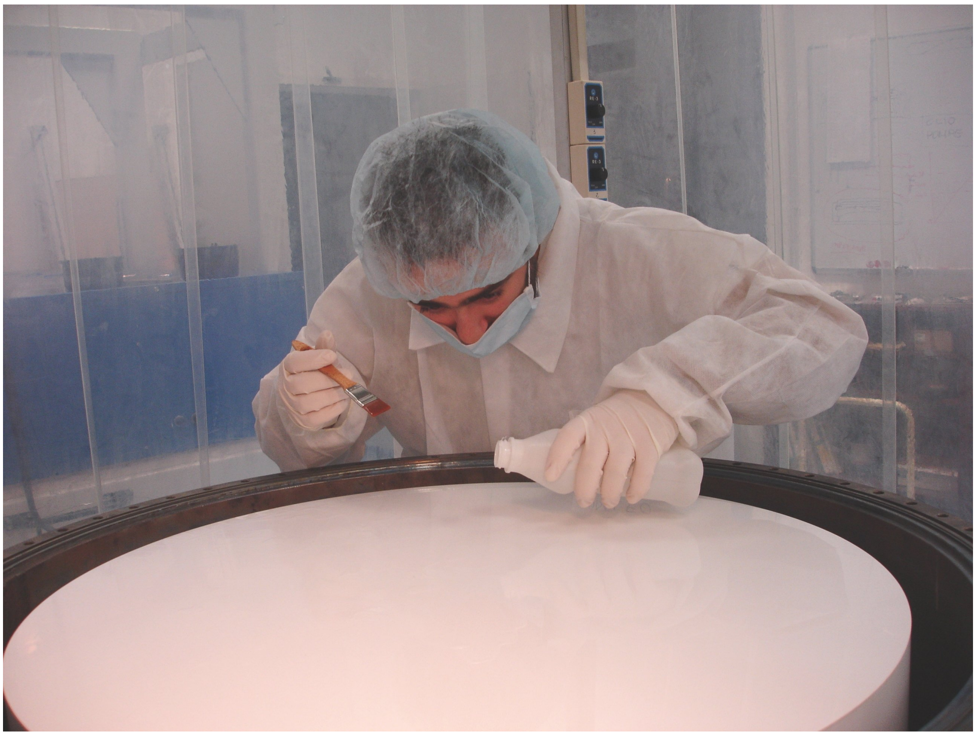

(b) The mould inside the muffle, application of the First Contact optical paint on it.

Figure 3.19: Mould and glass are brought inside a zone with a laminar air flux highly filtered (ISO 5) where the remaining phases of the process will be completed. The optical surfaces of the mould and glass are covered with a special paint for optical cleaning. It is important to spread a uniform and (enough) thick layer of paint.

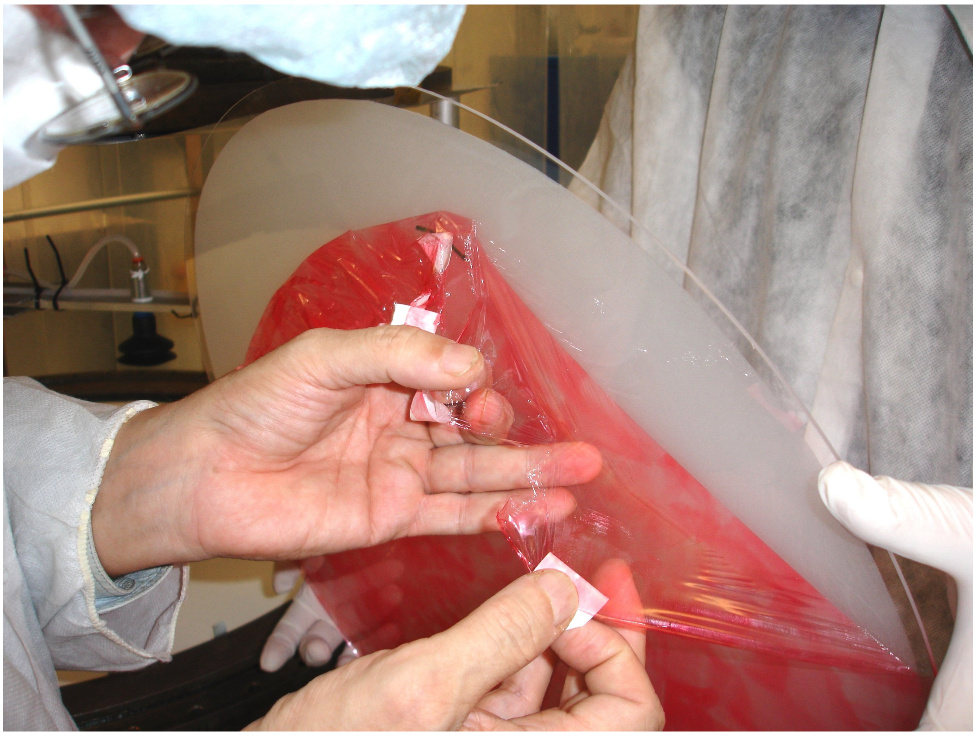

(a) Initial phase of the peeling off of the paint from the glass.

(b) Final stage of the paint peeling off from the mould.

Figure 3.20: Once the paint dries it forms a resistant thin film that can be peeled off. This action removes any dust particle present on the surfaces of the materials, leaving a surface with a elevated degree of cleaning. Obviously, it is very important to peel off completely the film, particular attention shall be done to the edges. The First Contact optical cleaning paint is sold in a colored or un-colored version.

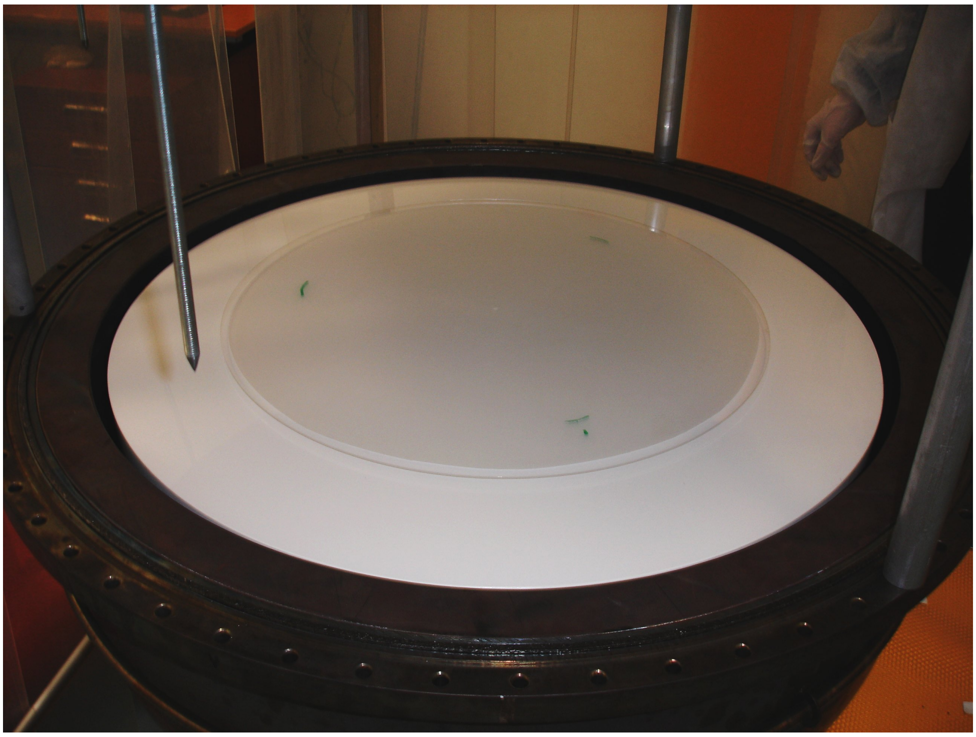

(a) Glass disk placed in position onto the central part of the mould. Looking carefully at the edges of the muffle it is visible the graphite rope used to assure the sealing.

(b) The muffle is closed and brought out from the clean zone. After this last delicate and tiring phase (about 40 bolts are screwed!) the "slumping crew" returns to smile.

Figure 3.21: Then, using a proper tool, the glass is stacked onto the mould. The muffle is closed and sealed.

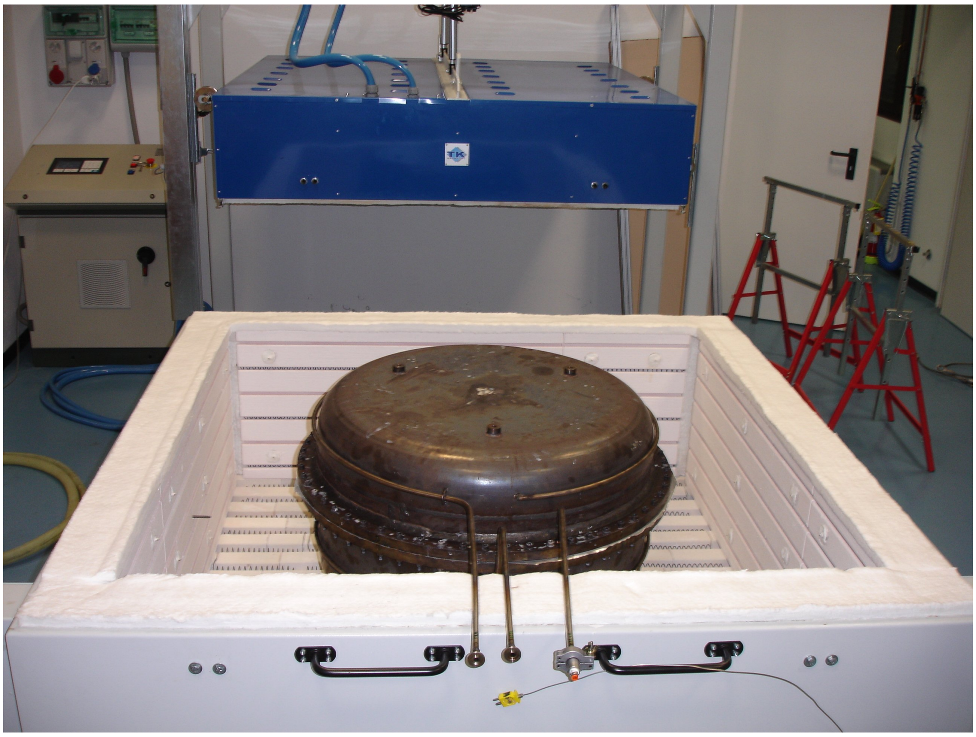

(a) The muffle is placed in the middle of the oven's cavity.

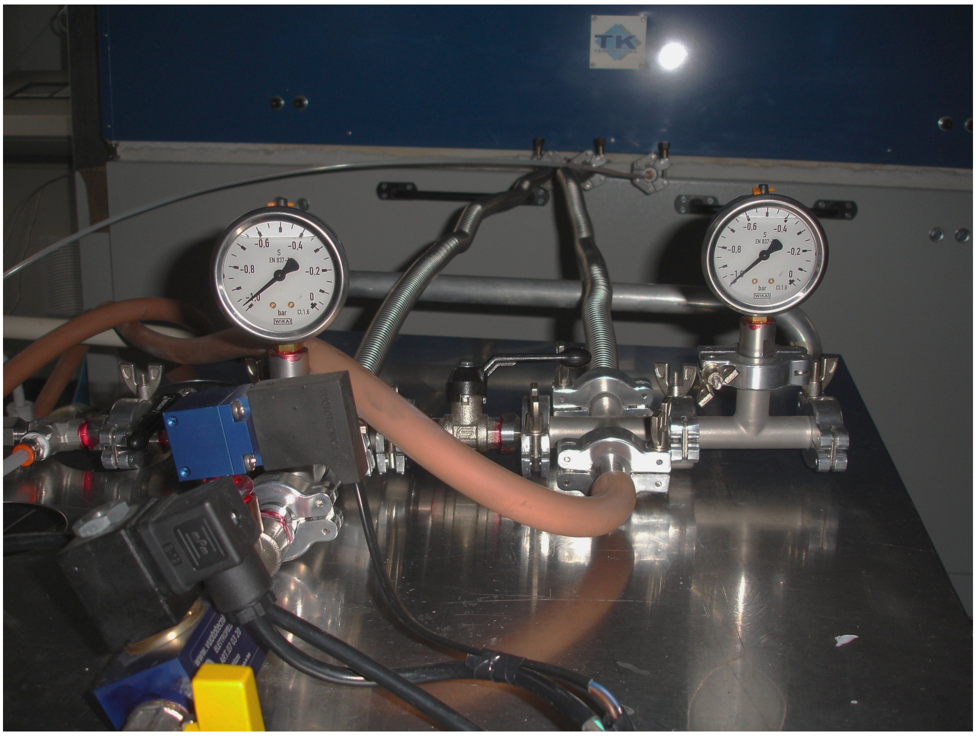

(b) Vacuometer used to check the air content inside the muffle.

Figure 3.22: The final stage consists in positioning the muffle inside the oven's cavity, the supports hold the muffle in the proper position to ensure the better heat uniformity. The air is slowly removed from the muffle and the thermal cycle can begin.

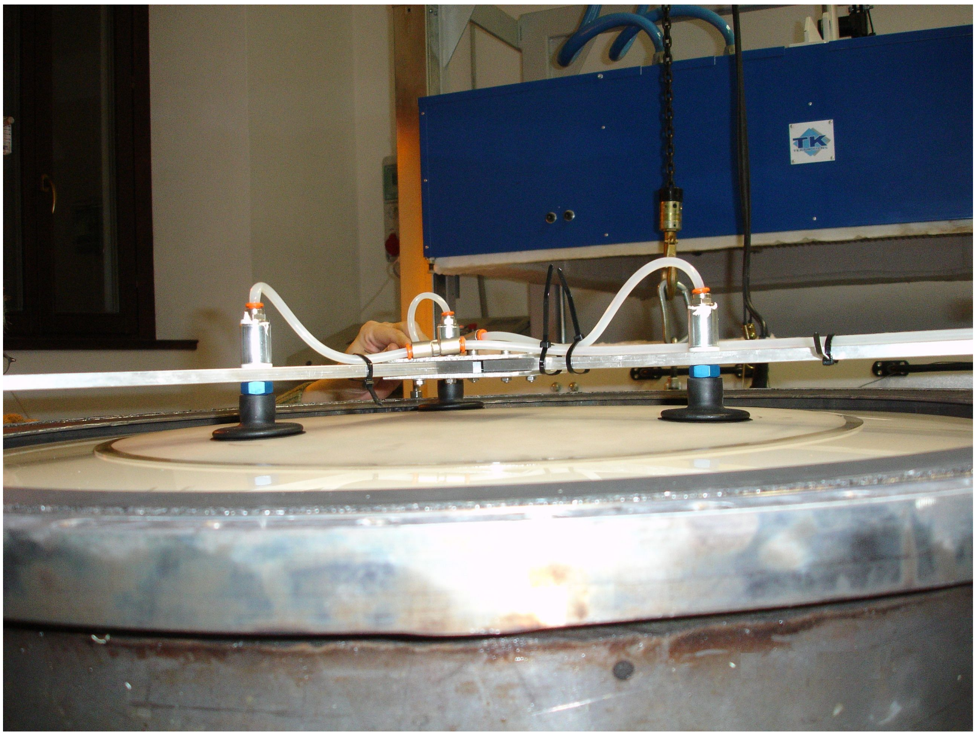

(a) The glass shell onto the mould after a slumping experiment.

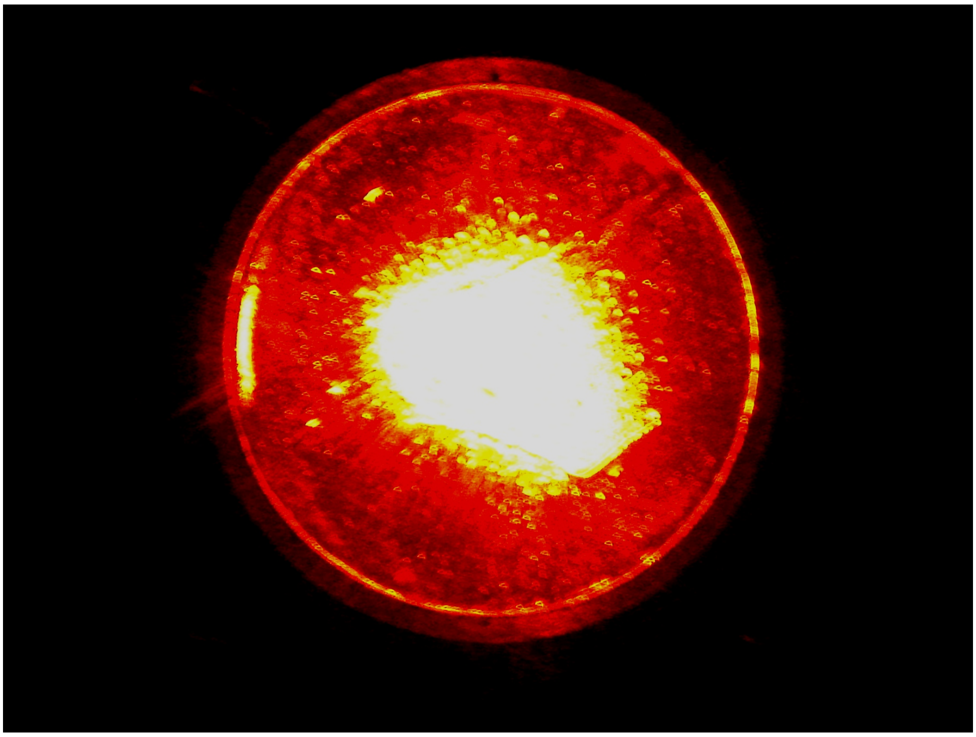

(b) Top view of the glass shell on the astatic support almost aligned with the optical axis of the interferometer.

Figure 3.23: At the end of the thermal cycle the glass shell is released from the mould using a proper tool, it has three suckers that keep the glass and lifts it. This operation is done without imposing translational movements and hence limiting the risk to scratch the surface of the mould. Then the shell is accommodated on the astatic support and aligned with the laser wavefront generated from the interferometer. If the picture had been taken with the shell perfectly aligned and from the curvature position, the surface was completely red.

Chapter 4

The measuring instrumentation

4.1 Interferometers

An interferometer is an instrument that uses the interference of light to make precise measurements of surfaces, thicknesses, surface roughness, optical power, material homogeneity, distances. Some basic definitions are the OPL that is proportional to the time the light takes to travel from a to b and the OPD between two beams that is $OPD = OPL_1 - OPL_2$. In order to observe interference fringes, several conditions must be met. The light in one beam must be both temporally and spatially coherent with the other beam in the region where interference fringes are to be observed. In addition, the polarization properties of the two beams must be compatible. Finally, the relative intensities of the two beams must be close in magnitude.

Temporal coherence is inversely proportional to the spectral bandwidth of the light source. For example, a laser is often modeled as a pure monochromatic source; that is its bandwidth is zero, hence the temporal coherence is infinite. Infinite temporal coherence means even if the light from the first beam is delayed relative to the second one of any amount of OPL, the two beams will still interfere. The temporal coherence of a source is usually given by the coherence length as:

$$L_c = \frac{\lambda_c^2}{\Delta\lambda} \tag{4.1}$$

where λ_c is the center wavelength of the source light and $\Delta\lambda$ is the spectral bandwidth, measured as the FWHM. A source can produce fringes as long as the OPD between the two beams is less than the L_c.

Two types of interference occur: constructive interference and destructive interference. When the test beam is in phase with the reference beam, there is constructive interference. The two intensities "add" to each other and the light

intensity is increased. This produces a bright area in the interferogram. When the two beams are 180° out of phase, there is destructive interference and a dark area occurs. In between, where the two beams are out of phase by some other angle there will be gray areas. The resolution of an interferometer is governed by the wavelength of light used and is on the order of a few nanometers. In order to determine the properties of the sample under test, an interferogram is captured and analyzed according to the type of interferometer that created it.
In the following are described the working principles of two-beam interferometers that return informations about the OPD between two beams (called reference and test beams). Absolute measurements can be made, but extra care must be taken in calibration and system characterization and are not here discussed.

4.1.1 The classic Fizeau interferometer

In classical Fizeau interferometer the part to be tested is placed on top of a *reference flat*. The Fresnel reflection from the bottom of the test piece is called *test beam*, while the reflection from the top surface of the reference flat is named *reference beam*. This instrument uses a spectral emission line to achieve a coherence length of a fraction of a millimeter. Figure 4.1 shows the one installed in the laboratory, the yellow light is produced by the emission lines from the doublet of the Sodium at about 590 nm. The coherence length of the Sodium light is of about a millimeter.
The OPD between the test and the reference beams is given by Eqn. 4.2. Since the reference beam travels the distance between the two surfaces twice, hence the factor two.

$$OPD = 2n_{air}t(x) \quad n_{air} \approx 1.0 \tag{4.2}$$

If these parts are being evaluated using test flats, the part is brought into optical contact with the test flat and then the fringes are counted. The only problem here is, that with a test flat, a certain amount of pressure is required to squeeze the air out of the gap. It is difficult to know when true optical contact has been made. If the air gap is wedge shaped because of a piece of dirt or lint, then there will be more fringes appearing there should be, and the part will be under-evaluated. On the other hand, if too much pressure is applied in order to produce optical contact, actual distortion of both the reference and the test flat may result. The result is that even for these simple evaluations (surfaces that are flat to a few fringes) serious errors can be made using test flats, particularly in inexperienced hands.

Fringes interpretation

The operator is faced with the problem of interpreting the interferogram and reducing the data to usable numerical values, typically P-V and rms. Fringes can

(a) Classical Fizeau interferometer installed in the lab.

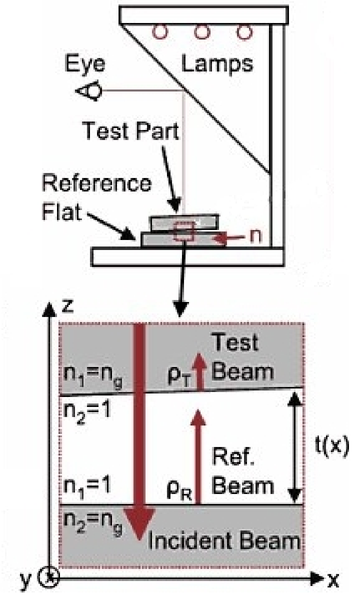

(b) Working princicle. Credits: [18].

Figure 4.1: The classical Fizeau interferometer operating with Sodium light.

be thought of as a contour lines of a contour map, can not be crossed each other and along any of them there is a constant OPD. The OPD between adjacent fringes (either bright or dark) corresponds to one wavelength of the source used. The Figure 4.2 shows four common interference fringes patterns, clockwise from top left: flat surfaces with a tilt, a defect on a flat surface, a flat reference with on top a slightly curved part and spherical surfaces with slightly different radii of curvature.

Perfectly flat surfaces, but tilted one to the other, produce straight fringes (see Figure 4.2(a)); however, if the test surface has a defect, such as a bump or hole, the fringes will curve around it (see Figure 4.2(b)). To determine if the defect is a bump or a hole on the surface, the direction of the increasing OPD must be identified. This can be determined by pushing on one side of the test piece and watching the number of fringes. If the number of fringes increases when pressure is applied, then this interferogram represent a hole on the bottom surface of the test piece. In the region of the defect, a fringe representing higher OPD is pulled in from the right, indicating that the reference beam traveled further in the region of the defect. Therefore, the defect is a hole with height h, fringes spacing S and fringe displacement Δ:

$$h = \frac{\lambda}{2}\frac{\Delta}{S} \tag{4.3}$$

The classical Fizeau is also useful for testing concave or convex surfaces. Two situations can be observed: Figure 4.2(c) describing a flat reference and a test surface with very long radius of curvature, Figure 4.2(d) describing two surfaces with similar radii of curvature but opposite inflection. In both cases, the surfaces will give concentric ring-shaped fringes that indicate either a concave or convex shaped part, this is called Newton's rings pattern. If the test surface has too much curvature the fringe frequency becomes too large and/or the OPD becomes larger than the coherence length. If the two surfaces are truly in contact at the center, then the center is always dark in reflection. This is because there is a 180° phase change for the reference beam due to the reflection at a boundary from lower index to higher index. Since the test beam has no phase change, and the OPD is zero, the two waves destructively interfere.

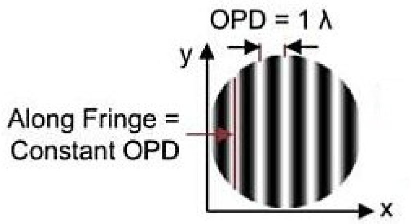

(a) Two flat surfaces tilted each other.

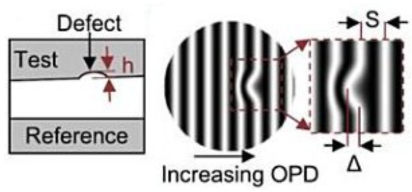

(b) Presence of a defect.

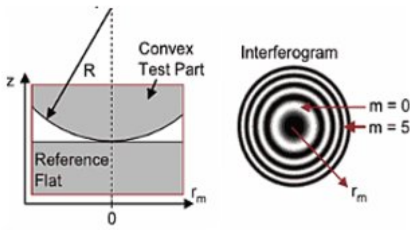

(c) A slightly curved surface upon a flat reference.

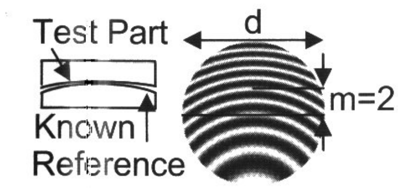

(d) Two surfaces with a small different radius of curvature, tilted each other.

Figure 4.2: Common types of interference fringes patterns visible with a classic Fizeau interferometer. Credits: [18].

In the first case (see Figure 4.2(c)), the radius of curvature R given in Eqn. 4.4 is found by counting the number of bright fringes to radial distance r_m, where the first bright fringe is $m = 0$.

$$R = \frac{r_m^2}{\lambda \left(m + \frac{1}{2}\right)} \tag{4.4}$$

In the second case (see Figure 4.2(d)), the variation of the radius of curvature between the two is given by the Eqn. 4.5 where m is the number of fringe spacing the fringes depart from straightness, d is the test part diameter, and R is the radius of the reference part. This methods is commonly used for checking the curvature of a lens surface versus a master surface during the lens grinding. The surfaces match when only tilt fringes remain.

$$\Delta R = \frac{4m\lambda R^2}{d^2} \tag{4.5}$$

In addition to the most common cases listed above, it is also possible to interpret others simple fringe patterns. In Figure 4.3 are shown interferograms from three aberrations i.e. spherical, coma and astigmatism and their combination. It worths note that the spherical aberration generates a fringe pattern similar to that of the spherical surfaces with different radii (see Figure 4.2(c) and 4.2(d)), but in this case the "fringe thickness" is constant along the radial distance.

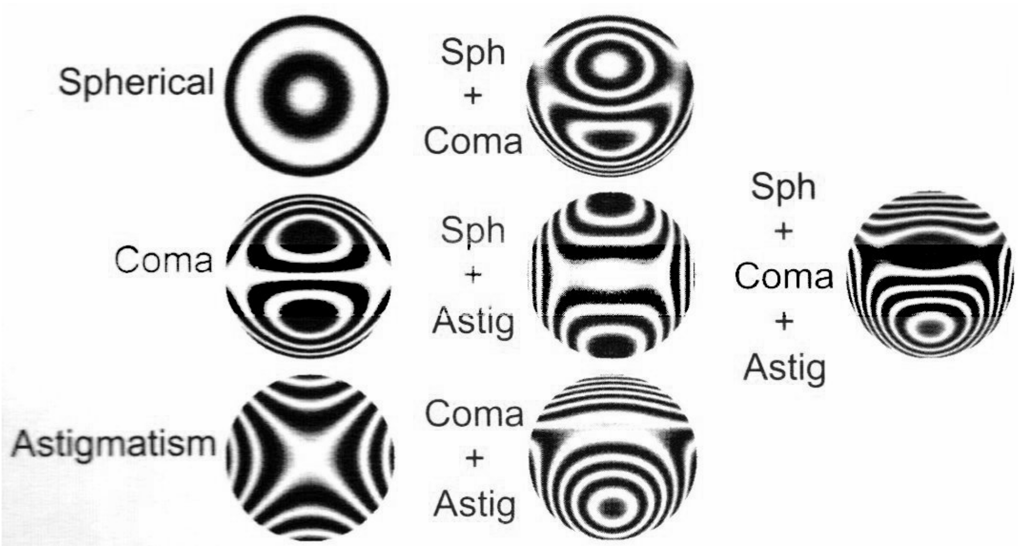

Figure 4.3: Interferograms generated by some common aberrations and their combination: spherical, coma and astigmatism. Credits: [18].

4.1.2 The laser-based Fizeau interferometer

Until the invention of the laser, short coherence length sources limited the range of interferometers configurations to those which closely match the path of the reference beam with the path of the test beam. Laser-based Fizeau overcomes this limitation due to the large coherence length of lasers. Typical laser source is the HeNe laser with wavelength of 632.8 nm and coherence length of more then 10 m.

Figure 4.4(a) is a schematic drawing of the most important features of a laser-based Fizeau interferometer. The light path begins at the laser which produces a coherent beam of small diameter (typically less than 1 mm).

The laser beam passes through a beam expander which increases the diameter of the beam so that it will fill the aperture of the interferometer. Then through a spatial filter to remove “noise” from the laser beam and minimize speckle*.
The expanding beam then passes through a beam splitter which divides the beam into two beams: one which passes through the beam splitter, and one which reflects from it at an angle of 90°.
The beam continues to expand and pass through a collimator (a lens or a system of lenses), after it the beam emerges as a parallel beam of the proper diameter (4 in for our instrument). This parallel beam still consists of highly coherent laser light.
The collimated beam of light now passes through a plate of high quality optical glass which has two highly precise surfaces. This optical element is usually called *transmission flat*. Its second surface, the second one that the light encounters along its path, is called *reference surface* and it will be used to produce the interferogram of the test piece. The first surface can be either coated with an anti-reflection coating or (more often) manufactured not precisely parallel† to the other one. For any measurements, the interferometer should be aligned with its second surface perpendicular to the collimated beam, so that the first one is not. This condition prevents any “unwanted reflection” from the first surface spoiling the interferogram.

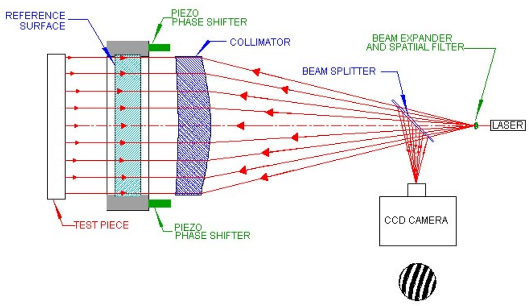

(a) Scheme of a laser-based Fizeau interferometer.

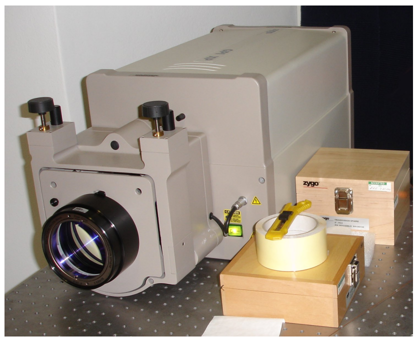

(b) The instrument equiped with a transmission sphere.

Figure 4.4: The ZYGO GPI XP 4 in interferometer available at INAF-OAB.

The region between the reference surface and the surface of the test piece is called the *cavity*.
When the light reaches the reference surface of the transmission flat, most of the

*The speckle effect is a result of the interference of many waves scattered at random angles. These waves still have coherence, but different phases which add together to give an image made of several bright and dark points. This results in noise.

†A deliberate wedge is inserted so to have a slight angle between the two surfaces.

light passes through the surface and travels on to the surface of the piece being tested. The rest of the light reflects from the reference surface and begins the return journey into the interferometer. This is the *reference beam.*
The test piece is normally mounted on a tip/tilt device that permits adjustment so that the surface under test can be made parallel to the reference surface.
When this condition is achieved, the light reflected from the test piece returns to the interferometer where it interferes with the reference beam. This backward beam is the *test beam.*
Two types of interference occur: constructive interference and destructive interference. They produce bright and dark areas in the interferogram. A *fringe* consists of one dark and one light area. Each fringe amounts to phase differences of 180°, so each fringe is equal to 1/2 wave (of the laser source).
After interference at the reference surface, the resultant beam returns to the beam splitter where half of the beam is reflected into the CCD camera where the interferogram is detected and displayed on the computer monitor.
In interferometry it is always desirable to obtain fringes of the highest possible contrast in order to obtain the best analyses. The contrast seen in an interferogram is dependent on the relative intensity of the reflections from the reference surface and the test piece. The reflection from the reference surface is dependent upon the reflective coating (or lack of a coating). An uncoated surface will reflect about 4% of the light back into the interferometer. If the test piece is made of almost any glass, the reflectance from it will also be around 4% to 5%. The interferogram produced by the interferometer will display the highest contrast image if the reflectance of the reference surface and the reflectance of the test piece are not grossly different. If the goal is to measure highly reflective surfaces such as that of a mirror, the interferometer will produce better contrast if the reference surface also has a higher reflectance coating. Special coatings can be applied to the reference surface to improve the fringe contrast over wide ranges of test piece reflectance.
This description covers the use of the interferometer making measurements of surfaces that are approximately flat. Interferometers are also used to measure curved surfaces by comparing the surface to a highly precise spherical surface known as *transmission sphere.* This last case is the one most used in the characterization presented in this dissertation. Interferometers are also used to measure transmitted wavefronts through a substrate, and can be used to determine the homogeneity and optical quality of an optical component or a train of components.
For highly precise and repeatable measurements of the test piece errors, a computer evaluation of the interferogram is recommended. Two basic types of computer analysis are discussed in the following paragraphs.

Static fringe interferogram analysis In these systems, the interferometer's CCD camera is connected directly to a "frame grabber" board in the computer. At the press of a button, all of the interferogram's imaging data is dumped into the frame grabber so that the computer can begin elaborate data processing of the fringe position and straightness.
It is possible to make a flatness evaluation based upon the position and shape of 2 or 3 fringes, the static fringe software looks a hundred or more data points on the fringes and performs sophisticated data reduction techniques to produce hard figures of rms flatness, P-V flatness, irregularity, etc. This permits the generation of elaborate graphical output of surface contour.

Phase shifting interferogram analysis In a phase shifting interferometer, under software control, piezoelectric transducers actually move the reference surface in a number (typically 5) of predetermined steps, usually 1/4 wave steps towards the test piece. At each position, the interferometer's frame grabber board captures an interferogram and stores it for analysis by the software.
The frame data are then processed by the computer to calculate optical wavefront errors. The software finds aberrations and computes both P-V and rms values. The operator has the option to subtract tilt, power, astigmatism, coma, and spherical aberrations from the data.

The choice between these two types of systems is dependent on a number of factors:

- phase-shifting interferometers are substantially more expensive than static fringe systems, although the same type of data and graphic output is provided by both systems, the phase-measuring interferometer will provide higher accuracy and repeatability;

- with a static fringe interferometer it is necessary to place a synthetic aperture around the part being measured as well as a synthetic obscuration about any holes in the part. This is required to tell the software "where not to look". Placing these apertures and obscurations is the responsibility of the operator, and can be a slow and nearly impossible task with some complex test pieces;

- with a phase-shifting interferometer this is unnecessary, since it looks at phase data, it never requires a synthetic aperture or obscuration. Not only does this save a lot of time and effort, but it also guarantees a higher level of accuracy;

- since the static fringe interferometers do not change the distance between the test piece and the reference surface, it is not possible to tell the difference between concave and convex. Phase-shifting interferometers do not face this problem, since they move the reference flat and the system can determine whether the test piece is concave or convex.

The instrument we used for the metrology is a ZYGO GPI XP 4 in aperture interferometer equipped with a phase shifting interferogram analysis software (see Figure 4.4(b)). The light source is a HeNe laser at 632.8 nm with a coherence lenght of about 100 m. The repeatability of the instrument is of about $\lambda/10000$ with a resolution of about $\lambda/8000$. With this system can be mounted either a transmission flat that generates a planar wavefront better than $\lambda/20$ P-V or a transmission sphere that generates a f/3 spherical wavefront better than $\lambda/20$ P-V.

4.2 The optical profilometer

The WYKO TOPO-2D system is a surface profilometer microscope-based instrument using visible polychromatic light interferometry to measure surface finish (i.e. microroughness) of optical surfaces. A schematic of this interferometer is shown in Figure 4.5(a). Light reflected from the surface under test interferes with light reflected from an internal reference surface. The resulting interference pattern is viewed through the eyepieces of the microscope. The interference pattern is also recorded by the image sensor and digitized by the computer. Deviations of the fringe pattern are related to surface height deviations.
Going in more details, the microscope objective has built into it a Mirau interferometer with an internal reference surface. The Mirau interferometer is mounted on a piezoelectric translator that is moved under computer control. Computerized movements of the interferometer introduce a known phase shift in the interferogram, and these are simultaneously recorded. The computer software converts movement of the interference fringe pattern to surface height deviations. The entire measurement cycle occurs in only a few tenths of a second.
The TOPO-2D system is equipped with two different objectives 20X and 2.5X. The first one allows profile measurement length of 0.66 mm with a spatial sampling interval is 0.65 μm, while the second one has profile measurement length of 5.25 mm with a spatial sampling interval of 5.1 μm. The optical resolution of the TOPO-2D system in the plane perpendicular to the surface (i.e. in the surface profile) is in the ångström range with a repeatability for profile height measurements is 0.01 nm rms.

4.3 The Nomarski interference microscope

The Nomarski microscope returns a surface image and it does not permit roughness measurements. Nevertheless, it is widely used to see the roughness of pol-

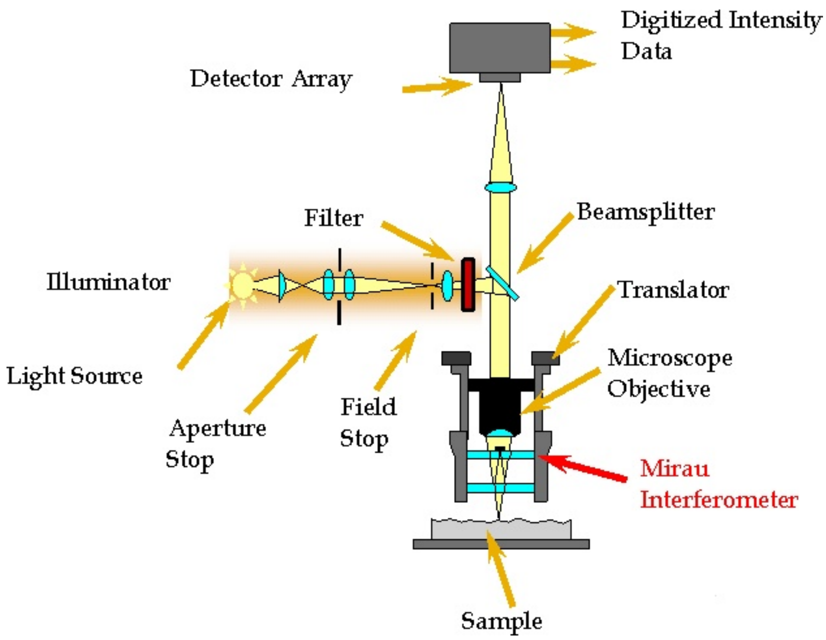

(a) Scheme of the WYKO TOPO 2D.

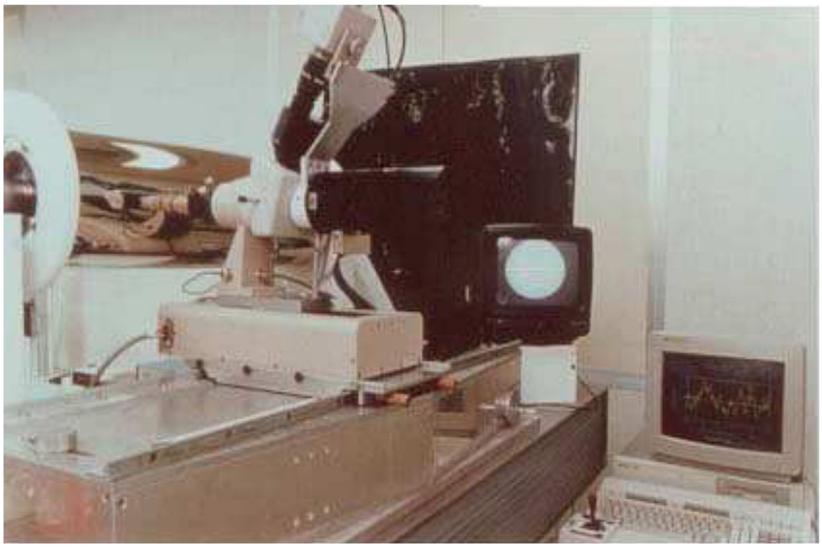

(b) The instrument while measuring a superpolished surface.

Figure 4.5: The WYKO TOPO 2D optical profilometer available at INAF-OAB.

ished samples, and to understand the size and origin of surface defects.
In Figure 4.6(a) is shown the scheme of its working principle. In the Nomarski microscope a white light source is used, followed by a polarizer which sets the angle of polarized light incident on a Wollaston prism. The Wollaston is made of two uniaxial crystals (different index of refraction for the two polarization states) with optical axes as shown. The change in index causes a polarization-dependent

refraction at the crystal interface. The Wollaston prism splits the light into two beams of orthogonal polarizations propagating at slightly different angles (see Figure 4.6(b)). A lens focuses the two beams at two positions on the surface under test, separated by a slight offset. If a surface defect is present, the two beams will be reflected back through the prism and are recombined with two different phase changes. After a further polarization plane rotation, the beams interfere in the image plane. The phase variation appears in the variable brightness of the image, returning a surface map with a sensitivity of 1 nm. The space resolution is near to the used light wavelength, i.e. 0.22 μm.
Many magnifications are selectable (from 5X up to 100X) and the phase difference may be shifted in order to highlight the features at the most interesting height.

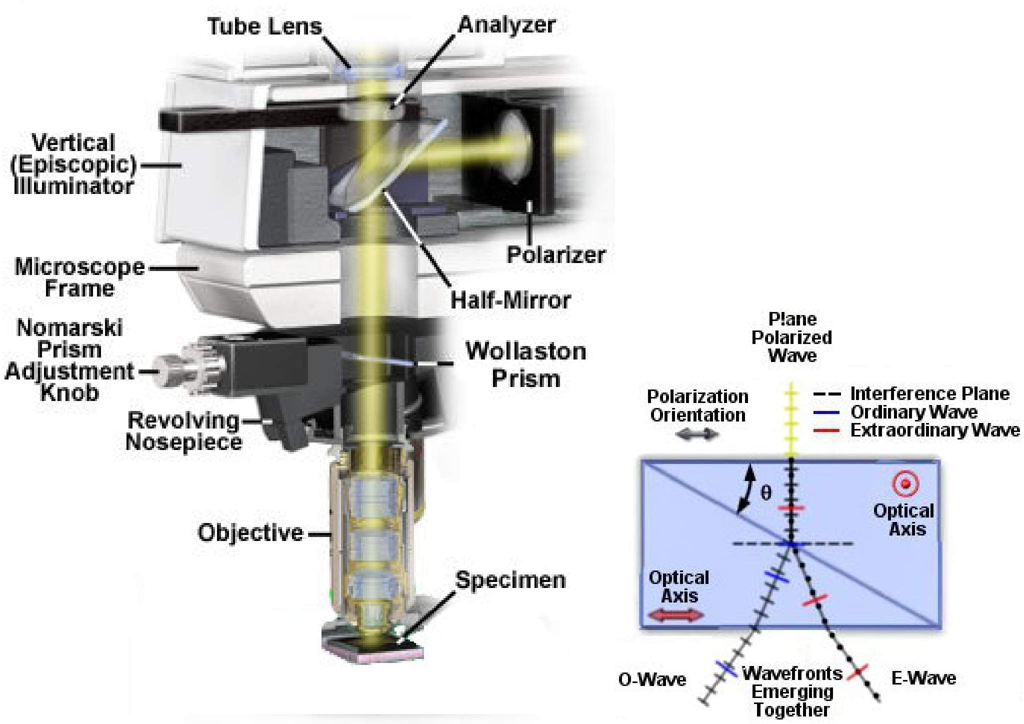

(a) Scheme of the Nomarski microscope. (b) Light path on a Wollaston prism.

Figure 4.6: The Nomarski phase contrast microscope.

4.4 The Long Trace Profilometer

The LTP is a sensitive slope-angle-measuring instrument, based on the original concept of the pencil-beam interferometer of Von Bieren, and developed by P. Tackacs et al. Since this instrument has a sensitivity to wavelength in the range

from meters to millimeters then it is very useful to characterize the shape's imperfection of mirrors, but it can not measure the surface roughness.
The LTP measurement principle is presented in Figure 4.7(a): a pencil laser beam scans the surface of a mirror, and the reflected beam direction changes according to the local surface slope at that position. A Fourier transform lens converts the angle variation of the reflected beam in a variation of position in its focal plane. Another part of the beam is focused on reference surface, in order to subtract the tilting and rotation of the optical head. An advantage of such a configuration is a significant weight reduction of the movable part of the interferometer with an obvious decrease of mechanical flexure of the scanning slide, and a side-mounting configuration for the surface under test that greatly reduces the gravity induced deformation on the optical element under test.

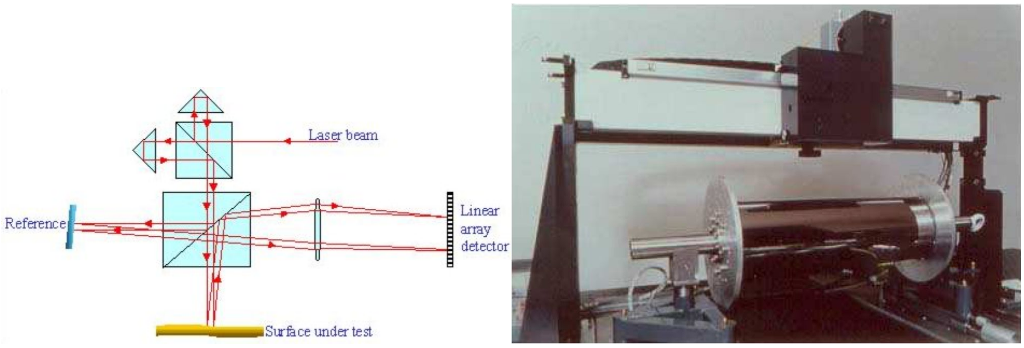

(a) Scheme of the LTP. (b) The LTP tracing a profile of a superpolished mandrel.

Figure 4.7: The LTP available at INAF-OAB.

The focused laser beam position is recorded by a linear array detector and the local slope of the mirror under test is obtained. With proper environmental conditions and periodic and precise calibrations of the instrument, LTP is able to measure slope profiles, with an accuracy better then 1 mrad rms.
The whole instrument is mounted on self-stabilizing, air-suspension table. This is necessary for isolation from ground vibrations. However, other important parameters to be checked are related to environmental changes while measuring, mainly temperature stability and air turbulence along the laser beam path.

Chapter 5

Metrology of slumped glass

In order to access the problematics related to the slumping of a large size glass were performed a number of preliminary tests. The aims of these experiments were multiple: to define the copy capability of the process, both for low and high spatial frequencies; to evaluate the influence that both the dust particles and the pressure force have on the shell's shape; to check the various transition temperatures of the BOROFLOAT® 33 glass type, in particular the lower annealing temperature (the strain point) it is very different from that reported on the data sheets; to define the optimal thermal cycle; to define a detailed procedure to get the best result from the process.
In this chapter are reported the results from the metrological characterizations.
A number of slumping tests were made using a dummy ZERODUR® K20 mould. This mould has both the surfaces grinded, figured and optically polished; on one side with an almost flat profile ($PV_{ref} \approx 7\ \mu m$, concave), on the other side with a convex spherical profile with a radius of curvature of 3956 ± 16 mm*. In the following we will call these two surfaces "flat" and "convex". The microroughness level of both sides was of about 5 nm rms.
In § 5.1 are reported some consideration derived from preliminary experiments done in "a very rough way". The aim was to have a quick evaluation of the performances of the slumping assisted just by gravity force and the influence of the dust particles. These tests were performed using both the sides of the dummy mould.
In § 5.2 are reported the results from tests made on the flat side of the dummy mould. These tests were made with BOROFLOAT® 33 glass pieces, 100×50 mm^2 size and 2 mm thick.

*The radius of curvature has been measured with a CMM system with a precision on the spatial position of the measured point of about $\pm1.5\ \mu m$ that translate to about ±16 mm in the radius of curvature

In § 5.3 are reported the results from tests made on the convex side of the dummy mould. These tests were made with BOROFLOAT® 33 glass pieces, circular disks with diameter of 130 mm and 2 mm thick.
The last two sections report the results obtained on the 0.5 m glass shell demonstrators replicated from the 0.7 m mould.

5.1 Evaluation of dust particles and gravity force

The initial trials were performed with a slumping procedure quite rough and assisted only by the own weight of the glass piece. In addition, the thermal cycles did not care about the cooling down phase, absent or limited annealing phase; the contact surfaces were cleaned from dust, but the slumping occurred without any kind of protection into the oven cavity.
In Figure 5.1 is visible the resulting OPD, after the slumping, of three different glass pieces placed above the mould. The irregular pattern of interference fringes gives directly a qualitative idea of the large shape difference between glass and mould.

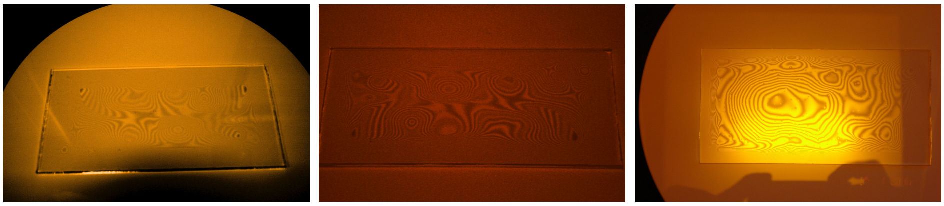

(a) (b) (c)

Figure 5.1: Some examples of slumping experiments assisted only by the gravity. The very irregular fringe patterns reveal, among other things, the presence of dust particles and the edges not completely slumped.

Points in full contact with the mould are limited to three or four at the corners of the glasses (see Figure 5.1(a) and 5.1(b)). Even a single dust grain can influence a large area of the glass, from 1 mm to 1 cm wide. Many of them were found trapped between glass and mould producing the concentric rings visible in the same pictures. The use of a muffle, preferably with vacuum (even if partial), reduces the thermal convection that brings small particles between the two surfaces.
In Figure 5.1(c) is reported the result from a slumping done onto the convex side of the mould. It is visible a corona of 10 mm width, along the perimeter of the glass, with dense fringes. This effect can be explained as follow: the glass touches the mould only on its center. Since the glass slumps by its own weight (that is distributed on the entire area), it progressively diminishes as soon as the glass

adapts to the mould. As the slumping proceeds, lesser weight is available for the edges and hence the air gap between glass and mould remains quite large. Strategies to reach a better contact on the edges consist both in increasing the soaking time at the slumping temperature and the use of an additional force to push the glass.
The inspection of the surface with the Nomarski microscope revealed other details (see Figure 5.2): small pits emerging from the surface, concentrated where the surface is not in optical contact with the mould. Their dimension is of about 10 μm and the number density seems to increase with the temperature or blowing up the soaking time. From a bibliographic search it is easy to suspect a recondensation of Tin on the glass surface. It is commonly known that float glasses are contaminated by Tin from the manufacturing process and from [19]

> [...] float glass samples, exhibiting different levels of their haze indices after reheating, have been investigated in terms of their surface morphology and surface composition. [...] It was found that a tin-enriched layer was formed at the surface, due to the migration of tin towards the surface during reheating. There was a linear correlation between the amount of tin enriched at the surface and the haze index after reheating. [...]

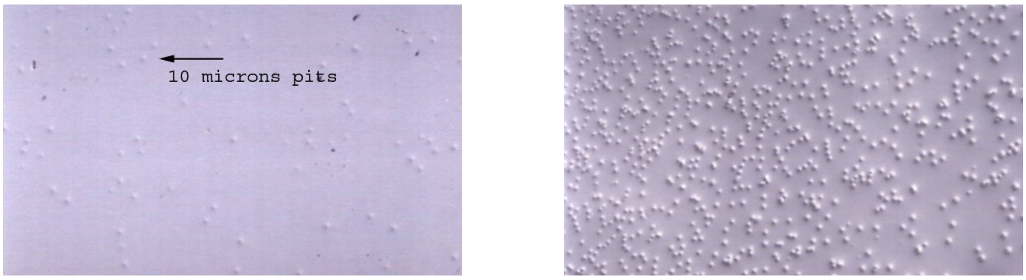

Figure 5.2: Microphotographs of a glass sample showing the Tin enrichment of the surface after reheating.

In Figure 5.3 are shown the results of two slumping performed on the convex side of the mould by using glass disks. For the experiments it was used a metallic cover placed above the mould, acting as protective cap against the dust; it was also applied a little pressure on the glass.
In Figure 5.3(a) a circular pattern of dense fringes is visible, due to a quite large difference in the radius of curvature of the two. There are patches not showing fringes. Some of these patches are still due to dust specks, but others are simply areas where the glass was not pushed well against the mould. The explanation is, most probably, the application of a not enough homogeneous pressure and hence some areas of the glass were unable to slump completely. In the second test

(see Figure 5.3(b)) the pressure force has been increased with a global benefit, however still to many dust particles are present.
These results shown a major improve from the previous slumping tests. Also, they are a proof of the concept that applies an additional force that pushes the glass is a viable technique to be pursued for the slumping of thin glass sheets.

(a)

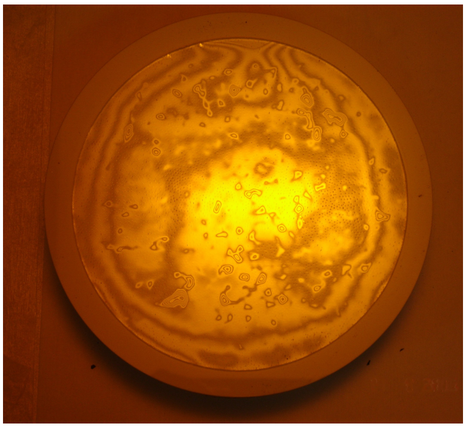

(b)

Figure 5.3: Two examples of glass disks slumped implementing a protective cover against the dust and some additional force to push the glass.

5.2 Assessment of medium and high spatial frequencies

The flat side of the mould was used to investigate the spatial frequencies copy capability of the slumping process [20]. Rectangular segments were slumped and then their surface inspected and characterized in term of PSD. Surface profiles were measured on the glass surface before and after the slumping process and compared, through a Fourier analysis, to that of the mould.
In Figure 5.4 is visible the interferometric fringes pattern (from a classical Fizeau setup) generated by the shape's differences by a rectangular glass piece placed above the mould. The three pictures refer to different phases of the process, from the top: 5.4(a) before the thermal cycle, glass as it comes from the manufacturing process; 5.4(c) just out from the oven after the slumping; 5.4(d) after the complete thermalization with the room.
The first photograph (see Figure 5.4(a)) shows the typical patter between a flat surface and a slightly curve one, with the fringes that densify going from the center to the edges of the glass. In this case the number increases very quickly, till the fringes became almost indistinguishable at the far edge. This means a large difference between the two surfaces: in particular the surface of the glass in contact with the mould is considerably convex, a raw count returns an OPD of

about 50 fringes. From the Eqn. 4.2 we obtain:

$$t(x) = OPD/2 \approx 15\ \mu m = PV_{ref} + PV_{test}$$

and hence the glass piece has a $PV_{test} \approx 8\ \mu m$, confirmed by its profiles measurement taken with the LTP and reported in Figure 5.4(b).

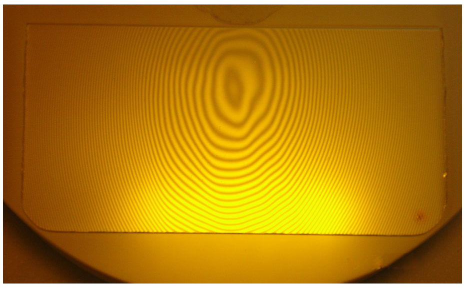

(a) Glass vs mould before the slumping.

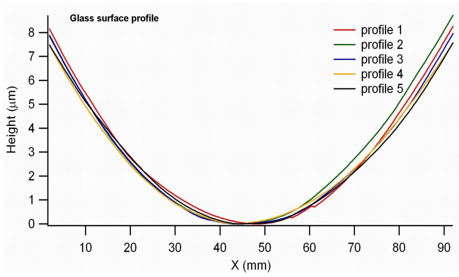

(b) Glass profiles before the slumping

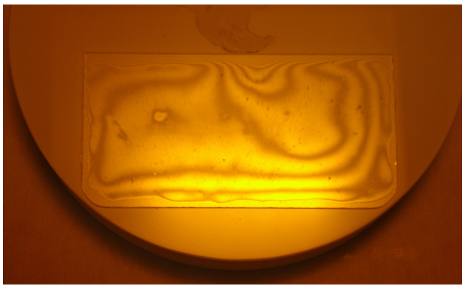

(c) Glass vs mould immediately after the slumping.

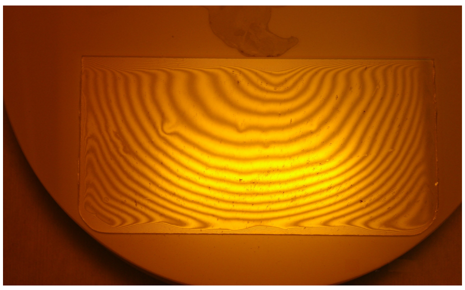

(d) Glass vs mould after completed thermalization.

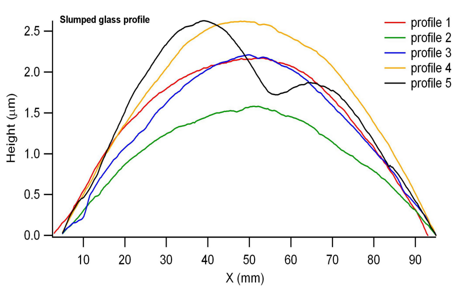

(e) Glass profiles after the slumping

Figure 5.4: Slumping experiment to evaluate the medium spatial frequencies.

After the slumping the glass has changed its surface profile approaching the one of the mould. The experiment was performed applying a uniform pressure of about 16 gr/cm^2 on the glass during the soaking time of the thermal cycle. The second photograph (see Figure 5.4(c)) has been taken just after the cooling down of the oven. The number of fringes is very limited indicating a good match between the two surfaces, the OPD counts less then 3 fringes up to the far edge. After several minutes the mould and the glass piece thermalized completely with the room and the patter of fringes obviously changed. Its final configuration is shown in the third photograph (5.4(d)): the OPD is of 14 fringes slowly increasing through the edges, this means a difference in the two profiles not pronounced. In fact, repeating the same of above

$$t(x) = OPD/2 \approx 4\ \mu m = PV_{ref} + PV_{test} \Rightarrow PV_{test} = 4 - PV_{ref} \approx -3\ \mu m$$

Once again in very good agreement with the LTP profiles measurement shown in the plot of Figure 5.4(e). Moreover, the glass profile is passed from concave to convex, as expected from the copy of the mould.
The explanation for the number of fringes has not to be searched in the differences between the thermal properties of the two materials, instead in the thermal behavior of the experiment. The CTE mismatch between the ZERODUR® K20 and the BOROFLOAT® 33 accounts for less then one fringe. The 14 fringes visible are instead generated from the combination of two other effects occurred during the annealing phase: a radial temperature gradient along the mould and a difference in temperature between the upper and lower side of the glass piece. Both these effects can introduce permanent stresses in the glass generating profile errors. The second effect produces a change in the radius of curvature quantified by the Eqn. 5.1:

$$\Delta R_{glass} = -\frac{R^2}{\tau} \cdot \alpha_{glass} \cdot \Delta T \tag{5.1}$$

where R is the radius of curvature of the mould, τ the thickness of the glass piece, α_{glass} is the CTE of the glass and $\Delta T = T_{back} - T_{front}$ is the difference in temperature between the two sides of the glass. With our setup, each tenth of a degree produces about 1 fringe in the OPD.
The changes of the surface profile are more clear analyzing the surface power spectrum. Figure 5.5 shows the comparison between the PSDs of the mould (dashed line), the glass piece before (full and dotted line) and after the slumping (dash-dotted line). The data were acquired both with the LTP and the ZYGO in the spatial range from about 90 mm to 0.7 mm. The PSD of the slumped glass is contained within the PSD curves of the mould and of the not slumped glass. This means that the amplitudes of the spatial frequencies describing the glass "before" were modified approaching those of the mould, at least down to about 1 mm. However, the tail at higher frequencies of the glass is almost un-

changed, meaning the slumping process is till not able to reproduce those features.

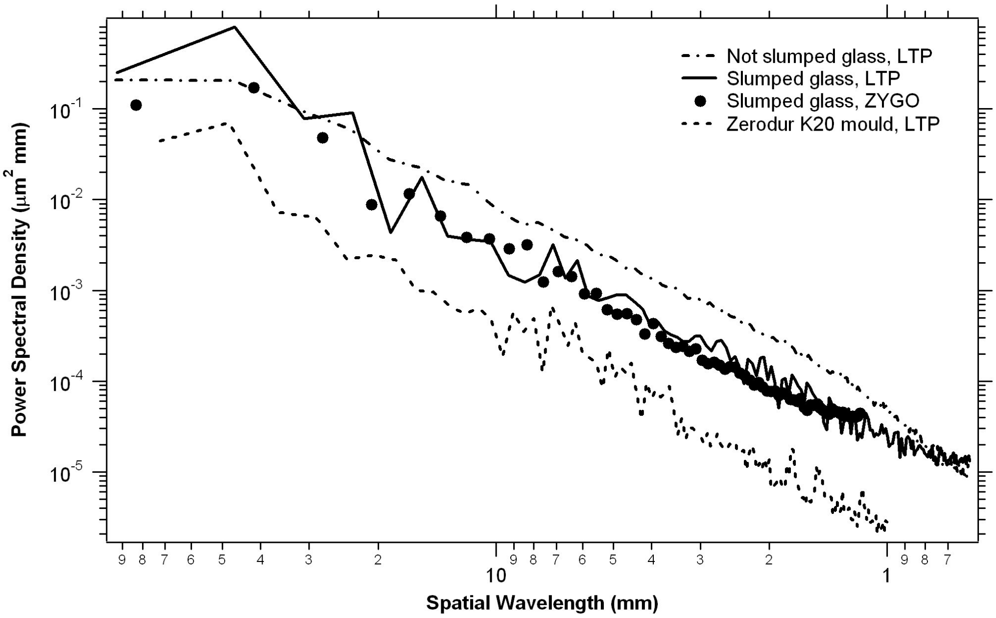

Figure 5.5: The evolution of the PSD of a glass sheet due the slumping process, compared with that of the mould.

To improve the process's copy capability in this frequencies range it has been conducted another test increasing the pressure at about 60 gr/cm^2 and lengthening the cooling phase. The result is an overall improvement both at lower and at higher frequencies. Almost just one fringe covers all the surface (see Figure 5.6(a)) and the PSDs overlap quite well (see Figure 5.6(b)). Moreover, microphotographs were taken with the Nomarski microscope: a scratch was present on the mould, this was used as reference point to find the same area on the glass surface. It was about 40 mm long and crossed by another lighter scratch. The picture shows the scratch on the mould (top) and on the glass (bottom). Clearly the features were fully copied together with the microroughness (see Figure 5.6(c)).
Finally, almost no visible dust particles were trapped between glass and mould.

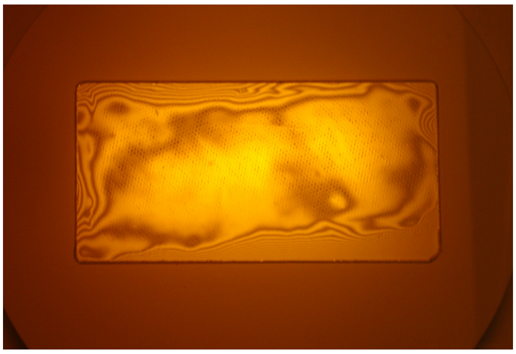

(a) Glass vs mould after the slumping

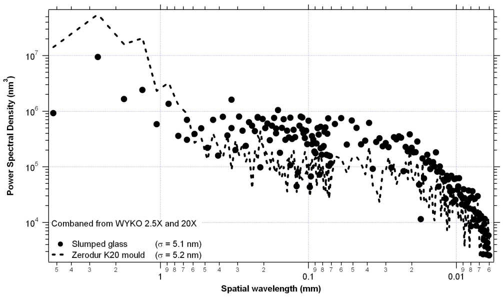

(b) Comparison of the PSDs.

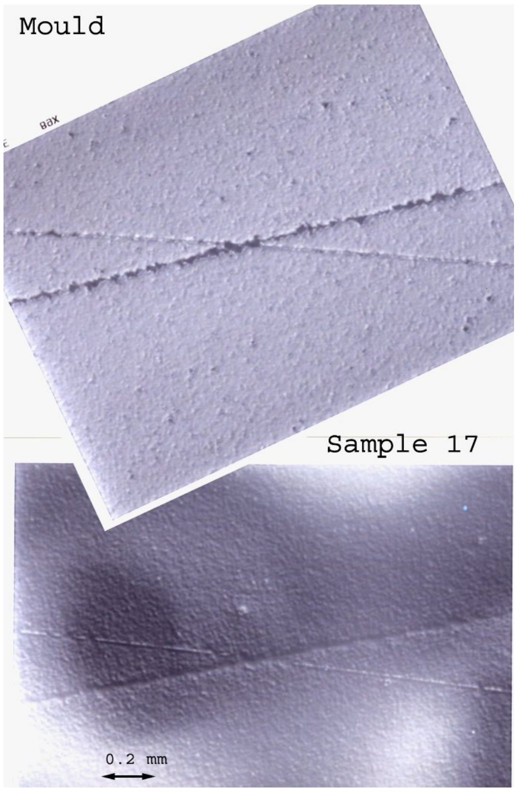

(c) Microphotographs of a scratch copied from the mould (top) to the glass (bottom).

Figure 5.6: Slumping experiment to evaluate the high spatial frequencies.

5.3 Small-size f/15 thin glass shells

Using the convex side of the dummy mould a number of glass disks 2 mm thick have been slumped with the aim to refine the process and verify its repeatability. The glass shells are been slumped with small changes in the process parameters (slumping temperature, heating and cooling rates, amount of pressure) and hence the results differ each other of some amount. The resulting glass shells have a diameter of 130 mm with a high focal ratio f/15.

These shells have been characterized in terms of focal length, using a collimated laser beam; shape errors respect the mould, with a classical Fizeau interferometer; and, finally, accurate shape, by means of a phase shifting interferometer. In this section are reported the results from the characterization of four different shells.

5.3.1 The radius of curvature

To check the radius of curvature, each shell was illuminated by a laser beam with 100 mm of aperture and the distance from the focal spot measured by mean of a tape measure. This raw measure returns to be very fast and effective to estimate each shell, the measure has an error of about ± 10 mm (hence ± 20 mm on the radius of curvature). The results are reported in Table 5.1. The repeatability of the process returns to be very high, in fact the error in the focal length is of few percentage.

Shell's ID	**Focal length** [mm]	**Radius of curvature** [mm]
shell #1	1990 ± 10	3980 ± 20
shell #2	2000 ± 10	4000 ± 20
shell #3	1950 ± 10	3900 ± 20
shell #4	1970 ± 10	3940 ± 20

Table 5.1: Measured focal length and radius of curvature for the f/15 glass shells.

For the shells #1 and #4 the values measured fall within the error bars of the measure of the mould, this means the parameters used for these two slumping tests deliver a replication of the radius of curvature that is better than the error of the measure. A strong confirm of this measure of the radius of curvature can be obtained from the estimation of the fringes visible in Figure 5.7(a). The picture shows quite circular and concentric rings and this is the typical pattern expected from a defocus between the two surfaces. Their number is much lower than that of the very initial tests shown in Figure 5.3(a). Despite it could be still considered quite high, it is possible to count 10 of them, applying the Eqn. 4.5 the radius returns to be $R = 3979 \pm 16$ mm, perfectly matching the other measure.
Since the fringes show quite a deviation from a circle hence a certain amount of errors at higher spacial frequencies are present in the shell. Their evaluation has been performed through the ZYGO interferometer, and are reported in the next section.
For the shells #2 and #3 the measures fall outside the error bars indicating that the changes applied at the process's parameters deliver a worse replication of the mould radius (the shape accuracy remains almost unchanged, see next section). However, the values of the radius are not far from the nominal value. In fact, for the shell #2 from the interpretation of the fringes of Figure 5.7(b) and from the Eqn. 4.5 the radius should be of $R = 3971 \pm 16$ mm, this range of values overlaps both the measure of the mould and the measure derived from the focal length.
Moreover, the fringes appear remarkably circular and smoother respect to the

shell #1 indicating a higher degree of fidelity in the shape's replication.
From this analysis returns that the errors introduced by the slumping process are smaller than the measuring accuracy on the radius of curvature. It worths noting also that the variation due to the difference in CTE between the glass and the mould amounts to an OPD of about 1.5 fringes, a deviation well visible as fringes but negligible in terms of radius of curvature (about 3 mm).

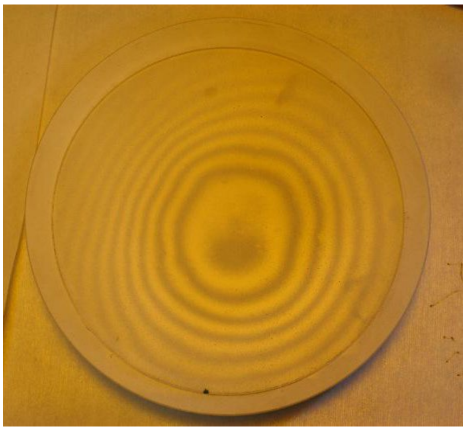

(a) Shell #1.

(b) Shell #2.

Figure 5.7: Interference fringes obtained positioning the f/15 shells onto the mould. The fringes are generated by the shape difference between the two.

5.3.2 The optical figure

The accurate measurement of the shape has been obtained from the comparison with the transmission sphere of the ZYGO interferometer installed in an ad-hoc setup on a vibration isolation optical table. The optical layout of the measure consists of a diverger lens (the transmission sphere) to generate a spherical laser wavefront. The glass shells where placed so that this beam is normally incident to their surface and their center of curvature is coincident with the focus of the diverger lens. In this way, the return beam retraces the same path back through the interferometer. To achieve the 4000 mm needed three highly precise flat folding mirrors have been positioned along the optical path. Since the transmission sphere has a focal ratio of f/3.3, this setup is able to deliver the full aperture characterization of the f/15 shells. The results obtained from these measurements are expressed as surface error rms in terms of λ (@632.8 nm). Figure 5.8 shows the setup just described.

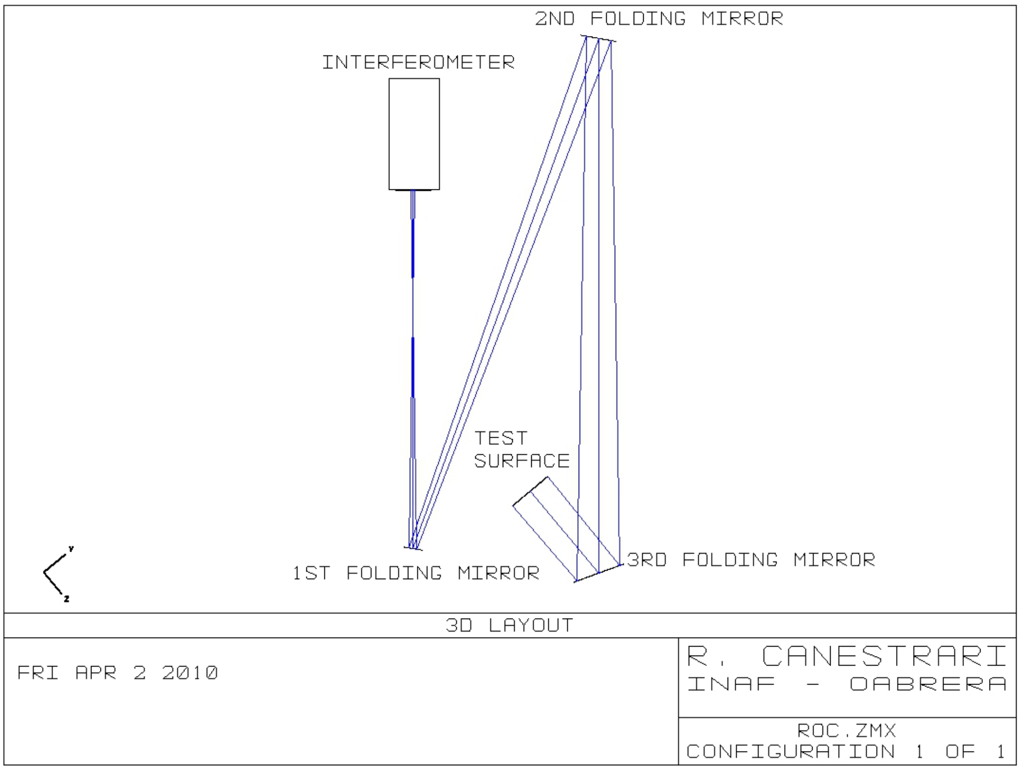

(a) Optical layout adopted to measure the f/15 glass shells.

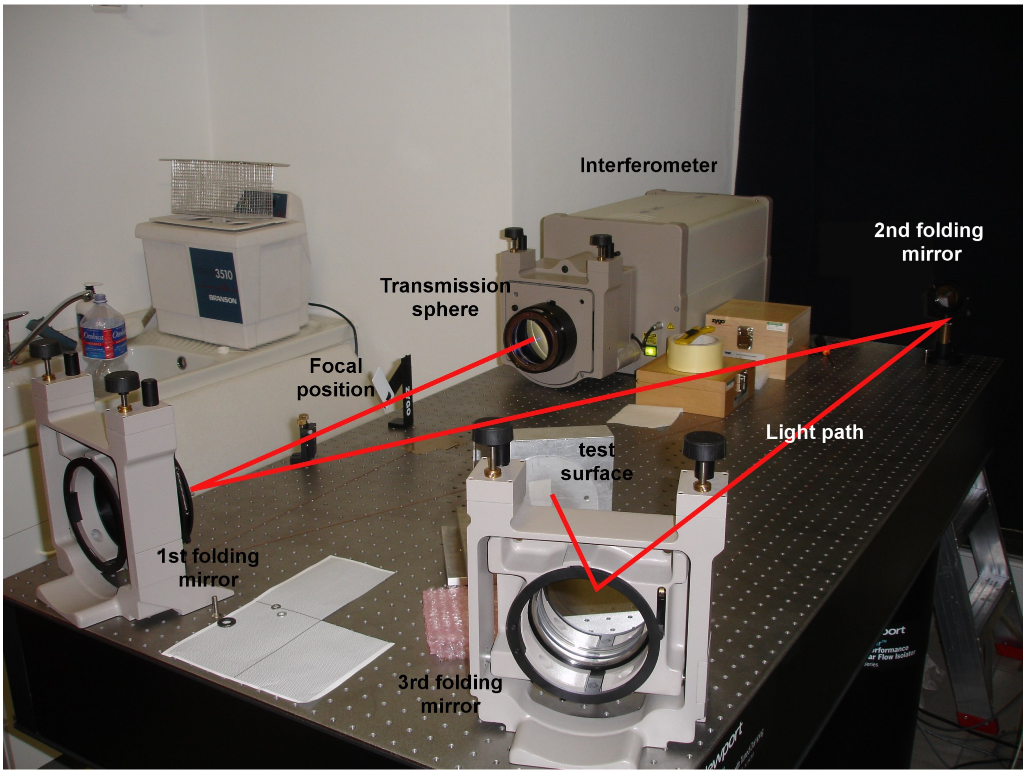

(b) Installed setup.

Figure 5.8: The interferometric setup has been installed on a vibration isolation optical table. The red line highlight the 4 m optical path of the laser beam.

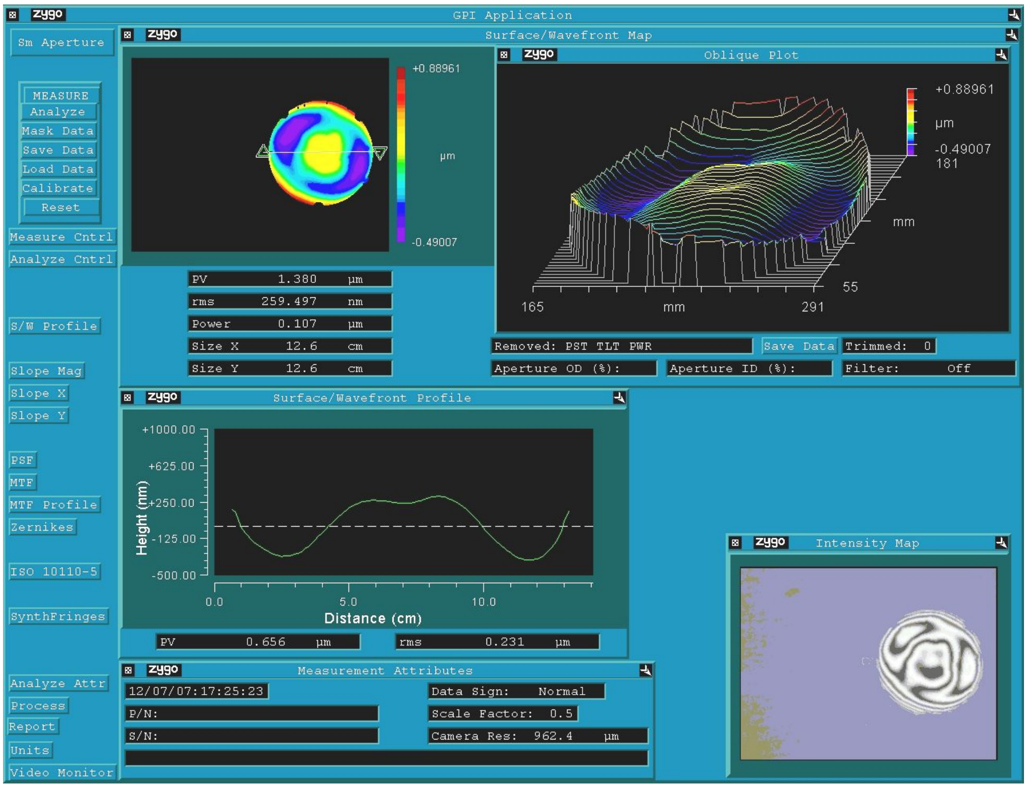

(a) Shell #1.

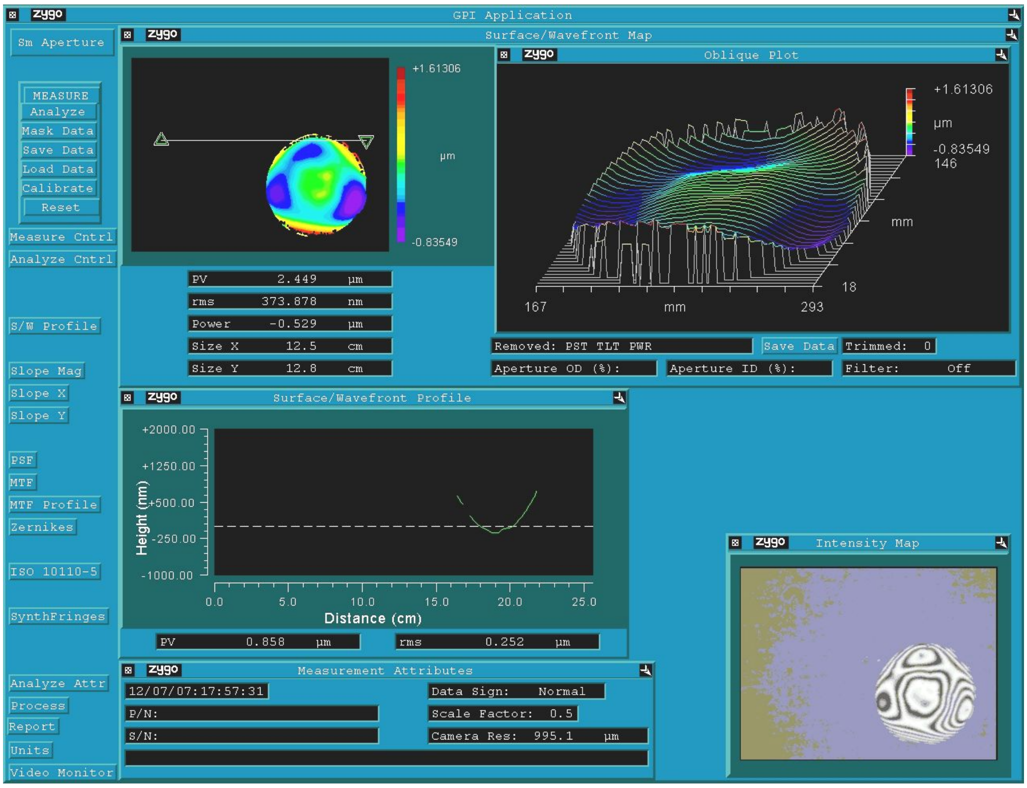

(b) Shell #2.

Figure 5.9: Interferometric measures of the shells #1 and #2 on the dummy mould.

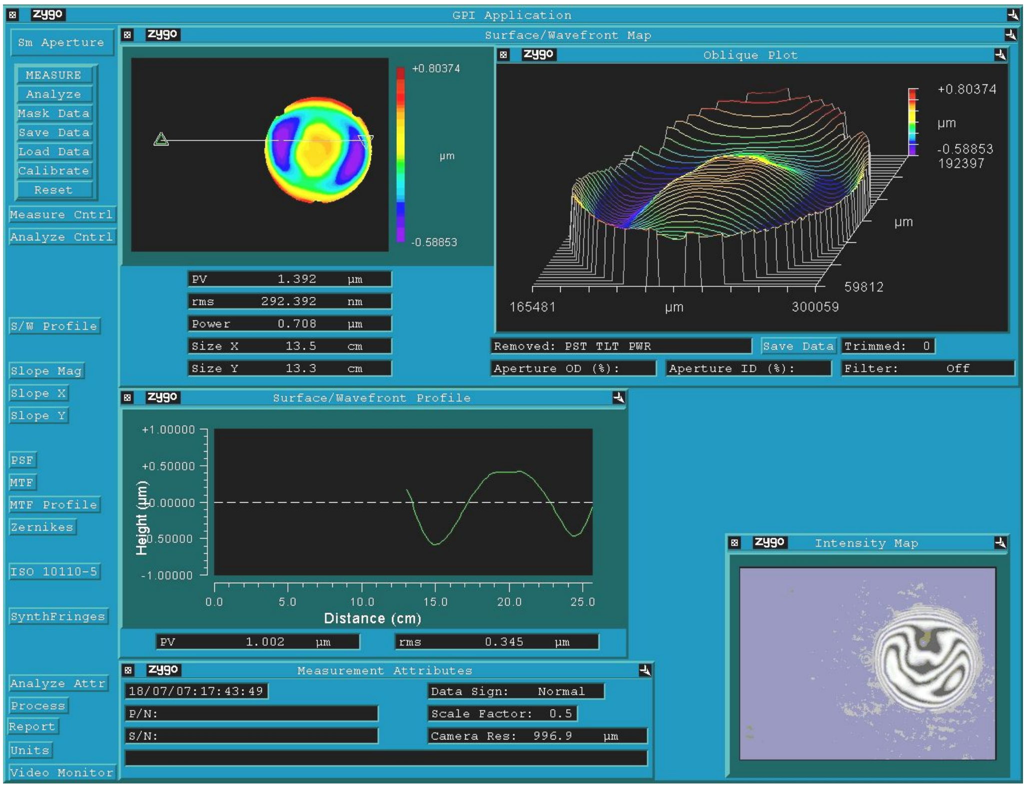

(a) Shell #3.

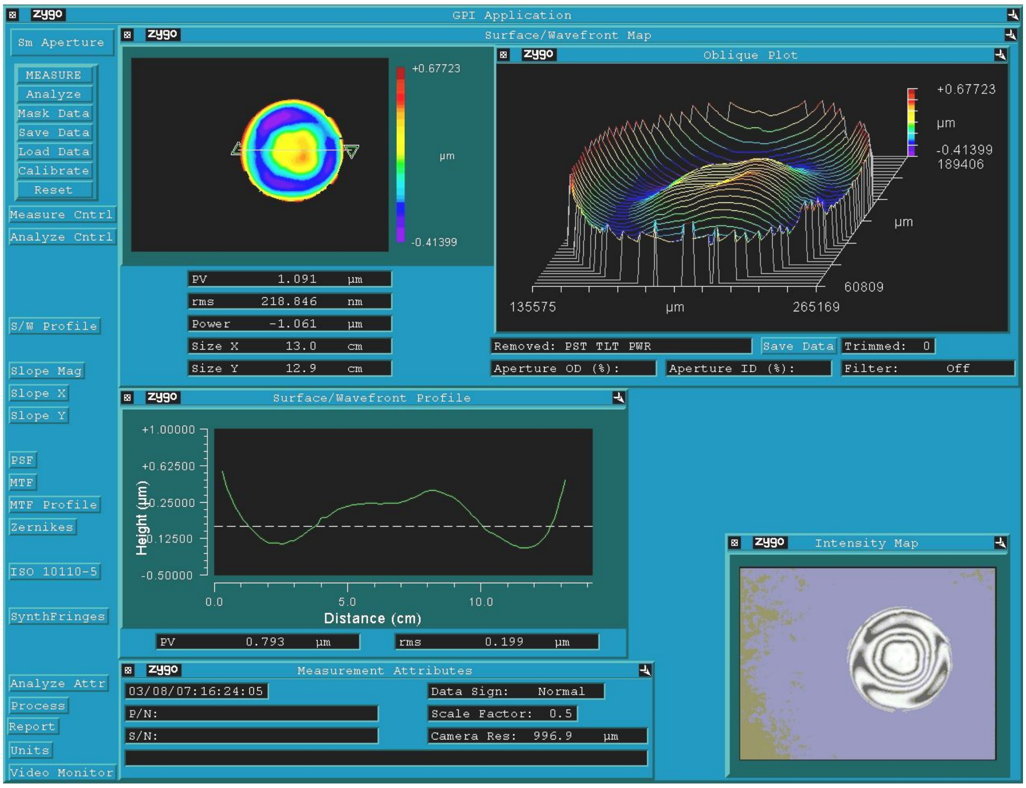

(b) Shell #4.

Figure 5.10: Interferometric measures of the shells #3 and #4 on the dummy mould.

The pictures of Figure 5.9 and 5.10 show the four interferometric measures obtained on the respective shells replicated from the dummy mould. In particular, these surfaces are the residuals after the subtraction of the piston, tilt and best sphere terms.
In all the surfaces is visible a pattern of features each time reproduced with good mutual similarity. This is particularly clear from Figure 5.9(a), Figure 5.10(a) and Figure 5.10(b). It is very likely that these features are characteristic of the mould surface and hence they are simply replicated onto the shell surface. This can be considered an indication that the process has a very good copy capability. From the point of view of the optic shape's accuracy, all the shells have a surface error of about $\lambda/2.5$ rms on full aperture. While, checking sub-apertures the optical quality of the surface increases showing residuals of few tens of nm rms (better then $\lambda/10$ rms).
In addition to the previous consideration on the surface errors, some other informations can be obtained looking to each interferogram. In the fringe pattern of Figure 5.9(a) it is possible to identify spherical (the fringes spacing is almost constant along the radius) and coma (the lobes surrounding the center) aberrations. The same is found analyzing the interferogram related to the shell #3 and even more marked on the shell #4. Since none of these are recognizable in the pictures of Figure 5.7 most probably means that the aberrations are residual errors of the optical figuring of the mould, then simply replicated on the surface of each shell. A different analysis shall be reserved for the shell #2. This shell was used to identify the BOROFLOAT® 33 strain point. Since this glass type is recommended also for high temperature application, we checked the maximum temperature at which the glass does not change its (optical) shape. This temperature was then considered to be the real strain point for our application, namely *safety temperature* up to that the cooling phase should be conducted very carefully.
Hence, the shell undergone a subsequent heating to 450 °C. The resulting interferogram of Figure 5.9(b) shows clearly a trefoil deformation in proximity of the three supporting points.
Finally, in Table 5.2 are reported the residuals describing the surfaces of the 4 shells obtained from sub-apertures of the measures of Figure 5.9 and 5.10. Regarding the shell #2, the values between brackets refer to the shell's shape after the heating.

Spatial wavelength range [mm]	SURFACE RMS			
	Shell #1	**Shell #2**	**Shell #3**	**Shell #4**
0-60	$\lambda/13$	$\lambda/14(11)$	$\lambda/9.7$	$\lambda/12.7$
0-80	$\lambda/9$	$\lambda/10(6)$	$\lambda/6.4$	$\lambda/11$
0-100	$\lambda/4.8$	$\lambda/n.a.(3)$	$\lambda/4$	$\lambda/7.1$
0-120	$\lambda/2.8$	$\lambda/n.a.(1.8)$	$\lambda/2.7$	$\lambda/3.8$
0-130	$\lambda/2.4$	$\lambda/n.a.(1.7)$	$\lambda/2.2$	$\lambda/2.9$

Table 5.2: Surface errors measured on different sub-apertures of the 4 shells f/15.

From all the previous considerations, these slumped shells most likely resemble very closely the surface of the dummy mould. Under this consideration, it is possible to speculate that the mould's figure limits the shape quality of these shells. However, it seems reasonable to argue that the procedure developed has the potential to deliver very high shape accuracy and that, very likely, it has not yet reached its limits in terms of accuracy in the copy.
It has been determined that an additional force pushing the glass against the mould is necessary; without it the timing to have a good contact between the two surfaces could be very long if not unattainable. A natural consequence is the tight requirement on the mould microroughness level that should be of 2-3 nm rms or better.

5.4 Large-size f/5 thin glass shell demonstrator

The result of the experiment is visible in Figure 5.11 and reported in [21]. The slumped shell is placed onto the mould and illuminated to show the shape errors respect to it. The pattern of fringes has a central area of about 300 mm with circular fringes and an outer corona.
In the inner part, it is possible to count almost 10 fringes that translates to about 6 mm of difference in the radius of curvature meaning a good copy of the radius, still better than the actual measuring tool. However, on the outer part of the shell the fringes do not follow a circular path, indeed they show indications of warping of the surface of the glass. Clearly, in this part there is not a good replication of the mould's shape.
A possible explanation could be the quite fast focal ratio of the mould: to bend a flat matching a sphere is a difficult task, the more difficult the more the sphere has a short radius of curvature. In some way similar to the more common opposite problem of the representation of the surface of the Earth on a flat map.
As a consequence of this behavior has been decided to change the radius of curvature of the mould going through slower focal ratio. The results obtained with the new configuration are reported in § 5.5.

5.4.1 The optical figure

Due to an inaccurate handling of the demonstrator during the alignment of the vertical optical bench, a major damage occurred to the glass. No measurement was possible to acquire and hence can not be performed any detailed analysis of the figure's errors.

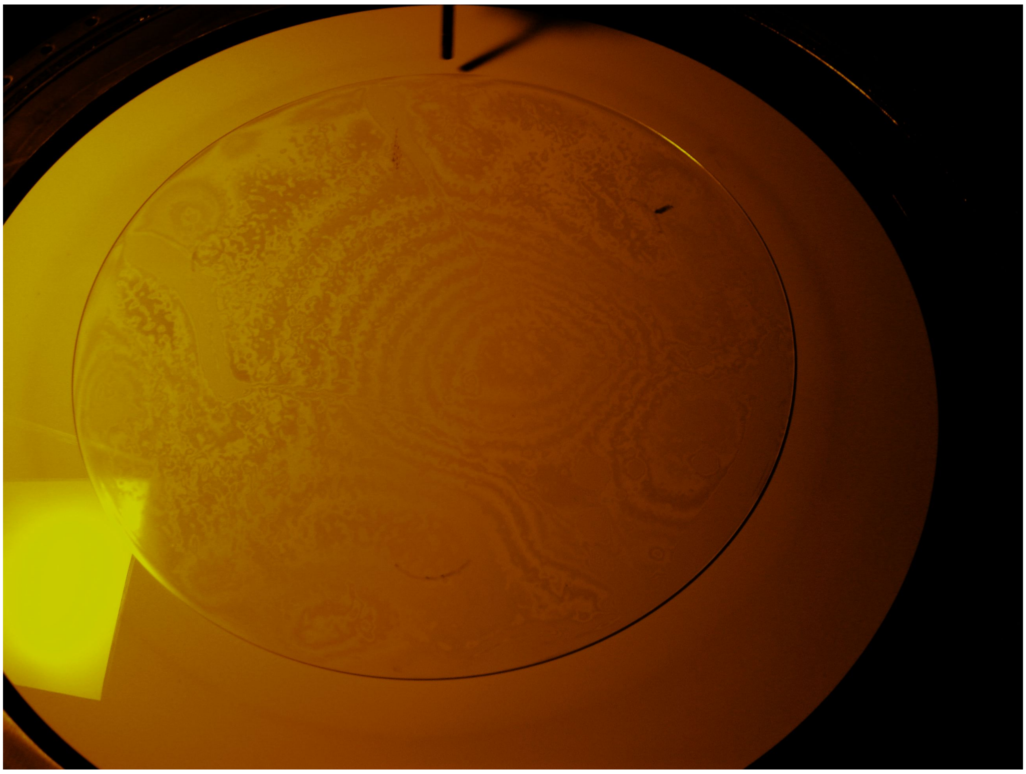

Figure 5.11: Interference fringes between the large f/5 shell demonstrator and the mould. The fringes are generated by the shape difference between the two.

5.5 Large-size f/10 thin glass shell demonstrator

Using the new configuration (see Page 58) a number of f/10 glass shells have been manufactured and characterized [22]. In Figure 5.13 are shown two of them obtained with a substantial change in the thermal cycle adopted.

5.5.1 The radius of curvature

Figure 5.13(a) is a picture of the shell #1 placed onto the mould, it has been taken just after the end of the thermal cycle; meanwhile the picture of Figure 5.13(b) was taken after the thermalization to room temperature. About 40 circular in-

terference fringes are covering the wide central area; the radius of curvature can be easily calculated through Eqn. 4.5. The calculation returns a value of about 9950 ± 50 mm close to that of the mould. This indicates a good copy of the mould for the overall shape. The perimeter of the shell is still presenting some residual stress.
In a similar way of the experiment described in the § 5.3, the radius of curvature has been measured using a laser source with a proper wavefront illuminating the shell. It has been sustained through the astatic support described in § 3.4 and the focus position has been measured. The result is reported in Table 5.3: the shell seems does not have a single "best focus" position, instead, going from the center to the edge, are found annular parts having their own radius of curvature and anyway not warped. In particular, a large inner part is in quite good agreement with the radius of the mould. The profile is sketched in Figure 5.12. This behavior was also noted in the interferometric measures as reported in the next section. A possible explanation could be attributed to the astatic support, in particular to a strong edge effect introduced by the sealing of the ferrofluid.
Also other fringes are visible, they are localized in six different patches on the shell and resemble the typical error introduced by dust particles trapped between the two surfaces.
The experiment has been conducted with a long thermal cycle covering a total time of more than 3 full days: about 38 hours for the heating ramp and about 24 hours for the controlled cooling, plus the free cooling.

Shell #1	
Shell's surface radius [mm]	**Radius of curvature** [mm]
$0 < r < 125$	10000 ± 50
$125 < r < 150$	11500 ± 50
$150 < r < 200$	11000 ± 50
$200 < r < 250$	10500 ± 50

Table 5.3: Measured radii of curvature for the f/10 glass shell #1.

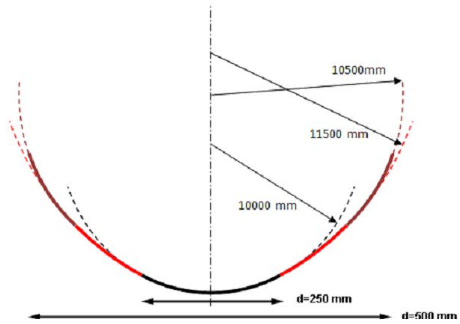

Figure 5.12: Representation of the radii of curvature for the f/10 glass shell #1.

On the contrary, Figure 5.13(c) shows the shell #2 resulting from the use of a faster thermal cycle. This experiment lasted for less than 2.5 days, exploiting both a faster heating of about 21 hours and a faster cooling for 20 hours. This timing has been able to provide a complete and uniform slump of the glass, but the shell has retained stress as visible by the complex pattern of interference fringes. Clearly this attempt to speed up the process has resulted in a not acceptable result and restates how much critical is the cooling phase of the process that has to be executed with the maximum care.

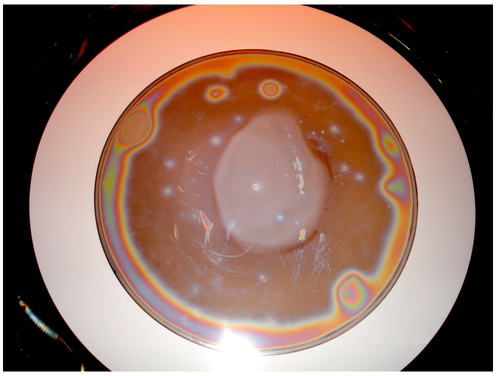

(a) Shell #1, just out from the oven. Result from a long thermal cycle.

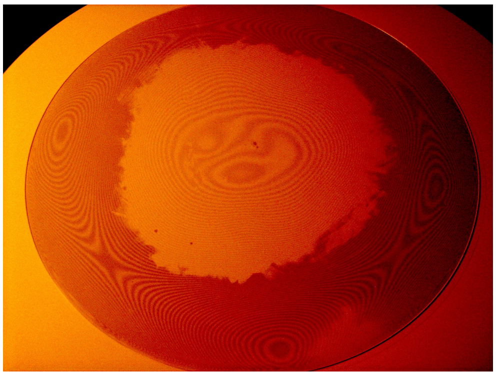

(b) Shell #1, after thermalization with the room. Result from a long thermal cycle.

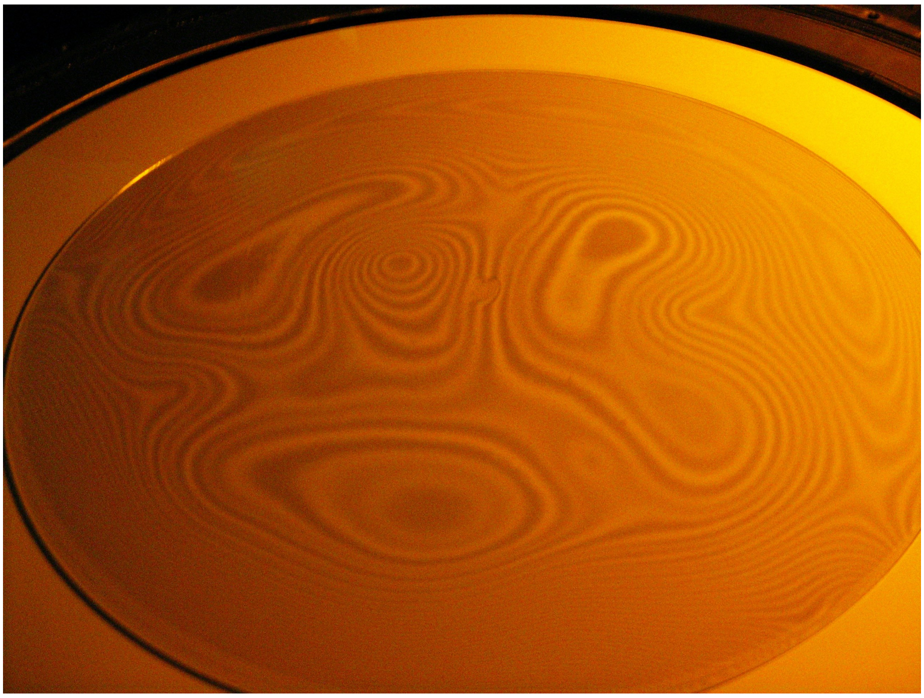

(c) Shell #2. Result from a quicker thermal cycle.

Figure 5.13: Interference fringes between the large f/10 shell demonstrator and the mould. The fringes are generated by the shape difference between the two.

5.5.2 The optical figure

The accurate measure of the surface of this kind of shells is a challenging task. However, interferometric measurements of the shape has been obtained. The optical configuration chosen to test them is the same adopted for the small f/15 glass shells. However, in this experiment we have to deal with more than 10 m of optical path. Nevertheless, the astatic support has to be used so to have the shell positioned horizontally respect to the ground meaning the optical bench should be vertical. Exploiting the solar tower area of the institute has been equipped a vertical optical bench along four floors of the building as shown in Figure 5.14. On the top of the tower the ZYGO interferometer has been placed together with a folding mirror that sends the light beam down to the ground floor where has been positioned the astatic support, the electronic boxes for the movements of the actuators of the fixed points and the readings of the load cells.

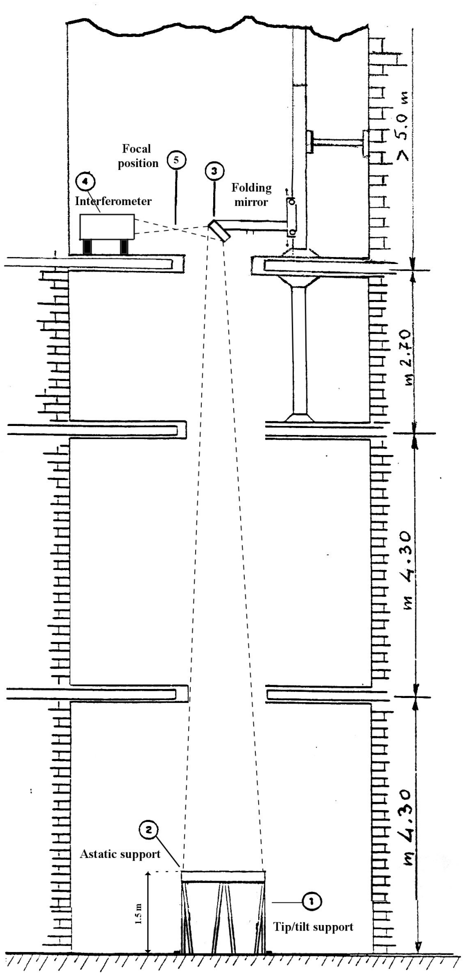

Figure 5.14: Section drawing of the solar tower where has been installed the 10 m vertical optical bench used to measure the f/10 shells.

The interferometric measure of the shell #1 is reported in Figure 5.15(a) where it is visible that only a fraction of the surface was measurable. In particular the inner part on about 220 mm in diameter, the same part with the radius of curvature compatible with the mould. The residual errors after the subtraction of a spherical profile return a surface accuracy of about $\lambda/2.5$ rms. Checking sub-apertures, the residuals decrease down to about $\lambda/30$ rms, the actual values are reported in Table 5.4. From the interferogram is also recognizable the presence of coma aberration.

Spatial wavelength range [mm]	**Surface rms**
0-60	$\lambda/28$
0-80	$\lambda/12$
0-100	$\lambda/6.5$
0-120	$\lambda/5$
0-140	$\lambda/4$
0-160	$\lambda/3.5$
0-180	$\lambda/3$
0-200	$\lambda/2.6$
0-220	$\lambda/2.5$

Table 5.4: Surface errors measured on different sub-apertures of the shell #1.

Concerning the shell #2, the interference fringes generated by the interferometer spherical wavefront are shown in Figure 5.15(b). The dark patches are areas of the shell that deviate from the reference wavefront so much that the light is not reflected back into the interferometer. The other areas have a quite large number of fringes. This situation reflects quite well the large errors from the mould shape already highlighted with the classical Fizeau. It was not possible to obtain a reliable measure of the surface.

The results obtained with this experiment show a net improvement respect the tests done with the small dummy mould for the f/15 shells. The use of a mould with optical figure of higher quality permits to obtain higher quality shells. This can be considered a proof that the process here developed is not limiting the figure of the shells and it is able to deliver very close copies of the mould.

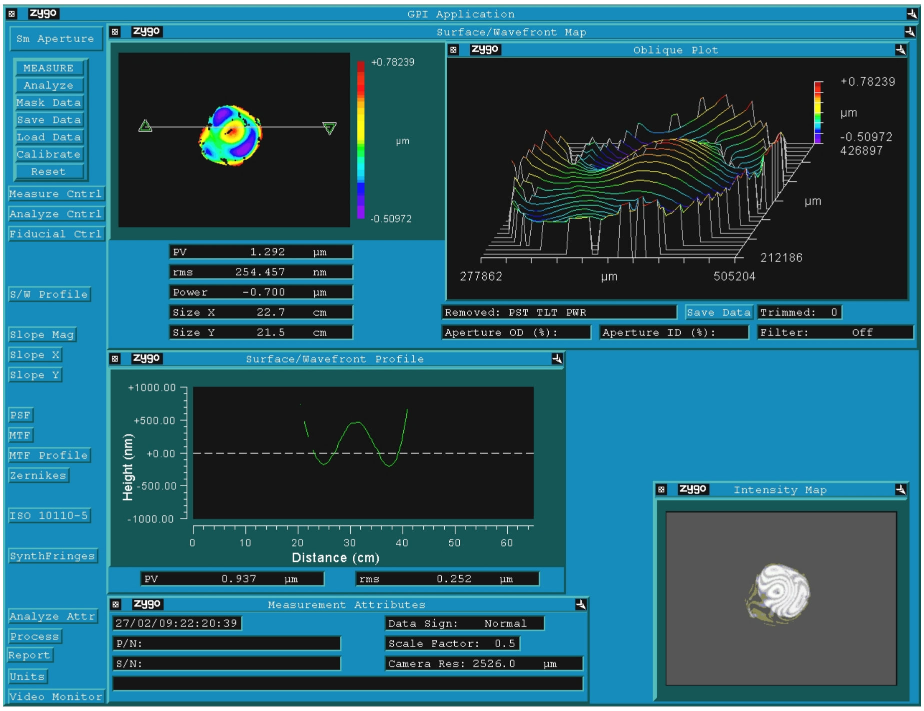

(a) Shell #1.

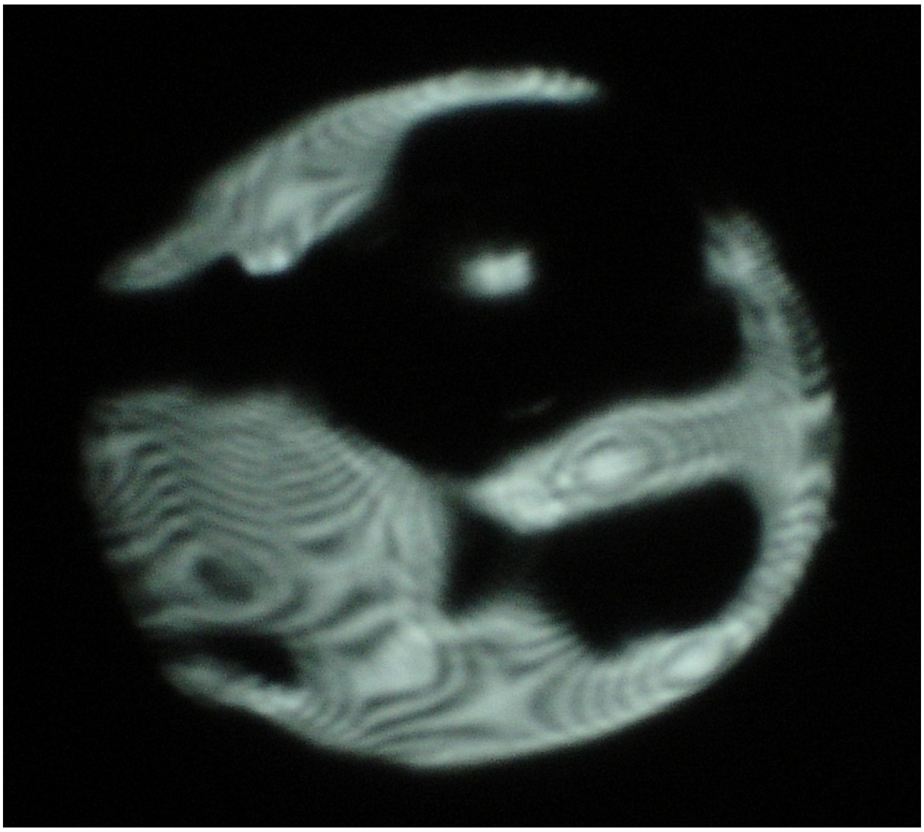

(b) Shell #2.

Figure 5.15: Interferometric measures.

Part II

Composite glass mirror panels for making IACT reflectors

Chapter 6

Facilities for VHE Gamma-ray astrophysics: present days

6.1 Historical overview

High-energy gamma rays are probing the "non-thermal" Universe. They can be produced by all those acceleration processes at work in extreme conditions that can be found in the proximity of black holes or in the very energetic shock waves created in stellar explosions. Otherwise they can be obtained from decays of heavy particles such as the hypothetical dark matter particles or cosmic strings, both relics which might be left over from the Big Bang. The flux and energy spectrum of the observed gamma rays bring important information on the emission processes and the physics producing them. Gamma rays at MeV-GeV energies have been typically observed with space-based instruments but at higher energies those instruments are completely unusable. With the advent of the IACTs in late 1980's, ground-based observation of TeV gamma-rays came into reality and, since the first source detected at TeV energies in 1989 the number of gamma-ray sources has rapidly grown up to over eighty now as shown in Figure 6.1 (see [23] and [24] for an extended review).

The IACT technique for the detection of VHE gamma rays (in the energy range 100 GeV - 10 TeV) was first pioneered by the Whipple experiment since 1985 leading to the discovery of TeV gamma-rays from the Crab Nebula in 1989 [25]. This first result was followed by the discovery of the TeV emission from the first extragalactic source (Mrk 421) [26], showing that acceleration processes are taking part in AGNs too. The third source, discovered in 1996, was still an extragalactic object (Mrk 501) which showed a violent flaring activity observed by the European experiment HEGRA [27] and [28]. The recent discovery

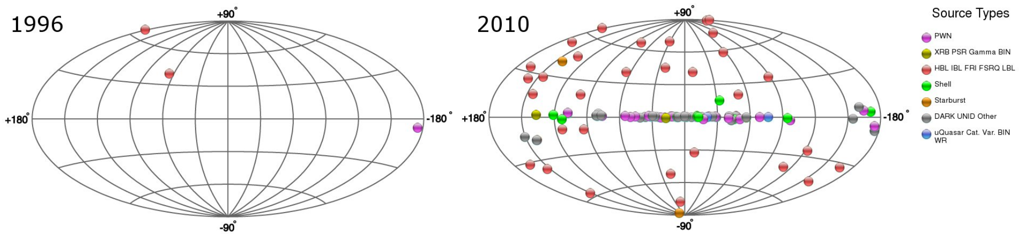

Figure 6.1: The improvement in the VHE astrophysics from 1996 (left panel) to 2010 (right panel). Images created using http://tevcat.uchicago.edu/

of flux variability on the time scale of few minutes from Mrk 501 and PKS 2155-304, obtained in 2007 by MAGIC [29] and by HESS [30] respectively, has shown that the observed γ-rays are coming from the innermost region of the central part of the AGN giving important information on the physical processes at work. The discovery of TeV emission from extragalactic objects was of fundamental importance to constrain the density of the Extragalactic Background Light and the transparency of the Universe to TeV photons [31]. In 2002 HEGRA discovered also the first unidentified TeV γ-ray source [32] showing for the first time that some of the celestial objects discovered at these wavelength emit most of their radiation in the VHE band, or are not detectable in any other waveband.
Since 2003, as the new generation experiments (HESS, MAGIC, CANGAROO and VERITAS) has been started to observe the gamma-ray sky, the number of VHE sources started to rapidly increase. New class of sources was detected at GeV-TeV energies both galactic (e.g. Galactic Center, Pulsar Wind Nebulae, Pulsars and Binary Systems) and extragalactic (e.g. Blazars, radiogalaxies, star-forming galaxies) as well as about a dozen of unknown new TeV sources. The survey of the galactic plane performed by HESS [33] is absolutely remarkable revealing a large population of sources including Pulsar Wind Nebulae and a considerable number of unidentified sources. It showed for the first time that an array of IACTs could be properly used as a real astronomical observatory able to survey a large portion of the sky with a high sensitivity. Among the most outstanding results obtained so far by TeV astronomy there is the recent discovery of pulsed γ-ray emission from Crab Pulsar by MAGIC [34]. This is a very important result providing a unique insight into the structure of pulsar magnetospheres and the main energy transfer processes at work. In March 2007, the HESS project was awarded by the Descartes Research Prize of the European Commission for offering “A new glimpse at the highest-energy Universe”. Thanks to the two experiments HESS and MAGIC, and to their forthcoming follow-ups HESS 2 [35] (commissioning phase) and MAGIC-2 [36] (recently become operational), the European community is now firmly leader in this research field.

6.2 The Cherenkov air showers

In 1934 the Russian physicist Pawel Alexejewitsch Cherenkov discovered the emission of bluish light from relativistic radioactive particles in water for which he received the Nobel Prize in 1958. Cherenkov radiation is an electromagnetic radiation due to the interaction of fast moving charged particles with other particles. If a particle passes through a transparent medium, the atoms along its trajectory become temporarily polarized and emit electromagnetic waves due to polarization. Usually, these waves interfere destructively. However, if the particle moves at a velocity that is faster than the speed of light in this medium, the waves no longer interfere in a destructive manner, as they develop faster than they extinguish each other. These effect is called Cherenkov effect and light is emitted within a Mach cone. One parameter that describes the Mach cone is its angle of aperture ϕ, which depends on the velocity ν of the particle and the speed of light c' of the medium which has the refraction index n. The angle ϕ can be within the range of $0.4° - 1.2°$ for Cherenkov light.
When a γ-ray impinges the top atmosphere, after interaction with the electric field of atmospheric molecules, it pair-produces an electron-positron couple:

$$\gamma(\gamma) \rightarrow e^+e^-$$

The reaction has an energy threshold of $h\nu = 2m_ec^2 \approx 1\ MeV$, and therefore normally takes place for γ-rays in the VHE band. Each electron-positron in turn generates new γ-rays via bremsstrahlung:

$$e^{\pm}(\gamma) \rightarrow e^{\pm}\gamma$$

where the secondary γ-ray takes away in first approximation half of the energy of the electron. Eventually the secondary γ-ray again pair-produces an electron and a positron and so on, and the γ-shower is initiated. A sketch of a schematic view of the shower development is shown in Figure 6.2. The energy of secondary particles produced in the shower decreases as the shower proceeds. When the mean energy of $e^{\pm}$ is below a critical energy E_c, which in air is ≈83 MeV, the dominant energy loss process for electrons becomes ionization, rather than bremsstrahlung. Almost contemporary, when the mean photon energy decreases below few MeV, the cross-section for Compton scattering and photoelectric absorption becomes dominant over pair-production. Rapidly the showers stop.
In addition to γ-showers, the atmosphere is strongly populated also by hadronic-showers. They are initiated by hadrons, mainly protons with small amount of helium and heavier elements. They interact strongly with atmospheric nuclei creating pions, kaons and nucleons. The secondary particles keep on multiplying in successive generations until the mean energy per particle drops below the pion production threshold at around 1 GeV. At that point, ionization becomes

the dominant process and the shower starts to die out. Heavier nuclei are less penetrating than lighter ones, and therefore they create showers with larger development. Moreover, the nuclear interaction lengths for hadrons are larger than the radiation length for γ-rays which implies that hadronic-shower has a larger transversal spread than that of a γ-shower of the same energy.

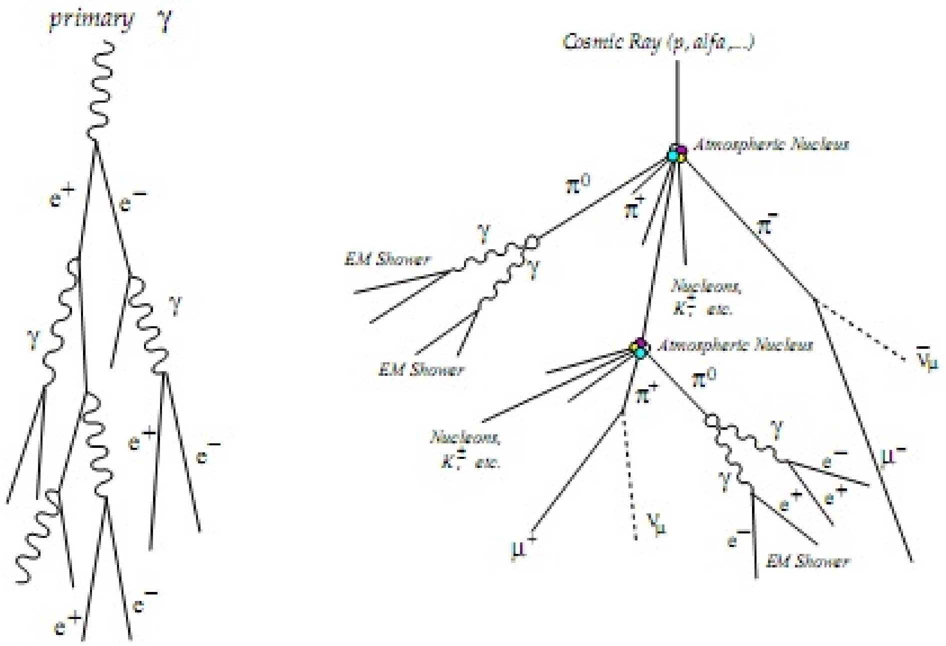

Figure 6.2: Schematic representation of air shower generated by a γ-ray (left) and by an hadron (right).

6.3 The IACT technique

Given the very low fluxes of γ-rays in the VHE regime, a few photons per m^2 per year above 1 TeV for strong sources, direct detection by space-based instruments is excluded. Ground-based instruments detect secondary products resulting from the development of γ-ray initiated air showers: either particles reaching the ground or Cherenkov light emitted by shower particles in the atmosphere. In contrast to the well-collimated electromagnetic air-showers induced by γ-rays (or electrons), air-showers initiated by cosmic ray nucleons typically feature a number of electromagnetic sub-showers induced by π_0 decays and contain muons from charged pion decays. Rejection of the background of showers initiated by charged cosmic rays is a key performance criterion for γ-ray detection systems, and is usually achieved on the basis of shower shape or muon content.
The field of ground-based gamma astronomy has been largely driven (with the

exception of the remarkable results from MILAGRO*) by the exceptional results obtained with the IACTs. As any other optical or radio telescopes, an IACT consists of three basic elements: a mechanical tracking system, which compensate the Earth's rotation, a collecting surface, which gathers the incident electromagnetic radiation and focuses it, and a receiver element, which converts the collected light in a recordable image of the observed field of view.
A peculiar feature of Cherenkov telescopes is that they do not detect directly the photon flux, but instead detect the Cherenkov light produced in the air shower induced by the primary photon. At the maximum of the shower development, around 10 km above sea level for TeV energies, the Cherenkov threshold for electrons is around 40 MeV and the Cherenkov angle is $0.7°$ or less. Light emitted at the Cherenkov angle reaches the ground within a circle of 100 m to 150 m radius depending on the height above sea level of the detection system. Multiple scattering angles of shower particles near the Cherenkov threshold are comparable to the Cherenkov angle, resulting in a more or less uniformly filled light pool, with typically 10 detected Cherenkov photons per TeV shower energy and m^2 mirror area for photomultiplier sensors. An optical telescope pointing to the source and located within the illuminated footprint of the shower can detect the air shower against the background light of the night sky, provided the camera is sufficiently fast to integrate the short Cherenkov flash of the order of few nsec.
With increasing energy, the central density in the light pool is enhanced due to deeper penetration of showers. Triggering and image reconstruction usually requires 50 to 100 detected photons and sets the scale for the dish size. The pixel size of the detection system should be matched to the size of features in air-shower images; simulation studies show saturation of performance for pixels much below $0.1°$ diameter, close to the typical rms width of a γ-ray image at TeV energies. The asymptotic collection area for IACTs is determined by the maximum impact distance for which shower images still fall within a camera and hence by the camera field of view. At 2000 m above sea level the impact distance limitation is approximately 100 m per degree of the opening angle of the camera field of view (for showers close to Zenith).

The Cherenkov technique takes advantage of the shower development information in the image of the telescope camera (see Figure 6.3). It is therefore possible to take a sort of "snapshot" of air showers resolved in space (and time). This information can then be used to distinguish the origin of the air shower (hadronic or γ-ray) using the different spatial development of γ- and hadron-induced air

*MILAGRO is an extensive air shower water Cherenkov detector located near Los Alamos, New Mexico (2650 m above see level), it consists of a central pond detector with an area of 60×80 m^2 at the surface and has sloping sides that lead to a 30×50 m^2 bottom at a depth of 8 m. It is filled with 5 million gallons of purified water and is covered by a light-tight high-density polypropylene line. Milagro consists of two layers of upward pointing 8 inch PMTs. The central pond detector is surrounded with an array of water tanks, and it has been operational since 2000. The array of water tanks was completed in 2004.

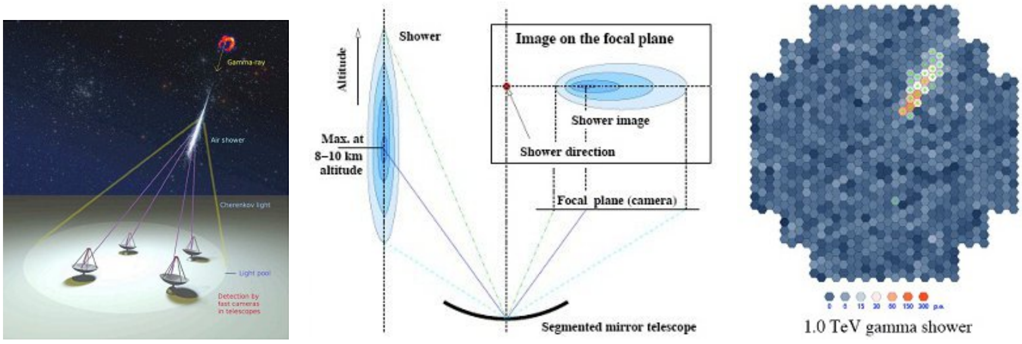

(a) Schematic of the Cherenkov light pool illuminating an array of telescopes.

(b) In the camera, the shower has an elliptical shape and the direction lays on the extension of its major axis; the image intensity is related to the primary energy.

(c) Image of a γ-induced air shower as it appears in the camera.

Figure 6.3: Schematic description of the IACT technique.

showers. The parameterization of such images is called "Imaging Technique", which dramatically improves the γ/hadron separation power and makes IACTs the most successful instrument for cosmic very high energy γ-ray observations (see Figure 6.4). Moreover, the measurement of the Cherenkov light provides a good indicator of the energy absorbed in the atmosphere, which is in fact acting as a calorimeter. Therefore, the total amount of light contained in the image gives the energy of the primary particle. In addition, orientation and shape of the image also provide information on the incoming direction of the primary particle. Two main parameters characterize an IACT: its sensitivity, i.e. the minimum detectable γ-ray flux in a given number of observation hours (usually defined as a 5σ excess during 50 hours of observation time), and its energy threshold.
Most modern instruments use multiple telescopes (a) to image the air-shower from different viewing angles for improved reconstruction of γ-ray direction and rejection of cosmic ray background and (b) to apply a coincidence requirement rejecting single-telescope triggers caused by cosmic ray muons with impact points close to a telescope mirror, or by night-sky background. Telescope spacing needs to be large enough to provide a sufficient baseline for stereoscopic measurements, but small enough that multiple telescopes fit within the Cherenkov light pool; the exact spacing tends to be uncritical within a range of $\sim$70 m to 150 m. The stereoscopic technique has become the nominal standard for all current and future installations.

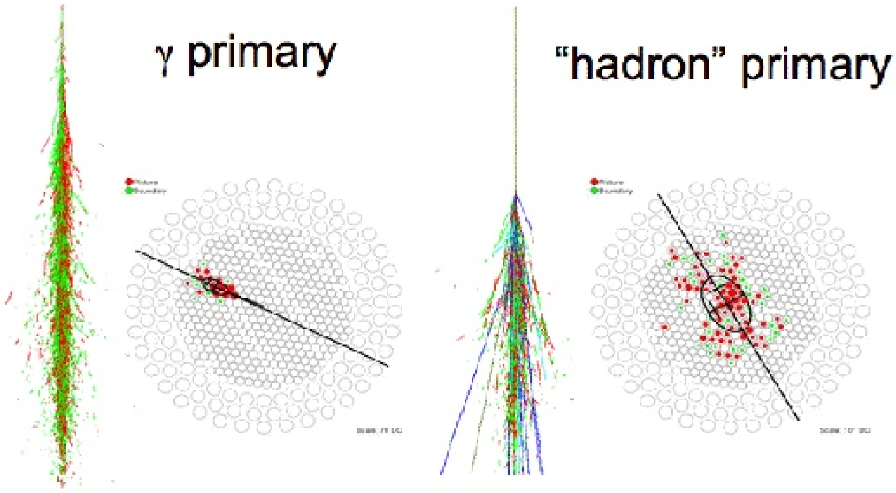

Figure 6.4: Typical spatial development of γ- and hadron-induced air showers.

6.4 Current status

The current generation of IACT instruments MAGIC and VERITAS (in the northern hemisphere) and HESS and CANGAROO (in the southern hemisphere) are now allowing imaging, photometry and spectroscopy of sources of high energy radiation with good sensitivity and good angular resolution. Table 6.1 summarizes the principal characteristics of these experiments. They are typically working in an energy range spanning between 50-100 GeV to about 100 TeV. The performance of these telescopes is typically characterized by the sensitivity to detect VHE sources with an energy flux down to 10^{-13} $erg \cdot cm^{-2} \cdot s^{-1}$ in 50 hours of observation time. This corresponds to a minimum detectable luminosity of $L_{min} \sim 10^{31}$ $erg \cdot s^{-1}$ for a galactic source at a distance of 1 kpc or $L_{min} \sim 10^{41}$ $erg \cdot s^{-1}$ for an extragalactic source at a distance of 100 Mpc. The angular resolution of each reconstructed primary γ-ray is typically better than few arcmin. The relative energy resolution is comparably good and reaches values of $\Delta E/E \sim 10 - 20\%$.

The extensions of MAGIC and HESS into phase II will lower the energy threshold and improve existing sensitivity. With MAGIC-II, stereoscopic observations will allow an increase in the sensitivity by at least a factor of 3 as well as further improvements in the energy and direction reconstruction. MAGIC will reach a sensitivity of 10 mCrab in 50 hours of data taking. The MAGIC experiment has confirmed that a single large telescope can reach a low energy threshold with a good sensitivity. HESS 2 is following the MAGIC strategy. A large telescope of about 500 tons with a mirror area of about 600 m^2 and a camera with a field of view of 3.5° and pixel size of 0.07° is scheduled to be installed in the center of the current HESS 1 array by 2010. The HESS 2 experiment will lower the energy threshold to about 20 GeV.

	HESS	**MAGIC**	**VERITAS**	**CANGAROO**
Location	Namibia	Canary Islands	Arizona	Australia
Latitude	-23°	+29°	+32°	-31°
Telescope number and collecting area	4x 108 m^2	2x 234 m^2	4x 110 m^2	4x 50 m^2
Operational since	2004	2004	2004	2007
Field of view	5°	3.5°	3.5°	4°
Threshold energy	100 GeV	<50 GeV	100 GeV	400 GeV
Sensitivity (5σ in 50 hrs)	0.7% Crab	1.6% Crab	1% Crab	15% Crab
Upgrades in progress	1×600 m^2	–	–	–

Table 6.1: Main characteristics of the current Cherenkov telescopes experiments.

6.5 MAGIC

MAGIC is a system of two IACTs. MAGIC-I started routine operation after commissioning in 2004. Construction of MAGIC-II has been completed in early 2009 and is operational since later same year. The project is funded primarily by the funding agencies BMFB (Germany), MPG (Germany), INFN (Italy), MICINN(Spain), and the ETH Zurich (Switzerland). The site is Roque de los Muchachos situated on the Canary island of La Palma, a volcanic island off the African coast at 28°N and 17°W. The site has excellent conditions for optical observations. It is also under consideration for E-ELT. MAGIC is at an altitude around 2200 m above sea level, surrounded by multiple high quality optical telescopes, as seen in the Figure 6.5. It shows the MAGIC telescopes in 2009, with the MAGIC control building with a red roof; above MAGIC, two optical telescopes: the Telescopio Nazionale Galileo (left), and the Gran Telescopio Canarias, with its 10.4 m segmented mirror the largest worldwide.

6.5.1 Mount and dish

MAGIC [37] [38] is characterized by the largest collection surface of any existing gamma-ray telescope worldwide: about 236 m^2 reflective surface each one. It employs an alt-azimuth mount running on six bogeys on a circular rail. Undercarriage and bogeys are constructed in steel; meanwhile, the space frame of 17 m diameter, carrying the segmented mirror, is made from CFRP tubes. The total moving weight in azimuth is 64 tons, while in altitude 20 tons. The azimuthal

Figure 6.5: The MAGIC telescopes on top of the Taburiente volcano at La Palma, Canary Islands, Spain. In background, Telescopio Nazionale Galileo and Gran Telescopio Canarias.

movement is performed by two driving motors, the altitude by just one; each motor has a maximal power of 11 kW. The angular positions are measured by 14-bit shaft encoders, and cross-checked by a starguider camera. A crucial design parameter is the re-orientation of telescope: a very fast repositioning has been chosen to catch short-lived phenomena, i.e. GRBs. Minimizing the instrument weight and automating the axis control, it is achieved a 40 seconds (average, with a maximum of 100 seconds) repositioning time to any point in the sky.

6.5.2 Mirror

MAGIC-I and MAGIC-II use a different mirror assembly. Both have a segmentation of the reflector in many facets mounted on the parabolic 17 m dish. In total, each of the MAGIC telescopes has 236 m^2 of mirror surface, each mirror panels is mounted on three points, two of which are computer-controlled actuators. Automatic adjustment of the mirror panel orientation by an Active Mirror Control system ensures optimum focusing for each telescope orientation. MAGIC-I reflector ($f/d = 1.03$) is an assembly of nearly 1000 individual mirror elements 49.5×49.5 cm^2. Four mirror elements (three at the four inclined edges and near the alt-axis) mounted on 1 m^2 panel and pre-adjusted. Each mirror is made by a lightweight aluminum panel, the reflecting surface being diamond grinding and diamond milled. Maximum deviation of individual mirror element from ideal shape is less than 10 μm, with a roughness level of about 4 nm rms. The average reflectivity, focused on a spot of 2 cm radius, is above 80% in the wavelength range 290-650 nm. The whole reflector is also equipped with 13 kW mirror heating system to prevent dew deposition and icing of the mirror surface [39].

MAGIC-II reflector is composed only by solid 1 m^2 mirror panels, but from two very different technologies. About half of the facets came from a development of the diamond milling technique already used in MAGIC-I [40]. The remaining 104 facets are manufactured by a composite sandwich structure were the reflecting surface is a thin glass sheet. These facets were provided by INAF, for further details see § 9.1, § 9.2 and [41] and [42].

6.5.3 Camera

The camera is held in position by single aluminum tubular arc, secured against transverse movements by a web of pre-stressed steel cables. The camera body is of hexagonal shape of 1.05 m diameter, corresponding to a field of view of 3.6°, with a total weight of about 600 kg.
The camera has an inner area of 396 PMTs of 1 inch diameter each, surrounded by 180 PMTs of 1.5 inch diameter, arranged in four concentric rings. All tubes have an hemispherical shape and hexagonal Winston cones (made from thin aluminized Mylar foil of mean reflectivity of 85%) in front of all PMTs. The resulting effective quantum efficiency is of 25% to 30%, the threshold for gamma detection is around 60-70 GeV. Analogue signals are transmitted from the camera to the control house via optical fibers (about 160 m distance). The camera has been kept as light as possible, in fact only the amplifiers and laser diode modulators for transmission are inside the camera housing.

6.6 HESS

HESS [43] is a stereoscopic system of IACT, where multiple telescopes view the same air shower. It investigates cosmic gamma rays in the 100 GeV to 100 TeV energy range. HESS is located in Namibia, near the Gamsberg mountain, an area well known for its excellent optical quality. The first of the four telescopes of phase I of the HESS project went into operation in Summer 2002; all four were operational in December 2003, and were officially inaugurated on September 28, 2004. In Phase II of the project, a single huge dish with about 600 m^2 mirror area will be added at the center of the array, increasing the energy coverage, sensitivity and angular resolution of the instrument. The name HESS stands for High Energy Stereoscopic System, and is also intended to pay homage to Victor Hess, who received the Nobel Prize in Physics in 1936 for his discovery of cosmic radiation.
The four HESS telescopes are arranged in form of a square with 120 m side length, to provide multiple stereoscopic views of air showers. The telescope spacing represents a compromise between the large base length required for good stereoscopic viewing of the showers, and the requirement that two or more telescopes are hit by light generated by a shower; a larger spacing would make increasingly un-

likely that multiple telescopes are illuminated simultaneously. The diagonal of the square is oriented North-South. The instrument allows scientists to explore gamma-ray sources with intensities at a level of a few thousandths of the flux of the Crab Nebula (the brightest steady source of gamma rays in the sky).

Figure 6.6: The HESS telescopes array, Namibia desert.

6.6.1 Mount and dish

In the design of the HESS telescopes, emphasis was placed on the mechanical stability and rigidity of the mount and dish. The telescopes use an alt-azimuth mount, to point the telescope at any point in the sky. A "base frame" rotates around a vertical axis and carries the dish, which rotates around the elevation axis. Both the base frame and the dish are realized as steel space frames. Both axes are driven under computer control to track a celestial object across the sky. The maximum speed of the drive systems is about $100°/min$, in order to allow rapid slewing from one object to another. The pointing is controlled by angular position encoders connected to both axes, which provide a resolution of a few arc-seconds. Telescope pointing is in addition monitored by an optical guide telescope equipped with a CCD camera, which serves to correct deviations from perfect pointing. The complete one telescope system weights about 60 tons including camera, drive systems, mirrors.

6.6.2 Mirror

The mirror is segmented into 382 round mirror facets of 60 cm diameter, made of aluminized glass with a quartz coating. The mirror has a focal length of 15 m and a f/d ratio of 1.2; the mirror facets are arranged in a Davies-Cotton design (see § 7.4), which provides good imaging also for off-axis rays. The total mirror area is 108 m^2 per telescope. Mirror reflectivity is >80% in the wavelength band 300 nm to 600 nm. Each mirror tile is individually tested for reflectivity and image quality before it is mounted. The orientation of each facet is adjustable by two remote-controlled motors. The alignment procedure is fully automatic; the initial alignment requires a few nights†. The specified PSF including alignment errors is 0.5 mrad D80 for rays on axis, 1 mrad for 2° off-axis rays. The measured PSF exceeds; however, over most of the field of view the spot is well contained within a single pixel.

6.6.3 Camera

The cameras of the HESS telescopes serve to capture and record the Cherenkov images of air showers. Design criteria included a small pixel size to resolve image details, a large field of view to allow observations of extended sources and surveys, and a triggering scheme which allows to identify the brief and compact Cherenkov images and to reject backgrounds, such as the light of the night sky. The complete electronics for image digitization, readout and triggering is integrated into the camera body. The camera dimensions are about 1.6 m diameter, 1.5 m length and weights about 800 kg. It covers a 5° field of view with a total of 960 photon detector elements, each subtending 0.16° angle, using 29 mm, 8-stage PMTs with borosilicate windows, equipped with Winston cones to improve light collection. Air cooling is used to remove close to 5 kW of heat dissipated in the circuitry of the camera. Air flow is provided by about 80 computer-controlled fans.

6.6.4 Central trigger system

HESS employs the stereoscopic reconstruction of air showers to determine their direction in space, the type and the energy of the primary particle. Therefore, only air showers which generate images in at least two telescopes are recorded.
The camera is triggered by a coincidence of signals detected in 3 to 5 pixels in (overlapping) 8×8 pixel sectors; typical signals required in a pixel (pixel trigger thresholds) are around 5 photoelectrons. The fast coincidence circuitry provides an effective coincidence window of about 1.5 ns, and allows for the efficient rejection of uncorrelated PMT signals caused by photons of the night sky background light.
Once a camera triggers on a shower image, it alerts a central trigger station. The central trigger system receives trigger signals from the individual telescopes and searches for coincidences between telescopes, properly accounting for the delays of the signals from the different telescopes, and their dependence on telescope pointing. If two or more telescope trigger simultaneously, this provides stereo images of an air shower and a trigger confirmation is sent back to the telescope

†To align the mirror facets, the image of a star in the focal plane is viewed by a CCD camera in the center of the dish. Before alignment of the facet, each one generates a light spot. One mirror at a time, the individual mirrors are then moved until all spots converge in the center. The effect of the alignment is visualized by comparing the image of a star before and after alignment. Alignment of mirrors is checked regularly; when required, a re-alignment can proceed in a few hours.

resulting in the read-out of telescope data. For non-coincident triggers, the telescope readout electronics is cleared after a few microseconds and is ready for the next event.

6.7 VERITAS

VERITAS [44] [45] is a new major ground-based gamma-ray observatory located at the Fred Lawrence Whipple Observatory near Amado, Arizona, U.S.A.. It consists of an array of four 12 m optical reflectors deployed such that they permit the maximum versatility and give the highest sensitivity in the 50 GeV - 50 TeV band (with maximum sensitivity from 100 GeV to 10 TeV). The array layout gives telescope baselines varying from 35 m to 108 m. The telescope design is based on the design of the existing 10 m gamma-ray telescope of the Whipple Observatory. The first telescope was operated initially in 2004 as a prototype, with one third of the mirror area and half of the PMTs of the completed telescope and the full array completed in spring 2007.

Figure 6.7: The VERITAS telescopes array, Arizona, United States of America.

6.7.1 Mechanics and tracking

The basic mechanical structure of the telescope consists of an altitude-over-azimuth positioner and a tubular steel Optical Support Structure (OSS). The camera is supported on a quadrupod, and a mechanical by pass of the upper quadrupod arm transfers this load directly to the counterweight support. The positioner is a commercial unit; the OSS is a steel space frame, custom designed and fabricated by Amber Steel (Chandler, Arizona). The maximum slew speed is measured to be $1°/s$. The telescope encoder measurements are written to a database at a rate of 4 Hz and indicate that the tracking is stable with a relative raw mechanical pointing accuracy of typically $< \pm 0.01°$.

6.7.2 Mirror

The telescope optics follows a Davies-Cotton design, but with a 12 m aperture reflector and a 12 m focal length. There reflector comprises 350 hexagonal mirror facets, each with an area of 0.322 m^2, giving a total mirror area of $\sim$110 m^2. The use of hexagonal facets allows the full area of the OSS to be exploited. The facets are made from glass, slumped and polished by DOTI (Roundrock, Texas), then cleaned, aluminized and anodized at the VERITAS optical coating laboratory. The reflectivity of the anodized coating at normal incidence is typically >90% at 320 nm. Each facet has a 24.0 m $\pm$ 1% radius of curvature and is mounted on the spherical front surface of the OSS (radius 12 m) using a triangular frame. Three adjustment screws allow each facet to be accurately aligned. The reflector facets are aligned manually using a laser system installed at a point facing the centre of the reflector at a distance of twice the focal length. After the alignment of the mirror facets the resulted PSF is reported to be $\sim 0.06°$ FWHM when pointing at 31° elevation, degrading at higher elevations due to flexure of the OSS. The technique of bias alignment, where the mirror facets are aligned such that the PSF is optimum over the most useful observing range, has been successfully employed on the Whipple 10 m telescope in the past and will be applied to the VERITAS telescopes to achieve a PSF $< 0.06°$ FWHM over the $40° - 80°$ elevation range.

6.7.3 Camera

The camera box is 1.8 m^2 and allows for future expansion to increase the camera field of view. The imaging camera's 499 pixels are Photonis 2.86 cm diameter, UV sensitive PMTs, with a quantum efficiency >20% at 300 nm. The angular pixel spacing is 0.15°, giving a total field of view of diameter about 3.5°. Light cones have not yet been installed; two different designs are being fabricated and will be tested. They are expected to significantly improve the total photon collection efficiency as well as to reduce the rate of off-axis background photons in each PMT. The PMT high voltage is provided by a multichannel modular commercial power supply which allows each PMT to be controlled individually. The high voltage is chosen to give a PMT gain of about $2 \cdot 10^5$. The signals are amplified by a high-bandwidth pre-amplifier integrated into the PMT base mounts. This circuit also allows the PMT anode currents to be monitored and calibrated charge pulses to be injected into the signal chain. Average currents are typically 3 μA (for dark fields) to 6 μA (for bright fields), corresponding to a night sky photoelectron background of 100-200 MHz per PMT at this site. Signals are sent via about 50 m of 75 Ω stranded cable to the telescope trigger and data acquisition electronics which is housed in the control room.

6.7.4 Trigger

In an IACT, precise timing between trigger channels is desirable in order to reduce the coincidence resolving time and hence lower the detector energy threshold. To achieve this, each channel is equipped with a custom designed constant fraction discriminator (CFD) which has a trigger time which is independent of the input pulse height. The CFD output width is programmable in 12 steps between 4 ns and 25 ns; a width of 10 ns was used as standard for telescope operations. A 3-bit, 6 ns programmable delay is provided for each channel so as to correct for systematic differences in the relative signal paths due to cable length differences and the voltage dependent PMT transit times. The CFD signals are copied and sent to a topological trigger system which is similar to that used successfully on the Whipple 10 m telescope, but with an improved channel-to-channel timing jitter of <1 ns. The system contains a memory look-up which can be pre-programmed in a few minutes to recognize patterns of triggered pixels in the camera; for example, any 3 adjacent pixels. The required overlap time between adjacent CFD signals is about 6 ns. The topological trigger system reduces the rate of triggers due to random fluctuations of the night sky background light and preferentially selects compact Cherenkov light images. Observations in 2005 were all made with a rather conservative CFD threshold corresponding to about 6-7 photoelectrons and a 3-fold adjacent pixel topological trigger configuration, giving a cosmic ray trigger rate at high elevation of about 150 Hz. VERITAS also include an array level trigger system which triggers the data acquisition on coincident events over a pre-defined number of telescopes.

6.8 CANGAROO

CANGAROO is an international collaboration for the gamma-ray astrophysics, aiming to study the existence and properties of very high energy gamma rays from celestial objects by utilizing the IACT technique with large aperture telescopes located near Woomera, South Australia (136.786°E, 31.099°S, 160 m above see level). The collaboration has observed various targets, such as pulsars, nebulae, SNR's, and AGN's in the southern sky since 1992. Among the increasing numbers of Cherenkov telescopes, CANGAROO-I telescope of 3.8 m reflector has been one of the pioneers in the VHE gamma-ray astronomy with its good quality mirror and high resolution camera of 256 small PMTs. A new telescope of larger mirror, called CANGAROO-II, has been constructed in Woomera, and started operation in March 1999. This 7 m diameter telescope has been expanded to 10 m diameter in March 2000 to increase its light collection. This upgrade will extend the CANGAROO observations down to multi-hundred GeV energy region. Even more sensitive observations are possible with the new array of four 10 m telescopes, called CANGAROO-III. The upgrade of the 7 m telescope to 10 m in March 2000 was the first step of this project. The second, third and fourth telescopes were completed in 2002, 2002 and 2003, respectively. The full operation has started in March 2004 and observations of gamma-ray candidate objects are going on.

Figure 6.8: The CANGAROO telescopes array, Australia.

6.8.1 Mirror

The CANGAROO-III 10 m reflector has a focal length of 8 m with a parabolic design in order to keep the synchronicity of arrival times of Cherenkov photons with in a few ns. The surface is tessellated with 114 spherical mirror facets of 80 cm diameter, with an effective light collecting area of 57 m^2. For the base material of the mirror, CFRP is used, which is the first case for an IACT. It weighs about one-third of a glass mirror, resulting in reduced gravitational deformation. The orientation of each mirror is remotely adjusted by stepping motors. The image of a star measured with a CCD camera was found to be spread over 0.20° FWHM. For the second telescope, the reflector design is almost the same as the first 10 m telescope. Glass FRP is adopted instead of the CFRP, which raises the rigidity of the mirror. The spot size of the reflector was measured to be 0.21° FWHM. Further fine tuning should decrease the size to 0.18° FWHM.

6.8.2 Camera

The camera consists of 552 PMTs of 0.5 inch diameter with light collecting cones to reduce the dead space between the photosensitive area of the PMTs. It covers a field of view of about 3°. Signals from the PMTs are fed into analog buffer amplifiers. The discriminated signals are measured with a timing resolution of 1 ns, which enables us to reject almost all the photons due to the night sky background. These event data are collected and stored in a disk with house-keeping data. From simulations, the energy threshold for gamma-rays with zenith angle about $10°$ is estimated to be about 500 GeV, while that of cosmic rays is estimated to be 800 GeV.

The second telescope was constructed with many improvements. The new imaging camera has a hexagonal design to minimize the dead space between PMTs. The total field of view of about $4°$ is covered by 427 PMTs of 3/4 inch diameter. The light guides have been redesigned to maximize photon collection for the new hexagonal arrangement. High voltages are supplied to PMTs individually. Each PMT base includes a preamplifier, and signals are transmitted via twisted cables to the electronics installed on the veranda of the telescope. The cosmic ray energy threshold was estimated to be lowered at about 320 GeV.

Chapter 7

Facilities for VHE Gamma-ray astrophysics: future

The present generation of imaging atmospheric Cherenkov telescopes has recently opened the realm of ground-based gamma ray astronomy in the energy range above a few tens of GeV. The facilities under study nowadays will thoroughly explore the universe in VHE gamma-rays and deeply investigate cosmic non-thermal processes, in close cooperation with observatories in other wavelength ranges of electromagnetic radiation, and those using other messenger types.
The proposed facilities of the next generation will consist of extended arrays of Cherenkov telescopes, aiming to (a) increase sensitivity by another order of magnitude for deep observations, (b) boost significantly the detection area and hence the detection rates, particularly important for transient phenomena and at the highest energies, (c) increase the angular resolution and hence the ability to resolve the morphology of extended sources, (d) provide wide and uniform energy coverage from some 10 GeV to beyond 100 TeV in the energy of the photons, and (e) enhance the all sky survey capability, the monitoring capability and the flexibility of operation.

7.1 The European project CTA

CTA will consist of arrays of IACTs detecting the faint light flashes that are generated by gamma-ray induced particle cascades in the upper atmosphere. Three different types of telescopes are proposed, optimized for the detection of gamma rays over almost four orders of magnitude in energy:

- from a few 10 GeV to 100 GeV over a detection area corresponding to a fraction of a square kilometer;

- from 100 GeV to 10 TeV range over about a square kilometer;
- from 10 TeV to 100 TeV range over up to 10 square kilometers.

In each case the increasing detection area compensates the decrease in the flux of very high energy gamma rays with increasing energy. The design features of CTA allow it to deliver far superior performance compared to previous instruments, achieved through the larger amount of light collected from each gamma-induced cascade, the increased number of views provided for each cascade, through its significantly larger field of view, and through its larger overall detection area. Optimized design of the telescopes will make the array affordable and reliable.

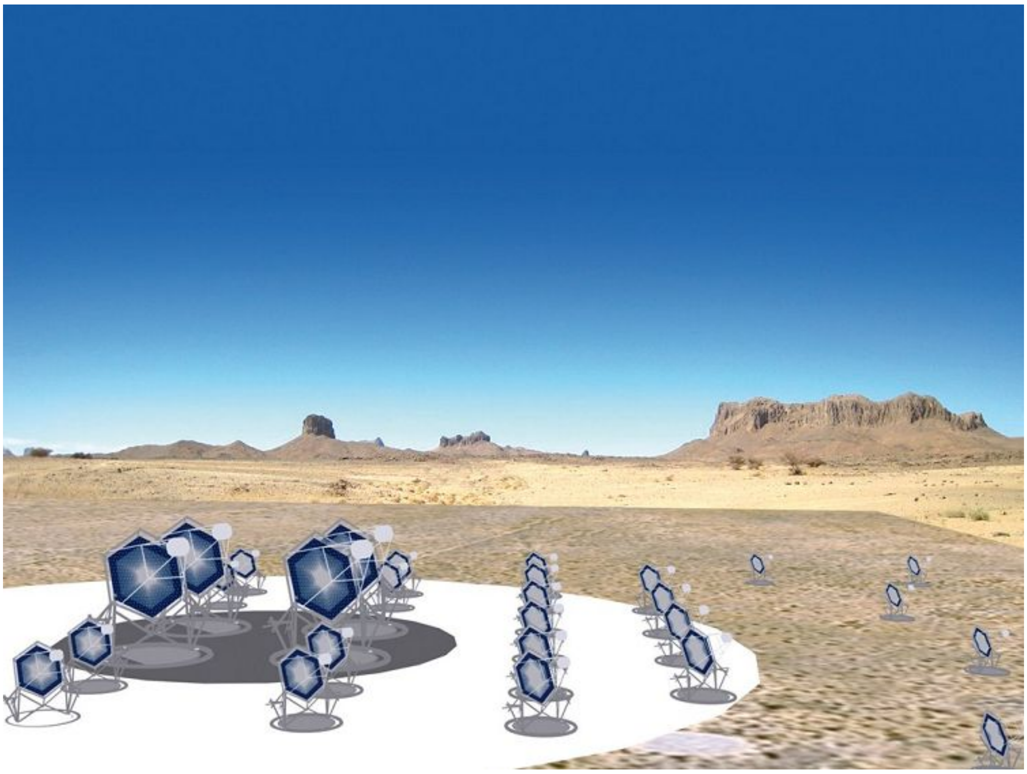

Figure 7.1: Artistic view of a possible CTA configuration, with three different telescopes types covering the overlapping energy ranges, and area coverage which increases with increasing gamma-ray energy.

CTA is planned to include two sites, one in the northern and one in the southern hemisphere, for the full-sky coverage. The main one in the southern hemisphere will cover the central part of the Galactic plane and the dominant fraction of Galactic sources given the wealth of sources and the richness of their morphological features. It will be designed to cover the full energy range. A second

complementary northern site will be primarily devoted to the study of AGNs and cosmological galaxy and star formation and evolution, not requiring coverage of the highest energies. Determining the arrangement and characteristics of the CTA telescopes in the two arrays is a complex optimization problem, balancing cost against performance in different bands of the spectrum.
Unlike current instruments, CTA will be operated as a proposal-driven open observatory, and will include a science data center which provides pre-processed data to the user, as well as tools for the common analysis techniques. Given the large amounts of data generated by this scientific infrastructure (and by their analysis), close cooperation with efforts in e-science and grid computing is envisaged. This solution will facilitate worldwide collaboration in the context of simulation studies and in the processing and analysis of scientific data. Moreover, CTA data will be accessible through the Virtual Observatory with varying interfaces matched to different levels of expertise of the scientists.

7.2 Array and telescopes layouts

7.2.1 Array layout

Given the wide energy range which is desirable to be covered, a uniform array of telescopes, with fixed spacing and identical characteristics, is most likely not the most efficient solution. A separation into three energy ranges, without sharp boundaries, appears appropriate:

The low-energy range below about 100 GeV: to detect showers in this range, down to a few tens of GeV, the Cherenkov light needs to be efficiently sampled and detected, with fraction of area covered by light collectors of order 10%, assuming conventional PMT light sensors. Since detection rates are high and systematic background uncertainties are likely to limit the achievable sensitivity, the area of this part of the array can be relatively modest, of order a few 10^4 m^2. Efficient photon detection can be reached either with few large telescopes or many telescopes of modest size. For very large telescopes, cost of the dish structures dominates, for small telescopes the photon detectors and electronics account for the bulk of the cost; a (shallow) cost optimum in terms of cost per telescope area is usually reached for medium size telescopes in the $10 - 15$ m diameter range. In case of small to medium-sized telescopes, the challenge is to trigger the array, since no individual telescope detects enough Cherenkov photons to provide a reliable trigger signal. Trigger systems which combine and superimpose images at the pixel level in real time, with time resolution of some ns, can address this issue but represent a significant challenge. CTA array design conservatively assumes a small number of very large telescopes, typically with about

$20-30$ m dish diameter, to cover the low energy range.

The core energy range from about 100 GeV to about 10 TeV: shower detection and reconstruction in this energy range is well-known from current instruments, and an appropriate solution seems a grid of telescopes of the $10-15$ m class, with a spacing in the 100 m range. Improved sensitivity is obtained both by the increased area covered, and by the higher quality of shower reconstruction since showers are typically imaged by a larger number of telescopes than for current few-telescope arrays. For the first time, array sizes will be larger than the Cherenkov light pool, ensuring that images will be uniformly sampled across the light pool, and that a number of images are recorded close to the optimum distance from the shower axis, about $70-150$ m, where the light intensity is large, where intensity fluctuations are small, and where the shower axis is view under a sufficiently large angle to efficiently reconstruct its direction. For example, in HESS four-telescope events provide significantly improved resolution and strongly reduced backgrounds, but represent only a relatively small fraction of events. An extended telescope grid operated with a two-telescope trigger condition will have a lower threshold than a small array, since always telescopes sufficiently close to the shower core can be found.

The high-energy range above 10 TeV: here, the key limitation is the number of detected gamma-ray showers and the array needs to cover multi-km^2 areas for best performance. Efficient detection makes use of the fact that at high energies the light yield is large, and that showers can be detected well beyond the Cherenkov light pool proper. Two implementation options can be considered: either a large number of small telescopes with mirror areas of a few m^2 and spacing matched to the size of the light pool of $100-200$ m (see Figure 7.2(b)), or a smaller number of larger telescopes with some 10 m^2 area which can see shower up to distance of 500 m and beyond, and can hence be deployed with spacing of 500 m and beyond, or in widely separated sub-clusters of a few telescopes (see Figure 7.2(a)). While it is not immediately obvious which options offers best cost/performance ratio at high energies, the sub-cluster concept with larger telescopes has the advantage of providing additional high-quality shower detection towards lower energies, for impact points near the sub-cluster.

Apart from that, the performance of an array of imaging atmospheric Cherenkov telescopes such as CTA depends on a large number of technical and design parameters. These include the general layout of the installation, with telescope sizes and locations, but also many other aspects like telescope optics, camera field of view and pixel size, signal shapes and trigger logic. In search for an optimum configuration of the array, extended Monte Carlo simulation should be performed

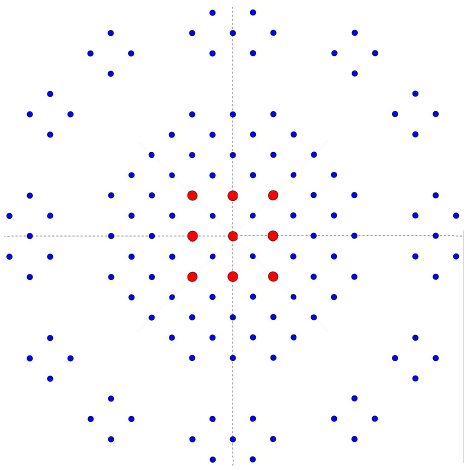

(a) Array layout without small telescopes. The blue clustered points in the outer region provide the detection of the higher energies.

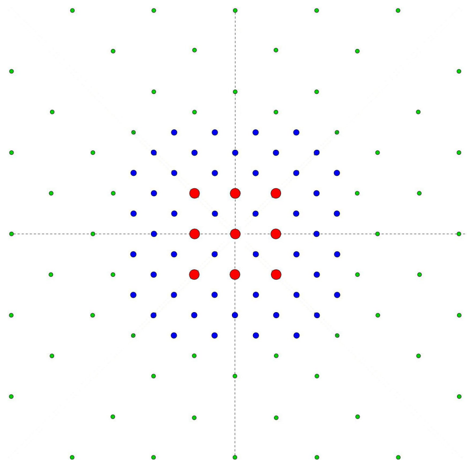

(b) Array layout with three different classes of telescopes.

Figure 7.2: Two possible geometries of arrays with separate regions optimized for low, intermediate and high energies. The three colors represent three different telescopes diameters (not drawn to scale), each one for an energy range.

to reach an acceptable trade-off between the many parameters, some of whom are intimately related, either technically or by constraints on the total cost. Studies performed so far serve the primary purpose of demonstrating that with an array of Cherenkov telescopes of plausible size and cost, the key performance targets for CTA are within the reach.

7.2.2 Telescopes layout

A Cherenkov telescope is primarily characterized by its light collection capability, by its field of view and by its pixel size, which limits the size of image features which can be resolved. The optical system of the telescope should obviously be able to achieve a point spread function compatible to the pixel size. The electronics for signal capture and triggering should provide a bandwidth matched to the length of Cherenkov light pulses of a few nanoseconds. The required light collection capability (in the different sections of the array) is determined by the energy thresholds and one size of IACT is only optimal for covering about 1.5 to 2 decades in energy. Hence, for the energy ranges proposed and from the indications of the Monte Carlo simulations (see § 7.3), at least two or three sizes of telescopes are needed to cover such a large energy band. Current design efforts concern three telescope classes:

Large Size Telescope (LST): it is devoted to the very low energy band (below

100 GeV) employing very large optical dishes with diameter of about $20-30$ m, a small field of view (about 5°) is sufficient to image showers impacting till distance less than 120 m; beyond this distance also twenty meter pupils and more are not enough large to trigger the faint Cherenkov light produced by gamma ray of several tens of GeV.
Work concentrates on a parabolic dish of 23 m diameter with $f/d = 1.2$ designed by the German firm MERO under the supervision of the MPI-P institute of Munich. This design has carbon fiber structure aiming for a total weight around 50 tons (Figure 7.3(a)). The dish uses 3 or 4 layers space frame, based on triangular elements, with hexagonal mirrors 1.5 m flat-to-flat supported from nodes of the space frame. The dish is supported by an alt-azimuthal mount moving on 6 bogies along a circular rail. An alternative design has been proposed by the Irfu CEA Saclay institute (France) and shown in Figure 7.3(b). A pit is dug under the telescope structure, so that the elevation axis of the dish structure remains close to the ground. The dish has a radial structure made of long carbon fiber tubes. Its rear face is a double conical surface, guaranteeing a good stiffness for every oriented position. The dish is hanged from two articulations located a few meters above it from which the elevation movement is made employing a swing-like concept.

Medium Size Telescope (MST): for the intermediate energy band ($0.1-10$ TeV) a number of 12 m telescopes will be implemented with Davis-Cotton optics, $f/d = 1.33$ and field of view of about $7-8°$. Several designs have been proposed by the community and are now under a detailed evaluation. Of particular interest are the two designs reported in Figure 7.3(c) and Figure 7.3(d).
The first one is proposed by the German institute DESY in collaboration with ANL; the structure is very simple and is composed mainly of square structural steel tubes. The dish is supported at the 3 and 9 o'clock positions by elevation bearings where the elevation drive system is also positioned, while the camera is supported by a four-truss structure as shown. The azimuth drive system is a gear driven system that uses inexpensive straight gear racks that are bend to the radius of the azimuth rails and then driven by a pinion attached to a motor. The drive systems will be mounted on a support structure that utilizes a center pintle bearing that provides accurate azimuth rotation. The support structure will ride on a stationary rail. The weight of the support structure and telescope will be transferred to the rails through 12 wheel blocks arranged on 6 bogies.
The other design is proposed by the Irfu CEA. The telescope has an alt-az mount, the dish structure is flat and lightweight, composed of a mesh formed with carbon-fiber epoxy tubes obtained from a fully industrial process. A

steel mount is rotating in azimuth on a rail fixed on concrete foundations. The elevation axis can be either fixed to a "U" support structure or, in a second option, being on a moving structure which kinematics allows the dish to lay very close to the ground when the mirror looks at the zenith.

Small Size Telescope (SST): in the extreme energy range (>10 TeV) the intensity of the Cherenkov signal allows to image very far showers using small optical dishes if designed with a sufficient wide field angle $8-10°$ or more. The angular resolution should also be as constant as possible along the field of view. Two completely different options can be implemented: a 7 m telescope with Davis-Cotton optics and a f/d of about 1.5 that allow a limited field of view; or a very small 4 m telescope with an innovative double-reflection design capable of a full $8-10°$ (or more) field of view with a superb angular resolution.
Designs for both the options have been proposed, Figure 7.3(e) shows a possible solution for the 7 m type proposed by an Argentinian group, while Figure 7.3(f) shows the innovative double-reflection design proposed by the Italian INAF community.
However, till now it is not completely clear which one provides better performance and both the options are under detailed evaluation.

Independently from the telescope class, the main mechanical components such are the mount with its associated drive systems, the dish supporting the mirrors and the camera support should follow some common design criteria:

Mechanical stability under observing conditions. The optical supporting structure should maintain a stable focus position independently of pointing position, presence of modest wind loads and temperature variations. Mirror facets have to be kept stable to below 1 arcmin, either by a suitable stiff structure or by active control. This structure, called dish, is a space frames; it can be either flat or approximate the optical layout of the reflector.

Mechanical strength under survival conditions. The overall structure has to survive with extreme conditions such are peak wind speeds up to 180 km/h and snow load.

Pointing and tracking position. The location of the image on the camera is determined by the precision of the tracking system, the overall deformations of the dish and the deformations of the camera support. Given the extremely short exposure times, pointing does not need to be stable or precise to more than a few arcmin, provided that the effective pointing is monitored with high precision.

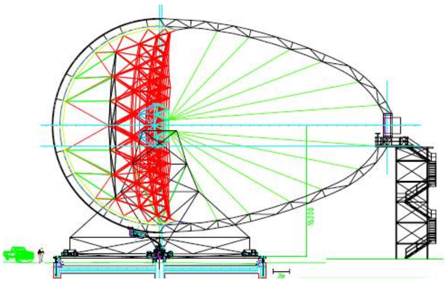

(a) LST designed by MPI-P in collaboration with MERO.

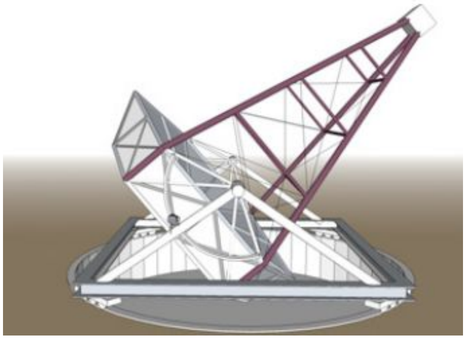

(b) LST designed by Irfu CEA. It is derived combining together ideas proposed for some MST designs.

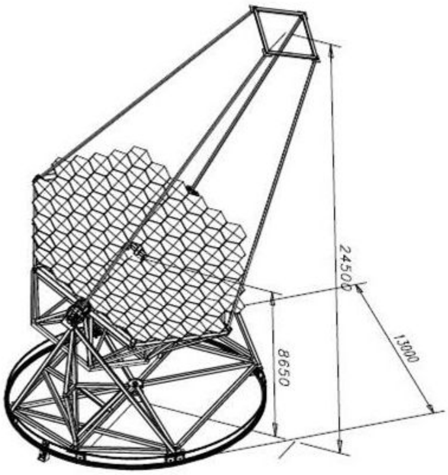

(c) MST designed by DESY in collaboration with ANL.

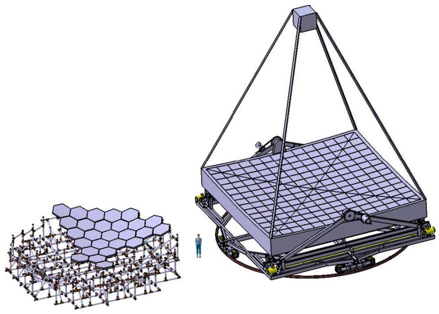

(d) MST designed by Irfu CEA.

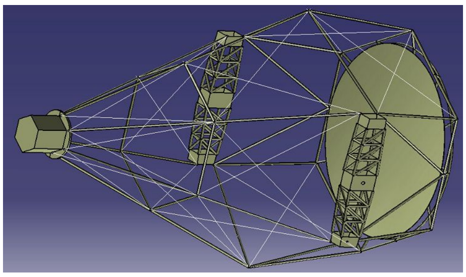

(e) SST designed by the Universidad Nacional de La Plata (Argentina).

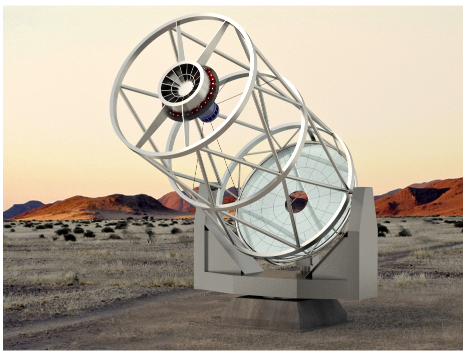

(f) SST designed by INAF in collaboration with BCV progetti.

Figure 7.3: Proposed designs for the three different classes of telescopes of CTA.

Slewing speed. Since those objects are usually tracked over tens of minutes before repositioning, a slew speed of 100°/min to 200°/min is sufficient. However, in case of GRBs follow-up it is requested a faster slewing speed.

Efficiency of construction, transport, installation and maintenance are key factors in reducing costs. For mass production of telescopes, it may be most efficient to set up a factory for assembly of telescope structural components at the instrument site, avoiding shipment of large parts. Minimal maintenance is requested for high efficiency of operation and to minimize on-site technical staff requirements.

Safety considerations. In particular, even in case of failures of drive systems or power it must be possible to return the telescope to its safe stow position.

7.3 Sensibility and Monte Carlo simulations

In first simulations studies for CTA, different telescope configurations were investigated. The main aim at this time was to cross-check the different simulation packages using benchmark telescope systems and to investigate how performance varies with telescope and array parameters. None of the configurations studies should be considered a close to final solution for CTA. Configurations investigated include:

9-telescope arrays with only LSTs covering just 0.0064 km^2 and located at different altitudes (2000 m and 5000 m), to investigate the low-energy performance of such arrays;

97-telescope array composed of 85 MSTs deployed at variable spacing supplemented in the center by three sets of 4 LSTs at different separations, for a total cover of about 0.25 km^2. Analysis does not include all of the telescopes, but selected subsets;

39-telescope array composed of only SSTs with the classical Davies-Cotton layout, the covering is about 4 km^2 with a clustered telescopes distribution, to investigate the very high energy performance of such arrays.

All systems assume conventional technology in terms of characteristics of mirrors, PMTs, read-out electronics, and standard analysis techniques.
A traditional way to represent the sensitivity of IACT instruments is in terms of integral sensitivity, including all events reconstructed above a given energy assuming a typical observation time of 50 hours. However, a more useful way to represent the sensitivity of possible CTA configurations is in terms of a differential sensitivity where a significant detection in each energy bin is required.
The sensitivity results for the 9-telescope configurations are shown in Figure 7.4(a).

For 2000 m elevation, the array has a useful sensitivity above 20 GeV and at higher energies dips below the 1% Crab line. However, performance in the 100 GeV to TeV range is not dramaticaly improved compared to systems such as HESS (despite the light collection area is higher to almost an order of magnitude). A high altitude installation is mainly relevant for specialized very low energy instruments.

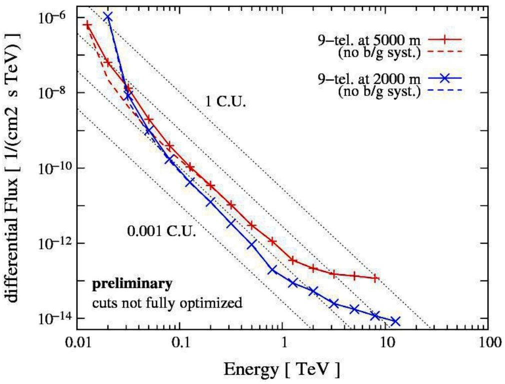

(a) Differential sensitivity for the 9-telescope layouts with only LST.

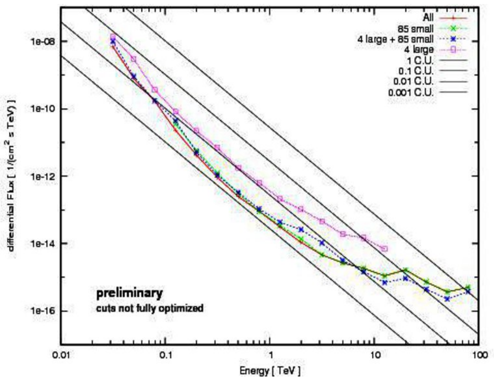

(b) Differential sensitivity for the 97-telescope layouts with LST and MST.

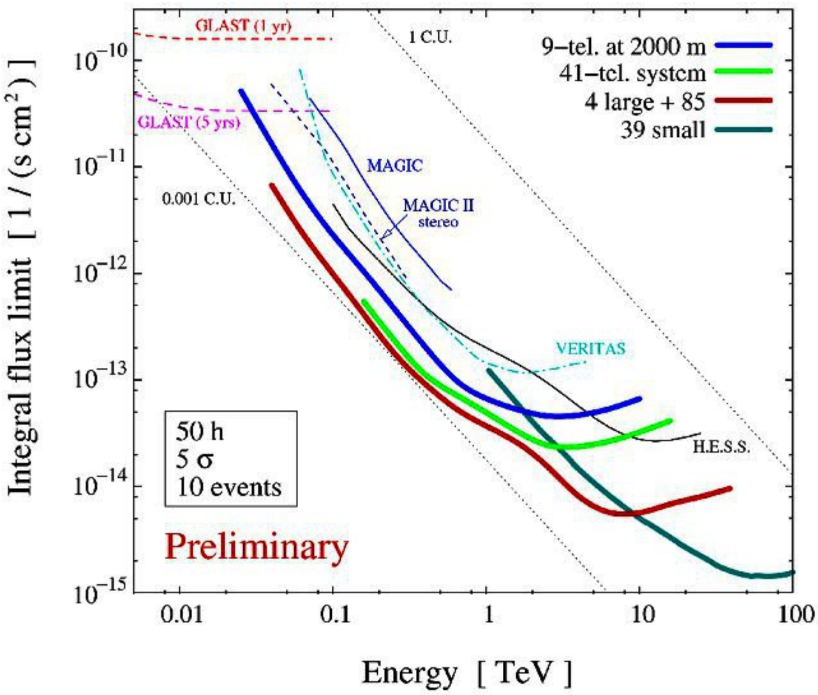

(c) Integrated sensitivity for CTA compared with present day experiments.

Figure 7.4: Simulated sensitivity of different array layouts for CTA.

To estimate the performance achievable with an instrument closer to the scale of CTA, simulations of the 97-telescope array are most suitable. Figure 7.4(b) illustrates the differential flux sensitivity achieved with this system if (a) all 97 telescopes are used, (b) only the 85 MSTs, (c) the 85 MSTs combined with 4 LSTs, and (d) only 4 LSTs. Optics parameters are for the MST a Davies-Cotton dish and 7° field of view, while for the LST a parabolic dish and 5° field of view. In the energy range from about 200 GeV to a few TeV, the medium telescopes alone approach mCrab flux, while the large telescopes extend the energy range down to a few 10 GeV at a sensitivity of 0.01 Crab. The combination of the two configurations improves performance even below the threshold of the LSTs. Finally, at energies of 10 TeV and above, sensitivity deteriorates due to the limited gamma-ray detection rate, indicating that the telescope array should be augmented by a sparse halo of telescopes for the highest energies.
Figure 7.4(c) summarizes the results showing the integral sensitivity for the different configurations discussed above, in comparison to existing instruments. The goal, mCrab sensitivity at intermediate energies and roughly a factor 10 improvement over existing telescopes, are essentially reached with the 85+4 configuration. At very high energies, a further extension of the array is necessary. The curve representing the 39 SSTs array is able to deliver the desired sensitivity up to about 100 TeV.

7.4 Telescopes optical designs

Apart from the total reflective area, determining the amount of light that can be collected and hence the energy threshold, important criteria for the reflector design are:

PSF: the reflector should be able to concentrate light from a point source into a single pixel, implying a rms width of the PSF less than half the pixel diameter, better 1/3 of the the pixel diameter.

Time dispersion: introduced among Cherenkov photons due to different light paths, which should not exceed the intrinsic width of the Cherenkov light pulse from a gamma-ray shower, about 3 ns.

Field of view: the PSF should be maintained as constant as possible along the field of view to ensure a good image reconstruction also for distant events. This is particularly important in case of wide field instruments.

The reflector is usually segmented into individual mirrors with a spherical profile. For the optics layout, most current instruments use either a parabolic reflector or a Davies-Cotton design [46]. In the Davies-Cotton layout, generated originally for solar concentrators, all reflector facets have the same focal length f, identical

to the focal length of the telescope as a whole. The mirror facets are arranged on a dish having a spherical profile of radius f (see Figure 7.5(a)). In a parabolic layout, mirrors are arranged on a dish with a paraboloidal profile and the focal length of the mirror facets varies with the distance from the optical axis. If implemented with small mirrors, both approaches provide an essentially point-like focus for rays parallel to the optical axis, but suffer from significant aberrations for light incident at an angle to the optical axis. While it is more accentuated in the parabolic layout, it has the advantage to be isochronous. In fact, the Davies-Cotton layout introduces time dispersion to the photons arrival time at the camera, that anyway does not exceed the intrinsic spread of the Cherenkov wavefront (few ns) for reflectors up to about 15 m in diameter.
From the above considerations, among single reflector designs a Davies-Cotton geometry provides the best imaging over a large field of view hence it is preferred for the MST; for the LST only a parabolic dish is possible to limit the large time dispersion produced by the Davies-Cotton design.

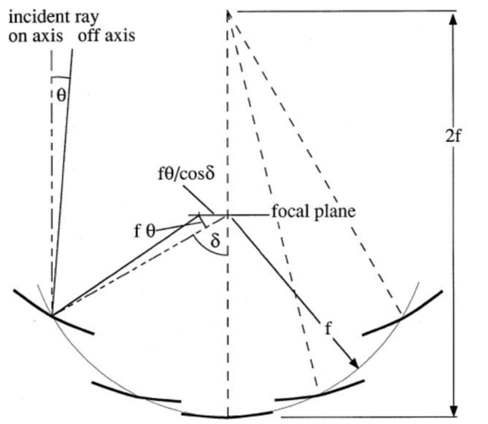

(a) Davies-Cotton optical design.

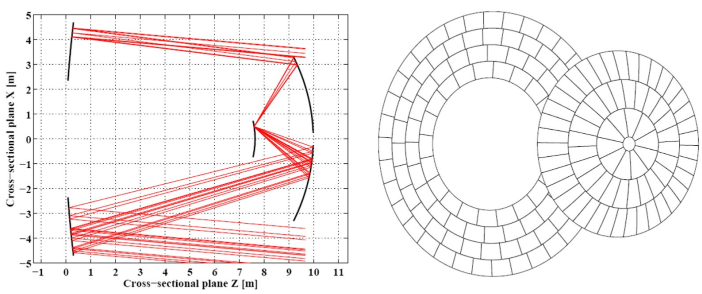

(b) Scharzschild-Couder optical design proposed for AGIS [47].

Figure 7.5: Possible optical designs adopted for CTA.

Concerning the SST the problematics are different and not yet completely understood. In fact, from Monte Carlo simulations, it is not clear if this class of telescopes should aim at the surveying of the sky with very large field of view or just serve as a merely bandwidth extension (toward the higher energies) for the MST. Two different options are under evaluation tailored to the two scientific roles, respectively: a Schwarzschild-Couder layout and the Davies-Cotton layout. Double-reflector telescopes have not been used yet in Cherenkov astronomy, they are discussed in depth with particular emphasis on a Schwarzschild-Couder design in [47]. Compared to single-reflector designs, where the camera is very large, heavyweight and has to be supported at a large distance from the dish, the double-reflector design is quite compact. It combines a small plate scale (appropriate to multi-anode PMTs as photosensors) with an improved compensation of optical errors over a wide field of view (below 1 mrad over a 10° field of view). Drawbacks include the fact that aspherical mirrors are used, which may be more difficult to fabricate, the tolerances on the relative alignment of optical elements are rather tight and an aplanar field of view.
While a Scharzschild-Couder telescope of 12 m diameter is planned to be built by the AGIS [48] collaboration (see Figure 7.5(b)), with some contributions by CTA partners, a modified design has been proposed by the INAF community and could be adopted for the SST.

7.4.1 Field of view

An important telescope design parameter is the field of view of the telescope. Therefore, in the choice of the field of view, one needs to balance and to quantify the science gains in relation to the cost and increased complexity. From the science point of view, large fields of view are of course highly desirable, since they:

- allow to detected high-energy showers with large impact distance without image truncation;
- allow the efficient study of extended sources and of diffuse emission regions;
- allow large-scale surveys of the sky and the parallel study of many clustered sources.

In addition larger field of view generally helps in improving the uniformity of the camera and reducing background systematics. Nevertheless, a large field of view helps primarily when several sources appear in typical fields of view, increasing the effective observation time per source by a corresponding factor when compared to a single source instrument which looks at each source in sequence.
On the other hand, large fields of view represent a technical challenge regarding the telescope optics. All the single mirror configurations used up to now have a

f/d ratios in the range up to 1.2 and deliver an acceptable PSF out to 4° to 5° of field of view. Larger fields of view require increased f/d ratios, in excess of 2 for a 10° field of view, see Figure 7.6 [49]. This result in a rapidly growing number of photosensors and of electronics channels making the focal plane instrument large and heavy. It needs to be supported at a larger distance from the dish making the telescopes mechanically difficult to realize.
Finally, a large telescope field of view (about 10°) is mandatory in case of widely spaced high energy telescopes, since image distance from the camera center scales with impact distance of the air shower. For the low- and intermediate energy arrays, the best choice of the telescope field of view is nontrivial to determine.
A very rough estimate obtained from Monte Carlo simulations, based on typical dish costs and per-channel pixel and readout costs suggests an economic optimum in the cost per source-hour around 6° to 8° field of view diameter. The final choice of the field of view will have to await detailed studies related to dish and mirror technology and the related costs, and the per-channel cost of the detection system.

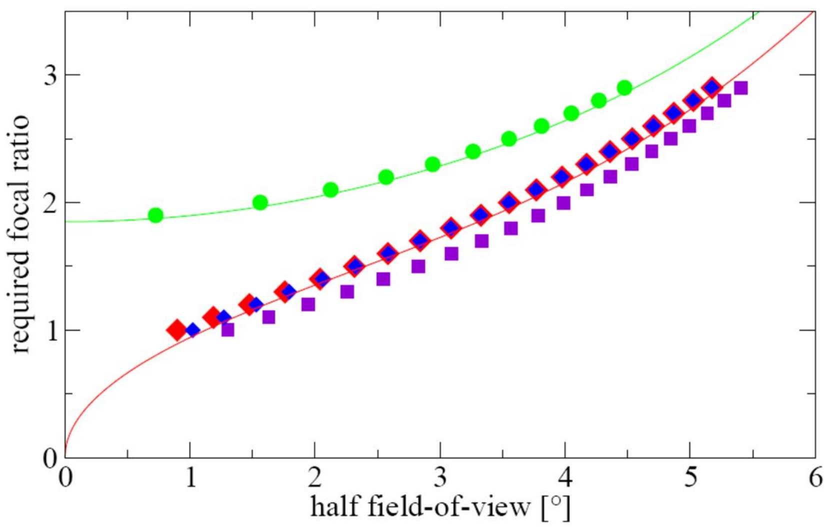

Figure 7.6: Focal ratio required to discriminate γ-rays from hadrons [49]. Points: simulation data for spherical design (green), parabolic design with constant radii (red), parabolic design with adjusted radii (blue) and Davies-Cotton design (violet). Lines: third-order approximation for single-piece sphere (green) and for single-piece paraboloid (red).

7.4.2 Pixel size

The size of focal plane pixel is another parameter which will deserve careful optimization since the cost of focal plane instrumentation is currently primarily

driven by the number of pixels and therefore scales like the square of the inverse pixel size.
Figure 7.7 illustrates how a shower image is resolved at different pixel sizes ranging from 0.28° (roughly the pixel size of the HEGRA telescopes) down to pixel sizes of 0.07°, as used in the large HESS 2 telescope. However, the gain due to small pixels depends strongly on the analysis techniques. In the classical second-moment analysis, performance seems to saturate for pixels smaller than 0.2° to 0.15° [50]. On the other hand, analysis techniques which use the full image distribution can extract the information contained in the well collimated head part of the image, as compared to more diffuse tail, and benefit from pixel size as small as 0.06° to 0.03° [51] and [47].
Pixel size will also influence the trigger strategies: for large pixels, gamma-ray images are contiguous allowing straightforward topological triggers whereas for small pixels, low-energy gamma-ray images may have gaps between triggered pixels.
The final decision concerning pixel size will be driven to a significant extent by the cost per pixel. Current simulations favor of good compromise pixel sizes of 0.09° for the large telescopes, allowing to resolve compact low energy images and reducing the rate of night sky background photons in each pixel, 0.18° for the medium size telescopes, similar to the pixel sizes used by HESS and VERITAS, and 0.25° for the pixels of the telescopes in the halo of the array, where large fields of view are required but shower images also tend to be long due to the large impact distances and resulting viewing angles.

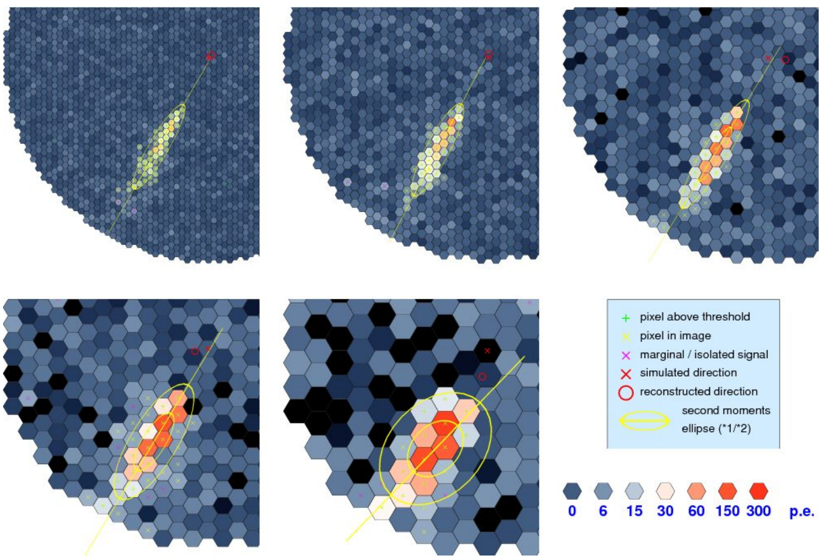

Figure 7.7: Identical fields of view diameters tasseled with different pixel sizes (0.07, 0.10, 0.14, 0.20, and 0.28°) and viewing the same shower (a 460 GeV gamma shower at a core distance of 190 m) a 420 m^2 telescope.

7.5 Camera and readout electronics

7.5.1 Camera

The camera is basically a kilo-pixel sensor devise covering, depending on the optics design, from few to less than one meter-square area. The pixels must have specific characteristics that well fit the requirements imposed by the project, they serve to detected the Cherenkov light with sensor response that should match the peak in the spectrum around 350 nm. At large wavelengths, beyond about 550 nm, the signal to noise becomes increasingly unfavorable because of the increasing intensity in the night sky background in these regions. The spectral sensitivity of conventional PMTs with their falling sensitivity at large wavelengths provides a reasonably good match to the needs. However, desirable is a larger peak quantum efficiency; given that the efficiency of current tubes peaks at only 25%, dish sizes could be halved for 100% efficient sensors.
Different solutions are under test to enhance the overall efficiency of the present PMTs. For example, the use of Winston-cone type light funnels serves a dual purpose: on one hand they collect the light in the gaps between active areas of adjacent photo sensors, on the other hand they limit the view angle of the photo sensor to the angle subtended by the dish and reduce albedo. Different schemes are in use to produce funnels: extruded and aluminized funnels or funnels lined by a reflective foil. The 80% throughput of current light funnels offers room to improved light collection power of a telescope at relatively modest cost and effort, if the reflectivity and geometry of funnels can be improved further. Indications are that PMTs with spherical entrance window and photocathode provide better efficiency than PMTs with a planar window. One other option under investigation is to use transparent solid funnels, an option already employed in the first HEGRA telescope but then abandoned because of the additional weight and the fake signals resulting from muons traversing the funnel. This latter problem is no longer relevant for telescope systems, where such events will not trigger.
Other criteria beyond spectral sensitivity include:

Sensor dimensions: single-pixel has to be chosen accordingly with the optical design and desired angular resolution of the telescope.

Sensor uniformity: sensor uniformity is not very critical, but large non uniformities should be avoided.

Sensor dynamic range and linearity: sensors should be able to detect single photons, and provide a dynamic range ideally up to some 10^4 photons, with deviations from linearity below a few %.

Temporal response: Cherenkov photons arrive with a timing dispersion of a few nanoseconds; matched short signal integration windows are used to reject night sky background noise. The photo sensor should not significantly lengthen the time structure of a Cherenkov light pulse; it is desirable to allow determination of pulse arrival time with sub-nanosecond precision for sufficiently large light pulses.

Sensor lifetime: should be provided a lifetime of 10 years given annual exposure in the 1500 hours range.

Rate of spurious signals: in particular photomultiplier sensors give spurious signals when residual gas atoms are ionized, they are called afterpulses. Unless the afterpulse probability is sufficiently low (10^{-4} or below) trigger's rates and trigger's thresholds may be dominated by afterpulses.

Operational characteristics: towards efficient and reliable operation of the systems, sensor should show good short- and medium-term stability, and gradual aging, if any. Sensors should survive excessive illumination.

In case of sensor arrays, such as multichannel photomultipliers, small cross talk between channels is essential. Last but not least, the sensors cost is a key factor as it is also their availability in large quantities; CTA will employ 100000 or more sensor channels.
Photomultiplier tubes with improved quantum efficiency are under advanced development and testing and may be available when the array is constructed; however, the long experience in the area of conventional photo-multiplier tubes provides a solid and certain basis, and a base-line for studies of the instrument's performance. Silicon photosensors can provide even higher quantum efficiencies, but they need further development and commercialization; depending on the time scales and cost, they provide an alternative to PMTs or, more likely, an upgrade path.

7.5.2 Readout electronics

Photosensor signals have an induced air-shower pulse width of few ns, superimposed on random night sky background. Typical rates are of some 10 MHz to more than 100 MHz, depending on mirror size and pixel size. Optimum capture of air-shower signals therefore implies high bandwidth and short integration times. The fast electronics needed to have been mastered long in this domain, even before such electronics became common-place with the GigaHertz transmission and processing used today in telephony, Internet, television, and PCs.
Ideally, the dynamic range and noise should be such that single-photoelectron signals are still resolved, and signals of a few 1000 photoelectrons are captured without truncation. The recording electronics must furthermore delay or store the signal while a trigger signal is generated, indicating that the event is to be

captured and read out. Generation of the trigger signal will take about 100 ns if a relatively simple coincidence logic acting on pixels of a given camera is used, up to 10 or more microseconds if signals from different telescopes are combined. Two techniques are in use. Flash-ADCs which digitize the photosensor signals at rates of a few 100 MSamples/s to a few GSamples/s, writing the output into a digital ring buffer. The modest cost of digital buffers allows large trigger latency; delays of tens of microseconds can be realized. The second approach uses analog memories, basically switched capacitors, to record the signal shape. The maximum recording depth is at most a few microseconds of trigger latency. In the current stage of CTA electronics design the two options (analog samplers and flash-ADCs) will be pursued in parallel.
Signal transmission from the photosensors to the recording electronics represents a critical design issue in case the electronics is located far from the photo sensors. Conventional cables limit bandwidth, are bulky and difficult to route across telescope bearings, and are costly. Mechanical packaging of the entire camera and sealing against the environment is crucial for stable performance. In its daytime configuration with closed camera lid, the camera body should be reasonably waterproof. Dust penetrating the camera and deposited on connectors and on optical components is a serious issue. To protect the photosensors and the light-collecting funnels and allow for easy cleaning, an optical entrance window made of near-UV transparent material is desirable. The light loss due to reflection and transmission is effectively recovered over time due to the absence of deterioration of the camera components.

7.6 Trigger characteristics

Performance of an array is also dependent on the triggering strategy where, based on individual images and global array information, Cherenkov emission from air showers has to be recognized in real time among the high flux of night sky background photons. The huge data stream from Cherenkov telescopes does not allow untriggered recording.
In most applications, it is required a multi-telescope trigger coincidence to reduce background noise already at the trigger level. The main issue here is how much information is exchanged between telescopes to generate a global trigger decision. One extreme scenario is to have each telescope that triggers independently from the others and only exchange a trigger's flag with neighboring telescopes, looking for coincident triggers. The energy threshold of the system is then determined by the minimum threshold at which a telescope can be triggered. The other extreme is to combine signals from different telescopes at the pixel level and to extract common image features. In this case, the system energy threshold could be well below thresholds of individual telescopes, particularly important when the array

is made up of many small or medium-size telescopes. However, technical complexity is significant. There is a wide range of intermediate solutions.
Trigger topology is another open issue. Triggers can either be derived locally within the array by some trigger fabric connecting neighboring telescopes. Alternatively, all trigger information can be routed to a central station and then propagate back to the telescopes. The first approach requires shorter signal storage at the telescopes and is easier scalable to larger arrays, the second provides maximum flexibility.
Current array trigger scheme for systems of Cherenkov telescopes provides a synchronous trigger decision, delaying telescope trigger signals by an appropriate amount to compensate for the time differences when the Cherenkov light reaches the telescopes. The time to reach a trigger decision and to propagate it back to the telescopes could be even more than 10 μs.
A new option for triggering of the array is a software-based asynchronous trigger. Pixel signals are readout and digitized after each telescope trigger, and are stored in digital memory, tagged with an event number. With each local trigger an absolute time stamp is captured for the event with an accuracy of the order of nsec and transmitted to the camera CPU. This computer collects the time stamps, and possibly additional trigger information, for each event and transmits them every $10 - 100$ msec to a dedicated central trigger computer. The central computer receives all time stamps from all telescopes and uses this information to test for time coincidences of the events and to derive the telescope system trigger decision, depending of the user-requested configuration for coincidences and possible subsystems. In such a trigger scheme, the central trigger decision is done in software, while using the very tight timing from the camera trigger decision. It is therefore scalable, fully flexible and all types of sub-systems can be served in parallel. At the same time it uses the shortest possible coincidence gates and provides an optimum suppression of accidental coincidences.
Whether local or global, trigger schemes will employ a multi-level hierarchy. At a first level, pixel signals are processed or encoded by a discriminator, or possible multiple discriminators with different thresholds. A second level uses these signals to identify concentrations of Cherenkov signals in local regions of the camera, again applying a threshold. A third level finally combines trigger information from different telescopes to select multi-telescope events.
Another important aspect is that the trigger system is very flexible and software-configurable, since observation modes may range from deep observations or survey applications. In the first case all telescopes follow the same source to monitoring, in the second one each group of a few telescopes or even single telescopes point at different fields.
At this stage of the study, no conclusion has emerged concerning the preferred trigger scheme for CTA telescopes; simulations of the different schemes are in

progress.

7.7 Site candidates

Selection of sites for CTA is obviously crucial towards achieving optimum performance and science output. Criteria for site selection include, among others, geographical conditions, observational and environmental conditions, and questions of logistics, accessibility, availability, stability of the host region and local support. The final decision among otherwise identical sites may rely on considerations such a financial or in-kind contributions by the host region.
As an example for a first rough selection, one can select sufficiently large and flat areas above 1500 m asl based on a topological model of the Earth, add the requirement that the artificial background light as determined from satellite images is minimal, and that average cloud coverage is less than about 40%. The resulting map is in Figure 7.8 and shows very few locations matching these criteria.
However, for identification of potential observatory sites special algorithms and high-resolution data are needed. Also for CTA has been started searches using the recently released ESO application FRIOWL that provides access to an extensive database of information for the last 40 years.

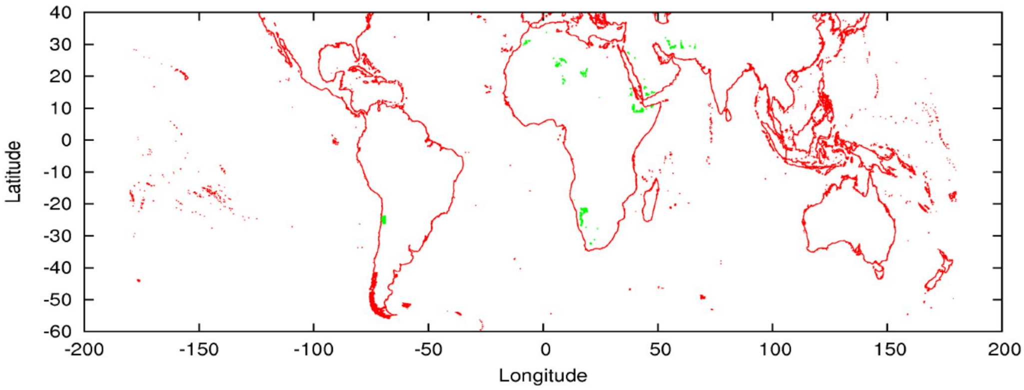

Figure 7.8: Sites above 1500 m asl which offer sufficiently flat areas, minimal artificial background light and an average cloud cover of less than 40%, selected on the basis to topological and satellite data.

Northern site candidates include:

Canary Islands La Palma and Tenerife: these are well-known and well-explored observatory sites at about 26°N, about 2400 m asl, with the Observatorio del Roque de los Muchachos on La Palma and the Observatorio del Teide on Tenerife.

Hanle in India, in the Western Himalayas: this high-altitude site (33°N, 4500 m asl) houses a small observatory, and an array of Cherenkov instruments is being deployed by Indian groups. Access to the site is non-trivial.

San Pedro Martir, Baja California: well-established astronomical site that hosts already two observatories run by the Universidad Autonoma de Mexico. It is situated at about 31°N, at 2800 m asl.

Southern site candidates include:

Khomas Highland of Namibia: at 1800 m asl and 23°S, a well-known astronomical site where it is sited the HESS instrument, the region offers a range of suitable large flat sites.

Chilean sites: some of the world's premier optical observatories are located here; availability of sufficiently large cites near these locations is limited. A possible site is north of La Silla at 29°S and 2400 m asl, site D. There is another potential site near Cerro Paranal, with even better observing conditions, but no sufficient flat area for a large array could be identified so far.

El Leoncito Reserve in Argentina: this site at 32°S and 2600 m asl hosts the El Leoncity Astronomical Observatory, but the weather is somewhat inferior to the best Chilean sites.

Puna HighLand in Argentina: the region offers some wide potential sites at 3700 m asl with sky quality equivalent to the best Chilean ones. As a bonus, these sites have easy access to railway traffic.

Chapter 8

The CTA's science case

CTA is a new and unique facility to probe electromagnetic radiation from space in the very high energy domain (between tens of GeV to hundreds of TeV) with unprecedented sensitivity, energy coverage, and angular resolution. CTA will serve a number of science communities, including astronomy and astrophysics, cosmology, astroparticle physics, and particle physics. It will explore the universe in intense interplay with facilities probing other wavebands of electromagnetic radiation such as radio, infrared, optical, X-rays and gamma rays. Furthermore, CTA will form a crucial partner to facilities using other messengers that probe extreme processes in the universe, including ultra high energy cosmic rays, high energy neutrinos, and gravitational waves.

8.1 Background

Radiation at these energies differs fundamentally from that detected by astronomical instruments at lower energies. GeV to TeV gamma rays cannot conceivably be generated thermally by emission from hot celestial objects since the energy of thermal radiation reflects the temperature of the emitting body. Apart from the Big Bang there is nothing hot enough to emit such gamma rays in the known Universe, instead, high-energy gamma rays probe a "non-thermal" Universe. Different mechanisms than thermal emission by hot bodies allow the concentration of large amounts of energy into a single quantum of radiation. High-energy gamma rays can be produced in a top-down fashion by decays of heavy particles such as the hypothetical dark matter particles or cosmic strings, both relics which might be left over from the Big Bang. In a bottom-up fashion, gamma rays can be generated when high-energy nuclei, accelerated for example in the gigantic shock waves created in stellar explosions, collide with ambient gas particles (i.e. the

Earth's atmosphere). The flux and energy spectrum of the gamma rays reflects the flux and spectrum of the high-energy nuclei. They can therefore be used to trace these cosmic rays in distant regions of our own Galaxy or even in other galaxies.
The first images of the Milky Way in VHE gamma rays were obtained in recent years, and reveal a chain of gamma-ray emitters lining the Galactic equator, demonstrating that sources of high energy radiation are ubiquitous in our Galaxy (see Figure 8.1). Sources of this radiation include supernova shock waves, where atomic nuclei are presumably accelerated and generate the observed gamma rays. Another important class of objects in this context is "nebulae" surrounding pulsars, where giant rotating magnetic fields give rise to a steady flow of high-energy particles. Some of the objects discovered are binary systems, where a black hole or neutron star orbits a massive star. These systems are particularly interesting in that they allow probing how particle acceleration processes respond to the varying ambient conditions. One of several surprises was the discovery of "dark sources", objects which emit high-energy radiation, but have no obvious counterpart in other wavelength regimes. In other words, there are objects in our Galaxy which are so far only visible and detectable in high-energy gamma rays.

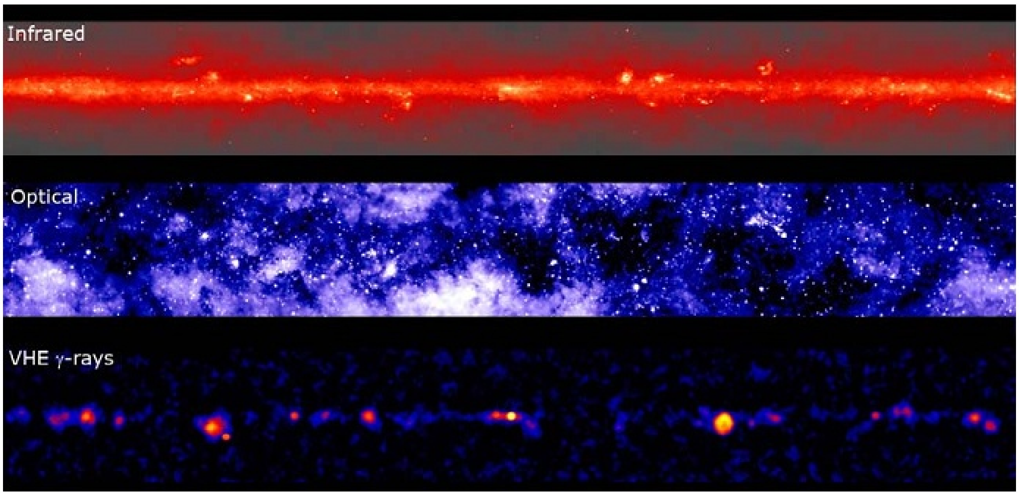

Figure 8.1: Images of the Milky Way in different energetic bands. From top: infrared, visible and VHE gamma-ray.

Beyond our Galaxy, well over a dozen extragalactic sources of high-energy radiation have been discovered, located in active galaxies, where a supermassive black hole at the center is fed by a steady stream of gas and is releasing enormous amounts of energy. Gamma rays are believed to be emitted from the vicinity of these black holes, allowing the study of the processes occurring in this violent and as yet poorly understood environment.
The high-energy phenomena, which can be studied with CTA, span a wide field

of galactic and extragalactic astrophysics, of plasma physics, particle physics, astroparticle physics, and fundamental physics of space-time. They encode information on the birth and death of stars, on the matter circulation in the Galaxy, and on the history of the Universe. Brief examples of the physics issues which it would be possible to address at a far more advanced level with an instrument with the capabilities of the CTA is presented. The list is certainly not exhaustive.

8.2 Galactic astrophysics

8.2.1 Supernovae remnants, pulsar wind nebulae, and cosmic rays

A paradigm of high-energy astrophysics is that of cosmic-ray acceleration in supernova explosion shocks. While particle acceleration up to energies well beyond 1014 eV has now clearly been demonstrated, it is by no means proven that supernovae accelerate the bulk of cosmic rays. The large sample of supernovae which will be observable with CTA and in particular the increased energy coverage towards lower and higher energies will allow sensitive tests of acceleration models and determination of their parameters. An invaluable insight has been provided by the HESS detection of gamma rays up to energies in excess of 10 TeV from a few remnants where non-thermal activity at other frequencies is also observed, this has strengthened the case in favor of supernovae remnants as plausible cosmic rays accelerators. An especially interesting case is that of RXJ1713-3946 shown in Figure 8.2 [52].
Pulsar wind nebulae are astrophysical sources powered by the rotation of a central pulsar that is responsible for the production of a magnetized relativistic wind, mainly made of electron-positron pairs. The particles in the wind are isotropized at a highly relativistic termination shock, where particles acceleration takes place and particles reach extremely large Lorentz factors, in excess of 10^8. The propagation and losses of electrons in the surrounding medium lead to the diffuse emission extending from the radio to the gamma-ray band that is observed as a pulsar wind nebula. Clearly the main improvement in our understanding of these complex objects, as already happened in X-rays, will come from a better angular resolution with future instruments, so to provide imaging of the emission in fine details. Pulsar wind nebulae are ideal laboratories to study particles acceleration at relativistic shocks, which is crucial not only for pulsar wind nebulae but also for a variety of other astrophysical objects. Some examples are shown in Figure 8.3.

8.2.2 Pulsar

Pulsar magnetospheres are known to act as efficient cosmic accelerators. However, yet there is no accepted model for this particle acceleration. The periodic emission

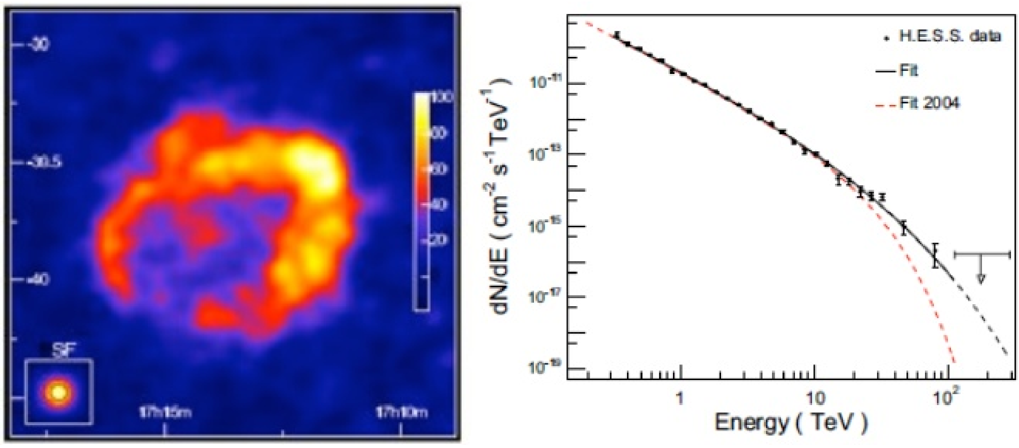

Figure 8.2: Image and energy spectrum of the supernova remnant RXJ1713-3946 obtained with HESS. It is worth noting as the morphology of the emission is also resolved.

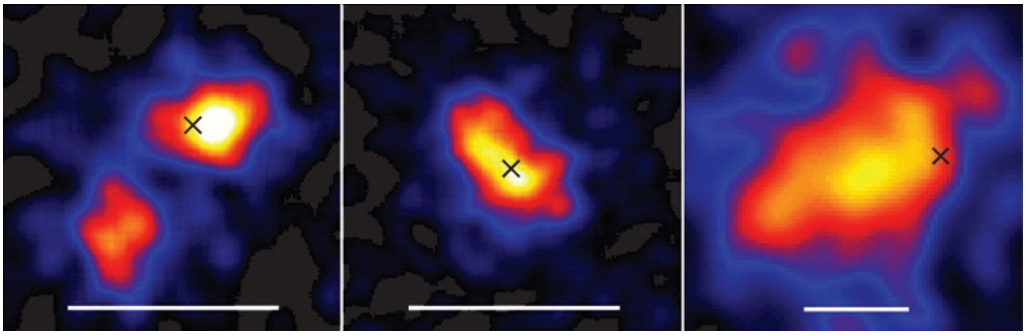

Figure 8.3: Thee examples of pulsar wind nebulae candidates observed by HESS. From left to right: the K3 and Rabbit pulsar wind nebulae in the Kookaburra Nebula, MSH15-52 and Vela X [53], [54] and [55].

of pulsars is generally attributed to electro-optical cascades that should originate in regions with non-screened, parallel electric field (the so called "gaps"), and then develop through the magnetosphere [56]. This basic scheme has however a vast number of ramifications and uncertainties. Pulsed gamma-ray emission allows the separation of processes occurring in the magnetosphere from the emission of the surrounding nebula. Competing models predict characteristic cut-off features in the spectra of pulsed gamma rays in the low-energy range of CTA. Compared to satellite instruments, CTA with its much larger detection rate is not affected by glitches in pulsar periods which may compromise periodicity measurements requiring very long integration times.

8.2.3 The Galactic Center

The Galactic Center hosts the nearest supermassive black hole, as well as a variety of other objects likely to generate high-energy radiation, including hypothetical dark-matter particles which may pair-annihilate and produce gamma rays. Indeed, the Galactic Center has been detected as a source of high-energy gamma rays, and indications for high-energy particles diffusing away from the central source and illuminating the dense gas clouds in the central region have been detected. In observations with improved sensitivity and resolution, the Galactic Center provides a rich reservoir of interesting physics from particle acceleration via the, not well known, diffusive propagation of cosmic-ray particles to exotic phenomena such as acceleration and curvature radiation of protons at the edge of rapidly spinning black holes.

8.2.4 Microquasars and X-ray binaries

Three very high energy gamma-ray emitters are currently known which are binary systems, consisting of a compact object (a neutron star or black hole) orbiting with a massive star. Whilst many questions have been opened concerning gamma-ray emission from such systems - in some cases it is not even clear if a pulsar-driven nebula around a neutron star or accretion onto a black hole is the energy source - it is evident that they offer a unique chance to “experiment” with cosmic accelerators: along the eccentric orbits of the compact objects, the environment (including crucially the radiation field) changes periodically, resulting in a modulation of the gamma ray flux, allowing the study of how particle acceleration reacts to these environmental conditions. Figure 8.4 shows the flux and spectral index of the VHE emission of LS5039 as a function of orbital phase, as measured using HESS. As the distance between the stars varies by a factor of $\sim$2 around the orbit, the observed modulation of flux and spectrum with period is not unexpected. The maximum flux occurs at inferior conjunction, the point where γ-γ absorption is expected to be at a minimum. However, the observed modulation is not consistent with the simple-minded expectation for such absorption (and/or cascading).
Equally interesting, the physics of microquasars in our own Galaxy resembles the processes occurring around supermassive black holes in distant active galaxies, except for the much faster time scales, providing insights into these mechanisms.

8.2.5 Stellar clusters and stellar systems

While the classical paradigm emphasizes supernova explosions as the dominant source of cosmic rays, it has been speculated that cosmic rays are also accelerated in stellar winds around massive young stars before they explode as supernovae, or around star clusters. Indeed, there is growing evidence in existing

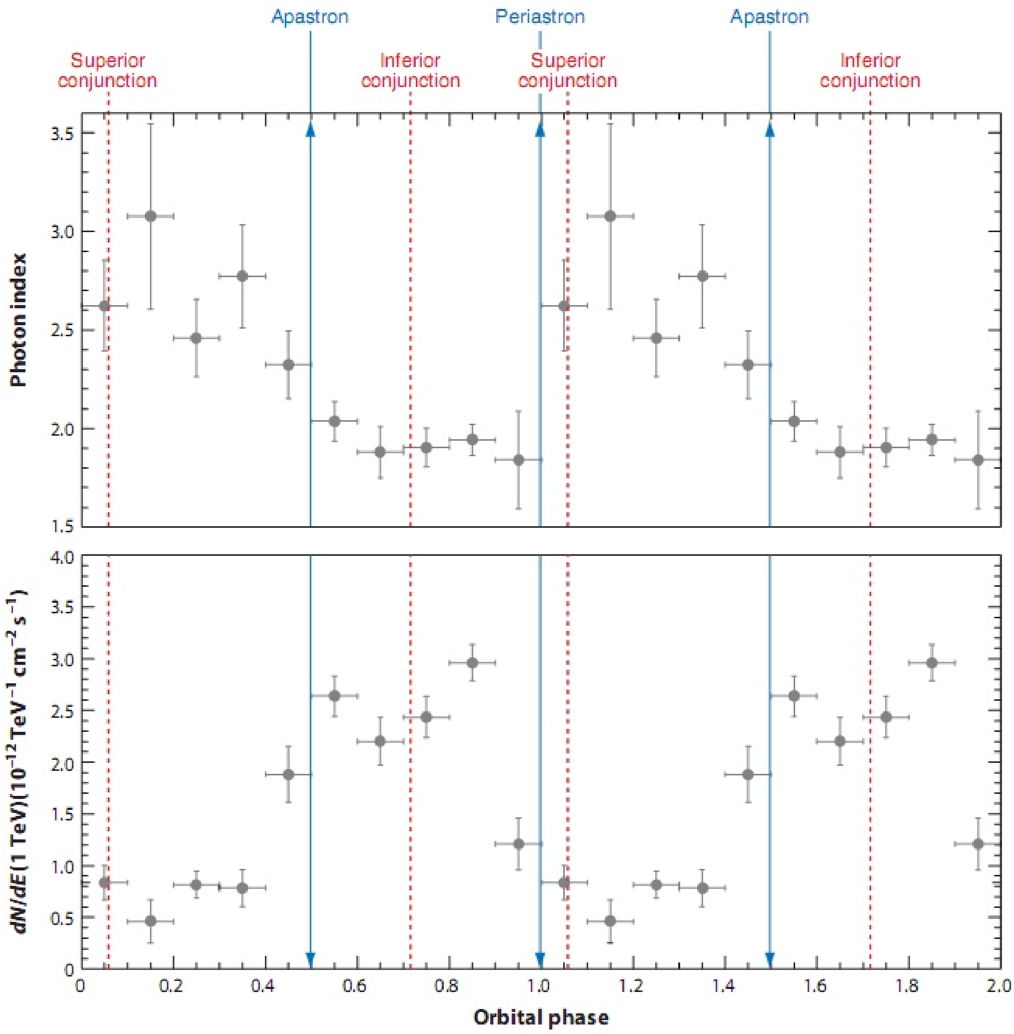

Figure 8.4: Phase-folded light curve and spectral index variations for the binary system LS5039 [57].

gamma-ray data for a population of sources related to young stellar clusters and environments with strong stellar winds. However, lack of instrument sensitivity currently prevents the detailed study and clear identification of these sources of gamma radiation.

8.3 Extra-galactic astrophysics

8.3.1 Active galaxies

The supermassive black holes at the cores of active galaxies are known to produce outflows which are strong sources of high-energy gamma rays. The fast variability of the gamma-ray flux, on minute time scales (see Figure 8.5), indicates that gamma-ray production must occur near the black hole, assisted by highly relativistic motion resulting in a contraction of time scales when viewed from an observer on Earth. Details of how these jets are launched by the black hole and even the kinds of particles of which they consist are poorly understood. Multiwavelength observations with high temporal and spectral resolution can distinguish different scenarios, but are at the edge of the capability of current instruments.

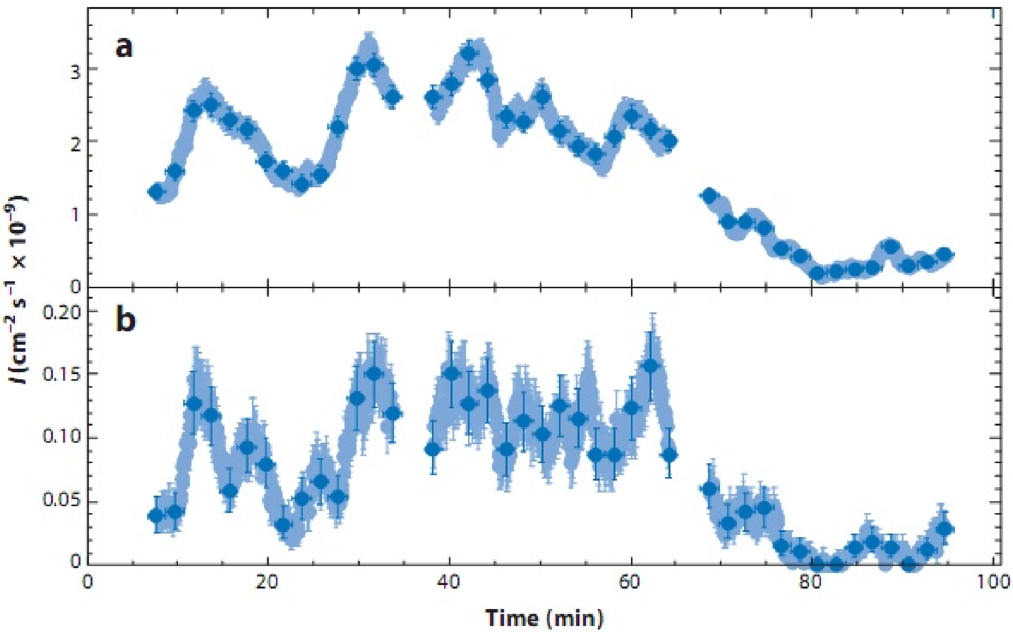

Figure 8.5: VHE light curve of PKS2155-304 during the July 2006 flare, in two energy bands: (a) 200-800 GeV and (b) above 800 GeV [58]. The light curve is sampled in two-minute intervals around each point.

8.3.2 Galaxy clusters

Galaxy clusters act as storehouses of cosmic rays, since all cosmic rays produced in cluster galaxies since the beginning of the Universe will be confined to the cluster. Probing the density of cosmic rays in clusters via their gamma-ray emission thus provides a calorimetric measure of the total integrated non-thermal energy output of galaxies. Accretion/merger shocks outside cluster galaxies provide an additional source of high-energy particles. Emission from galaxy clusters is predicted at levels just below the sensitivity of current instruments.

8.3.3 Cosmic radiation fields and cosmology

Via their interaction with extragalactic light, high-energy gamma rays from distant galaxies allow the extraction of cosmological information on the density of light in extragalactic space and therefore about the formation history of stars in the Universe. Gamma rays experience an energy-dependent attenuation when propagating through intergalactic space, due to electron-positron pair production on the extragalactic background light. This phenomenon allows determination of extragalactic light levels, unimpeded by the overwhelming amount of foreground light from the solar system and the Galaxy, which makes direct measurements prone to very large systematic uncertainties. Pair-production halos surrounding strong active galaxies may even allow measurement of the evolution of light intensity with redshift.

8.4 New physics

8.4.1 Search for Dark Matter

The dominant form of matter in the Universe is a yet unknown type of dark matter, most likely in form of a new class of particles such as predicted in supersymmetric extensions to the standard model of particle physics. Dark matter particles accumulate in, and cause, wells in gravitational potential, and with high enough density they are predicted to have annihilation rates resulting in detectable fluxes of high-energy gamma rays. CTA would provide a sensitive probe of this annihilation radiation, and will help to verify if such particles (which by then might be discovered at the Large Hadron Collider) form the dark matter in the Universe.

8.4.2 Probing space-time

Due to their extremely short wavelength and long propagation distances, very high-energy gamma rays are sensitive to the microscopic structure of space-time. Small-scale perturbations of the smooth space-time continuum, as predicted in theories of quantum gravity, should manifest themselves in a (tiny) energy dependence of gamma-ray propagation speeds. Burst-like events of gamma-ray production, e.g. in active galaxies, allow this energy dependent dispersion of gamma-rays to be probed and can be used to place limits on certain classes of quantum gravity scenario, and may possibly lead to the discovery of effects associated with quantum gravity.

Chapter 9

Development of composite glass mirrors: the case of MAGIC II

For Cherenkov telescopes high collecting area is needed, achievable by the use of a large diameter primary, made of a mosaic of many (possibly light-weight) reflecting facets, like the ones needed for future next generation ground based optical telescopes such as the 42 m E-ELT telescope studied by ESO.
While in both cases a high volume production has to be achieved, for making the reflecting panels for Cherenkov telescopes the angular resolution is not an issue: each panel should present a PSF with a diameter at 90% focusing better than about few arcmin, compared to the 0.1 arcsec value requested for each E-ELT panel. The PSF should be anyway smaller than the pixel size over the entire field of view.
However the cost-effective design and the lightweight of the mirrors of large Cherenkov telescopes is non trivial. They should maintain the cost below 2000 €$/m^2$ and weight below 25 kg/m^2; for comparison, the same target parameters for E-ELT are around 300 k€$/m^2$ and 70 kg/m^2 respectively.
Different technologies have been adopted so far for the production of the Cherenkov segmented mirrors. The different technologies can be divided into two main groups:

aluminized ground-glass mirrors. They are manufactured with standard technique starting from raw blanks. Ground-glass mirror solution has been often preferred (e.g. HEGRA, CAT, HESS and VERITAS) primarily because of its technical maturity, but at cost of a quite long time of production. Moreover, the ground-glass mirrors are quite heavy translating into increasing cost and complexity for the telescope mechanical structure;

composite sandwich structure mirrors. Thanks to the limits of the ground-glass technology, the idea to make use of lightweight mirror consisting of composite sandwich structure came to pass since the very beginning of IACT astronomy. In sandwich construction, membranes (such as sheets of steel, aluminum, glass, or plastic) are bonded to both side of a core material. This type of construction is widely utilized in products ranging from doors and tables to aircrafts, boats and satellites and is characterized by high strength-to-weight. The first Cherenkov telescope employing composite sandwich mirrors had been the MARK 3 experiment, for which a replication process had been developed by making use of aluminum honeycomb core and Alanod® face sheets [59]. The CANGAROO III telescope, instead, adopts composite sandwich mirrors consisting of rigid foamed core pinched by Fiber Reinforced Plastic sheets; in this case the structure is placed on a mould and curved in an autoclave for shape replication [60]. Also the MAGIC mirrors are composite structures:

- composite sandwich structure mirrors manufactured via **direct machining** of each individual piece: in this case consisting of an aluminum face sheet curved in autoclave to spherical shape and glued to an aluminum honeycomb inside a thin aluminum box making up a so called "raw blank". Each individual raw blank is subsequently polished by a diamond milling process [39]. For the MAGIC II telescope 136 one squared meter mirrors have been manufactured in this way [40].
- composite sandwich structure mirrors manufactured via **replication process** from a mould: the mirror elements have a sandwich like structure where the reflecting and backing membranes are bonded to both sides of an aluminum honeycomb core. The membranes are thin sheets of glass, aluminized for the reflecting one. Since the radius of curvature of these optics is high and the thickness of the glass sheet is sufficiently low, the sheet is mechanically bended and conformed to the shape of the master by means of vacuum action.

9.1 The cold glass slumping approach

The cold glass slumping is a new method derived from a similar technique proposed for the manufacturing of X-ray optics of the XEUS mission [61], that fits the requirements of Cherenkov telescopes. It has been developed by the Media Lario Technologies company in collaboration with INAF-OAB. Media Lario Technology has been also in charge of the mirror panels production and quality control for MAGIC II.

The fabrication process is hereafter described and the main steps are shown in Figure 9.1:

1. a master has to be worked with the same optical precision needed for the mirrors, because every defect on its surface will be reproduced on the glass. Diamond milling is used in order to achieve the best shape accuracy possible without the need for further polishing. The master has been produced by the LT-Ultra company (Germany). The master has a spherical convex curvature of the surface;

2. the shape of the master is replicated by the reflecting glass sheet taking advantage that for large curvature radii the glass sheet can be elastically deformed and pressed against the master using vacuum suction. A backing glass sheet is assembled with an interposed aluminum honeycomb core element giving the proper rigidity. In principle from a single master one could think that only one radius of curvature for the mirror could be obtained. Nevertheless, by a careful control of the spring-back effect during the gluing process, one can obtain several mirrors with curvature different than the master's one;

3. the connection of the parts is achieved through epoxy resin structural adhesive bonding with curing under elevated temperature while maintaining the vacuum suction;

4. the glass sheets adopted are floating glasses available on the market with a very good roughness and do not require any polishing step. The process ensures on the reflecting glass sheet the required shape accuracy after separation from the master and the preservation of the starting surface roughness of the glass sheet;

5. the reflecting coating is deposited after the manufacturing of the sandwich structure by means of physical vapor deposition in a dedicated high vacuum chamber. The reflecting glass sheet is coated in order to provide a high reflectivity at wavelengths in the range from 300 nm to 600 nm. Aluminum coating provides the best reflectivity at these wavelengths, especially in the range of short wavelengths (300 nm to 450 nm) that contains most intensity of the Cherenkov light. To avoid oxidation of the aluminum layer, a protective coating of Quartz is also applied;

6. sealing of the sandwich structure borders is assured by a silicon based sealant. The edges of the sandwich have an external plastic PVC rim. This solution assures higher rigidity and mechanical protection of the mirror corners.

All the materials within process are off-the-shelf and the higher cost is one time expenditure relevant to the manufacturing of the master. Moreover the master is not subjected to significant degradation during the process.

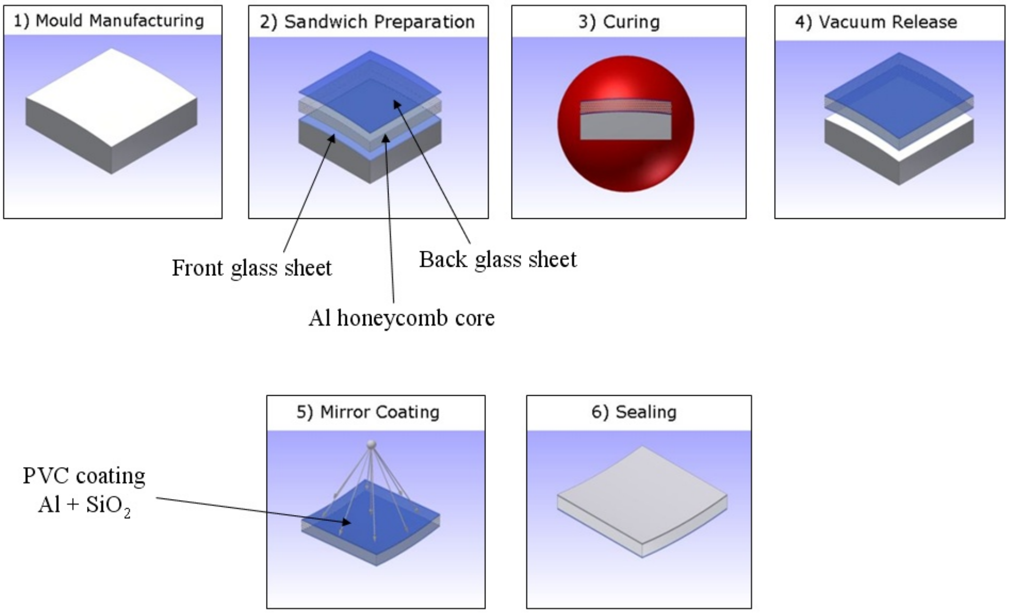

Figure 9.1: Flow chart of the cold glass slumping technology. Credits: Media Lario Technologies.

9.2 Glass mirror panels structure

For the MAGIC II telescope 100 one-squared meter mirrors have been manufactured in this way (for details see [42] and [41]), a picture with a finished panel is reported in Figure 9.2.

To assure that the optical characteristics required by the telescope design are maintained during operations the mechanical structure of the panel has been evaluated with FEA under different load cases. The final design for the panel is the following:

- panel shape and dimensions: square 985×985 mm^2;
- radius of curvature of the spherical shape: about 35 m (varying accordingly with the panel position into the telescope dish);
- sandwich structure with the following characteristics:
  - glass reflecting skin: 1.7 mm thick
  - bonding layer: 0.2 mm thick
  - Aluminum honeycomb core: 20 mm thick
  - bonding layer: 0.2 mm thick
  - glass backing skin: 1.7 mm thick

- panel total mass: 12 kg
- three rigid supports glued in the backing skin (stainless steel plates 80×80 mm). These supports are placed at a radius equal to 2/3 of the mirror structure side.

Figure 9.2: Picture of a coated panel taken before the optical characterization. Credits: Media Lario Technologies.

9.3 Panels qualification and test

Mirrors produced via cold glass slumping have been qualified following a rigid quality control process in order to assure that specifications required by the MAGIC II telescope design have been fulfilled. In the following, the activities performed for the environmental qualification of these mirrors are briefly presented together with their performance in terms of angular resolution and reflectivity. Some qualification tests have been performed at the level of samples (smaller with respect to the final dimension but fully representative of the manufacturing process) and some other tests have been performed on one squared meter prototype. In some cases the tests have been performed both on the samples and on the prototype mirrors. In particular, curvature radius measurement and PSF spot size have been tested on the full batch of the production. Table 9.1 shows a summary.

Qualification test	**On each mirror**	**On mirror prototype**	**On sample**
Curvature radius	X	X	X
PSF spot size	X	X	X
PSF spot size after thermal cycling		X	
Glass microroughness			X
Reflectivity		X	X
Reflectivity before and after weathering test			X
Reflectivity before and after Salt and fog test			X
Coating adhesion test		X	X
Sealing test		X	

Table 9.1: Summary of the qualification tests performed on the MAGIC II mirrors produced via cold glass slumping.

PSF spot size and curvature radius

For the PSF and radius of curvature measurements, the mirror was placed at a distance of about 35 m (the assumed radius of curvature of the mirror) and illuminated with a point light source. The point-like light source has been simulated by a laser diode with a microscope objective and a pin-hole in front. The distance between the mirror and the point source is equal to the nominal curvature radius (or twice the focal length) of the mirror itself, in such a way a point image is reflected again into a point image. A screen is placed close to the diode, at the same distance to the mirror. The distance from the mirror and the diode was adjusted searching for the best image position. The reflected spot was imaged with a 16 bit CCD camera and used for the PSF evaluation test. Figure 9.3(a) shows the layout of the optical bench described.
The focusing quality of each mirrors has been evaluated measuring on the focal plane the radius containing the 90% of the reflected light, a typical PSF is shown in Figure 9.3(b) having a value of about $r_{90} = 12.5\,mm = 0.7\,mrad$.
Moreover, the shape accuracy of some panels has been verified also mapping the surface though a CMM system. A comparison with the shape of the mould is pre-

sented in Figure 9.3(d) and 9.3(e). The replication process typically introduces a worsening in the shape's accuracy of about a factor 3 in P-V and rms.

PSF after thermal cycling

The measurements of the PSF of the prototype mirrors and the radius of curvature measurements have been performed before and after 5 thermal cycles. These tests were aimed at the verification of the maintenance of the optical performance of the mirror in the survival condition. Each thermal cycle has been performed passing quickly from 20°C to -20°C (plateau of 12 hours) and then from -20°C to 60°C (plateau of 4 hours). After each cycle the radius of curvature and the angular resolution have been measured showing that no changes occurred with respect to the starting parameter before thermal cycling.

Glass microroughness

About microroughness of the glass, profiles taken with a WYKO TOPO-2D interferometer system (see § 4.2) have been taken on a glass sample used for prototyping. Results are shown in Figure 9.4 (red lines) together with a comparison of the surface of the aluminum mirrors used for MAGIC I (blue line). As expected glass roughness is an order of magnitude less than Aluminum case, the latter being affected by the typical grooves structure due to the diamond milling.

Reflectivity before and after weathering test

The reflectivity of 3 samples with dimension 200×200 mm^2 have been measured before and after accelerated aging test by means of IRIS 908RS2 portable instrument. The accelerated aging test (or weathering test) lasted 42 days with continuous variation of temperature profile, relative humidity profile and ultraviolet radiation power. The light power irradiating the samples had been switched during the test between the following values:
- 2.2 mW/cm^2 with the lightening of 5 lamps at distance of 65 cm;
- 4.4 mW/cm^2 with the lightening of 10 lamps at distance of 65 cm.

The reflectivity measurements reported that the reflectivity of the mirrors is not significantly affected by the weathering conditions (less than 1%).

Reflectivity before and after salt-fog test

In order to assess the corrosion resistance of the mirror coating, a salt-fog test have been performed on some representative samples. Salt-fog test produces an accelerated corrosive attack in order to predict the coating suitability in use as a protective finish on corrosive environments. The salt-fog test has been performed with an atomized fog of water having a high salt content (higher than 5%) for the duration of 24 hours. Even if there is no clear correlation between 24 hours

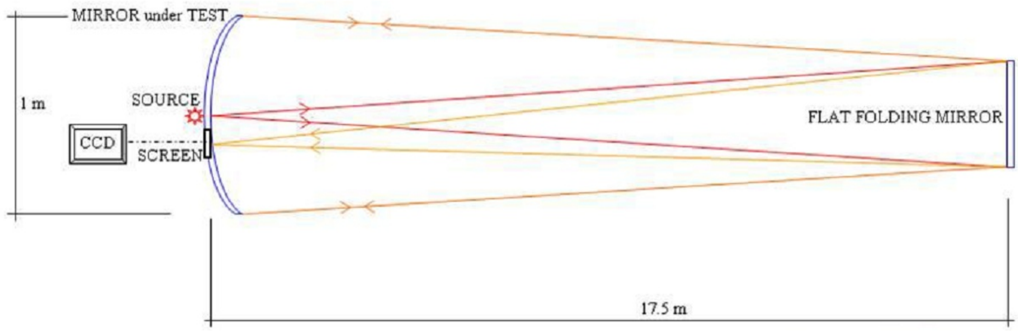

(a) Layout of the optical bench used for the measurement of the curvature radius and of the PSF; it has been used a flat folding mirror for achieving the 35 m distance from mirror and light source.

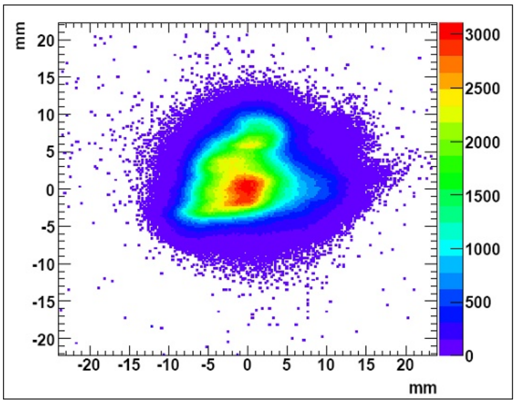

(b) Typical PSF spot of a cold glass slumped mirror panel. Credits: MPI Munich.

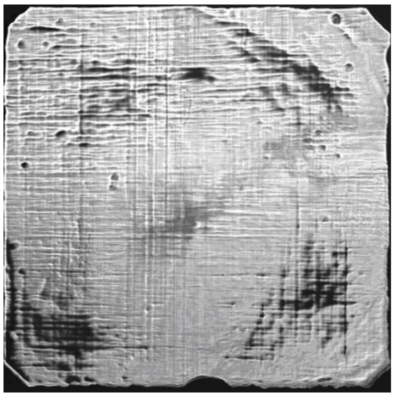

(c) Mirror panel from the focal position fully illuminated by a point-like source. Credits: Media Lario Technologies.

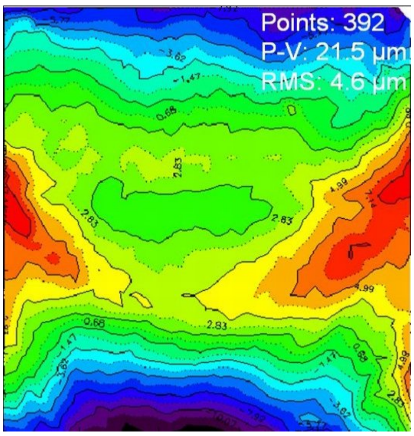

(d) Surface map of the mould. Measure obtained with a CMM system.

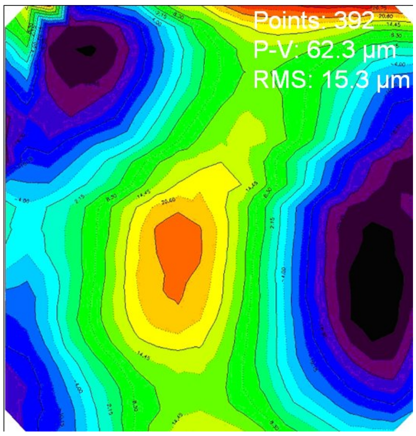

(e) Surface map of a typical panel of MAGIC II. Measure obtained with a CMM system.

Figure 9.3: Measurements of a glass mirror.

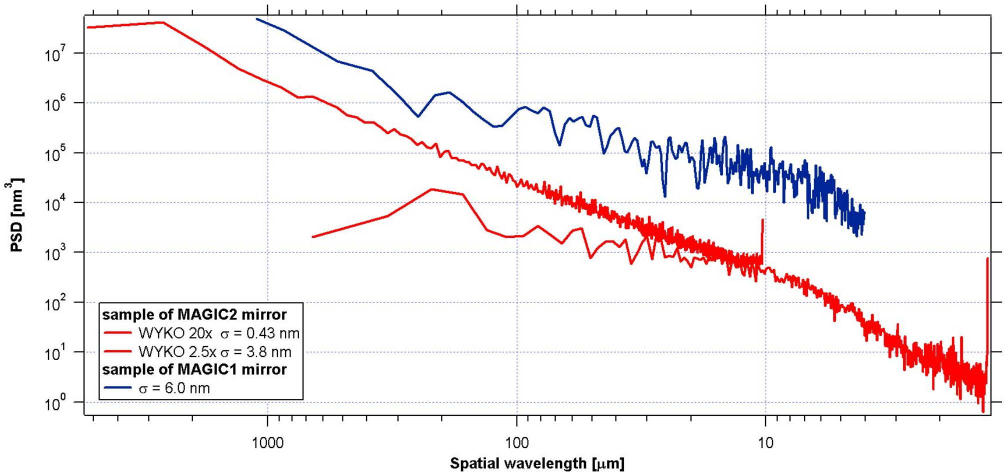

Figure 9.4: Glass microrougness PSD in comparison with the MAGIC I mirror one obtained with the WYKO TOPO-2D microscope.

of exposure with a 5% solution to a long period of exposure in an actual corrosive atmosphere, the test has been performed without showing signs of corrosion on the samples. Also the reflectivity of the coating has not been affected by the salt-fog test as measured with the IRIS 908RS2 portable instrument.

Coating adhesion test

The adhesion of the coating has been checked by a peel-off test performed both on samples and on prototype mirror. The processes of aluminization and protective quartz layer deposition are performed under high vacuum (about 10^{-6} mbar) in a dedicated chamber via physical vapor deposition; the reflecting surface is cleaned through ion etching before the deposition. Pressure sensitive tape has been applied and removed over different areas in the coating. The areas have been subsequently inspected for removal of coating from the substrate giving no indication of detachments. Coating adhesion tests have been performed also after weathering and salt-fog tests performed on representative samples without giving indication of detachment of the coating.

Sealing tightness test

For pressure exchange between sandwich mirror interior and external environment, required by the sealing tightness test, a venting hole has been provided on one side of some prototype mirrors. Sealing tightness of prototype mirror has been tested by means of a vacuum pump. The internal pressure has been reduced from ambient to 0.2 bar and the vacuum circuit has been therefore closed. No leakage has been detected within 15 minutes. As additional test, some mirror prototypes have been dipped completely into water for the duration of 24 hours.

The weight of the mirrors before and after the test was exactly the same giving indication that no penetration of water inside the sandwich structure occurred.

Chapter 10

Development of glass mirror panels with foam core for CTA

Production techniques that foresee the optical machining of each mirror panel, difficultly meet the requirements in particular in terms of costs and production schedule. Indeed, the most promising technologies are those that foresee the accurate replication of a precise mould. This is supported by [62]:

> [...] The design goal for the mirrors is to develop a low-cost, light-weight, robust ad reliable mirrors of $1-2$ m^2 in size with adequate reflectance and focusing qualities and demanding very little maintenance. Currently IACTs mostly use polished glass or diamond-milled aluminum mirrors, both requiring cost, time and labor intensive machining. [...]

and by [63]:

> [...] Mirror facets for CTA are tentatively assumed to have hexagonal shape of 1 m^2 to 2.5 m^2 size. Large mirror facets minimize the number of facets on a dish and the number of support points and alignment elements required. On the other hand, in particular for Davies-Cotton optics the optical performances worsen as mirror facets become larger. Also, the choice of manufacturing technologies becomes rather limited. For these reasons, the current baseline is to use hexagonal mirrors of 1.2 m (flat-to-flat) size. Performance criteria for facets are equivalent to those for current instruments and include the spot size, the reflectance and requirements on the long-term durability. The reflected light should largely be contained in a 1 mrad diameter area, the reflectance in the 300 nm to 600 nm range

must exceed 80%, and facets must be robust against aging when exposed to the environment for several years. Spherical facets are in most cases a sufficiently good approximation. [...]

For the reasons above mentioned, one of the most promising method is the cold glass slumping approach described in § 9.1 and successfully adopted for the production of the mirrors for MAGIC II as reported in § 9.2.
However, this method requires some further development in order to fully satisfy the requirement of CTA. Taking advantage of the experience done with MAGIC II, we have recently started a development roadmap aimed to:

- improve the replication accuracy in terms of radius of curvature and shape's deviation from the mould;
- improve the repeatability of the optical quality exhibited by each panel;
- lower the final cost of the panel.

The way we are pursuing to reach these goals can be summarized in the following main points:

- use of thinner glass sheets translate in a more flexibility of the optical surface. This permits an ease bend of the glass and hence a more detailed copy of the mould, in particular for the medium spatial frequencies band;
- replacing the honeycomb core with a stiffer structure can strongly reduce the spring-back effect to which the panel is subjected. This is especially true if the core part of the panel is pre-processed to accommodate the curvature of the mould;
- use of cheaper materials, in particular concerning the core part of the panel and the epoxy glue used to assemble together the sandwich;
- reduce the production's steps where possible, especially if they are critical and/or manpower consuming such as the sealing of edges.

10.1 Design of an hexagonal mirror for the MST

In parallel to practical activities described in other sections, we have performed some FEA to design a proper mechanical structure for a mirror panel for the MST. We have investigated its behavior with different loads cases, in particular for operative and survival conditions [64].
Operative condition is defined when the loads acting on the panel are: gravity (any orientation), wind pressure at 50 km/h, wind pressure generated by telescope movement and push from the active mirror control system. In such loads

condition, the stiffness of the panel should be high enough so that the mechanical deformations are kept as low as possible and do not affect the optical properties of the mirror.
Survival condition is defined when the loads acting on the panel are: gravity (any orientation), wind pressure at 180 km/h and snow weight. In such loads condition, the stiffness of the panel should be adequate to avoid breaks.
The analysis have been performed with the software ANSYS. It has been modeled a regular hexagon with dimension of 1.2 m face-to-face; the total area is about 1.25 m^2. The panel has one concave side corresponding to the optical surface, with a radius of curvature of 32000 mm; the other side is flat. The sandwich is composed as follow:

- glass sheet;
- foam core;
- glass sheet;

the glue has been added as extra weight. The panel is supported by three fixed points located at 2/3 of the inner radius, along the apothem. Figure 10.1 shows the model generated.

Figure 10.1: Model adopted with ANSYS to conduct the FEA.

10.1.1 Loads determination

During standard operation conditions, the panel is subjected to several forces. Each force generates deformations on the panel itself, and the panel should be stiff enough to counteract those effects. For design purpose we consider the worst situation in which the panel is placed parallel to the ground up-side and each loads act normally to the optical surface. Moreover, we have adopted more severe wind loads as reported in the following. The sum of the loads is passed to the three fixation points. Different loads are considered:

- **gravity load**: as stated before the gravity force will act on the whole surface of the panel. The panel is supported by three circular pads of 40 mm in radius;
- **wind load**: the wind acts as a kinetic pressure P_{wind} over the panel surface according to
  $$P_{wind} \approx \frac{v^2}{2} \cdot \rho$$
  where v is the wind speed and ρ is the air density (varying with altitude). ρ has been kept to its nominal value, i.e. the worst condition. We consider as upper limit for operative condition
  $$v_{wind,op} = 65\ km/h \Rightarrow P_{wind,op} \cong 0.2\ kPa$$
  Whereas, the upper limit in case of violent wind storm or hurricane is
  $$v_{wind,surv} = 200\ km/h \Rightarrow P_{wind,surv} \cong 1.9\ kPa$$
- **actuators push**: each panel has two actuators pushing on its back side during the (re-)alignment procedure. Each actuator pushes with a force of about 200 N over the interface pad (80 mm diameter). Thus, the total pressure applied on each pad is $P_{act} = 40\ kPa$. This pressure is considered as an additional pressure and will be later on added to the stress developed on the fixation points;
- **telescope movement**: the rapid repositioning of the telescope in case of e.g. GRB alert is considered. The speed can be up to 200 $°/min$. Hence, the peripheral panels suffer a linear velocity of about 1 $km/h \ll v_{wind,op}$. This load can be neglected;
- **snow load**: since the telescope is not protected by any dome, snow can deposits and accumulate on the reflector. We consider as upper limit a layer of snow of 30 cm. Since, the density of the snow is about 30% of the density of water, over an area of 1 m^2 are deposited about 90 kg, i.e. $P_{snow} = 0.9\ kPa$.

10.1.2 Panel in operative condition

About hundred configurations have been investigated varying:

- glass sheet material: BOROFLOAT® 33 from Schott and Microfloat™ from Pilkington;
- glass sheet thickness: $0.7 - 1.1 - 1.75 - 2$ mm and $1.2 - 1.4 - 1.5 - 1.7$ mm, respectively for BOROFLOAT® 33 and Microfloat™;
- core material: F-type and T4-type Foamglas® and Earthstone®;
- core thickness: $30 - 40 - 50 - 60$ mm.

An initial selection has been done using the following acceptance criteria: a) maximum weight $\leq 35\ kg/panel$ and b) maximum slope P-V error $\leq 0.5\ mrad$. Since many configurations were compliant, we decided to add more acceptance criteria and to tighten the above ones: a) maximum weight $\leq 20\ kg/panel$ and b) maximum slope P-V error $\leq 0.3\ mrad$. The added criteria are: c) for overall cost reasons (in case of mirrors production) we discarded the BOROFLOAT® 33 and d) from practical experiments the F-type Foamglas® seems to be the better core material.
In this way we can restrict the detailed study to the nine configurations reported in Table 10.1.

Conf. ID	**Glass thickness** [mm]	**Core thickness** [mm]	**Areal density** [kg/m^2]	**Slope P-V** [mrad]	**Surface P-V** [μm]	**Total stress into core** [MPa]	**Total stress on glass** [MPa]
1	1.2	30	10.25	0.163	66.8	0.155	2.87
2	1.2	40	11.89	0.092	37.9	0.133	2.06
3	1.4	30	11.24	0.146	60.2	0.150	2.66
4	1.5	30	11.75	0.139	57.6	0.148	2.58
5	1.2	50	13.54	0.063	25.3	0.122	1.62
6	1.4	40	12.89	0.088	34.5	0.130	1.95
7	1.7	30	12.74	0.134	53.2	0.145	2.51
8	1.2	60	15.20	0.047	18.6	0.115	1.41
9	1.4	50	14.54	0.061	23.2	0.119	1.63

Table 10.1: Configurations resulting after the application of the selection criteria.

The best trade-off configuration is the # 2, composed by glass sheets 1.2 mm thick and a core of 40 mm thick. This configuration provides very good values in terms of panel's weight, slope P-V and maximum stress developed on the core. Figure 10.2 shows the results from FEA performed on the configuration # 2. However, three other configurations can be considered noticeable and worth to be further investigated. In particular, we refer to configuration # 5 as the second choice, the # 8 because it shows the better slope P-V and the minimum stress and the # 7 since it has the thicker glass sheets (i.e. the more robust optical surface).

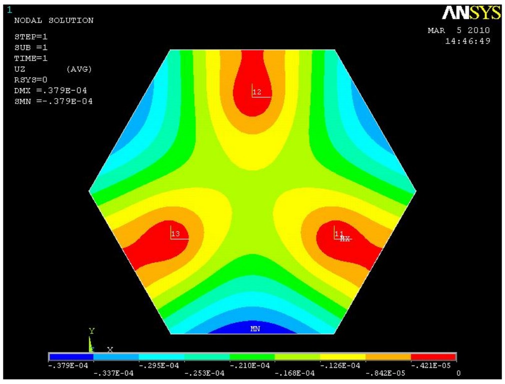

(a) Displacement on the optical surface, surface P-V.

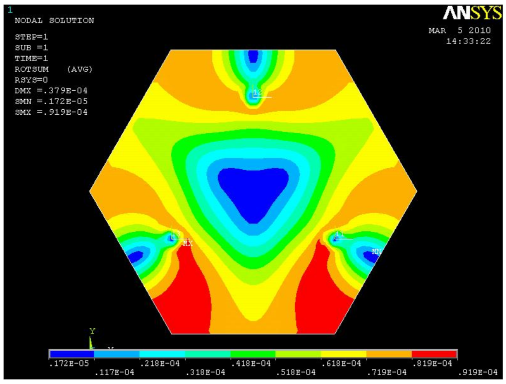

(b) Sum of the slopes on the optical surface, slope P-V.

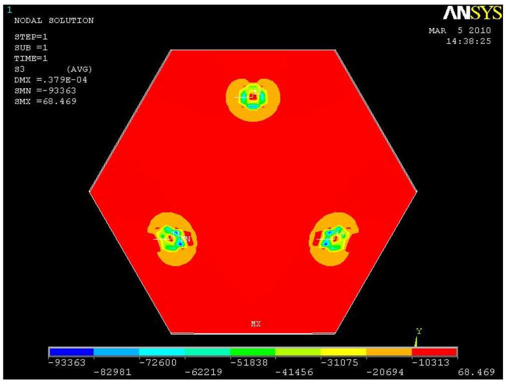

(c) 3rd principal stress developed on the foam core, maximum stress.

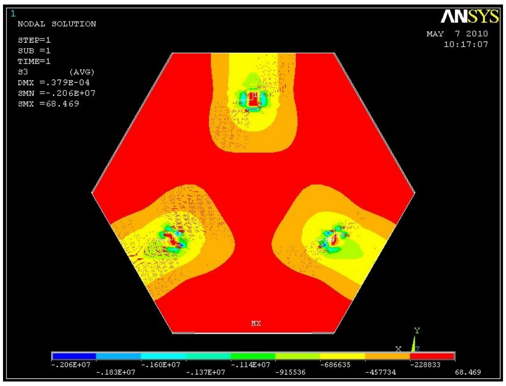

(d) 3rd principal stress developed on the back glass sheet, maximum stress.

Figure 10.2: Results from the FEA made on the configuration # 2 in operative condition.

10.1.3 Panel in survival condition

On the four selected configurations have been investigated also the behavior in extreme conditions. As described before, this condition is that where the panel must survive against strong atmospheric turbulence:

- gravity load;
- wind load up to 200 km/h, equivalent to 1.9 kPa;
- 30 cm of snow load, equivalent to 0.9 kPa

Under these conditions the optical performances of the panel are not of interest, while the stress suffered by the various materials which compose the panel itself must not exceed their Yield strength limit:

- for glass: 100 MPa;

- for F-type Foamglas®: 1.6 MPa

Table 10.2 shows the maximum values of the stresses developed on the foam and on the glass sheets. The glass sheets do not experience problems of survival since the maximum stress developed is well below the Yields strength of 100 MPa. Opposite situation occurs on the foam, where in some configurations it is approached the Yields strength of 1.6 MPa. Even if all the values obtained are below that limit, it is important to provide a good margin of safety. In fact, the value of 1.6 MPa already takes a factor two of safety.
Hence, the value of stress developed on the foam becomes the most important parameter to be evaluated. However, we should also notice that these conditions are very extreme and unusual and the site for CTA is not yet chosen, but this does not alter the nature of being even more violent.

Conf. ID	**Glass thickness** [mm]	**Core thickness** [mm]	**Areal density** [kg/m^2]	**Total stress into core** [MPa]	**Total stress on glass** [MPa]
2	1.2	40	11.89	1.1	26.50
5	1.2	50	13.54	0.92	20.50
7	1.7	30	12.74	1.21	31.80
8	1.2	60	15.20	0.86	16.80

Table 10.2: Configurations selected for the detailed analysis in survival condition.

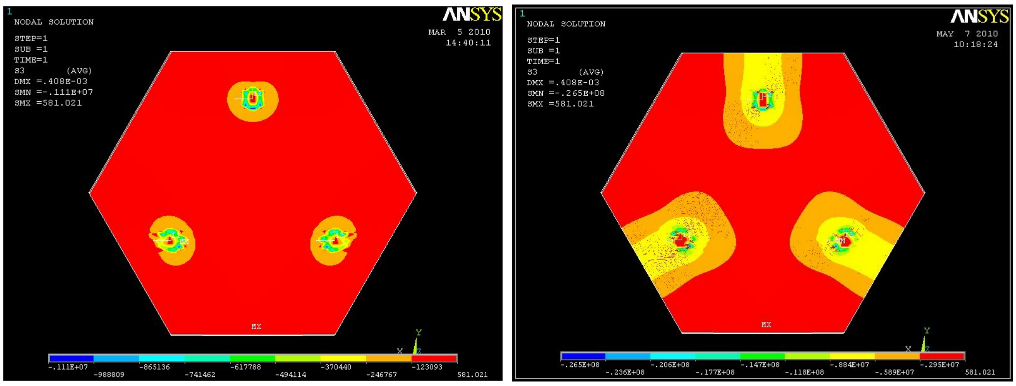

(a) Principal stress developed on the foam core, maximum stress.

(b) Principal stress developed on the back glass sheet, maximum stress.

Figure 10.3: Results from the FEA made on the configuration # 2 in survival condition.

10.1.4 Fixation points layout

A further investigation concerns the location of the fixation points, i.e. where the panel will be anchored to the telescope's dish and/or actuators. Figure 10.4 shows the six different condition simulated, in each layout there are 3 fixation points positioned on the vertexes of an equilateral triangle. The fixations are dishes of 40 mm in radius. The layouts are: a) 2/3 of the inner radius along the apothem, b) close to the edges, c) 2/3 of the inner radius along the diagonal, d) close to the corners. There are two other layouts with the dishes enlarged to 50 mm in radius: e) 2/3 of the inner radius along the apothem and f) close to the corners. In particular, placing the fixations as close as possible to the corners provides the better positioning accuracy of the mirror's alignment system.

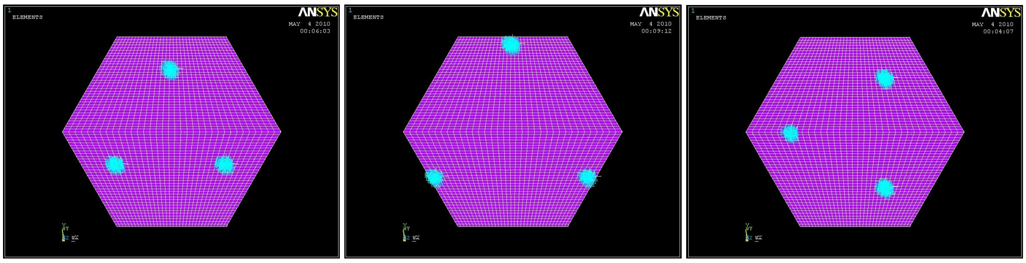

(a) 2/3 of the inner radius along the apothem, 40 mm. (b) Close to the edges, 40 mm. (c) 2/3 of the inner radius along the diagonal, 40 mm.

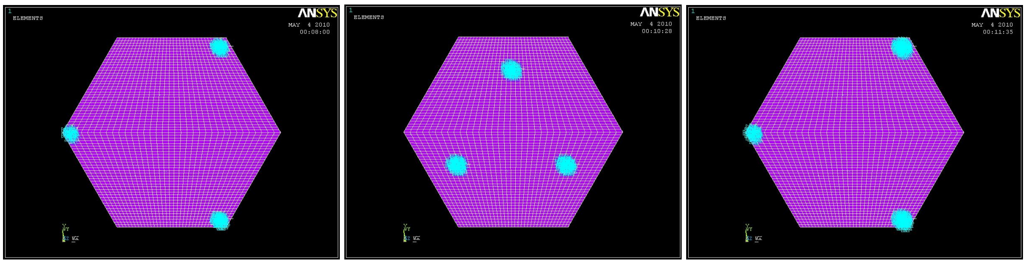

(d) Close to the corners, 40 mm. (e) 2/3 of the inner radius along the apothem, 50 mm. (f) Close to the corners, 50 mm.

Figure 10.4: Different layouts investigated for the fixation points.

The following Table 10.3 shows the values obtained for the four panel's configurations selected in the previous section, i.e. #2, #5, #7 and #8. These layouts have been studied both in operative and survival conditions. We report the values of the slope P-V, surface P-V, the maximum stress on the foam and on the glass.

Configuration ID		**Condition**	**Parameters**	**Fixation layouts**					
				a)	**b)**	**c)**	**d)**	**e)**	**f)**
	#2	Operative	Slope P-V [mrad]	0.092	0.232	0.092	0.315	0.086	0.288
			Surface P-V [μm]	37.90	62.60	43.60	94.00	35.40	86.10
			Stress foam [MPa]	0.090	0.256	0.090	0.288	0.072	0.267
			Stress glass [MPa]	2.06	4.55	2.07	5.21	1.68	6.49
		Survival	Stress foam [MPa]	1.11	2.81	–	3.14	–	–
			Stress glass [MPa]	26.50	49.70	–	56.90	–	–
	#5	Operative	Slope P-V [mrad]	0.063	0.157	0.059	0.215	0.057	0.198
			Surface P-V [μm]	25.30	40.60	29.00	63.10	23.50	61.60
			Stress foam [MPa]	0.082	0.212	0.083	0.234	0.069	0.222
			Stress glass [MPa]	1.62	3.63	1.70	4.10	1.34	5.19
		Survival	Stress foam [MPa]	0.95	2.26	–	2.48	–	–
			Stress glass [MPa]	20.50	38.50	–	43.40	–	–
	#7	Operative	Slope P-V [mrad]	0.134	0.328	0.130	0.442	0.124	0.404
			Surface P-V [μm]	53.20	86.70	61.00	146.00	49.70	129.00
			Stress foam [MPa]	0.105	0.283	0.097	0.302	0.078	0.281
			Stress glass [MPa]	2.51	5.89	2.65	6.87	2.05	8.26
		Survival	Stress foam [MPa]	1.21	3.06	–	3.25	–	–
			Stress glass [MPa]	31.80	63.70	–	73.90	–	–
	#8	Operative	Slope P-V [mrad]	0.047	0.113	0.045	0.156	0.043	0.144
			Surface P-V [μm]	18.60	30.00	21.30	46.20	17.20	42.70
			Stress foam [MPa]	0.075	0.182	0.077	0.196	0.065	0.190
			Stress glass [MPa]	1.41	3.05	1.48	3.37	1.68	4.35
		Survival	Stress foam [MPa]	0.86	1.88	–	2.01	–	–
			Stress glass [MPa]	16.80	31.40	–	34.70	–	–

Table 10.3: Investigation of different fixation points layouts.

In operative condition, it can be noted that there is a slight improvement of the slope P-V accompanied by a slight worsening of stress if the fixation points are placed along the diagonal, configurations c) vs a). In any case, if the fixations are placed far away from the center there is a sharp worsening of all the parameters of at least a factor 2, configurations b) and d) vs a) and c). However, for the panel's configurations #2, #5 and #8 for every fixation's layout the mirror still meets the specs (in particular in term of slope P-V). The configuration #7 is the lesser stiff and does not fall into the specifications if are adopted the layouts b) and d).

In survival condition, the most important parameters to be checked are the stresses on the foam and on the glass. For all the panel's configurations #2, #5, #7 and #8 the only fixation's layout that guarantees the panel's survival is the a). In all the other cases, layouts b), c) and d), the stress developed into the foam exceeds the threshold of the Yields strength of the material.

Enlarging the surface of the fixations there is a slight improvement (about 5% to 10%) of all the parameters.

10.2 Mechanical characterization of glass foam

At this regard, we are exploring an innovative material: a foam fully made of recycled borosilicate glass. Foamglas® [65] is an all-glass closed-cell structure material composed of millions of completely sealed glass cells. It is produced by Pittsburg Corning for the construction industry. It shows a number of interesting characteristics that made it particularly attractive for application in Cherenkov mirrors. It comes in lightweight boards produced in several thicknesses, from 40 mm to 120 mm, and density ranging from 120 kg/m^3 to 165 kg/m^3, it is stiff and easy to work. Moreover, it is waterproof, stable in time with a low CTE of about 9 $\mu m/m \cdot K$. Last but not least, the cost was about tens of Euro per square meter. Table 10.4 summarizes the main mechanical properties of the Foamglas® as reported in its data sheet plus an additional foam material, Earthstone, still made in recycled glass.

The mirror as a whole must be stiff enough to prevent deformation of the optical surface during the observation such as to avoid performance deterioration. This condition is guaranteed in part by the sandwich structure and in part by the intrinsic rigidity of the materials. For this reason, one of the parameters to take into greater consideration during the panel design and FEA is the Young's modulus of the materials making up the sandwich. The two sheets of glass that form the upper and lower sides of the panel, although intrinsically very rigid, they are also very thin. Hence, it is important to know with some confidence the value of Young's modulus of the material which forms the central part of the panel, i.e. the foam glass.

The Young's modulus is a quantity that indicates the stiffness of an isotropic elastic material. It is defined as the ratio of the uniaxial stress over the uniaxial strain in the range of stress in which Hooke's law holds:

$$\sigma = E\epsilon$$

where σ is the tensile stress evaluated as the applied force P/A, E is the Young's modulus and ϵ is the strain evaluated as the differential deformation l/L. This can be experimentally determined from the slope, in the linear part, of a stress-strain curve created during tensile/compressive tests conducted on a sample of the material, see Figure 10.5. Moreover, evaluating the knee of the curve it is possible to deduce the Yield strength: the lowest stress that gives permanent deformation in a material. These can be evaluated through a number of experiments, we have performed two: a) measuring the compression of the material upon a certain applied load; b) evaluating the flexure of a rod upon a certain applied load.

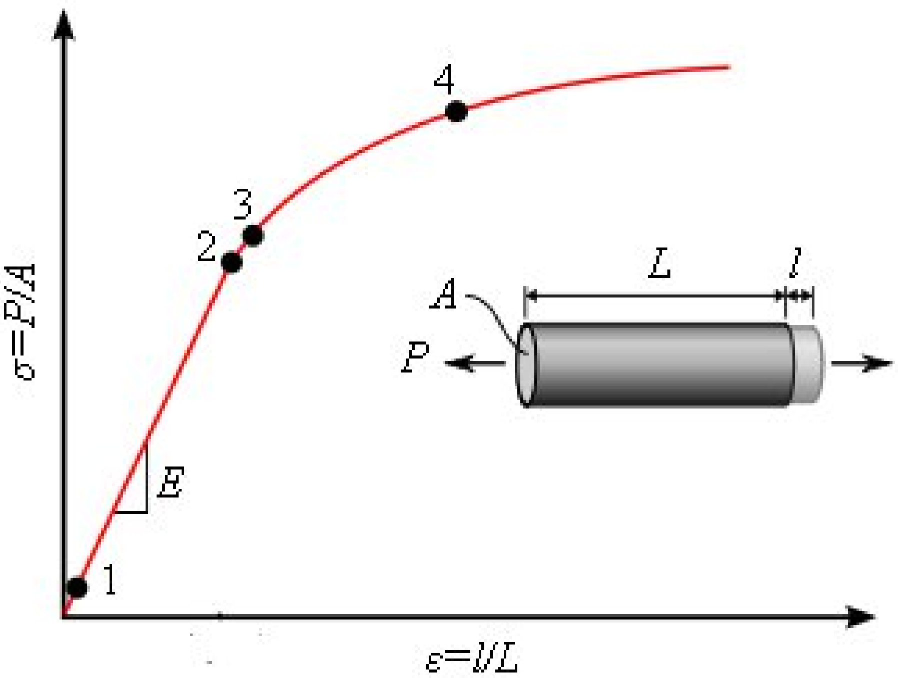

Figure 10.5: Typical stress-strain curve: points 1-2 delimit the elastic region, while points 3-4 delimit the plastic deformation region. After that, the rapture occurs for brittle materials such as glass or glass foam.

10.2.1 Compression of the rod

This test was carried out in close collaboration with the Polytechnic of Milan by using a 858 Mini Bionix® II equipment. This machine has two jaws that can compress/pull along the vertical axis of specimens attached to it. To make these measures were used cylindric specimens about 15 cm long and 3.5 cm in diameter. Three different foam materials were tested (see Figure 10.6(a)). These specimens, lying in the proper supports, were attached to the press and tested, see Figure 10.6(b), 10.6(c) and 10.6(d). The press keeps track of the force applied (in Newtons) and the corresponding squeezing in millimeters.
From each measurement it is therefore possible to generate the stress-strain graph from which derive the Young's modulus of each specimen. Figure 10.6(e) graphs the whole stress-strain curve for a sample of F-type Foamglas®. In the first part of the curve (red circle), where it remains linear, it is interpolated a line whose slope is the Young's modulus of the material. Also, going to consider the stress value at which the curve deviates (green circle) we have obtained the Yield strength of foam.

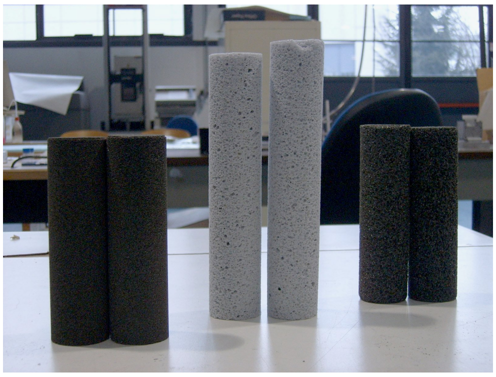

(a) Cylinders used to perform the compression test. From left to right: F-type Foamglas®, Earthstone and T4-type Foamglas®.

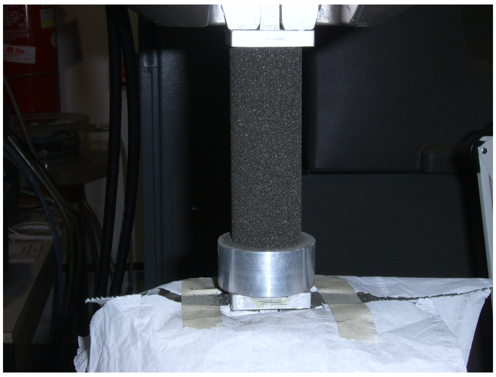

(b) F-type Foamglas® specimen during the test.

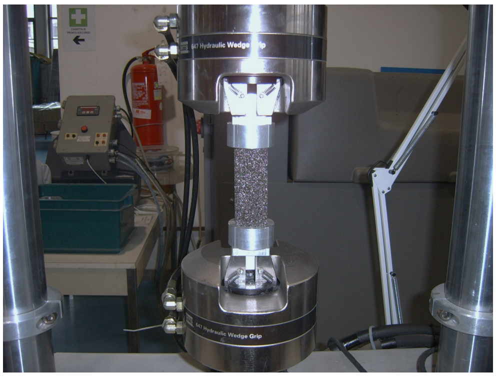

(c) T4-type Foamglas® specimen.

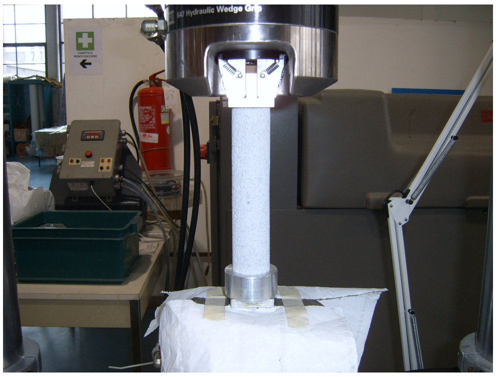

(d) Earthstone specimen.

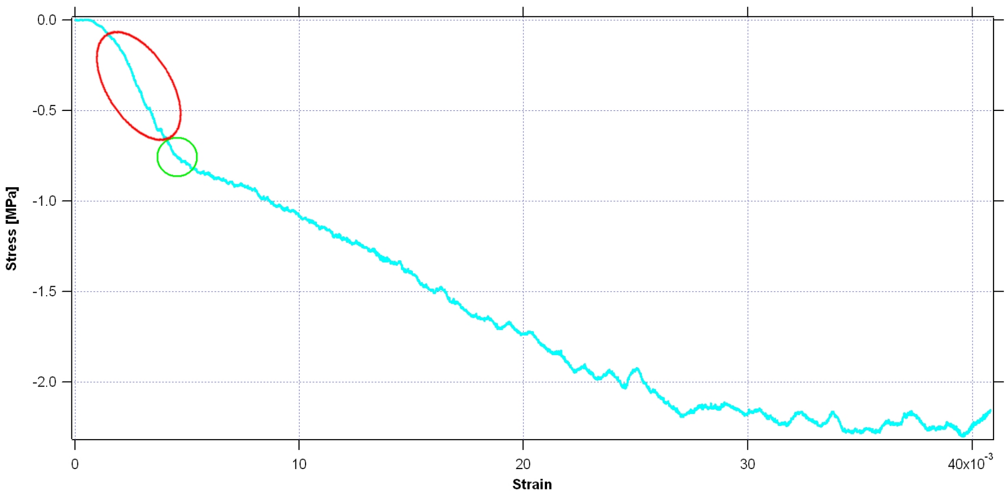

(e) Stress-strain curve obtained from a specimen of glass foam. The red circle indicates the linear region where the deformations are elastic; while the green circle region has been used to evaluate the Yield strength.

Figure 10.6: Setup of the compression test used to assess the Young's modulus.

10.2.2 Flexure of the rod

In this experiment was measured the deflection of a long and narrow rod fixed to an endpoint and loaded to the opposite one. The equation of the elastic line allows to link the measured sag of the beam to the value of the Young's modulus of the material as described below (see Figure 10.7(a)):

$$s = \frac{PL^3}{3EJ}$$

where s is the measured sag, P is the applied force, L is the lever arm of the rod, E is the Young's modulus and $J = (1/12)bh^3$ is the momentum of inertia of the rod (b and h are the width and thickness of the rod).

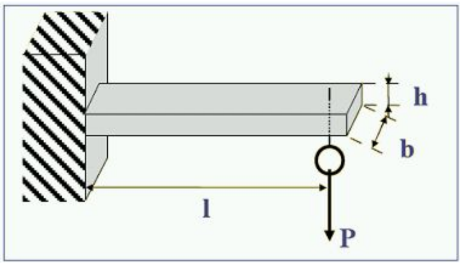

(a) Drawing describing the experiment.

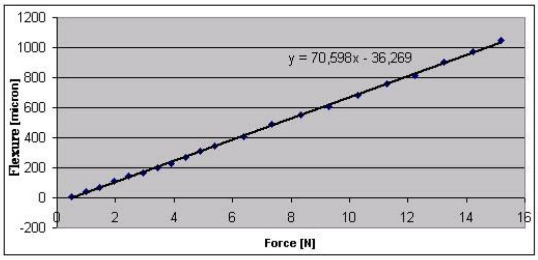

(b) Example of a curve obtained measuring the flexure of a rod.

Figure 10.7: The experiment of the flexion of a rod adopted to measure the Young's modulus.

The rod has been fixed on a hard surface through clamps that prevent displacements and rotations. The free endpoint of the rod has been loaded with increasing weight. For each weight added, the flexure of the rod has been recorded by means of a dial gauge. Similarly to the stress-strain graph obtained from the compression experiment, in this situation the graph plots the flexure versus the applied force. The slope of the line is proportional to the Young's modulus. Figure 10.7(b) shows an example of the measured data.

In total, both experiments have been performed on the three different types of foam evaluated. The data has been analyzed and the resulting values for the Young's modulus and the Yield strength are reported in brackets in Table 10.4. For reference, we report also the data from the datasheet, if available. A comparison with the Aluminum honeycomb adopted for MAGIC II is also reported.

		Foam materials		
Properties	Hex-cell honeycomb	Foamglas® T4-type	Foamglas® F-type	Earthstone
Young's modulus [MPa]	1280	(200)-800	(800)-1500	(650)-n.a.
Yield strength [MPa]	3.5	(0.54)-0.63	(3.3)-1.61	(1.7)-n.a.
Density [g/cm^3]	0.072	0.12	0.165	(0.2)-n.a.
CTE @ 25℃ [$\mu m/(m \cdot K)$]	24	9	9	n.a.
Thermal conduct. [$W/(m \cdot K)$]	117	0.04	0.05	n.a.
Specific heat capacity [$J/(kg \cdot K)$]	904	840	840	n.a.
Machinability	good	easy	easy	easy
Material's sellers	Many	Pittsburg Corning	Pittsburg Corning	Earthstone
Scalability to ø > 1.5 m	Difficult	Sectors brazing	Sectors brazing	Sectors brazing
Cost [€/m^2]	> 100	< 30	< 30	n.a.

Table 10.4: Properties of the three foam materials investigated for the core part of the panel. The values reported in brackets have been directly measured by the author.

10.3 Investigation for new glues

The adhesive is an important structural component of these reflectors. It is used to join together the two sheets of glass with the core. It must ensure the bonding between the porous/irregular surface of the foam (or honeycomb or whatever) and the smooth surface of the glass. The adhesive must also preserve the shape imparted to the front glass during the cold slumping phase through a low shrinkage behavior. Hence, both the technique adopted for gluing and the glue itself are very important.
From the practical point of view, the glue should be easy to handle and be prepared, this facilitates and speeds up the assembly of the panel. It should not introduce excessive stresses on the surface of foam to avoid to weaken the cellular structure of the surface of the foam.
From the optical point of view, it is preferable that the glue polymerizes at room temperature, it has the lowest possible shrinkage and does not introduce stress on the surface of the glass sheet so as not to deform its optical shape. It should also show a low coefficient of thermal expansion and exhibit a limited aging upon ultraviolet radiation exposure (daily solar exposure).

EA Hysol 9309.3NA from Henkel Corporation Aerospace Group is commonly used in aeronautics and it is specifically designed to bond glass with Aluminum honeycomb. It has been used for the production of the 100 mirrors for MAGIC II; it shows the characteristics suitable for this application. In the following, the Hysol will be used as reference; it is the only glue used, till now, to assemble prototype mirrors with foam core.
Other adhesives have been looked for; in particular to deliver suitable performances for our application. One additional point taken into account on the survey was the cost impact. In total, three new adhesives have been investigated, namely: P-82F from Bacon Industries, Ocean EpoxyCrystal and Uretan NG from Cores. Tests were performed on bonding strength and aging to UV radiation.

10.3.1 Bonding strength experiment

To evaluate the bonding strength exercised by the glue between the sheet of glass and the core of the panel, we have performed a dedicated experiment. The experiment has been conducted in close collaboration with the Polytechnic of Milan by using a 858 Mini Bionix® II equipment. The specimens used model, albeit small, the sandwich structure of a real panel, i.e. they are composed by:

- front glass plate; 5×5 cm^2, 3 mm thick;
- a very thin layer of glue, about 0.3 mm thick;
  - F-type Foamglas® core; 5×5×4 cm^3

    – or alternatively –

  - Aluminum honeycomb; 5×5×2 cm^3;
- a very thin layer of glue, about 0.3 mm thick;
- back glass plate; 5×5 cm^2, 3 mm thick.

With the Foamglas® core will be possible to investigate the bonding strength of the overall sandwich in relation to the glue used, this is because we suspect that the brittle nature of the glass cells can suffer different behaviors with different glues. While, using the Aluminum honeycomb core will be directly evaluated the goodness of the adhesive itself, because of the strength of the honeycomb. Figure 10.8 shows some phases of the specimens preparation. The sides of each specimen were glued with the same quantity of glue. The amount used ensures a bonding layer of about 0.3 mm thick. The glue was dripped in the center of the surface of the foam, verifying the amount with an accurate balance. Then, the glass plate was carefully lowered and was applied a little pressure with the fingers so that the glue spreads out circularly and evenly up to cover the entire bonding surface. Finally, the glue in excess (if any) was removed. The specimens were cured in an oven at about 50℃ for about 2 days.

(a) Preparation and mixing of the part A and B of the glue.

(b) Dripping of the glue on the foam.

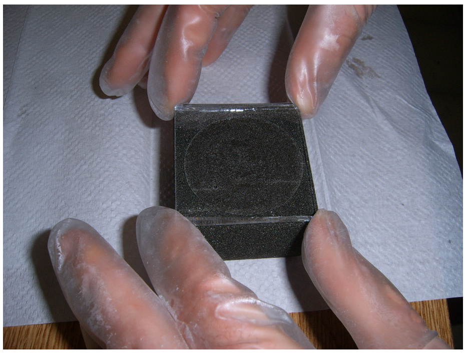

(c) Spread out of the glue through manual application of a little pressure.

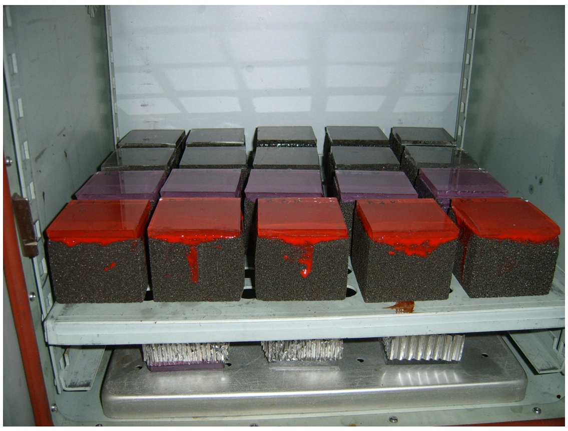

(d) Curing of the glue into an oven.

Figure 10.8: Main phases of the preparation of specimens for the bonding strength test.

In total, five samples were made using F-type Foamglas® for each type of glue plus one (for type of glue) in which the foam core has been replaced by the same Aluminum honeycomb structure used for the mirrors of MAGIC II. This allows us to have information both on the behavior of the sandwich (foam specimens) and of the glues (honeycomb specimens) as stated before. Ultimately, we have produced and tested a set of (see Figure 10.8(d)):
nr. 5 samples glass-Hysol-foam-Hysol-glass;
nr. 1 samples glass-Hysol-honeycomb-Hysol-glass;
nr. 5 samples glass-Bacon-foam-Bacon-glass;
nr. 1 samples glass-Bacon-honeycomb-Bacon-glass;
nr. 5 samples glass-Ocean-foam-Ocean-glass;
nr. 1 samples glass-Ocean-honeycomb-Ocean-glass;
nr. 5 samples glass-Uretan-foam-Uretan-glass;
nr. 1 samples glass-Uretan-honeycomb-Uretan-glass.

On both sides of the specimens were glued two Aluminum interfaces, 4×4 cm^2, comprising the fastening system to the traction machine. The equipment was programmed to exert an axial traction force. Each specimen was anchored to the machine, a tensile force was applied and has been measured and recorded the elongation which occurred. Evaluating the tensile strength at the rupture can be assessed the overall glass-core-glass system and/or the glue only (respectively, if the core breaks or if the core separates from the glass plate). An example of the experiment assembly is shown in Figure 10.9.

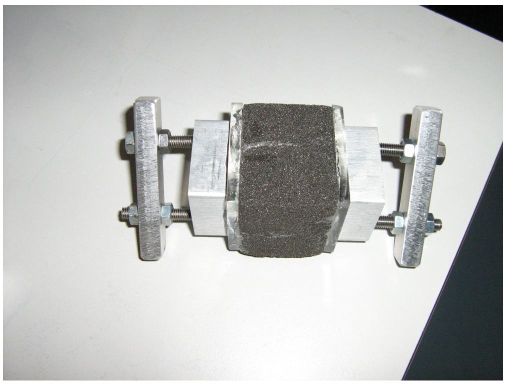

(a) Specimen with foam core and interfaces.

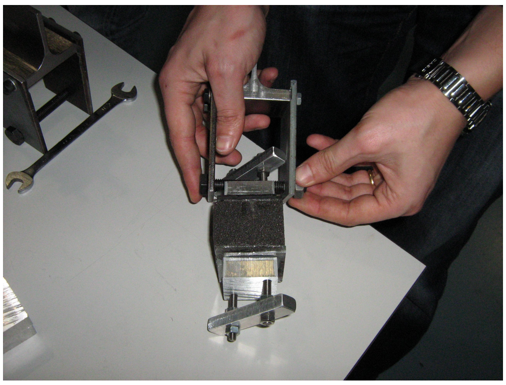

(b) Fastening system.

Figure 10.9: Some phases of bonding strength experiment.

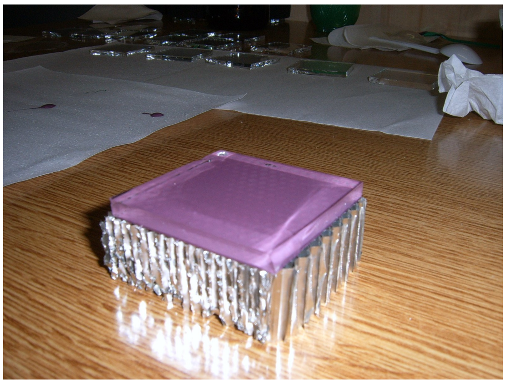

(a) Specimen with Aluminum honeycomb during its preparation.

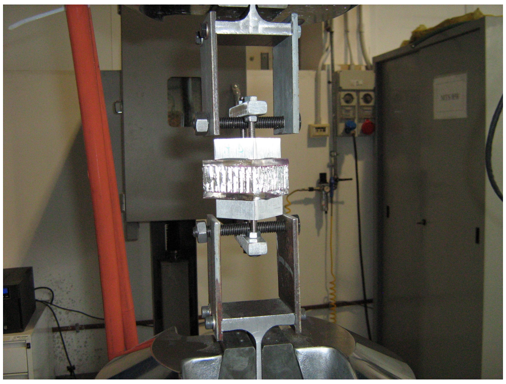

(b) Specimen anchored to the traction machine.

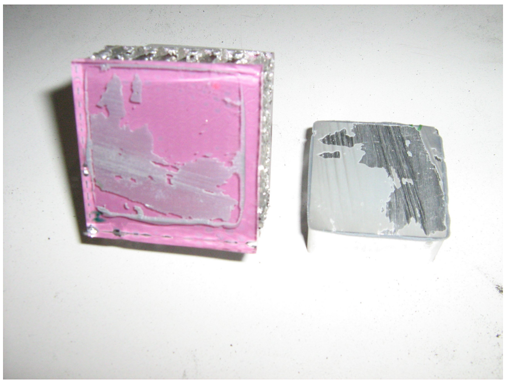

(c) Specimen glued with Hysol. To be noted the failure of the fastening interface.

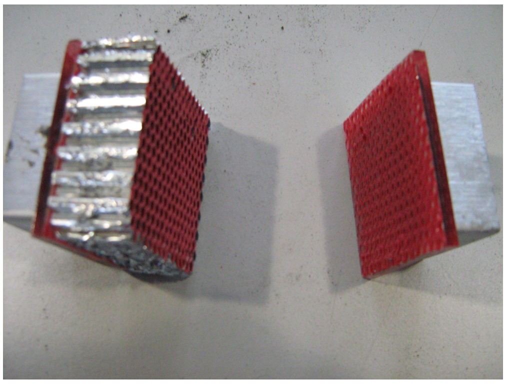

(d) Specimen glued with P-82F.

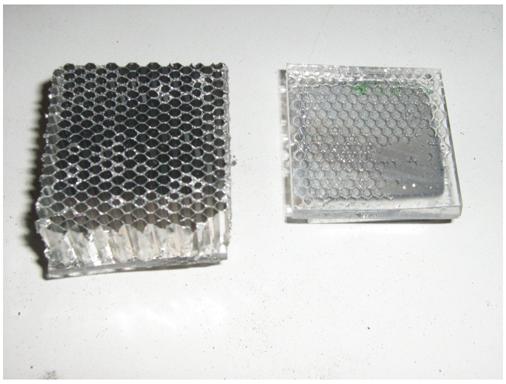

(e) Specimen glued with Ocean EpoxyCrystal.

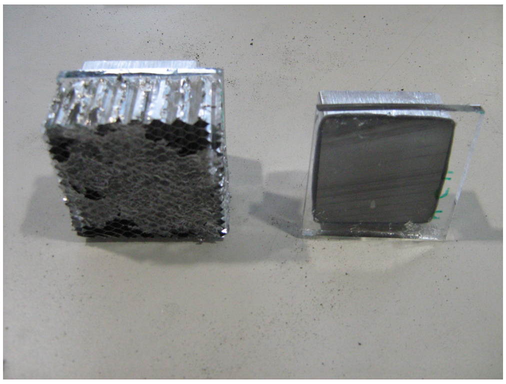

(f) Specimen glued with Uretan NG.

Figure 10.10: Results of the bonding strength experiment, specimens with Aluminum honeycomb.

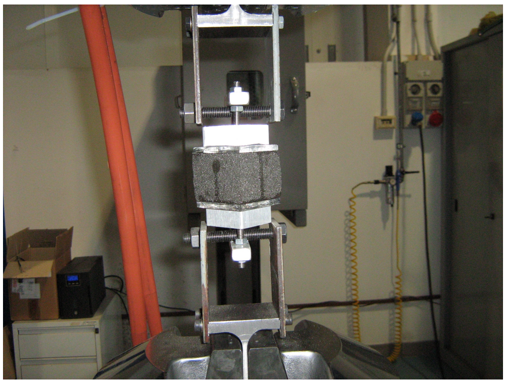

(a) Specimen anchored to the traction machine.

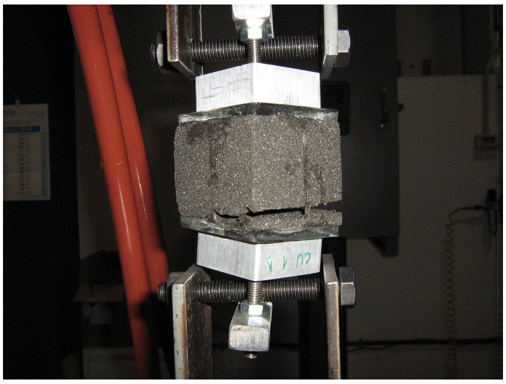

(b) Rupture of the core.

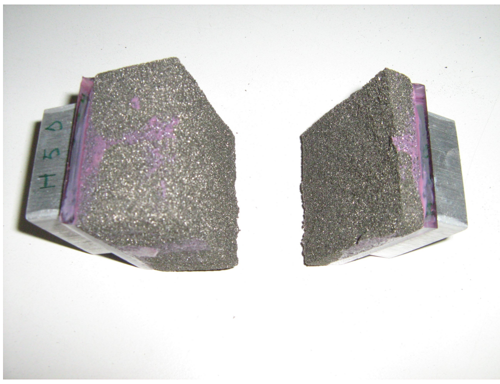

(c) Specimen glued with Hysol.

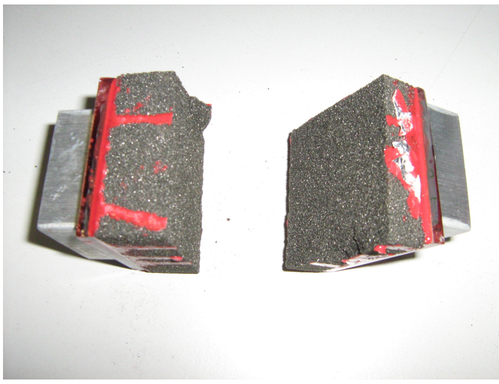

(d) Specimen glued with P-82F.

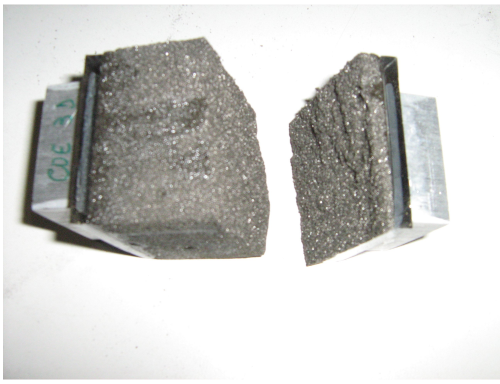

(e) Specimen glued with Ocean EpoxyCrystal.

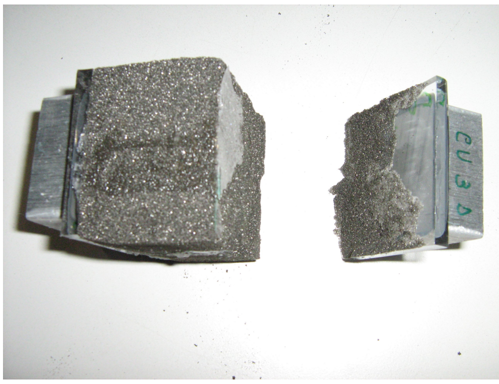

(f) Specimen glued with Uretan NG. To be noted the poor bonding strength of the glue with the foam.

Figure 10.11: Results of the bonding strength experiment, specimens with Foamglas®.

The tests performed on the specimens with honeycomb core gave us a direct insight on the goodness of the glues. The results are shown in Figure 10.10 and can be summarized as follow:

- Hysol: failure of the interfaces, excellent performance;
- P-82F: the layer of glue is perfectly divided into two thin layers, perfect bonding;
- Ocean EpoxyCrystal: half of the glue remained on the glass and half on the honeycomb, still good bonding;
- Uretan NG: very poor adherence, bad for this application.

While, for all the specimens having the F-type Foamglas® (see Figure 10.11), with the exception of Cores Uretan NG ones, has been noticed the rupture of the foam, which indicates a proper behavior of the bonding. The glue that reported the strongest bonding is the Hysol, but also the Ocean EpoxyCrystal showed very similar performances. The P-82F reveled to be of lesser quality, while the Uretan NG has been the worst.

10.3.2 Aging upon UV-A exposure

In addition to the bonding strength test, it was carried out also a preliminary test to check the aging produced by UV light irradiation. Some pieces were made by glass-glue-foam; the glue had a very long curing at room temperature. The specimens were exposed for more than 10 hours to an intense UV-A light source with power of about 40 mW/cm^2 (energy band: $300 - 600$ nm; energy peak: 370 nm).
We noticed a strong yellowing of the Hysol, a slight yellowing of the Ocean, a marked change in opacity and probably also of the polymerization state of the Uretan. No apparent changes occurred on the P-82F.

10.3.3 Comments on the glues

Hysol: purple mat, it shows a pot life at room temperature of about 30 minutes. It is a bi-component glue. It is very viscous before preparation, it should be mixed throughly and vigorously to blend the two parties, this could also incorporate air bubbles. After mixed, it remains fairly viscous. The applicability is not immediately easy, it must be performed by means of a spatula and it is not easy to obtain a thin and uniform layer. However, its color can help in qualitatively assess the goodness of the layer applied, but does not allow to inspect the presence of bubbles.
Hysol shows the best performance in terms of adhesion to the honeycomb and to the foam.

The curing can take place at room temperature, although the outer surface of the glue seems that it never hardens completely even after tens of days. We recommend to cure the glue in temperatures at about $70-80$°C for several hours.
This glue suffers a marked yellowing when exposed to UV-A radiation, therefore needs to be protected with a cover.
The product is very expensive, about 230 €/kg.

P82-F: bright red, it shows a pot life at room temperature of few minutes. It is a bi-component glue very dense and viscous (more than Hysol) prior to preparation. It is necessary to mix the two parts at a temperature of $70-80$°C and stir very vigorously with the risk of incorporating air bubbles. After mixed, it remains workable for a sufficient amount of time only if maintained at a temperature above 50°C, however, it remains very viscous. The application is more difficult than the Hysol (also in this case must be performed by means of a spatula), but it seems easier to obtain a uniform layer (the glue shows a kind of self-leveling behavior). Its color can help in qualitatively assess the goodness of the layer applied, but does not allow to inspect the presence of bubbles.
P82-F shows tolerable performance in terms of adhesion to the honeycomb and to the foam.
The curing must follow a precise thermal cycle consisting of two phases at increasing temperatures (above 100°C) to obtain the performances listed in the data sheet, in particular concerning the shrinkage. However, the curing can take place even at room temperature in about a week.
This glue does not seem to suffer any change in color or state of polymerization when exposed to UV-A radiation.
The product is very expensive, about 210 €/kg.

Ocean EpoxyCrystal: transparent color, it shows a pot life at room temperature over 60 minutes. It is a bi-component glue, low density and low viscosity. It can be treated simply by means of syringes, working at room temperature. It wets the bonding surface and spreads easily. The low viscosity makes ease the application in thin and uniform layer, the transparent color makes ease the inspection of air bubbles and evaluation of degasing timing. It can be applied very quickly through spray methods.
Ocean EpoxyCrystal is a glue that shows good performance in terms of adherence to the honeycomb; adherence to the foam is comparable to that shown by the Hysol.
The complete curing can take place at room temperature in about $2-3$ days or in few hours at about 50°C.
This glue seems to suffer only a slight yellowing when exposed to UV-A radiation.
The product is inexpensive, about 25 €/kg, a factor ten compared to the Hysol.

Uretan NG: transparent color, it shows a pot life at room temperature of only 10-15 minutes. It is a bi-component glue, the most difficult to mix and dose due to high viscosity. The mixing process encompasses many air bubbles, very evident through the transparent color. After a few minutes from the preparation it becomes difficult to spread out.
Uretan NG shows the worst performance in terms of adhesion to the honeycomb and to the foam. In particular, it seems to have a low adhesion to glass.
The complete curing can take place at room temperature in about $2-3$ days or in few hours at about 50°C.
This glue seems to suffer a net change of the state of polymerization when exposed to UV-A radiation, in fact it becomes whitish and opaque.
The product is inexpensive, around 20 €/kg, a factor ten compared to the Hysol.

	Epoxy Adhesives			
Properties	Hysol EA9309.3NA	Bacon Ind. P-82F	Cores Ocean EpoxyCrystal	Cores Uretan NG
Color	Purple	Red	Transparent	Transparent
Density [g/cm^3]	1.7	1.85	1.05	1.11
CTE @ 25°C [$\mu m/(m \cdot K)$]	56	25	n.a.	n.a.
Shrinkage	low	very low	low	low
Pot life at 25°C [min]	(30)35	(10) 60 @70 °C	(60)40	(10)60
Curing [hrs]	1 @ 82°C	3 @ 70°C + 16 @ 100°C	2 @ 50°C	2 @ 50°C
Tensile strength [MPa] with honeycomb with foam	(> 3.5) (0.7)	(1.7) (0.45)	(2.8) (0.65)	(0.22) (0.37)
Applicability	easy with spatula	difficult, high viscosity	very easy, spray possible	not easy
Aging upon intense UV-A exposure	strong yellowing	none	slight yellowing	change in polymerization
Cost [€/kg]	230	200	25	20

Table 10.5: Properties of the four epoxy glues investigated. Values in brackets are measured by the author.

Summarizing, Table 10.5 lists the main characteristics of the glues, some of them come from datasheet and some other come from practical experience.
For its already proven use in Cherenkov mirrors and to be extensively tested, the Hysol glue should be considered of reference and baseline. This sentence remains valid also in case of using the Foamglas® as core part of the panels.
However, the Ocean EpoxyCrystal has mechanical performances comparable to

those of the Hysol, less aging due to UV irradiation and an easier applicability. Moreover, it introduces some other interesting advantages (such as the low temperature needed for the curing) that makes it worthy of being further investigated. Last but not least, it allows a considerable cost saving.

10.4 Panel prototypes with foam core

In the present section are reported a number of results obtained from mirror panel prototypes realized by the author [66]. The prototypes have been realized exclusively using equipments available in INAF-OAB's labs, in particular the mould is coming from the mirrors production of MAGIC II. It has a squared tile shape of 1040 mm side, while the surface is a convex sphere of about 36300 mm radius of curvature. The measured figure P-V is of about 21 μm and the rms of 4.5 μm (see Figure 9.3(d)). Moreover, all the measurements (such as PSF spot size) and tests (such as thermal cycling) here reported have been performed using equipments installed in our labs.

10.4.1 Making of a prototype

The purpose of this activity is to optimize the technique of the cold glass slumping respect to the construction of mirrors with glass foam core. The prototypes realized have two thin glass skins made of BOROFLOAT® 33 and a core made of F-type Foamglas®. The glass sheets are 1.1 mm thick, while the core is 40 mm thick. The core has been machined to allocate the curvature of the mould. Figure 10.12 illustrates the different phases of the manufacturing.

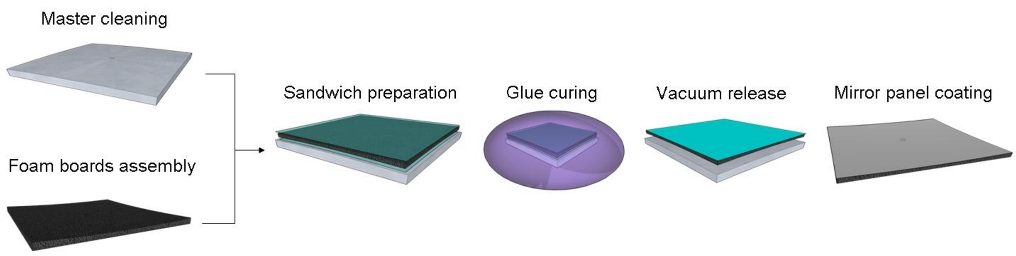

Figure 10.12: Cold glass slumping technique as modified to adopt the foam core.

The procedure for the realization of a prototype can be described as follow:

Phase 1: prepare the Foamglas® board and the core of the panel. Foam boards are flattened and assembled together on a glass sheet to form a solid body. This glass sheet will be the back plate of the panel (see Figure 10.13(a)).

Phase 2: machining of the core to match the curvature of the mould. This part has been done using an *ad hoc* equipment capable of milling the foam to the proper shape (see Figure 10.13(b)).

Phase 3: slumping of the front glass sheet and spread of the glue. It is done using a vacuum suction to make adhere the glass to the mould. The glue was spread using a proper tool (with knife edge) that permits to have a uniform thin layer of about 0.3 mm thick (see Figure 10.13(c)).

Phase 4: the core is bonded to the front glass sheet and the overall system is cured. The polymerization is obtained heating up the mould up to about 80°C for few hours (see Figure 10.13(d)).

We have realized a number of small prototypes. The panels are squares of 300 mm by side and are assembled using the Hysol adhesive. Later on, it has been realized also a larger prototype of 600 mm by side.

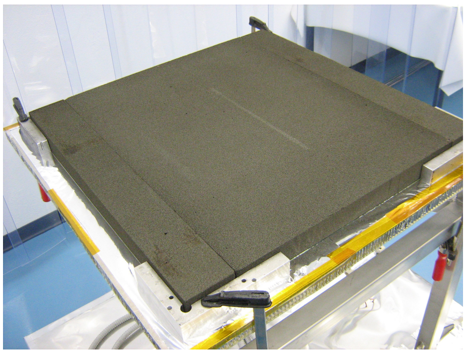

(a) Preparing the core, foam boards assembling.

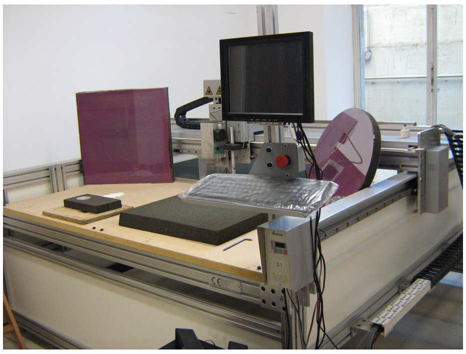

(b) Core machining.

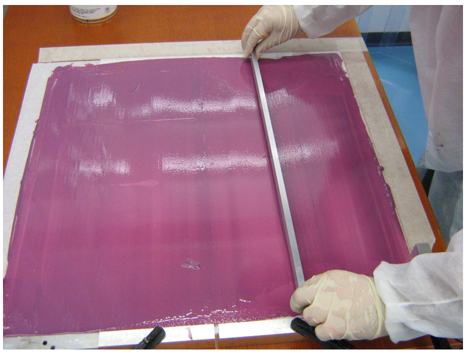

(c) Spreading out the Hysol glued.

(d) Curing of the glue.

Figure 10.13: Main phases of the realization of a prototype with F-type Foamglas® core.

10.4.2 Qualitative inspection

Figure 10.14(a) shows an aluminized small panel prototype. As visible, there is a clear effect on the edges coming from the replication process. In fact, to protect the soft surface of the mould from the deterioration that could arise from the process itself, we use a thin foil of a breathable material. This foil prevents the complete contact of glass edges with the mould's surface and hence, the shape of the glass sheet deviates (locally) from that of the mould. In Figure 10.14(b) is visible, projected on a building wall, the image of the Sun generated by the panel. The spot is round and well defined, this means that the edges do not affect in a significant way the focusing quality of the mirror.

Figure 10.14(c) shows the larger prototype till now realized, the 600×600 mm^2 panel after the vacuum release. The panel is not aluminized and the purple color comes from the Hysol glue. The panel has an areal density of about 12 kg/m^2, a value fully into specs for what required by the next generation of Cherenkov telescopes. Once again, in Figure 10.14(d) is visible the image of the Sun generated by the panel. The spot is round but less defined than the previous one, this means that the process needs to be refined going to larger dimensions.

(a) 300×300 mm^2 prototype, the surface is aluminized.

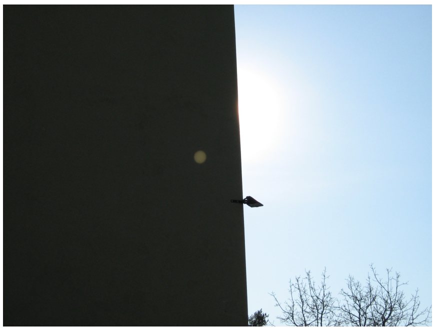

(b) Image of the Sun generated by the small prototype.

(c) 600×600 mm^2 prototype, the surface is not aluminized.

(d) Image of the Sun generated by the larger prototype.

Figure 10.14: Prototypes made with F-type Foamglas® core.

10.4.3 PSF spot size and curvature radius

Due to the observation technique adopted by the Cherenkov telescopes, the FWHM is not the best parameter to describe such mirrors. Since the major part of the light should be contained into a single pixel, it is more convenient to define a stricter parameter: the radius containing the 90% of the focused energy, in the following indicated as r_{90}.

The measurements have been done using the long horizontal optical bench as described at Page 162.

In Figure 10.15(a) is shown a typical focal spot generated by a 300 mm side prototype. The value for the r_{90} is of about 0.25 mrad, well below the requirements. However, the best focus position has been measured at about 32000 mm, a value quite less than what expected. This behavior was already noticed during the production of the mirrors for MAGIC II. In particular the mirrors show a radius typically shorter of about 800 mm. In this case the variation exceeds this amount. Indeed, several identical panels have been replicated from the same position onto the mould's surface, and we are confident that the error is due to a local deviation of the mould shape from the nominal one. In fact, the replication of a larger area of the mould minimizes this effect (see below).

Also for the 600 mm side panel we have measured the focal spot size as reported in Figure 10.15(b). As argued from the evaluation of the Sun's image, the r_{90} is worse and not yet fully in specs (but still very close). The value is of about 0.6 mrad. Nevertheless, masking the mirror so to measure just its central part the value drops to about 0.35 mrad. As claimed before, the best focus position is (as expected) slightly less than the mould's radius, it is at about 35800 mm.

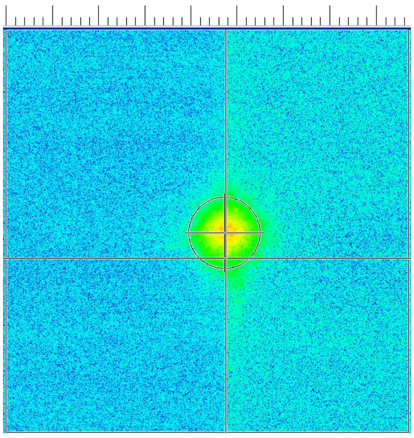

(a) 300×300 mm^2 prototype, best focus position at 32000 mm.

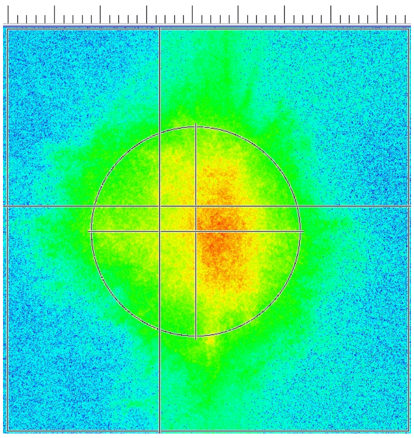

(b) 600×600 mm^2 prototype, best focus position at 35800 mm.

Figure 10.15: PSFs spot size for prototypes made with F-type Foamglas® core.

10.4.4 PSF after thermal cycling

In addition, panels have been tested also after undergoing thermal cycling. The adopted cycles were spanning from -20°C up to +60°C, each thermal cycle lasted several hours (see Figure 10.16(a)). The PSF spot size of a few mirrors, with dimensions of 300×300 mm^2, has been checked after the thermal cycle. This has been repeated for a number of times; the results have been compared to check degradations of the focusing quality of the mirrors (see Figure 10.16(b)). Till now the mirrors tested did not have shown any appreciable degradation of the r_{90}. However, this result must be carefully considered due to the very small dimensions of the prototypes tested. Nevertheless, it is an encouraging result that must be repeated on full scale panels since these kind of mirrors have to be intensively tested for survival.

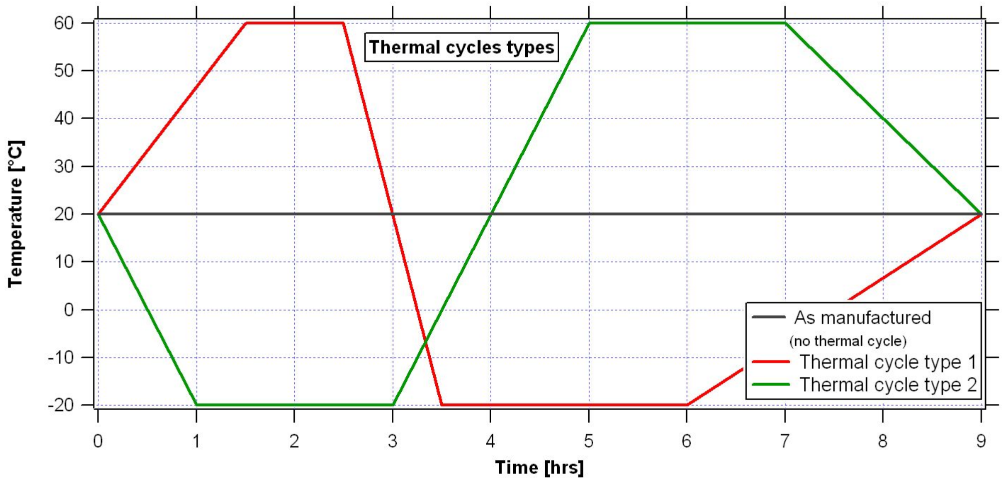

(a) Thermal cycles adopted.

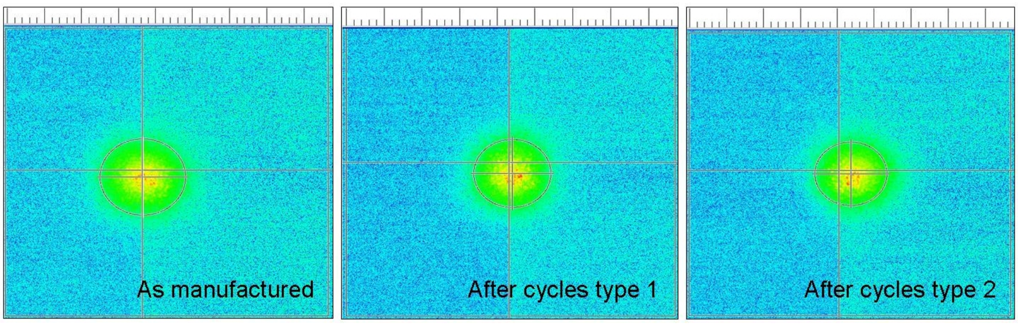

(b) Evolution of the PSF.

Figure 10.16: PSFs after thermal cycling for prototypes made with F-type Foamglas® core.

Chapter 11

Conclusions

Following the structure used in this dissertation the conclusions are also split into two parts.

Part I

In Chapter 3 is described the glass slumping technique applied to manufacture thin glass mirror shells for AO. This work has followed a roadmap within a time-frame of 2.5 years. The study is part of the OPTICON activities financed by the FP6 of the European Community. The investigation is also part of a larger effort dedicated to the the E-ELT Design Study.
In this framework, the author in collaboration with scientists of INAF-OAB has contributed to study and develop the "Hot Press Direct Slumping" process. The process is based on the replica concept, where a number of identical objects can be produced in a fast and cheap manner coping the shape of the mould. In this process we slump a thin ($1 - 2$ mm) borosilicate glass sheet onto the surface of an accurate mould. The mould is made in a suitable ceramic material, it has the negative profile of the desired mirror and it is optically polished and figured. The goal of the process is to copy within optical accuracy its shape. The glass shells obtained from this process should be used as mirror substrates for adaptive optics.
The author gave contributions on the materials selection and characterization, from interferometric optical testing and surface metrology. Moreover, the author contributes to the process development, in particular concerning the capability to apply and maintain a controlled uniform pressure at high temperature.
The slumping technique developed so far shows the potentiality to produce glass shells with very high shape accuracy depending on the mould accuracy. The results obtained with small shells having diameter of 130 mm (see § 5.3) have

shown a very good copy capability of the master mould, permitting to obtain optical surfaces whose accuracy was limited only by the mould shape itself.
In a second part of the development, it has been initiated the scaling-up of the process. It has been equipped a dedicated lab for the slumping, an interferometric tower for the optical characterization. Also, it has been produced a larger mould with a higher shape accuracy from which replicate glass shells with diameter of 500 mm. The scaling-up has introduced some difficulties mainly related to the strong curvature of the mould (see § 5.4).
This problem has been solved re-designing the mould with a larger radius of curvature passing from 5 m to 10 m. With this radius of curvature it has been shown that it is possible to obtain glass shells without warping of the optical surface. However, the process is not yet able to replicate completely the shape of the mould. Indeed, it has been produced a shell whose central area is very close to the mould's shape, and anyway with higher optical quality respect to the initial tests, but having an outer corona that deviate (see § 5.5).
The author gave contributions on the setting-up of the new process and on the optical characterization of the large shells. In particular concerning the development of the astatic support which exploits the innovative concept of the "air cushion".
The results achieved are also reported in a number of papers for which the author is prime or co-author; the activities are been presented to international congresses and workshops.

Part II

The second half of the PhD program has been dedicated to the new field of ground-based Very High Energy Gamma-ray Astrophysics. In Chapter 9 is described the innovative technique ideated and developed by INAF-OAB expressly for mirror panels for Imaging Atmospheric Cherenkov Telescopes. These panels have a composite sandwich-like structure composed by two skins of thin borosilicate glass sheets and a reinforcing core. Despite they require a limited optical quality (few arcminutes are sufficient), the main features of this kind of mirrors should be robustness to strong environmental and atmospheric conditions, reduced weight and limited cost.
In this framework, the author in collaboration with scientists of INAF-OAB, INAF-OAPadua and Media Lario Technologies has contributed to study and develop the "Cold Glass Slumping" process. The process is based on the replica concept, where a number of identical objects can be produced in a fast and cheap manner coping the shape of the mould. In this process we elastically deform a thin ($1-2$ mm) and large (1 m^2) borosilicate glass sheet onto the surface of an accurate mould by means of a vacuum suction. The mould is made in Aluminum, it has the negative profile of the desired mirror and it is figured through a dia-

mond milling fly cutting technique. The goal of the process is to copy within the requested accuracy its shape and to retain it when the suction is stopped.
The author followed this activities since 1.5 years as part of a study financed by the Italian national grant PRIN-INAF 2006 for the development and production of half of the mirror panels of the MAGIC II Cherenkov telescope. Nowadays, this investigation is also part of a larger effort dedicated to the CTA FP7 Preparatory Phase.
At this regard, in Chapter 10 are described and reported the latest advancements gained. The author is conducting a step further in the development of the technology to make it fully compliant to the requirements of CTA. In particular concerning the cost target we are investigating innovative and cheapest materials such as glass foam and glues; this materials come from different markets (than optics manufacturing) and need to be characterized.
The author has realized and tested with success a number of 300×300 mm^2 mirror prototypes. These panels have focusing performances typically below 1 mrad as requested for Cherenkov telescopes. They survived to a number of rapid thermal cycles from -20°C to +60°C with no appreciable deformations of the focal spot. Also, it has been realized and tested a larger size prototype (600×600 mm^2) showing a focusing quality close to 1 mrad. All these results are very promising in view of using glass foam as core material for the reflecting panels. Nevertheless, these new kind of materials have to be intensively tested.
In the next months will be realized a full scale mirror panel compliant with the CTA requirements and adopting the new materials. A detailed schedule of tests is going to be defined to check the focusing performances, survival and operational conditions, aging and reflectivity.
The results achieved are also reported in a number of papers for which the author is prime or co-author; the activities have been presented to international congresses, workshops and internal meetings of the CTA consortium.

List of Publications and Oral contributions

Publications

2010 **Canestrari, R.**, Motta, G., Pareschi, G., Basso, S., Doro, M., Giro, E., Lessio, L. *Composite panels for optical mirrors for Cherenkov Telescopes: development of the cold glass slumping technology.* Society of Photo-Optical Instrumentation Engineers (SPIE) Conference Series 7739.

2010 **Canestrari, R.**, Pareschi, G., Ghigo, M. *Replica Process for Mirror Manufacturing; Glass Slumping and Foamglas Backing.* Chapter 22 in: *"Alt-Az Intiative: Telescopes, Mirrors, & Instrumental Developments."* April 2010. Genet, R., Johnson, J. & Wallen, V. editors.

2009 **Canestrari, R.**, Ghigo, M., Pareschi, G., Basso, S., Motta, G., Doro, M., Giro, E., Lessio, L. *Techniques for the manufacturing of stiff and lightweight optical mirror panels based on slumping of glass sheets: concepts and results.* Society of Photo-Optical Instrumentation Engineers (SPIE) Conference Series 7437.

2009 Ghigo, M., Basso, S., **Canestrari, R.**, Proserpio, L. *Development of hot slumping technique and last optical performances obtained on a 500 mm diameter slumped segment prototype for adaptive optics.* Society of Photo-Optical Instrumentation Engineers (SPIE) Conference Series 7439.

2009 Förster, A., Doro, M., Brun, P., **Canestrari, R.**, Chadwick, P., Font, L., Ghigo, M., Lorenz, E., Mariotti, M., Michalowski, J., Niemiec, J., Pareschi, G., Peyaud, B., Seweryn, K. *Mirror development for CTA.* Society of Photo-Optical Instrumentation Engineers (SPIE) Conference Series 7437.

2009 Ghigo, M., Basso, S., **Canestrari, R.**, Conconi, P., Citterio, O., Civitani, M., Dell'Orto, E., Gallieni, D., Pareschi, G., Parodi, G., Proserpio, L.,

Spiga, D. *Hot slumping glass technology and integration process to manufacture a grazing incidence scaled prototype for the IXO telescope modules.* Society of Photo-Optical Instrumentation Engineers (SPIE) Conference Series 7437.

2009 Ghigo, M., Cornelli, S., **Canestrari, R.**, Garegnani, D. *Development of a large ion beam figuring facility for correction of optics up to 1.7 m diameter.* Society of Photo-Optical Instrumentation Engineers (SPIE) Conference Series 7426.

2009 Doro, M., Förster, A., Brun, P., **Canestrari, R.**, Chadwick, P., Font, L., Ghigo, M., Lorenz, E., Mariotti, M., Niemiec, J., Pareschi, G., Peyaud, B., Seweryn, K., Stodulski, M. *Mirror Facet Technologies for the Telescopes of the CTA Observatory.* Proceedings of the 31st ICRC.

2009 Pareschi, G., Ghigo, M., **Canestrari, R.**, Proserpio, L., Basso, S., Citterio, O. *Stiff and Lightweight Optical Mirrors Made by Glass Slumping with Foamed Core.* American Astronomical Society Meeting Abstracts 214, #600.03.

2009 Pareschi, G., Ghigo, M., Basso, S., Citterio, O., **Canestrari, R.**, Dell'Orto, E., Conconi, P., Parodi, G., Proserpio, L. *Design And Development The IXO Mirrors By Innovative Slumping Glass Technologies.* Bulletin of the American Astronomical Society 41, 359.

2009 Genet, R., Aurigema, A., Badger, S., Bartels, M., Brodhacker, K. L., **Canestrari, R.**, Chen, P., Connelley, M., Davis, D., Ghigo, M., Jones, G., Liu, T., Mendex, E., Pareschi, G., Richardson, T., Rowe, D., Schmidt, J., Shah, K., Villasenor, E. *Lightweight Mirror Developments.* Society for Astronomical Sciences Annual Symposium 28, 27.

2009 Spiga, D., Freyberg, M., Burkert, W., Hartner, G., Budau, B., Mattarello, V., Garoli, D., Boscolo Marchi, E., Basso, S., Valtolina, R., Mattaini, E., **Canestrari, R.**, Garegnani, D., Tagliaferri, G., Pareschi, G., Moretti, A. *X-ray tests at PANTER on Nickel-Cobalt EM#3 (phase A) SIMBOL-X optic prototype.*, INAF/OAB internal report 01/2009.

2008 **Canestrari, R.**, Ghigo, M., Pareschi, G., Basso, S., Proserpio, L. *Investigation of a novel slumping technique for the manufacturing of stiff and lightweight optical mirrors.* Society of Photo-Optical Instrumentation Engineers (SPIE) Conference Series 7018.

2008 **Canestrari, R.**, Ghigo, M., Basso, S., Spiga, D., Proserpio, L. *Lightweight optical segment prototype for adaptive optics manufactured by hot slumping.*

Society of Photo-Optical Instrumentation Engineers (SPIE) Conference Series 7015.

2008 Ghigo, M., **Canestrari, R.**, Proserpio, L., Dell'Orto, E., Basso, S., Citterio, O., Pareschi, G., Parodi, G. *Slumped glass option for making the XEUS mirrors: preliminary design and ongoing developments.* Society of Photo-Optical Instrumentation Engineers (SPIE) Conference Series 7011.

2008 Pareschi, G., Giro, E., Banham, R., Basso, S., Bastieri, D., **Canestrari, R.**, Ceppatelli, G., Citterio, O., Doro, M., Ghigo, M., Marioni, F., Mariotti, M., Salvati, M., Sanvito, F., Vernani, D. *Glass mirrors by cold slumping to cover 100 m^2 of the MAGIC II Cherenkov telescope reflecting surface.* Society of Photo-Optical Instrumentation Engineers (SPIE) Conference Series 7018.

2008 Novi, A., **Canestrari, R.**, Ghigo, M., Hayano, Y. *Wavefront corrective lens for the Subaru Laser Launching Telescope.* Society of Photo-Optical Instrumentation Engineers (SPIE) Conference Series 7018.

2008 Spiga, D., Pareschi, G., **Canestrari, R.**, Cotroneo, V. *Estimation of the X-ray scattering impact in imaging degradation for the SIMBOL-X telescope.* Memorie della Societa Astronomica Italiana 79, 278.

2008 Spiga, D. , Sironi, G. , Cotroneo, V. , **Canestrari, R.** , Destefanis, G. *Silicon mirrors for the XEUS X-ray telescope pore optics: microroughness characterization.*, INAF/OAB Technical report 01/2008.

2007 Ghigo, M., **Canestrari, R.**, Basso, S., Spiga, D. *Development of lightweight optical segments for adaptive optics.* Society of Photo-Optical Instrumentation Engineers (SPIE) Conference Series 6691.

2007 Ghigo, M., **Canestrari, R.**, Spiga, D., Novi, A. *Correction of high spatial frequency errors on optical surfaces by means of ion beam figuring.* Society of Photo-Optical Instrumentation Engineers (SPIE) Conference Series 6671.

2007 Spiga, D., Pareschi, G., Cotroneo, V., **Canestrari, R.**, Vernani, D., Mirone, A., Ferrero, C., Ferrari, C., Lazzarini, L. *Multilayer coatings for x-ray mirrors: extraction of stack parameters from x-ray reflectivity scans and comparison with transmission electron microscopy results.* Optical Engineering 46, 086501.

2007 Spiga, D., **Canestrari, R.**, Pareschi, G., Basso, S., Bruni, R., Budau, B., Burkert, W., Colombo, D., Destefanis, G., Freyberg, M., et al. *Results of tests performed at PANTER and INAF/OAB on the X-ray optic 349 manufactured at MSFC and Harvard-CfA.*, INAF-OAB technical report 02/2007.

2007 **Canestrari, R.**, Spiga, D., Pareschi, G., Ghigo, M., Arumainathan, S., Destefanis, G., Fabbri, P., Ferrari, C., Guaita, C., Nicolosi, P., et al. *Surface roughness and bulk characterization of SiC and Aluminium samples with PECVD-SiC cladding.*, Internal report INAF/OAB 03/2007.

2007 Spiga, D., **Canestrari, R.**, Pareschi, G., Basso, S., Bruni, R., Burkert, W., Budau, B., Freyberg, M., Gorenstein, P., Hartner, G., et al. *X-ray optic 346 manufactured at MSFC and Harvard-CfA: results of tests at PANTER facility and surface characterization.*, INAF/OAB internal report 01/2007.

2006 **Canestrari, R.**, Spiga, D., Pareschi, G. *Analysis of microroughness evolution in X-ray astronomical multilayer mirrors by surface topography with the MPES program and by X-ray scattering.* Society of Photo-Optical Instrumentation Engineers (SPIE) Conference Series 6266.

2006 Spiga, D., Mirone, A., Pareschi, G., **Canestrari, R.**, Cotroneo, V., Ferrari, C., Ferrero, C., Lazzarini, L., Vernani, D. *Characterization of multilayer stack parameters from x-ray reflectivity data using the PPM program: measurements and comparison with TEM results.* Society of Photo-Optical Instrumentation Engineers (SPIE) Conference Series 6266.

2006 Muleri, F., Bellazzini, R., Costa, E., Soffitta, P., Lazzarotto, F., Feroci, M., Pacciani, L., Rubini, A., Morelli, E., Baldini, L., Bitti, F., Brez, A., Cavalca, F., Latronico, L., Massai, M. M., Omodei, N., Pinchera, M., Sgrò, C., Spandre, G., Matt, G., Perola, G. C., Citterio, O., Pareschi, G., Cotroneo, V., Spiga, D., **Canestrari, R.** *An x-ray polarimeter for hard x-ray optics.* Society of Photo-Optical Instrumentation Engineers (SPIE) Conference Series 6266.

2006 **Canestrari, R.**, Pareschi, G. *Characterization of an antenna for RFID systems.* INAF-OAB Internal report 07/2006.

2006 **Canestrari, R.**, Valtolina, R., Spiga, D., Pareschi, G. *Characterization of a PECVD-SiC replicated mirror sample.*, INAF/OAB Internal report 04/2006.

2006 Spiga, D., **Canestrari, R.**, Vernani, D., Freyberg, M., Bukert, W., Hartner, G., Budau, B., Pareschi, G. , Citterio, O., Basso, S., et al. *Mirror shell 338 (Jet-X mandrel n.1 sized shell): Achieved tests at Panter facility and INAF/OAB.*, INAF/OAB Internal Report 02/2006.

2005 Spiga, D., Burkert, W., Hartner, G., Budau, B., Vernani, D., **Canestrari, R.**, Pareschi, G., Citterio, O., Basso, S., Mazzoleni, F., et al. *X-ray and topographic characterization of a W/Si graded multilayer coated mirror shell* *(n.333) at PANTER facility (april 2005).*, INAF/OAB Internal Report 08/2005.

Oral contributions

2010 *Composite panels for optical mirrors for Cherenkov Telescopes: development of the cold glass slumping technology.* Society of Photo-Optical Instrumentation Engineers (SPIE) Conference Series 7739, San Diego (CA, USA) Convention Center, 06/2010

2010 *INAF activities on the SST: a critical comparison of different layouts.* CTA general meeting, DESY (Berlin, Germany), 05/2010.

2010 *Update on the mirror activities of INAF.* CTA general meeting, DESY (Berlin, Germany), 05/2010.

2010 *INAF activities on the SST: a critical comparison of different layouts.* Joint meeting CTA-WP-MIR and CTA-WP-TEL, Max-Planck-Institut für Kernphysik (Heidelberg, Germany), 03/2010.

2010 *Update on the mirror activities of INAF.* Joint meeting CTA-WP-MIR and CTA-WP-TEL, Max-Planck-Institut für Kernphysik (Heidelberg, Germany), 03/2010.

2009 *The INAF contribu1on to the CTA small telescope design study: an update.* CTA general meeting, Zurich University (Zurich, Switzerland), 10/2009.

2009 *Preliminary Conceptual Design of class Φ 7 m IACT.* Joint meeting CTA-WP-MIR and CTA-WP-TEL, IRFU CEA (Saclay, France), 09/2009.

2009 *Replica glass mirrors technologies for CTA telescopes.* Joint meeting CTA-WP-MIR and CTA-WP-TEL, IRFU CEA (Saclay, France), 09/2009.

2009 *Techniques for the manufacturing of stiff and lightweight optical mirror panels based on slumping of glass sheets: concepts and results.* Society of Photo-Optical Instrumentation Engineers (SPIE) Conference Series 7437, San Diego (CA, USA) Convention Center, 08/2009

2009 *Development of hot slumping technique and last optical performances obtained on a 500 mm diameter slumped segment prototype for adaptive optics.* Society of Photo-Optical Instrumentation Engineers (SPIE) Conference Series 7439, San Diego (CA, USA) Convention Center, 08/2009.

2009 *Mirrors for astronomy made by hot slumped thin glass shells.* The Alt-Az Initiative workshop @ 214th American Astronomical Society meeting, Pasadena (CA, USA). Invited talk, 06/2009.

2009 *Glass mirror panels for MAGIC II Cherenkov Light Telescope.* The Alt-Az Initiative workshop @ 214th American Astronomical Society meeting, Pasadena (CA, USA). Invited talk, 06/2009.

2009 *Update on "cold slumped" glass mirror panels: ongoing thermal tests.* CTA general meeting, Conference Center of the Jagiellonian University (Krakow, Poland), 05/2009.

2009 *Update on "cold slumped" glass mirror panels.* Joint meeting CTA-WP-MIR and CTA-WP-TEL, Max-Planck-Institut für Kernphysik (Heidelberg, Germany), 04/2009.

2009 *Glass mirror panels technologies for Cherenkov Telescopes: CTA and AGIS.* Workshop on CTA, INAF Headquarter (Rome, Italy), 03/2009.

2008 *Glass mirror panels technologies for Cherenkov Telescopes.* CTA general meeting, University of Padua (Italy), 11/2008.

2008 *Hot Press Direct Slumping: an option to manufacture deformable optics.* ACTive x-ray OPtics workshop, Synchrotron Elettra (Trieste, Italy), 10/2008.

2008 *Investigation of a novel slumping technique for the manufacturing of stiff and lightweight optical mirrors.* Society of Photo-Optical Instrumentation Engineers (SPIE) Conference Series 7018, Marseille (France) Convention Center, 06/2008.

Acknowledgements

It was a long way since I arrived in Merate in early 2005 for my Laurea Thesis. A month ago (April 2010), citing José Mário dos Santos Félix Mourinho (to long and pompous name for a coach of Inter FC), someone told me: "*Zeru tituli, Zeru tituli!*", and now I finished my PhD.

A special thanks goes to my family for their constant support in my choices. To my father and mother that are proud of me, and to my brother who always asks me: "*Come va il dottorato?*".

Thanks to Mauro, who taught me a lot about how to observe and investigate the results also just using the eyes. Thanks to his genius in propose and actuate ideas, I hope I have stolen a bit...

Thanks to Giovanni who had trust in me and (I hope) he still has it. Thanks to give me the opportunity to do science in complete autonomy, following my feelings and my ideas. It was (and it is) a great opportunity and pleasure for me.

Thanks to the INAF's team of CTA, and in particular to Bruno Sacco, Stefano Vercellone, Paolo Conconi and Giancarlo Parodi for many usefull discussions, suggestions and activities we share.

Thanks to my friends from Brianza lands: the Giuriato sisters, Davide & Valentina (La Mugliera), Simo, i Colombi (Erika & Alberto), il Capo (la Marina) and her husband Stefano, my friend and shoulder (for sketches and bullshits!). And some "outsiders": Pg, Sabrina, Susy & Tommy. Thanks to share your freetime with me.

Bibliography

[1] G. Monnet and R. Gilmozzi. Status of the European ELT. *The Messenger*, 123:4–+, March 2006. [cited at p. 3]

[2] R. Gilmozzi. ESO's Telescopes In memoriam Daniel Enard. *The Messenger*, 136:2–7, June 2009. [cited at p. 5]

[3] Various Authors. Report presented by the elt telescope design working group, May 2006. [cited at p. 5, 7, 221]

[4] B. Delabre. Optical design for an adaptive anastigmatic five-mirror extremely large telescope. *Astronomy and Astrophisycs*, 487:389–397, August 2008. [cited at p. 5]

[5] R. Gilmozzi and J. Spyromilio. The European Extremely Large Telescope (E-ELT). *The Messenger*, 127:11–+, March 2007. [cited at p. 6, 9, 10, 221]

[6] J. Spyromilio, F. Comerón, S. D'Odorico, M. Kissler-Patig, and R. Gilmozzi. Progress on the European Extremely Large Telescope. *The Messenger*, 133:2–8, September 2008. [cited at p. 11, 15, 17, 221]

[7] R. Gilmozzi and J. Spyromilio. The 42m European ELT: status. In *Society of Photo-Optical Instrumentation Engineers (SPIE) Conference Series*, volume 7012 of *Society of Photo-Optical Instrumentation Engineers (SPIE) Conference Series*, August 2008. [cited at p. 13, 14, 15, 16, 17, 18, 221]

[8] J. Spyromilio. The European Extremely Large Telescope: the Arne way. In *Society of Photo-Optical Instrumentation Engineers (SPIE) Conference Series*, volume 6986 of *Society of Photo-Optical Instrumentation Engineers (SPIE) Conference Series*, May 2008. [cited at p. 15, 17, 221]

[9] M. Sarazin. Site considerations for ELTs. In P. Whitelock, M. Dennefeld, & B. Leibundgut, editor, *The Scientific Requirements for Extremely Large Telescopes*, volume 232 of *IAU Symposium*, pages 34–39, 2006. [cited at p. 18, 19, 221]

[10] Various Authors. Science cases and requirements for the eso elt, April 2006. [cited at p. 22]

[11] R. J. McLure and J. S. Dunlop. On the black hole-bulge mass relation in active and inactive galaxies. *MNRAS*, 331:795–804, April 2002. [cited at p. 27]

[12] L. Pasquini, S. Cristiani, H. Dekker, M. Haehnelt, P. Molaro, F. Pepe, G. Avila, B. Delabre, S. D'Odorico, J. Liske, P. Shaver, P. Bonifacio, S. Borgani, V. D'Odorico, E. Vanzella, F. Bouchy, M. Dessauges-Lavadsky, C. Lovis, M. Mayor, D. Queloz, S. Udry, M. Murphy, M. Viel, A. Grazian, S. Levshakov, L. Moscardini, T. Wiklind, and S. Zucker. CODEX: Measuring the Expansion of the Universe (and beyond). *The Messenger*, 122:10–14, December 2005. [cited at p. 29]

[13] S. Basso. Furnace and mould thermal fem analyses. Technical report ELT-TRE-INA-09300-0008, INAF - Osservatorio Astronomico di Brera, November 2006. [cited at p. 38]

[14] W. W. Zhang, D. A. Content, T. T. Saha, R. Petre, S. L. O'Dell, W. D. Jones, W. N. Davis, and W. A. Podgorski. Development of x-ray reflectors for the Constellation-X observatory. In O. Citterio & S. L. O'Dell, editor, *Society of Photo-Optical Instrumentation Engineers (SPIE) Conference Series*, volume 5168 of *Society of Photo-Optical Instrumentation Engineers (SPIE) Conference Series*, pages 168–179, February 2004. [cited at p. 46]

[15] P. Friedrich, B. Aschenbach, H. Braeuninger, G. Hasinger, O. Citterio, M. Ghigo, F. Mazzoleni, G. Pareschi, U. Dinger, W. Egle, and A. Matthes. Recent results on manufacturing of segmented x-ray mirrors with slumped glass. In O. Citterio & S. L. O'Dell, editor, *Society of Photo-Optical Instrumentation Engineers (SPIE) Conference Series*, volume 5900 of *Society of Photo-Optical Instrumentation Engineers (SPIE) Conference Series*, pages 258–265, August 2005. [cited at p. 46]

[16] A. Riccardi. Optical figuring specifications for thin shells to be used in adaptive telescope mirrors. Technical report, INAF - Osservatorio Astrofisico di Arcetri, April 2004. http://www.arcetri.astro.it/pubblicazioni/Reports/04/4_04.html. [cited at p. 60]

[17] M. Ghigo, S. Basso, O. Citterio, F. Mazzoleni, and D. Vernani. Manufacturing of lightweight glass segments for adaptive optics. In *Society of Photo-Optical Instrumentation Engineers (SPIE) Conference Series*, volume 6272 of *Society of Photo-Optical Instrumentation Engineers (SPIE) Conference Series*, July 2006. [cited at p. 63]

[18] P. Goodwin and James C. Wyant. *Field Guide to Interferometric Optical Testing*. SPIE Press, Bellingham, WA, 2006. [cited at p. 75, 76, 77, 223]

[19] Y. Hayashi, R. Akiyama, and Kudo M. Surface characterization of float glass related to changes in the optical properties after reheating. *Surface and Interface Analysis*, 31, February 2001. [cited at p. 87]

[20] M. Ghigo, R. Canestrari, S. Basso, and D. Spiga. Development of lightweight optical segments for adaptive optics. In *Society of Photo-Optical Instrumentation Engineers (SPIE) Conference Series*, volume 6691 of *Society of Photo-Optical Instrumentation Engineers (SPIE) Conference Series*, September 2007. [cited at p. 88]

[21] R. Canestrari, M. Ghigo, S. Basso, D. Spiga, and L. Proserpio. Lightweight optical segment prototype for adaptive optics manufactured by hot slumping. In *Society of Photo-Optical Instrumentation Engineers (SPIE) Conference Series*, volume 7015 of

Presented at the Society of Photo-Optical Instrumentation Engineers (SPIE) Conference, July 2008. [cited at p. 99]

[22] M. Ghigo, S. Basso, R. Canestrari, and L. Proserpio. Development of hot slumping technique and last optical performances obtained on a 500mm diameter slumped segment prototype for adaptive optics. In *Society of Photo-Optical Instrumentation Engineers (SPIE) Conference Series*, volume 7439 of *Presented at the Society of Photo-Optical Instrumentation Engineers (SPIE) Conference*, August 2009. [cited at p. 100]

[23] H. J. Völk and K. Bernlöhr. Imaging very high energy gamma-ray telescopes. *Experimental Astronomy*, 25:173–191, August 2009. [cited at p. 109]

[24] A. de Angelis, O. Mansutti, and M. Persic. Very-high energy gamma astrophysics. *Nuovo Cimento Rivista Serie*, 31:187–246, April 2008. [cited at p. 109]

[25] T. C. Weekes, M. F. Cawley, D. J. Fegan, K. G. Gibbs, A. M. Hillas, P. W. Kowk, R. C. Lamb, D. A. Lewis, D. Macomb, N. A. Porter, P. T. Reynolds, and G. Vacanti. Observation of TeV gamma rays from the Crab nebula using the atmospheric Cerenkov imaging technique. *The Astrophysical Journal*, 342:379–395, July 1989. [cited at p. 109]

[26] M. Punch, C. W. Akerlof, M. F. Cawley, M. Chantell, D. J. Fegan, S. Fennell, J. A. Gaidos, J. Hagan, A. M. Hillas, Y. Jiang, A. D. Kerrick, R. C. Lamb, M. A. Lawrence, D. A. Lewis, D. I. Meyer, G. Mohanty, K. S. O'Flaherty, P. T. Reynolds, A. C. Rovero, M. S. Schubnell, G. Sembroski, T. C. Weekes, and C. Wilson. Detection of TeV photons from the active galaxy Markarian 421. *Nature*, 358:477–+, August 1992. [cited at p. 109]

[27] J. Quinn, C. W. Akerlof, S. Biller, J. Buckley, D. A. Carter-Lewis, M. F. Cawley, M. Catanese, V. Connaughton, D. J. Fegan, J. P. Finley, J. Gaidos, A. M. Hillas, R. C. Lamb, F. Krennrich, R. Lessard, J. E. McEnery, D. I. Meyer, G. Mohanty, A. J. Rodgers, H. J. Rose, G. Sembroski, M. S. Schubnell, T. C. Weekes, C. Wilson, and J. Zweerink. Detection of Gamma Rays with E ¿ 300 GeV from Markarian 501. *Astrophysical Journal Letters*, 456:L83+, January 1996. [cited at p. 109]

[28] F. Aharonian, A. G. Akhperjanian, J. A. Barrio, K. Bernloehr, J. J. G. Beteta, S. M. Bradbury, J. L. Contreras, J. Cortina, A. Daum, T. Deckers, E. Feigl, J. Fernandez, V. Fonseca, A. Frass, B. Funk, J. C. Gonzalez, V. Haustein, G. Heinzelmann, M. Hemberger, G. Hermann, M. Hess, A. Heusler, W. Hofmann, I. Holl, D. Horns, R. Kankanian, O. Kirstein, C. Koehler, A. Konopelko, H. Kornmayer, D. Kranich, H. Krawczynski, H. Lampeitl, A. Lindner, E. Lorenz, N. Magnussen, H. Meyer, R. Mirzoyan, H. Moeller, A. Moralejo, L. Padilla, M. Panter, D. Petry, R. Plaga, J. Prahl, C. Prosch, G. Puehlhofer, G. Rauterberg, W. Rhode, R. Rivero, A. Roehring, V. Sahakian, M. Samorski, J. A. Sanchez, D. Schmele, T. Schmidt, W. Stamm, M. Ulrich, H. J. Voelk, S. Westerhoff, B. Wiebel-Sooth, C. A. Wiedner, M. Willmer, and H. Wirth. Measurement of the flux, spectrum, and variability of TeV γ-rays from MKN 501 during a state of high activity. *Astronomy and Astrophysics*, 327:L5–L8, November 1997. [cited at p. 109]

[29] J. Albert, E. Aliu, H. Anderhub, P. Antoranz, A. Armada, C. Baixeras, J. A. Barrio, H. Bartko, D. Bastieri, J. K. Becker, W. Bednarek, K. Berger, C. Bigongiari, A. Biland, R. K. Bock, P. Bordas, V. Bosch-Ramon, T. Bretz, I. Britvitch, M. Camara, E. Carmona, A. Chilingarian, J. A. Coarasa, S. Commichau, J. L. Contreras, J. Cortina, M. T. Costado, V. Curtef, V. Danielyan, F. Dazzi, A. De Angelis, C. Delgado, R. de los Reyes, B. De Lotto, E. Domingo-Santamaría, D. Dorner, M. Doro, M. Errando, M. Fagiolini, D. Ferenc, E. Fernández, R. Firpo, J. Flix, M. V. Fonseca, L. Font, M. Fuchs, N. Galante, R. J. García-López, M. Garczarczyk, M. Gaug, M. Giller, F. Goebel, D. Hakobyan, M. Hayashida, T. Hengstebeck, A. Herrero, D. Höhne, J. Hose, D. Hrupec, C. C. Hsu, P. Jacon, T. Jogler, R. Kosyra, D. Kranich, R. Kritzer, A. Laille, E. Lindfors, S. Lombardi, F. Longo, J. López, M. López, E. Lorenz, P. Majumdar, G. Maneva, K. Mannheim, O. Mansutti, M. Mariotti, M. Martínez, D. Mazin, C. Merck, M. Meucci, M. Meyer, J. M. Miranda, R. Mirzoyan, S. Mizobuchi, A. Moralejo, D. Nieto, K. Nilsson, J. Ninkovic, E. Oña-Wilhelmi, N. Otte, I. Oya, D. Paneque, M. Panniello, R. Paoletti, J. M. Paredes, M. Pasanen, D. Pascoli, F. Pauss, R. Pegna, M. Persic, L. Peruzzo, A. Piccioli, E. Prandini, N. Puchades, A. Raymers, W. Rhode, M. Ribó, J. Rico, M. Rissi, A. Robert, S. Rügamer, A. Saggion, T. Saito, A. Sánchez, P. Sartori, V. Scalzotto, V. Scapin, R. Schmitt, T. Schweizer, M. Shayduk, K. Shinozaki, S. N. Shore, N. Sidro, A. Sillanpää, D. Sobczynska, A. Stamerra, L. S. Stark, L. Takalo, F. Tavecchio, P. Temnikov, D. Tescaro, M. Teshima, D. F. Torres, N. Turini, H. Vankov, V. Vitale, R. M. Wagner, T. Wibig, W. Wittek, F. Zandanel, R. Zanin, and J. Zapatero. Variable Very High Energy γ-Ray Emission from Markarian 501. *The Astrophysical Journal*, 669:862–883, November 2007. [cited at p. 110]

[30] F. Aharonian, A. G. Akhperjanian, A. R. Bazer-Bachi, B. Behera, M. Beilicke, W. Benbow, D. Berge, K. Bernlöhr, C. Boisson, O. Bolz, V. Borrel, T. Boutelier, I. Braun, E. Brion, A. M. Brown, R. Bühler, I. Büsching, T. Bulik, S. Carrigan, P. M. Chadwick, A. C. Clapson, L.-M. Chounet, G. Coignet, R. Cornils, L. Costamante, B. Degrange, H. J. Dickinson, A. Djannati-Ataï, W. Domainko, L. O. Drury, G. Dubus, J. Dyks, K. Egberts, D. Emmanoulopoulos, P. Espigat, C. Farnier, F. Feinstein, A. Fiasson, A. Förster, G. Fontaine, S. Funk, S. Funk, M. Füßling, Y. A. Gallant, B. Giebels, J. F. Glicenstein, B. Glück, P. Goret, C. Hadjichristidis, D. Hauser, M. Hauser, G. Heinzelmann, G. Henri, G. Hermann, J. A. Hinton, A. Hoffmann, W. Hofmann, M. Holleran, S. Hoppe, D. Horns, A. Jacholkowska, O. C. de Jager, E. Kendziorra, M. Kerschhaggl, B. Khélifi, N. Komin, K. Kosack, G. Lamanna, I. J. Latham, R. Le Gallou, A. Lemière, M. Lemoine-Goumard, J.-P. Lenain, T. Lohse, J. M. Martin, O. Martineau-Huynh, A. Marcowith, C. Masterson, G. Maurin, T. J. L. McComb, R. Moderski, E. Moulin, M. de Naurois, D. Nedbal, S. J. Nolan, J.-P. Olive, K. J. Orford, J. L. Osborne, M. Ostrowski, M. Panter, G. Pedaletti, G. Pelletier, P.-O. Petrucci, S. Pita, G. Pühlhofer, M. Punch, S. Ranchon, B. C. Raubenheimer, M. Raue, S. M. Rayner, M. Renaud, J. Ripken, L. Rob, L. Rolland, S. Rosier-Lees, G. Rowell, B. Rudak, J. Ruppel, V. Sahakian, A. Santangelo, L. Saugé, S. Schlenker, R. Schlickeiser, R. Schröder, U. Schwanke, S. Schwarzburg, S. Schwemmer, A. Shalchi, H. Sol, D. Spangler, Ł. Stawarz, R. Steenkamp, C. Stegmann, G. Superina, P. H. Tam, J.-P. Tavernet, R. Terrier, C. van Eldik, G. Vasileiadis, C. Venter, J. P. Vialle, P. Vincent, M. Vivier,

H. J. Völk, F. Volpe, S. J. Wagner, M. Ward, and A. A. Zdziarski. An Exceptional Very High Energy Gamma-Ray Flare of PKS 2155-304. *The Astrophysical Journal*, 664:L71–L74, August 2007. [cited at p. 110]

[31] J. A. Zweerink, C. W. Akerlof, S. D. Biller, P. Boyle, J. H. Buckley, A. Burdett, J. Bussons Gordo, D. A. Carter-Lewis, M. Catanese, M. F. Cawley, D. J. Fegan, J. P. Finley, J. A. Gaidos, A. M. Hillas, F. Krennrich, R. C. Lamb, R. W. Lessard, J. E. McEnery, G. Mohanty, J. Quinn, A. J. Rodgers, H. J. Rose, F. W. Samuelson, M. S. Schubnell, G. Sembroski, R. Srinivasan, T. C. Weekes, and C. Wilson. The TeV Gamma-Ray Spectrum of Markarian 421 during an Intense Flare. *Astrophysical Journal Letters*, 490:L141+, December 1997. [cited at p. 110]

[32] F. Aharonian, A. Akhperjanian, M. Beilicke, K. Bernlöhr, H. Börst, H. Bojahr, O. Bolz, T. Coarasa, J. Contreras, J. Cortina, S. Denninghoff, V. Fonseca, M. Girma, N. Götting, G. Heinzelmann, G. Hermann, A. Heusler, W. Hofmann, D. Horns, I. Jung, R. Kankanyan, M. Kestel, J. Kettler, A. Kohnle, A. Konopelko, H. Kornmeyer, D. Kranich, H. Krawczynski, H. Lampeitl, M. Lopez, E. Lorenz, F. Lucarelli, N. Magnussen, O. Mang, H. Meyer, M. Milite, R. Mirzoyan, A. Moralejo, E. Ona, M. Panter, A. Plyasheshnikov, J. Prahl, G. Pühlhofer, G. Rauterberg, R. Reyes, W. Rhode, J. Ripken, A. Röhring, G. P. Rowell, V. Sahakian, M. Samorski, M. Schilling, F. Schröder, M. Siems, D. Sobzynska, W. Stamm, M. Tluczykont, H. J. Völk, C. A. Wiedner, W. Wittek, Y. Uchiyama, T. Takahashi, and HEGRA Collaboration. An unidentified TeV source in the vicinity of Cygnus OB2. *Astronomy and Astrophysics*, 393:L37–L40, October 2002. [cited at p. 110]

[33] F. Aharonian, A. G. Akhperjanian, A. R. Bazer-Bachi, M. Beilicke, W. Benbow, D. Berge, K. Bernlöhr, C. Boisson, O. Bolz, V. Borrel, I. Braun, F. Breitling, A. M. Brown, P. M. Chadwick, L.-M. Chounet, R. Cornils, L. Costamante, B. Degrange, H. J. Dickinson, A. Djannati-Ataï, L. O. Drury, G. Dubus, D. Emmanoulopoulos, P. Espigat, F. Feinstein, G. Fontaine, Y. Fuchs, S. Funk, Y. A. Gallant, B. Giebels, S. Gillessen, J. F. Glicenstein, P. Goret, C. Hadjichristidis, M. Hauser, G. Heinzelmann, G. Henri, G. Hermann, J. A. Hinton, W. Hofmann, M. Holleran, D. Horns, A. Jacholkowska, O. C. de Jager, B. Khélifi, N. Komin, A. Konopelko, I. J. Latham, R. Le Gallou, A. Lemière, M. Lemoine-Goumard, N. Leroy, T. Lohse, J. M. Martin, O. Martineau-Huynh, A. Marcowith, C. Masterson, T. J. L. McComb, M. de Naurois, S. J. Nolan, A. Noutsos, K. J. Orford, J. L. Osborne, M. Ouchrif, M. Panter, G. Pelletier, S. Pita, G. Pühlhofer, M. Punch, B. C. Raubenheimer, M. Raue, J. Raux, S. M. Rayner, A. Reimer, O. Reimer, J. Ripken, L. Rob, L. Rolland, G. Rowell, V. Sahakian, L. Saugé, S. Schlenker, R. Schlickeiser, C. Schuster, U. Schwanke, M. Siewert, H. Sol, D. Spangler, R. Steenkamp, C. Stegmann, J.-P. Tavernet, R. Terrier, C. G. Théoret, M. Tluczykont, G. Vasileiadis, C. Venter, P. Vincent, H. J. Völk, and S. J. Wagner. The H.E.S.S. Survey of the Inner Galaxy in Very High Energy Gamma Rays. *The Astrophysical Journal*, 636:777–797, January 2006. [cited at p. 110]

[34] E. Aliu, H. Anderhub, L. A. Antonelli, P. Antoranz, M. Backes, C. Baixeras, J. A. Barrio, H. Bartko, D. Bastieri, J. K. Becker, W. Bednarek, K. Berger, E. Bernardini, C. Bigongiari, A. Biland, R. K. Bock, G. Bonnoli, P. Bordas, V. Bosch-Ramon, T. Bretz, I. Britvitch, M. Camara, E. Carmona, A. Chilingarian, S. Commichau,

J. L. Contreras, J. Cortina, M. T. Costado, S. Covino, V. Curtef, F. Dazzi, A. De Angelis, E. De Cea del Pozo, R. de los Reyes, B. De Lotto, M. De Maria, F. De Sabata, C. Delgado Mendez, A. Dominguez, D. Dorner, M. Doro, D. Elsässer, M. Errando, M. Fagiolini, D. Ferenc, E. Fernandez, R. Firpo, M. V. Fonseca, L. Font, N. Galante, R. J. Garcia Lopez, M. Garczarczyk, M. Gaug, F. Goebel, D. Hadasch, M. Hayashida, A. Herrero, D. Höhne, J. Hose, C. C. Hsu, S. Huber, T. Jogler, D. Kranich, A. La Barbera, A. Laille, E. Leonardo, E. Lindfors, S. Lombardi, F. Longo, M. Lopez, E. Lorenz, P. Majumdar, G. Maneva, N. Mankuzhiyil, K. Mannheim, L. Maraschi, M. Mariotti, M. Martinez, D. Mazin, M. Meucci, M. Meyer, J. M. Miranda, R. Mirzoyan, M. Moles, A. Moralejo, D. Nieto, K. Nilsson, J. Ninkovic, N. Otte, I. Oya, R. Paoletti, J. M. Paredes, M. Pasanen, D. Pascoli, F. Pauss, R. G. Pegna, M. A. Perez-Torres, M. Persic, L. Peruzzo, A. Piccioli, F. Prada, E. Prandini, N. Puchades, A. Raymers, W. Rhode, M. Ribó, J. Rico, M. Rissi, A. Robert, S. Rügamer, A. Saggion, T. Y. Saito, M. Salvati, M. Sanchez-Conde, P. Sartori, K. Satalecka, V. Scalzotto, V. Scapin, T. Schweizer, M. Shayduk, K. Shinozaki, S. N. Shore, N. Sidro, A. Sierpowska-Bartosik, A. Sillanpää, D. Sobczynska, F. Spanier, A. Stamerra, L. S. Stark, L. Takalo, F. Tavecchio, P. Temnikov, D. Tescaro, M. Teshima, M. Tluczykont, D. F. Torres, N. Turini, H. Vankov, A. Venturini, V. Vitale, R. M. Wagner, W. Wittek, V. Zabalza, F. Zandanel, R. Zanin, J. Zapatero, O. C. de Jager, E. de Ona Wilhelmi, and MAGIC Collaboration. Observation of Pulsed γ-Rays Above 25 GeV from the Crab Pulsar with MAGIC. *Science*, 322:1221–, November 2008. [cited at p. 110]

[35] P. Vincent. H.E.S.S. Phase II. In *International Cosmic Ray Conference*, volume 5 of *International Cosmic Ray Conference*, pages 163–+, 2005. [cited at p. 110]

[36] F. Goebel. Status of the second phase of the MAGIC telescope. In *International Cosmic Ray Conference*, volume 3 of *International Cosmic Ray Conference*, pages 1485–1488, 2008. [cited at p. 110]

[37] C. Baixeras, D. Bastieri, C. Bigongiari, O. Blanch, G. Blanchot, R. Bock, T. Bretz, A. Chilingarian, J. A. Coarasa, E. Colombo, J. C. Contreras, D. Corti, J. Cortina, C. Domingo, E. Domingo, D. Ferenc, E. Fernández, J. Flix, V. Fonseca, L. Font, N. Galante, M. Gaug, M. Garczarczyk, J. Gebauer, M. Giller, F. Goebel, T. Hengstebeck, P. Jacone, O. C. de Jager, O. Kalekin, M. Kestel, T. Kneiske, A. Laille, M. López, J. López, E. Lorenz, K. Mannheim, M. Mariotti, M. Martínez, K. Mase, M. Merck, M. Meucci, L. Miralles, R. Mirzoyan, A. Moralejo, E. O. Wilhelmi, R. Orduña, D. Paneque, R. Paoletti, D. Pascoli, N. Pavel, R. Pegna, L. Peruzzo, A. Piccioli, A. Roberts, R. Reyes, A. Saggion, A. Sánchez, P. Sartori, V. Scalzotto, T. Schweizer, A. Sillanpaa, D. Sobczynska, A. Stamerra, A. Stepanian, R. Stiehler, L. Takalo, M. Teshima, N. Tonello, A. Torres, N. Turini, V. Vitale, S. Volkov, R. M. Wagner, T. Wibig, and W. Wittek. Commissioning and first tests of the MAGIC telescope. *Nuclear Instruments and Methods in Physics Research A*, 518:188–192, February 2004. [cited at p. 116]

[38] The MAGIC Collaboration: H. Anderhub, L. A. Antonelli, P. Antoranz, M. Backes, C. Baixeras, S. Balestra, J. A. Barrio, D. Bastieri, J. Becerra González, J. K. Becker, W. Bednarek, K. Berger, E. Bernardini, A. Biland, R. K. Bock, G. Bonnoli, P. Bordas, D. Borla Tridon, V. Bosch-Ramon, D. Bose, I. Braun, T. Bretz, D. Britzger,

M. Camara, E. Carmona, A. Carosi, P. Colin, S. Commichau, J. L. Contreras, J. Cortina, M. T. Costado, S. Covino, F. Dazzi, A. De Angelis, E. de Cea del Pozo, C. Delgado Mendez, R. De los Reyes, B. De Lotto, M. De Maria, F. De Sabata, A. Domínguez, D. Dominis Prester, D. Dorner, M. Doro, D. Elsaesser, M. Errando, D. Ferenc, E. Fernández, R. Firpo, M. V. Fonseca, L. Font, N. Galante, R. J. García López, M. Garczarczyk, M. Gaug, N. Godinovic, F. Goebel, D. Hadasch, A. Herrero, D. Hildebrand, D. Höhne-Mönch, J. Hose, D. Hrupec, C. C. Hsu, T. Jogler, S. Klepser, D. Kranich, A. La Barbera, A. Laille, E. Leonardo, E. Lindfors, S. Lombardi, F. Longo, M. López, E. Lorenz, P. Majumdar, G. Maneva, N. Mankuzhiyil, K. Mannheim, L. Maraschi, M. Mariotti, M. Martínez, D. Mazin, M. Meucci, J. M. Miranda, R. Mirzoyan, H. Miyamoto, J. Moldón, M. Moles, A. Moralejo, D. Nieto, K. Nilsson, J. Ninkovic, R. Orito, I. Oya, R. Paoletti, J. M. Paredes, M. Pasanen, D. Pascoli, F. Pauss, R. G. Pegna, M. A. Perez-Torres, M. Persic, L. Peruzzo, F. Prada, E. Prandini, N. Puchades, I. Puljak, I. Reichardt, W. Rhode, M. Ribó, J. Rico, M. Rissi, A. Robert, S. Rügamer, A. Saggion, T. Y. Saito, M. Salvati, M. Sánchez-Conde, K. Satalecka, V. Scalzotto, V. Scapin, T. Schweizer, M. Shayduk, S. N. Shore, A. Sierpowska-Bartosik, A. Sillanpää, J. Sitarek, D. Sobczynska, F. Spanier, S. Spiro, A. Stamerra, L. S. Stark, T. Suric, L. Takalo, F. Tavecchio, P. Temnikov, D. Tescaro, M. Teshima, D. F. Torres, N. Turini, H. Vankov, R. M. Wagner, V. Zabalza, F. Zandanel, R. Zanin, and J. Zapatero. MAGIC Collaboration: Contributions to the 31st International Cosmic Ray Conference (ICRC 2009). *ArXiv e-prints*, July 2009. [cited at p. 116]

[39] C. Bigongiari, D. Bastieri, N. Galante, E. Lorenz, M. Mariotti, R. Mirzoyan, A. Moralejo, A. Pepato, L. Peruzzo, A. Saggion, V. Scalzotto, and N. Tonello. The MAGIC telescope reflecting surface. *Nuclear Instruments and Methods in Physics Research A*, 518:193–194, February 2004. [cited at p. 117, 158]

[40] M. Doro, D. Bastieri, A. Biland, F. Dazzi, L. Font, M. Garczarczyk, M. Ghigo, E. Giro, F. Goebel, R. Kosyra, E. Lorenz, M. Mariotti, R. Mirzoyan, L. Peruzzo, G. Pareschi, and J. Zapatero. The reflective surface of the MAGIC telescope. *Nuclear Instruments and Methods in Physics Research A*, 595:200–203, September 2008. [cited at p. 118, 158]

[41] G. Pareschi, E. Giro, R. Banham, S. Basso, D. Bastieri, R. Canestrari, G. Ceppatelli, O. Citterio, M. Doro, M. Ghigo, F. Marioni, M. Mariotti, M. Salvati, F. Sanvito, and D. Vernani. Glass mirrors by cold slumping to cover 100 m^2 of the MAGIC II C̀erenkov telescope reflecting surface. In *Society of Photo-Optical Instrumentation Engineers (SPIE) Conference Series*, volume 7018 of *Society of Photo-Optical Instrumentation Engineers (SPIE) Conference Series*, July 2008. [cited at p. 118, 160]

[42] D. Vernani, R. Banham, O. Citterio, F. Sanvito, G. Valsecchi, G. Pareschi, M. Ghigo, E. Giro, M. Doro, and M. Mariotti. Development of cold-slumping glass mirrors for imaging C̀erenkov telescopes. In *Society of Photo-Optical Instrumentation Engineers (SPIE) Conference Series*, volume 7018 of *Society of Photo-Optical Instrumentation Engineers (SPIE) Conference Series*, July 2008. [cited at p. 118, 160]

[43] W. Hofmann and The H. E. S. S. Collaboration. Status of the H.E.S.S. project. In *International Cosmic Ray Conference*, volume 7 of *International Cosmic Ray Conference*, pages 2785–+, August 2001. [cited at p. 118]

[44] J. Holder, R. W. Atkins, H. M. Badran, G. Blaylock, S. M. Bradbury, J. H. Buckley, K. L. Byrum, D. A. Carter-Lewis, O. Celik, Y. C. K. Chow, P. Cogan, W. Cui, M. K. Daniel, I. de La Calle Perez, C. Dowdall, P. Dowkontt, C. Duke, A. D. Falcone, S. J. Fegan, J. P. Finley, P. Fortin, L. F. Fortson, K. Gibbs, G. Gillanders, O. J. Glidewell, J. Grube, K. J. Gutierrez, G. Gyuk, J. Hall, D. Hanna, E. Hays, D. Horan, S. B. Hughes, T. B. Humensky, A. Imran, I. Jung, P. Kaaret, G. E. Kenny, D. Kieda, J. Kildea, J. Knapp, H. Krawczynski, F. Krennrich, M. J. Lang, S. Lebohec, E. Linton, E. K. Little, G. Maier, H. Manseri, A. Milovanovic, P. Moriarty, R. Mukherjee, P. A. Ogden, R. A. Ong, D. Petry, J. S. Perkins, F. Pizlo, M. Pohl, J. Quinn, K. Ragan, P. T. Reynolds, E. T. Roache, H. J. Rose, M. Schroedter, G. H. Sembroski, G. Sleege, D. Steele, S. P. Swordy, A. Syson, J. A. Toner, L. Valcarcel, V. V. Vassiliev, S. P. Wakely, T. C. Weekes, R. J. White, D. A. Williams, and R. Wagner. The first VERITAS telescope. *Astroparticle Physics*, 25:391–401, July 2006. [cited at p. 121]

[45] J. Holder, V. A. Acciari, E. Aliu, T. Arlen, M. Beilicke, W. Benbow, S. M. Bradbury, J. H. Buckley, V. Bugaev, Y. Butt, K. L. Byrum, A. Cannon, O. Celik, A. Cesarini, L. Ciupik, Y. C. K. Chow, P. Cogan, P. Colin, W. Cui, M. K. Daniel, T. Ergin, A. D. Falcone, S. J. Fegan, J. P. Finley, G. Finnegan, P. Fortin, L. F. Fortson, A. Furniss, G. H. Gillanders, J. Grube, R. Guenette, G. Gyuk, D. Hanna, E. Hays, D. Horan, C. M. Hui, T. B. Humensky, A. Imran, P. Kaaret, N. Karlsson, M. Kertzman, D. B. Kieda, J. Kildea, A. Konopelko, H. Krawczynski, F. Krennrich, M. J. Lang, S. Lebohec, G. Maier, A. McCann, M. McCutcheon, P. Moriarty, R. Mukherjee, T. Nagai, J. Niemiec, R. A. Ong, D. Pandel, J. S. Perkins, M. Pohl, J. Quinn, K. Ragan, L. C. Reyes, P. T. Reynolds, H. J. Rose, M. Schroedter, G. H. Sembroski, A. W. Smith, D. Steele, S. P. Swordy, J. A. Toner, L. Valcarcel, V. V. Vassiliev, R. Wagner, S. P. Wakely, J. E. Ward, T. C. Weekes, A. Weinstein, R. J. White, D. A. Williams, S. A. Wissel, M. Wood, and B. Zitzer. Status of the VERITAS Observatory. In F. A. Aharonian, W. Hofmann, & F. Rieger, editor, *American Institute of Physics Conference Series*, volume 1085 of *American Institute of Physics Conference Series*, pages 657–660, December 2008. [cited at p. 121]

[46] J.M. Davies and E.S. Cotton. Design of the quartermaster solar furnace. *Journal of Solar Energy Science Engineering.* [cited at p. 137]

[47] V. Vassiliev, S. Fegan, and P. Brousseau. Wide field aplanatic two-mirror telescopes for ground-based γ-ray astronomy. *Astroparticle Physics*, 28:10–27, September 2007. [cited at p. 138, 139, 141]

[48] V. Vassiliev and AGIS Collaboration. The Advanced Gamma-ray Imaging System (AGIS): Next-generation Cherenkov telescopes array. In *AAS/High Energy Astrophysics Division*, volume 11 of *AAS/High Energy Astrophysics Division*, pages 47.04–+, February 2010. [cited at p. 139]

[49] A. Schliesser and R. Mirzoyan. Wide-field prime-focus imaging atmospheric C̀erenkov telescopes: A systematic study. *Astroparticle Physics*, 24:382–390, December 2005. [cited at p. 140, 224]

[50] F. Aharonian, A. Heusler, W. Hofmann, C. A. Wiedner, A. Konopelko, A. Plyasheshnikov, and V. Fomin. On the optimization of multichannel cameras for

imaging atmospheric C̀erenkov telescopes. *Journal of Physics G Nuclear Physics*, 21:985–993, July 1995. [cited at p. 141]

[51] W. Hofmann. Performance Limits for C̀erenkov Instruments. *ArXiv Astrophysics e-prints*, March 2006. [cited at p. 141]

[52] F. Aharonian, A. G. Akhperjanian, A. R. Bazer-Bachi, M. Beilicke, W. Benbow, D. Berge, K. Bernlöhr, C. Boisson, O. Bolz, V. Borrel, I. Braun, E. Brion, A. M. Brown, R. Bühler, I. Büsching, S. Carrigan, P. M. Chadwick, L.-M. Chounet, G. Coignet, R. Cornils, L. Costamante, B. Degrange, H. J. Dickinson, A. Djannati-Ataï, L. O'C. Drury, G. Dubus, K. Egberts, D. Emmanoulopoulos, P. Espigat, F. Feinstein, E. Ferrero, A. Fiasson, G. Fontaine, S. Funk, S. Funk, M. Füßling, Y. A. Gallant, B. Giebels, J. F. Glicenstein, B. Glück, P. Goret, C. Hadjichristidis, D. Hauser, M. Hauser, G. Heinzelmann, G. Henri, G. Hermann, J. A. Hinton, A. Hoffmann, W. Hofmann, M. Holleran, S. Hoppe, D. Horns, A. Jacholkowska, O. C. de Jager, E. Kendziorra, M. Kerschhaggl, B. Khélifi, N. Komin, A. Konopelko, K. Kosack, G. Lamanna, I. J. Latham, R. Le Gallou, A. Lemière, M. Lemoine-Goumard, T. Lohse, J. M. Martin, O. Martineau-Huynh, A. Marcowith, C. Masterson, G. Maurin, T. J. L. McComb, E. Moulin, M. de Naurois, D. Nedbal, S. J. Nolan, A. Noutsos, J.-P. Olive, K. J. Orford, J. L. Osborne, M. Panter, G. Pelletier, S. Pita, G. Pühlhofer, M. Punch, S. Ranchon, B. C. Raubenheimer, M. Raue, S. M. Rayner, A. Reimer, O. Reimer, J. Ripken, L. Rob, L. Rolland, S. Rosier-Lees, G. Rowell, V. Sahakian, A. Santangelo, L. Saugé, S. Schlenker, R. Schlickeiser, R. Schröder, U. Schwanke, S. Schwarzburg, S. Schwemmer, A. Shalchi, H. Sol, D. Spangler, F. Spanier, R. Steenkamp, C. Stegmann, G. Superina, P. H. Tam, J.-P. Tavernet, R. Terrier, M. Tluczykont, C. van Eldik, G. Vasileiadis, C. Venter, J. P. Vialle, P. Vincent, H. J. Völk, S. J. Wagner, and M. Ward. Primary particle acceleration above 100 TeV in the shell-type supernova remnant ¡ASTROBJ¿RX J1713.7-3946¡/ASTROBJ¿ with deep HESS observations. *Astronomy and Astrophysics*, 464:235–243, March 2007. [cited at p. 151]

[53] F. Aharonian, A. G. Akhperjanian, K.-M. Aye, A. R. Bazer-Bachi, M. Beilicke, W. Benbow, D. Berge, P. Berghaus, K. Bernlöhr, C. Boisson, O. Bolz, I. Braun, F. Breitling, A. M. Brown, J. Bussons Gordo, P. M. Chadwick, L.-M. Chounet, R. Cornils, L. Costamante, B. Degrange, A. Djannati-Ataï, L. O'C. Drury, G. Dubus, D. Emmanoulopoulos, P. Espigat, F. Feinstein, P. Fleury, G. Fontaine, Y. Fuchs, S. Funk, Y. A. Gallant, B. Giebels, S. Gillessen, J. F. Glicenstein, P. Goret, C. Hadjichristidis, M. Hauser, G. Heinzelmann, G. Henri, G. Hermann, J. A. Hinton, W. Hofmann, M. Holleran, D. Horns, O. C. de Jager, B. Khélifi, N. Komin, A. Konopelko, I. J. Latham, R. Le Gallou, A. Lemière, M. Lemoine-Goumard, N. Leroy, T. Lohse, O. Martineau-Huynh, A. Marcowith, C. Masterson, T. J. L. McComb, M. de Naurois, S. J. Nolan, A. Noutsos, K. J. Orford, J. L. Osborne, M. Ouchrif, M. Panter, G. Pelletier, S. Pita, G. Pühlhofer, M. Punch, B. C. Raubenheimer, M. Raue, J. Raux, S. M. Rayner, I. Redondo, A. Reimer, O. Reimer, J. Ripken, L. Rob, L. Rolland, G. Rowell, V. Sahakian, L. Saugé, S. Schlenker, R. Schlickeiser, C. Schuster, U. Schwanke, M. Siewert, H. Sol, R. Steenkamp, C. Stegmann, J.-P. Tavernet, R. Terrier, C. G. Théoret, M. Tluczykont, G. Vasileiadis, C. Venter, P. Vincent, H. J. Völk, and S. J. Wagner. Discovery of extended VHE gamma-

ray emission from the asymmetric pulsar wind nebula in MSH 15-52 with HESS. *Astronomy and Astrophysics*, 435:L17–L20, May 2005. [cited at p. 152, 225]

[54] F. Aharonian, A. G. Akhperjanian, K.-M. Aye, A. R. Bazer-Bachi, M. Beilicke, W. Benbow, D. Berge, P. Berghaus, K. Bernlöhr, C. Boisson, O. Bolz, C. Borgmeier, I. Braun, F. Breitling, A. M. Brown, J. Bussons Gordo, P. M. Chadwick, L.-M. Chounet, R. Cornils, L. Costamante, B. Degrange, A. Djannati-Ataï, L. O'C. Drury, G. Dubus, T. Ergin, P. Espigat, F. Feinstein, P. Fleury, G. Fontaine, S. Funk, Y. A. Gallant, B. Giebels, S. Gillessen, P. Goret, C. Hadjichristidis, M. Hauser, G. Heinzelmann, G. Henri, G. Hermann, J. A. Hinton, W. Hofmann, M. Holleran, D. Horns, O. C. de Jager, I. Jung, B. Khélifi, N. Komin, A. Konopelko, I. J. Latham, R. Le Gallou, A. Lemière, M. Lemoine, N. Leroy, T. Lohse, A. Marcowith, C. Masterson, T. J. L. McComb, M. de Naurois, S. J. Nolan, A. Noutsos, K. J. Orford, J. L. Osborne, M. Ouchrif, M. Panter, G. Pelletier, S. Pita, G. Pühlhofer, M. Punch, B. C. Raubenheimer, M. Raue, J. Raux, S. M. Rayner, I. Redondo, A. Reimer, O. Reimer, J. Ripken, L. Rob, L. Rolland, G. Rowell, V. Sahakian, L. Saugé, S. Schlenker, R. Schlickeiser, C. Schuster, U. Schwanke, M. Siewert, H. Sol, R. Steenkamp, C. Stegmann, J.-P. Tavernet, R. Terrier, C. G. Théoret, M. Tluczykont, G. Vasileiadis, C. Venter, P. Vincent, B. Visser, H. J. Völk, and S. J. Wagner. Very high energy gamma rays from the composite SNR G 0.9+0.1. *Astronomy and Astrophysics*, 432:L25–L29, March 2005. [cited at p. 152, 225]

[55] F. Aharonian, A. G. Akhperjanian, A. R. Bazer-Bachi, M. Beilicke, W. Benbow, D. Berge, K. Bernlöhr, C. Boisson, O. Bolz, V. Borrel, I. Braun, A. M. Brown, R. Bühler, I. Büsching, S. Carrigan, P. M. Chadwick, L.-M. Chounet, R. Cornils, L. Costamante, B. Degrange, H. J. Dickinson, A. Djannati-Ataï, L. O'C. Drury, G. Dubus, K. Egberts, D. Emmanoulopoulos, P. Espigat, F. Feinstein, E. Ferrero, A. Fiasson, G. Fontaine, S. Funk, S. Funk, M. Füßling, Y. A. Gallant, B. Giebels, J. F. Glicenstein, P. Goret, C. Hadjichristidis, D. Hauser, M. Hauser, G. Heinzelmann, G. Henri, G. Hermann, J. A. Hinton, A. Hoffmann, W. Hofmann, M. Holleran, D. Horns, A. Jacholkowska, O. C. de Jager, E. Kendziorra, B. Khélifi, N. Komin, A. Konopelko, K. Kosack, I. J. Latham, R. Le Gallou, A. Lemière, M. Lemoine-Goumard, T. Lohse, J. M. Martin, O. Martineau-Huynh, A. Marcowith, C. Masterson, G. Maurin, T. J. L. McComb, E. Moulin, M. de Naurois, D. Nedbal, S. J. Nolan, A. Noutsos, K. J. Orford, J. L. Osborne, M. Ouchrif, M. Panter, G. Pelletier, S. Pita, G. Pühlhofer, M. Punch, B. C. Raubenheimer, M. Raue, S. M. Rayner, A. Reimer, O. Reimer, J. Ripken, L. Rob, L. Rolland, G. Rowell, V. Sahakian, A. Santangelo, L. Saugé, S. Schlenker, R. Schlickeiser, R. Schröder, U. Schwanke, S. Schwarzburg, A. Shalchi, H. Sol, D. Spangler, F. Spanier, R. Steenkamp, C. Stegmann, G. Superina, J.-P. Tavernet, R. Terrier, C. G. Théoret, M. Tluczykont, C. van Eldik, G. Vasileiadis, C. Venter, P. Vincent, H. J. Völk, S. J. Wagner, and M. Ward. Energy dependent γ-ray morphology in the pulsar wind nebula HESS J1825-137. *Astronomy and Astrophysics*, 460:365–374, December 2006. [cited at p. 152, 225]

[56] V. M. Kaspi, M. S. E. Roberts, and A. K. Harding. *Isolated neutron stars*, pages 279–339. April 2006. [cited at p. 152]

[57] F. Aharonian, A. G. Akhperjanian, A. R. Bazer-Bachi, M. Beilicke, W. Benbow, D. Berge, K. Bernlöhr, C. Boisson, O. Bolz, V. Borrel, I. Braun, A. M. Brown, R. Bühler, I. Büsching, S. Carrigan, P. M. Chadwick, L.-M. Chounet, R. Cornils, L. Costamante, B. Degrange, H. J. Dickinson, A. Djannati-Ataï, L. O'C. Drury, G. Dubus, K. Egberts, D. Emmanoulopoulos, P. Espigat, F. Feinstein, E. Ferrero, A. Fiasson, G. Fontaine, S. Funk, S. Funk, M. Füßling, Y. A. Gallant, B. Giebels, J. F. Glicenstein, P. Goret, C. Hadjichristidis, D. Hauser, M. Hauser, G. Heinzelmann, G. Henri, G. Hermann, J. A. Hinton, A. Hoffmann, W. Hofmann, M. Holleran, D. Horns, A. Jacholkowska, O. C. de Jager, E. Kendziorra, B. Khélifi, N. Komin, A. Konopelko, K. Kosack, I. J. Latham, R. Le Gallou, A. Lemière, M. Lemoine-Goumard, T. Lohse, J. M. Martin, O. Martineau-Huynh, A. Marcowith, C. Masterson, G. Maurin, T. J. L. McComb, E. Moulin, M. de Naurois, D. Nedbal, S. J. Nolan, A. Noutsos, K. J. Orford, J. L. Osborne, M. Ouchrif, M. Panter, G. Pelletier, S. Pita, G. Pühlhofer, M. Punch, B. C. Raubenheimer, M. Raue, S. M. Rayner, A. Reimer, O. Reimer, J. Ripken, L. Rob, L. Rolland, G. Rowell, V. Sahakian, A. Santangelo, L. Saugé, S. Schlenker, R. Schlickeiser, R. Schröder, U. Schwanke, S. Schwarzburg, A. Shalchi, H. Sol, D. Spangler, F. Spanier, R. Steenkamp, C. Stegmann, G. Superina, J.-P. Tavernet, R. Terrier, M. Tluczykont, C. van Eldik, G. Vasileiadis, C. Venter, P. Vincent, H. J. Völk, S. J. Wagner, and M. Ward. 3.9 day orbital modulation in the TeV γ-ray flux and spectrum from the X-ray binary LS 5039. *Astronomy and Astrophysics*, 460:743–749, December 2006. [cited at p. 154, 225]

[58] F. Aharonian, A. G. Akhperjanian, U. Barres de Almeida, A. R. Bazer-Bachi, Y. Becherini, B. Behera, M. Beilicke, W. Benbow, K. Bernlöhr, C. Boisson, A. Bochow, V. Borrel, I. Braun, E. Brion, J. Brucker, P. Brun, R. Bühler, T. Bulik, I. Büsching, T. Boutelier, S. Carrigan, P. M. Chadwick, A. Charbonnier, R. C. G. Chaves, L.-M. Chounet, A. C. Clapson, G. Coignet, L. Costamante, M. Dalton, B. Degrange, C. Deil, H. J. Dickinson, A. Djannati-Ataï, W. Domainko, L. O. '. Drury, F. Dubois, G. Dubus, J. Dyks, K. Egberts, D. Emmanoulopoulos, P. Espigat, C. Farnier, F. Feinstein, A. Fiasson, A. Förster, G. Fontaine, M. Füßling, S. Gabici, Y. A. Gallant, L. Gérard, B. Giebels, J. F. Glicenstein, B. Glück, P. Goret, C. Hadjichristidis, D. Hauser, M. Hauser, S. Heinz, G. Heinzelmann, G. Henri, G. Hermann, J. A. Hinton, A. Hoffmann, W. Hofmann, M. Holleran, S. Hoppe, D. Horns, A. Jacholkowska, O. C. de Jager, I. Jung, K. Katarzyński, S. Kaufmann, E. Kendziorra, M. Kerschhaggl, D. Khangulyan, B. Khélifi, D. Keogh, N. Komin, K. Kosack, G. Lamanna, J.-P. Lenain, T. Lohse, V. Marandon, J. M. Martin, O. Martineau-Huynh, A. Marcowith, D. Maurin, T. J. L. McComb, C. Medina, R. Moderski, E. Moulin, M. Naumann-Godo, M. de Naurois, D. Nedbal, D. Nekrassov, J. Niemiec, S. J. Nolan, S. Ohm, J.-F. Olive, E. de Oña Wilhelmi, K. J. Orford, J. L. Osborne, M. Ostrowski, M. Panter, G. Pedaletti, G. Pelletier, P.-O. Petrucci, S. Pita, G. Pühlhofer, M. Punch, A. Quirrenbach, B. C. Raubenheimer, M. Raue, S. M. Rayner, M. Renaud, F. Rieger, J. Ripken, L. Rob, S. Rosier-Lees, G. Rowell, B. Rudak, J. Ruppel, V. Sahakian, A. Santangelo, R. Schlickeiser, F. M. Schöck, R. Schröder, U. Schwanke, S. Schwarzburg, S. Schwemmer, A. Shalchi, J. L. Skilton, H. Sol, D. Spangler, Ł. Stawarz, R. Steenkamp, C. Stegmann, G. Superina, P. H. Tam, J.-P. Tavernet, R. Terrier, O. Tibolla, C. van Eldik, G. Vasileiadis, C. Venter,

J. P. Vialle, P. Vincent, M. Vivier, H. J. Völk, F. Volpe, S. J. Wagner, M. Ward, A. A. Zdziarski, and A. Zech. Limits on an Energy Dependence of the Speed of Light from a Flare of the Active Galaxy PKS 2155-304. *Physical Review Letters*, 101(17):170402–+, October 2008. [cited at p. 155, 225]

[59] K. T. Brazier, A. Carraminana, P. M. Chadwick, T. R. Currell, and N. A. Dipper. The University of Durham Southern Hemisphere VHE gamma ray telescope. *Experimental Astronomy*, 1:77–99, 1989. [cited at p. 158]

[60] H. Kubo, A. Asahara, G. V. Bicknell, R. W. Clay, Y. Doi, P. G. Edwards, R. Enomoto, S. Gunji, S. Hara, T. Hara, T. Hattori, S. Hayashi, C. Itoh, S. Kabuki, F. Kajino, H. Katagiri, A. Kawachi, T. Kifune, L. T. Ksenofontov, T. Kurihara, R. Kurosaka, J. Kushida, Y. Matsubara, Y. Miyashita, Y. Mizumoto, M. Mori, H. Moro, H. Muraishi, Y. Muraki, T. Naito, T. Nakase, D. Nishida, K. Nishijima, M. Ohishi, K. Okumura, J. R. Patterson, R. J. Protheroe, N. Sakamoto, K. Sakurazawa, D. L. Swaby, T. Tanimori, H. Tanimura, G. Thornton, F. Tokanai, K. Tsuchiya, T. Uchida, S. Watanabe, T. Yamaoka, S. Yanagita, T. Yoshida, and T. Yoshikoshi. Status of the CANGAROO-III project. *New Astronomy Review*, 48:323–329, April 2004. [cited at p. 158]

[61] M. Ghigo, O. Citterio, F. Mazzoleni, G. Pareschi, B. Aschenbach, H. Bräuninger, P. Friedrich, G. Hasinger, T. Döhring, H. Esemann, R. Jedamzik, E. Hoelzel, and G. Parodi. The manufacturing of the XEUS x-ray glass segmented mirrors: status of the investigation and last results. In O. Citterio & S. L. O'Dell, editor, *Society of Photo-Optical Instrumentation Engineers (SPIE) Conference Series*, volume 5168 of *Society of Photo-Optical Instrumentation Engineers (SPIE) Conference Series*, pages 180–195, February 2004. [cited at p. 158]

[62] A. Förster, M. Doro, P. Brun, R. Canestrari, P. Chadwick, L. Font, M. Ghigo, E. Lorenz, M. Mariotti, J. Michalowski, J. Niemiec, G. Pareschi, B. Peyaud, and K. Seweryn. Mirror development for CTA. In *Society of Photo-Optical Instrumentation Engineers (SPIE) Conference Series*, volume 7437 of *Society of Photo-Optical Instrumentation Engineers (SPIE) Conference Series*, August 2009. [cited at p. 167]

[63] CTA collaboration. The Cherenkov Telescope Array CTA, An advanced facility for ground-based high-energy Gamma-ray astronomy. Letter of Intent written by the CTA consortium, 2009. [cited at p. 167]

[64] Gianpaolo Motta. Sviluppo di segmenti di specchi leggeri per telescopi cherenkov. Laurea Thesis, April 2010. [cited at p. 168]

[65] Pittsburg Corning. http://www.foamglas.com/. [cited at p. 176]

[66] R. Canestrari, M. Ghigo, G. Pareschi, S. Basso, G. Motta, M. Doro, E. Giro, and L. Lessio. Techniques for the manufacturing of stiff and lightweight optical mirror panels based on slumping of glass sheets: concepts and results. In *Society of Photo-Optical Instrumentation Engineers (SPIE) Conference Series*, volume 7437 of *Society of Photo-Optical Instrumentation Engineers (SPIE) Conference Series*, August 2009. [cited at p. 189]

List of Symbols and Abbreviations

Abbreviation	Description	Definition
AGN	Active Galactic Nuclei	page 109
ALMA	Atacama Large Millimeter/submillimeter Array	page 24
AO	Adaptive Optics	page 10
BMFB	BundesMinisterium für Bildung und Forschung	page 116
CANGAROO	Collaboration of Australia and Nippon for a GAmma Ray Observatory in the Outback	page 110
CFRP	Carbon Fiber Reinforced Plastic	page 116
CMM	Coordinate Measuring Machine	page 47
CTA	Cherenkov Telescope Array	page 127
CTE	Coefficient of Thermal Expansion	page 45
ESO	European Southern Observatory	page 3
ELT	Extremely Large Telescope	page 3
E-ELT	European-Extremely Large Telescope	page 3
ETH Zurich	Eidgenössische Technische Hochschule Zürich	page 116
FEA	Finite Element Analysis	page 36
FP6	Sixth Framework Programme	page 33
FWHM	Full Width Half Maximum	page 73
HEGRA	High Energy Gamma Ray Astronomy experiment	page 109
HESS	High Energy Spectroscopic System	page 110
HST	Hubble Space Telescope	page 21
IACT	Imaging Atmospheric Cherenkov Telescope	page 107
INAF	Istituto Nazionale di AstroFisica	page 43
INFN	Istituto Nazionale di Fisica Nucleare	page 116
JWST	James Webb Space Telescope	page 24
LGS	Laser Guide Star	page 10
LST	Large Size Telescope	page 135
LTP	Long Trace Profilometer	page 83
MAGIC	Major Atmospheric Gamma-ray Imaging Cherenkov telescope	page 110

Abbreviation	Description	Definition
MICINN	MInisterio de Ciencia e INNovacin	page 116
MPE	Max-Planck-institut für Extraterrestrische physik	page 46
MPG	Max-Planck-Gesellschaft	page 116
MSFC	Marshall Space Flight Center	page 46
MST	Medium Size Telescope	page 135
OAB	Osservatorio Astronomico di Brera	page 43
OPD	Optical Path Difference	page 73
OPL	Optical Path Length	page 73
OPTICON	OPTical Infrared COordination Network for astronomy	page 33
OWL	OverWhelmingly Large	page 3
PAH	Polycyclic Aromatic Hydrocarbon	page 24
PMT	Photon Photomultiplier Tube	page 129
PSD	Power Spectral Density	page 88
PSF	Point Spread Function	page 12
P-V	Peak-to-Valley	page 50
rms	root mean square	page 74
SST	Small Size Telescope	page 135
VERITAS	Very Energetic Radiation Imaging Telescope Array System	page 110
VHE	Very High Energy	page 109
VLT	Very Large Telescope	page 11
VLTI	Very Large Telescope Interferometer	page 24

List of Figures

List of Tables